JOURNAL OF THE AERONAUTICAL SCIENCES

VOLUME 22 AUGUST, 1955 NUMBER 8

ST. LOUIS PUBLIC LIBRARY AUG 19 1955

CONTENTS

Experimental Investigation of Influence of Edge Shape on the Aerodynamic Characteristics of Low Aspect Ratio Wings at Low Speeds.....G. E. BARTLETT AND R. J. VIDAL 517

General Air-Frame Dynamics of a Guided Missile.....BARNEY L. BYRUM AND E. RUSSELL GRADY 534

Propagation of Stall in a Compressor Blade Row.....FRANK E. MARBLE 541

An Application of Variation Methods to the Computation of the Deformation of a Cantilever Plate Subjected to Nonuniform and Aeroelastically Induced Loads.....EUGENE E. COVERT 555

Analysis of Peak-Holding Optimalizing Control....H. S. TSIEN AND S. SERDENGECTI 561

Readers' Forum: "Solution of Combined Bending and Torsion Problems by Means of the Electrical Conducting Sheet Analogy," by N. E. Friedmann and D. Rosenthal; "Turbulent Boundary Layers on Nozzle Liners," by R. E. Meyer; "On a Class of Two-Dimensional Channel Flows with a Straight Sonic Line," by A. J. A. Morgan; "Simultaneous Measurements of Velocity and Temperature Profiles for Adiabatic Supersonic Flow of Air in a Tube," by Joseph Kaye, George A. Brown, Julius C. Westmoreland, and Edward F. Kurtz, Jr.; "Brachistocronic Maneuvers of a Variable Mass Aircraft in a Vertical Plane," by Placido Cicala and Angelo Miele; "Note on a Formula of H. W. Emmons," by J. A. Steketee; "A Simplified Expression for the Dihedral Effect of a Flexible Wing," by W. P. Rodden; "Some Static Aeroelastic Design Considerations Relating to Flap-Type Control Surfaces," by Martin Zlotnick; "On Approximate Solutions for the Compressible Flow Around Oscillating Thin Wings," by Marten Landahl, Holt Ashley, and Erik Mollo-Christensen; "A Remark on 'A Simple Laminar Boundary Layer with Secondary Flow,'" by M. Z. v. Krzywoblocki; "A Short Cut in Computing Product of Inertia," by Kenneth G. Merriam; "Interaction Equation for the Buckling of Unstiffened Cylinders Under Combined Bending, Torsion, and Internal Pressure," by Bertram Klein; "The Effect of Axial Flow in a Burner on Combustion Oscillation Frequencies," by R. T. Newton and J. C. Truman; "Note on the Compressible Laminar Boundary Layer with Heat Transfer and Pressure Gradient," by Eli Reshotko and Clarence B. Cohen; "Engineering Relations for Friction and Heat Transfer to Surfaces in High Velocity Flow," by E. R. G. Eckert; "Remark on Supersonic Nozzle Design," by R E. Meyer..571–588

Published by

INSTITUTE OF THE AERONAUTICAL SCIENCES, INC.

JOURNAL OF THE AERONAUTICAL SCIENCES

Editor: HUGH L. DRYDEN, *Director, NACA*
Associate Editor: ROBERT R. DEXTER
Managing Editor: RITA J. TURINO
Editorial Assistant: CAROLINE TAYLOR

Editorial Committee

Aerodynamics

Dean R. Chapman
Francis H. Clauser
Antonio Ferri
Alexander Flax
R. Paul Harrington
R. T. Jones
Carl Kaplan
H. W. Liepmann
C. C. Lin
H. F. Ludloff
Harold Luskin
John R. Markham
Clark B. Millikan
Shatswell Ober
W. Bailey Oswald
C. D. Perkins
Elliott G. Reid
H. J. E. Reid
Russell Robinson
George S. Schairer
G. B. Schubauer
W. R. Sears
John Stack
Theodore Theodorsen
Th. von Kármán

Air Transport

Charles Froesch
J. A. Herlihy
R. D. Kelly
Otto E. Kirchner
Jerome Lederer
John C. Leslie
R. Dixon Speas

Flight Testing

R. R. Gilruth
Melvin N. Gough
W. L. Howland
W. F. Milliken, Jr.
E. G. Stout

Structures and Materials

W. B. Bleakney
E. W. Conlon
John E. Duberg
E. C. Hartmann
N. J. Hoff
Samuel Levy
J. F. McBrearty
Alfred S. Niles
W. Ramberg
F. R. Shanley
C. R. Strang
S. Timoshenko
H. S. Tsien

Rotating Wing Aircraft

F. B. Gustafson
K. H. Hohenemser
Bartram Kelley
R. B. Maloy
Ralph McClarren
R. H. Miller
R. H. Prewitt
Igor I. Sikorsky

Vibration and Flutter

Lee Arnold
M. A. Biot
R. L. Bisplinghoff
William Bollay
Chieh-Chien Chang
J. P. Den Hartog
I. E. Garrick
Martin Goland
Theodore Theodorsen

Aircraft Design

W. E. Beall
E. H. Heinemann
Hall L. Hibbard
Richard Hutton
C. L. Johnson
A. A. Kartveli
E. G. Stout
F. K. Teichmann
Robert J. Woods

Electronics in Aviation

Welcome W. Bender
K. C. Black
M. V. Kiebert, Jr.
David S. Little
S. B. Rogers
Paul Rosenberg
L. M. Sherer

Physiologic Problems

H. G. Armstrong
Louis H. Bauer
Robert J. Benford
W. Randolph Lovelace, II
Ross A. MacFarland

Fuels and Oils

D. P. Barnard
J. H. Doolittle
Graham Edgar
R. T. Goodwin
A. M. Rothrock

Flight Propulsion

George W. Brady
Frank W. Caldwell
L. S. Hobbs
E. E. Johnson
Joseph Keenan
R. P. Kroon
Hans Reissner
Abe Silverstein
C. Fayette Taylor
E. S. Taylor
P. B. Taylor
E. S. Thompson
H. S. Tsien

Instruments

Allan G. Binnie
Charles H. Colvin
Frank R. Cook
C. S. Draper
S. G. Eskin
O. E. Esval
C. F. Savage
R. C. Sylvander

Meteorology

C. F. Brooks
D. M. Little
F. W. Reichelderfer
K. C. Spengler

SUBSCRIPTION RATES

JOURNAL OF THE AERONAUTICAL SCIENCES, Published Monthly.—United States and Possessions: 1 Year, $12.00; Single Copies, $1.50. Foreign Countries Including Canada (American Currency Rates): 1 Year, $13.00; Single Copies, $1.50.

AERONAUTICAL ENGINEERING REVIEW, Published Monthly.—United States and Possessions: 1 Year, $3.00; Single Copies, $0.50. Foreign Countries Including Canada (American Currency Rates): 1 Year, $3.50; Single Copies, $0.50.

Notices of change of address should be sent to the Institute at least 30 days prior to actual change of address.

Manuscripts for publication, proofs, and all correspondence should be addressed to the Editorial Office of the JOURNAL.

Correspondence regarding subscriptions may be addressed to Publication Office, 20th and Northampton Sts., Easton, Pa., or to the Editorial Office of the JOURNAL OF THE AERONAUTICAL SCIENCES, 2 East 64th Street, New York 21, N.Y.

Copyright, 1955, by the Institute of the Aeronautical Sciences, Inc.

Entered as Second Class Matter at the Post Office, Easton, Pa., May 1, 1937. Acceptance for mailing at a special rate of Postage provided for in the Act of August 24, 1912. Authorized April 29, 1937.

JOURNAL OF THE AERONAUTICAL SCIENCES

VOLUME 22 AUGUST, 1955 NUMBER 8

Experimental Investigation of Influence of Edge Shape on the Aerodynamic Characteristics of Low Aspect Ratio Wings at Low Speeds*

G. E. BARTLETT† AND R. J. VIDAL‡

Cornell Aeronautical Laboratory, Inc.

SUMMARY

Some of the more significant results of an experimental investigation of the influence of edge shape on the aerodynamic characteristics of a family of low aspect ratio wings ($AR \geq 2$), having straight trailing edges and taper ratios between zero and one, are presented.

The results are shown to correlate with the approximate linear lifting-surface theory of Lawrence and with the semiempirical nonlinear theory of Flax and Lawrence. The discussion centers around (1) the effects of various leading and side-edge shapes, (2) the influence of leading edges, and (3) the effects of retreating side edges. Implications of the results as regards such design factors as lift-curve slope, stability and control, and leading-edge suction and drag are discussed. In addition, the possibility of developing a new type of roll control for low aspect ratio wings, based on edge-flow-separation effects, is considered.

INTRODUCTION

PRIOR TO THE ADVENT of the transonic and supersonic airborne vehicle, there was relatively little need for the low aspect ratio wing, and consequently only a minimum amount of research was forthcoming on such configurations. Requirements in the field of military aviation over the past few years have, however, been responsible for the introduction of the low aspect ratio lifting surface as a desirable and necessary component of high-speed aircraft and missiles.

Considerable effort, both experimental and theoretical, has been expended on low aspect ratio configurations at supersonic speeds, and methods have been developed that afford rapid and satisfactory predictions of the aerodynamic characteristics of these configurations. The aerodynamic behavior of these same configurations are not as well understood at subsonic and transonic speeds. Many of the design criteria for transonic and supersonic aircraft apply to the subsonic regime. For this reason, satisfactory methods for predicting the aerodynamic characteristics of low aspect ratio lifting surfaces are of interest.

The present paper includes experimental results together with theoretical correlations for a series of low aspect ratio wing tests, run at low speeds. These tests were designed to attempt to fill some of the gaps in available data disclosed by previous investigations at Cornell Aeronautical Laboratory.

The investigation included studies of the effects of variation of wing plan form, edge shape, Reynolds Number, and aspect ratio on the linear and nonlinear aerodynamic forces. In addition, pressure distributions near the wing edges were obtained to aid in the analysis and interpretation of the data. Most of the wings tested had straight trailing edges; one series, however, had retreating trailing edges (trailing-edge span smaller than the maximum span). The questions investigated were mainly in connection with viscous effects on edge separation which may result in nonlinear increments of lift. The bulk of the discussion in this paper pertains to the implications of sharp and round side edges, leading-edge influence, and retreating side edges on such design parameters as lift-curve slope, stability and control, and leading-edge suction and drag.

Presented at the Aerodynamics Session, National Summer Meeting, IAS, Los Angeles, June 21–24, 1954.

* This paper is based upon research carried out under Contract Number AF33(038)-17397, E. O. Number 465-2 BR-1, administered by the Aeronautical Research Laboratory of the Wright Air Development Center. The project was under the technical direction of Fred L. Daum of that Laboratory.

† Head, Applied Aerodynamics Section, Aerodynamics Research Department.

‡ Associate Aerodynamicist.

Background Information

A pronounced nonlinear relationship between aerodynamic coefficients and angle of attack is typical of wings of nearly all plan forms when the aspect ratio is less than approximately 3. Since the usual lifting-surface theory predicts linear relationships, it is apparent that new expressions must be developed before low aspect ratio wing aerodynamic coefficients can be predicted with suitable accuracy.

Bollay,[1] Weinig,[2] Kriesis,[3] Scholz,[4] and others have presented nonlinear lifting-surface theories for low aspect ratio wings. Although the predictions from these theories are in accord with many experimental results, none are adequate for general usage. Recognizing the viscous origin of the nonlinear lift, Legendre,[5] Adams,[6] Brown and Michael,[7] Edwards,[8] Cheng,[9] and others have recently attempted more rigorous solutions to this problem by representing the vortices due to edge separation as free vortices embedded in a potential flow at some position above the wing. By making suitable assumptions concerning the forces acting on the free vortices and the vortex sheets connecting the separation point and the free vortices, these authors show that the viscous lift is of the order, $(AR)^{1/3}(\alpha)^{5/3}$.

These results presuppose a knowledge of the point at which separation occurs, and for practical purposes, are necessarily restricted to sharp edged wings.

Flax and Lawrence,[10] in 1951, examined the available experimental data on low aspect ratio wings and observed that there were unmistakable correlations between the characteristics of such wings and the geometry of the wing leading and side edges. Since none of the theories previously mentioned allow edge geometry as a parameter, they are limited in applicability to the class of airfoils for which they were developed. The theories of references 1–4 are further limited in that they offer no means of predicting moment characteristics.

Since these early observations regarding edge influences, Cornell Aeronautical Laboratory has been endeavoring to develop expressions that will have adequate versatility and be accurate enough for engineering application. The C.A.L. approach to this problem has involved drawing on the linearized theory of a lifting surface in a steady flow for a basic term to which is added one or more nonlinear terms. Lawrence[11, 12] has developed a theory suitable for predicting the linear aerodynamic characteristics for all plan forms of aspect ratio below 4 and having straight trailing edges. Goodman[13] has numerically evaluated the basic equation of Lawrence's theory and prepared charts of $dC_L/d\alpha$ and dC_M/dC_L for a large number of plan forms. Stone[14] has carried out numerical calculations of the effects of flap deflection, aileron deflection, and dynamic-stability derivatives.

The development of general expressions suitable for predicting the nonlinear viscous effects that are inherent in the aerodynamic characteristics of low aspect ratio wings is not in as satisfactory state as is the derivation of the linear expressions. The magnitudes of the nonlinear effects are, however, large enough so that they can not be disregarded in calculations of low aspect ratio wing coefficients.

The cross-flow drag concept suggested in reference 3 and, earlier, by Betz[15] for low aspect ratio wings, and suggested for use on slender bodies of revolution by Allen[16] and Van Dyke,[17] appears to suffice providing adequate attention is given to the geometry of the wing edges. The cross-flow drag theory presumes that there is an additional normal force on each transverse cross section of a very low aspect ratio wing, stemming from the drag associated with the two-dimensional viscous flow around a long cylinder of similar section characteristics. The significant velocity is that component of the free-stream velocity normal to the wing.

In applying viscous cross-flow theory, only terms of order α and α^2 need be retained, and the viscous contribution to normal force is taken as a constant times α^2 rather than a constant times the more rigorous $\sin^2 \alpha$. The total lift coefficient on a low aspect ratio wing then is expressed by the equation

$$C_L = (dC_L/d\alpha)_0\alpha + C_{D_c}\alpha^2 \quad (1)$$

and the total moment coefficient (positive nose up) about the apex is expressed by

$$C_M = (dC_M/dC_L)_0\,(dC_L/d\alpha)_0\,\alpha - (\bar{x}/c)C_{D_c}\alpha^2 \quad (2)$$

where $\bar{x}$ is the distance from the wing apex or leading edge to the centroid of area, and c is the root chord. $(dC_M/dC_L)_0$ and $(dC_L/d\alpha)_0$ are the slopes of the pitching moment and lift curves respectively at zero degrees angle of attack.

The selection of a cross-flow drag coefficient, C_{D_c}, which is appropriate for a given configuration, involves the consideration of many factors such as edge shape, plan form, thickness ratio, Reynolds Number, etc. A thin sharp-edged wing of virtually any plan form will exhibit cross sections transverse to its fore and aft axis that closely approach a two-dimensional flat plate; consequently, one would be justified in selecting a C_{D_c} of 2, the well-established cross-flow drag coefficient for a two-dimensional flat plate. Furthermore, the sharp edges of the wing preclude the possibility of the flow behaving in any manner other than separating right at the edge, thereby removing the necessity for any consideration of the Reynolds Number influence. A thick wing having a varying cross section, on the other hand, should have its cross-flow drag force calculated by integrating the drag force per unit length. Consider, for example, the delta wings tested by Lange and Wacke[18] which had NACA 0012 sections. The cross section near the nose of these wings more nearly approximates a body of revolution than a thin plate, while the cross section of the major portion of the wing may be likened to a plate of finite thickness with round edges. It can be seen that a good approximation to the cross-flow effects could be obtained by experimentally determining the cross-flow drag of each section falling between these two limits and by integrating to obtain the average value for the wing. In-

CONFIG-URATION	ASPECT RATIO	TAPER RATIO	THICKNESS TO CHORD RATIO	LEADING EDGE SWEEP ANGLE	EDGE GEOMETRY CROSS SECTION NORMAL TO EDGE		
					LEADING	SIDE	TRAILING
	1.500	0	5.00%	-	2" 14°15'		
	1.500	0	7.50%	-	3" 6"		"
	1.500	0	10.00%	-	4"		"
	2.000	0	5.00%	-	SAME AS 1		"
	2.000	0	7.50%	-	SAME AS 2		"
	2.000	0	10.00%	-	SAME AS 3		"
	1.500	1.000	7.50%	0°	SAME AS 1		"
	1.397	0.884	6.61%	10°	"	"	"
	1.317	0.786	5.89%	20°	"	"	"
	1.232	0.698	5.23%	30	"	"	"
	1.080	0.500	5.00%	0°	SAME AS 3	"	"
	1.080	0.500	10.00%	0°	"		4" 8"

TABLE 1. Model geometric characteristics.

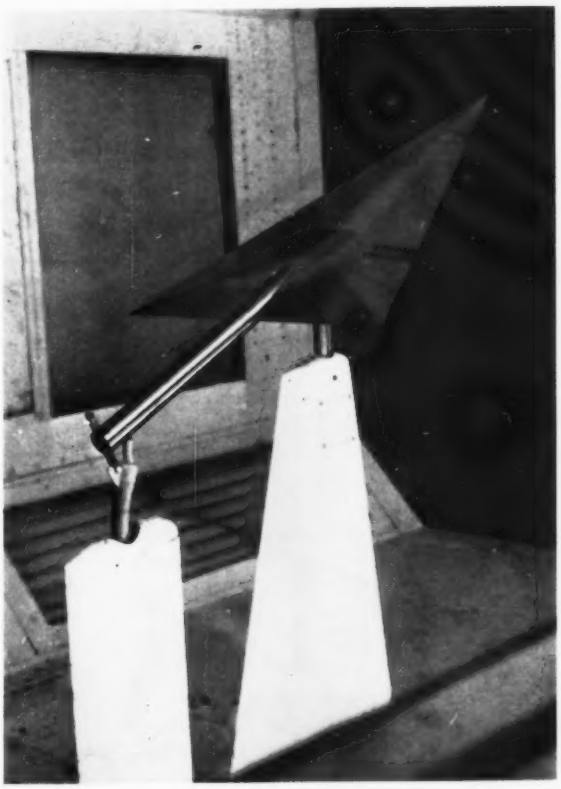

FIG. 2. Typical wind tunnel installation aspect ratio 1.5 sharp-edged delta wing.

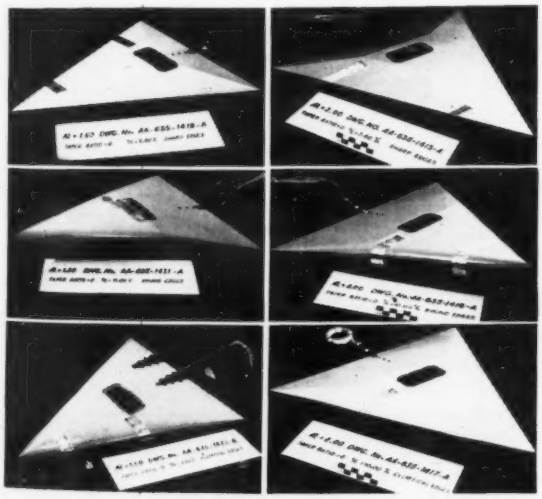

FIG. 1. Aspect ratio 1.5 and 2.0 delta wings.

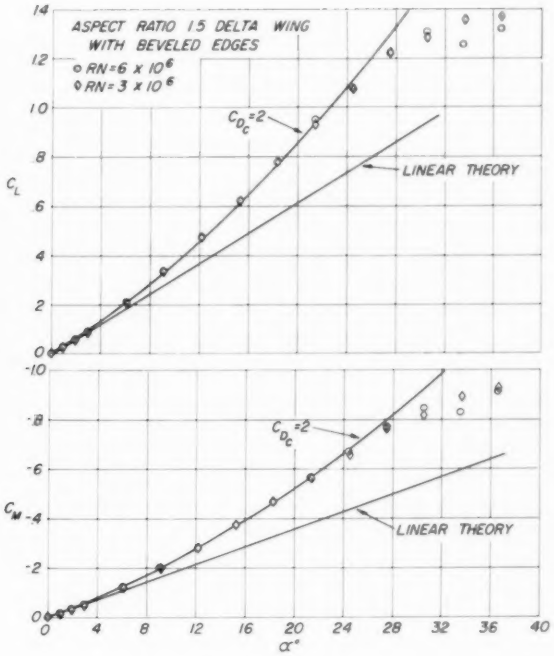

FIG. 3.

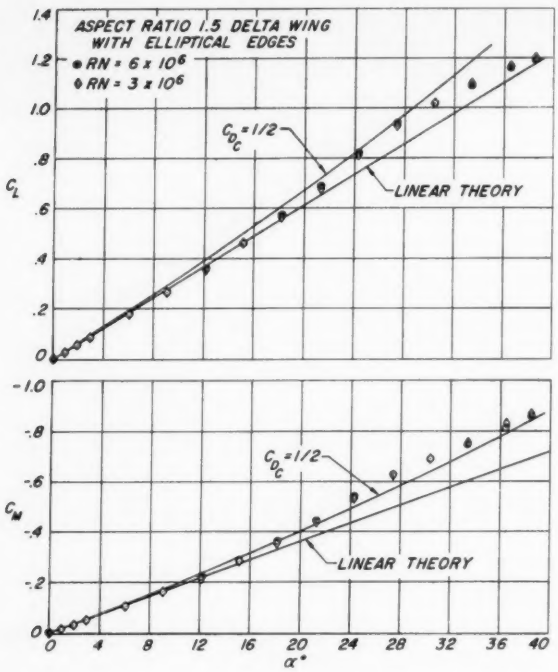

FIG. 4.

deed, this approximation would be useful if it were feasible to predict the value of $U\alpha$, the cross-flow velocity, at which each section would first come under the influence of separation. If such a calculation could be made, a cross-flow drag coefficient as a function of angle of attack would be obtained, and as a consequence, it is expected that the use of such a coefficient in predicting the nonlinear characteristics of a wing would be laborious. Rather than attempt such a time-consuming calculation, it might be more desirable to consider an "average" or effective cross-flow drag coefficient; that is, a coefficient which would not predict exactly the viscous effects at each angle of attack, but would approximate the effects at all angles of attack with engineering accuracy. Recognizing the limitations of such an approach, in most cases it is not justifiable to rigorously obtain an effective cross-flow drag coefficient from chordwise integrations, but rather to obtain this average value by correlating experimental determinations of the nonlinear or viscous lift with $C_{D_c}\alpha^2$. It is not surprising that the experimental lifts of the Lange-Wacke wings show good correlation with theory for $C_{D_c} = 0.50$ because this is of the order of an average value between the turbulent drag coefficient of a circular cylinder, namely 0.35, and the C_{D_c} value of 1.0 associated with a two-dimensional thick plate having round edges. For thin wings with rounded edges, one would expect that this average cross-flow drag coefficient should lie closer to that of a two-dimensional flat plate with rounded edges, and would therefore expect a degree of correlation with $C_{D_c} = 1$.

The cross-flow theory as presented assumes that the cross flow separates immediately at small angles of attack. It should be recognized that this assumption is often erroneous, particularly for the case of wings with rounded edges. However, the cross-flow drag coefficient for these wings is small enough to result in small errors for small angles of attack before separation actually occurs.

The fact that we are dealing with viscous flow when examining the nonlinear effects on the aerodynamic coefficients of wings requires that the Reynolds Number of the cross flow be considered. It is mainly of importance for wings with rounded edges since the nature of the flow may well determine whether such an edge acts as a round or sharp edge. Plates with sharp edges do not exhibit any great variation in drag with Reynolds Number.

One might be inclined, and certainly entitled, to view the application of the viscous cross-flow concept to wings with some reservations. Certainly the flow in transverse planes cannot behave two-dimensionally when the cross section is rapidly changing, as in a wide delta wing. The leading and trailing edges must influence those portions of the wing near them. It seems even more incredible that there can be a coexistence of the flow identified with the cross-flow drag concept—i.e., separated from the side edges, and the potential flow identified with lifting-surface theory. On the other hand, one is forced to concede that even with the introduction of a minimum of empirical constants, extremely good agreement between theory and experiment has been exhibited for both the lift and moment on wings and wing-body combinations.[10, 19] In addition, data from references 20–28 and others have been correlated with the cross-flow theory with similarly good results.

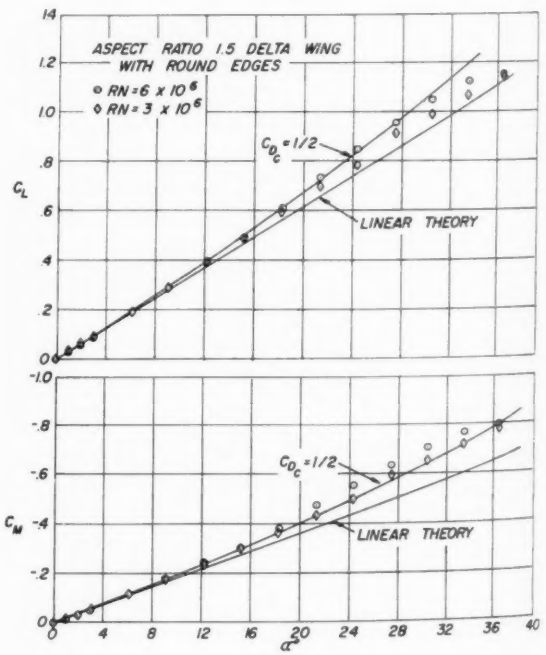

FIG. 5.

A plausible explanation of how there can be the seeming coexistence of the viscous cross flow and the potential flow requisite to lifting-surface theory is suggested in reference 10. The flow which has separated from the edges of the wing is assumed to have a relatively small component of velocity normal to the plate. This separated flow is carried in close proximity to the surface of the plate by the streamwise component of velocity plus the downwash velocity. It can be likened, in most respects, to an addition to the upper-surface boundary layer and an effective addition to the airfoil thickness. The problem then becomes one of considering the wing plus the wake due to cross-flow drag as a new thicker rigid body embedded in a potential flow. Since this added thickness will result in no alteration of the formula for apparent mass, $(\pi\rho b^2)/4$, which is valid for a two-dimensional elliptic cylinder having any length minor axis, the slender-body potential lift should remain unchanged.

Discussion of Experimental Investigation

The present experimental program was initiated at C.A.L. in order to provide additional verification for the cross-flow concept, and in order to consider in greater detail some of the effects originally noted in reference 10. Among those effects investigated were (1) the effects of various leading and side-edge shapes, (2) the conditions under which a leading edge ceases to act as such and acts as a side edge, and (3) the effects of retreating side edges; that is, wings which have a maximum span at some point other than the trailing edge.

Edge-Shape Effects

In reference 10, an attempt was made to establish three general classes of edge shapes; sharp edges ($C_{D_c} = 2$), thin rounded edges ($C_{D_c} = 1$), and thick rounded edges ($C_{D_c} = 1/2$). In order to investigate what constitute aerodynamically round and sharp edges, a series of six delta wings were tested and the data correlated with the existing cross-flow theory. This series of wings consisted of three aspect ratio 1.5 and three aspect ratio 2.0 constant thickness delta wings with beveled edges, elliptical edges, and thick round edges. These wings are illustrated in Fig. 1 and their pertinent physical characteristics are tabulated in Table 1. Fig. 2 shows a typical model installation in the Consolidated-Vultee wind tunnel where all these tests were made. As a matter of interest, the separation vortices can be seen in this photograph as vapor trails emanating from the wing apex. The beveled-edge wings, the elliptical-edge wings, and the round-edge wings had thickness-chord ratios (based on maximum chord) of 5 per cent, $7\frac{1}{2}$ per cent, and 10 per cent respectively. These wings were tested at Reynolds Numbers of 0.9×10^6 per ft. and 1.8×10^6 per ft., and pressure data over the wing edges as well as six component force data were obtained.

The 1.5 aspect ratio wing lift and moment data have been correlated with the linear theory of reference 11 and with the cross-flow theory previously outlined, and these correlations are shown in Figs. 3, 4, and 5. It should be noted that all Reynolds Numbers are based on the root chord. It can be seen that for the beveled-edge wing, the cross-flow theory yields an excellent prediction for lift and moment for all angles of attack of practical interest, and that the results are essentially independent of Reynolds Number. The fact that Reynolds Number does not appreciably alter the data below the stall is expected since the flow must separate at the sharp edge of the wing regardless of the nature of the boundary layer.

Examination of the lift and moment data for the wing with elliptical-edge shape indicates that for low angles of attack, these data correlate best with the linear theory and that the viscous effects are felt only at angles of attack greater than about 15°. This indicates that the cross flow does not begin to separate from the upper surface noticeably until relatively high angles of attack are attained. This conclusion is qualitatively borne out when the pressure distributions over the edges are examined (see Fig. 6). The cross-flow separation is manifested in a vortex motion of the fluid on the upper-wing surface, and consequently the center of the vortex or separated region is characterized as an unusually high negative pressure region on the upper wing surface. It can be seen that this unusual negative pressure region is first apparent at angles of attack between 15° and 18°. These pressure diagrams point out two phenomena of general interest. It is observed that the separation first appears at the aft station ($x/c_{max.} = 0.57$, $15° \leq \alpha \leq 18°$) and then becomes apparent at the forward station ($x/c_{max.} = 0.25$) at $24° \leq \alpha \leq 27°$. This indicates that the separation is a progressive phenomenon, and in this case its progression is relatively slow. For the beveled-edge wing, the pressure distributions indicated that separation occurred almost simultaneously on all transverse wing sections.

The pressure distributions also illustrate the fact that on the wing with elliptical edges, the separation does not occur at the transverse section extremity, but rather well inboard on the wing. The result is that outboard of this separation point the flow pattern is essentially that of a potential flow and that the peak negative pressures at the section extremity are preserved. Since this leading-edge suction continues to exist after separation occurs, it is expected that the drag characteristics will reflect this thrust component.

The lift and moment data for the wing with the thick round edges are seen to correlate well with the cross-flow theory ($C_{D_c} = 1/2$) to high angles of attack, and unexpectedly well at low angles of attack. This low angle of attack correlation would indicate that separation occurred at very low angles of attack, and the pressure distributions (see Fig. 7) indicate that separation first became apparent at the aft station for $9° \leq \alpha \leq 12°$, and at the forward station for $21° \leq \alpha \leq 24°$. At first it would appear that these pressure data are

not in agreement with the force data since the latter suggests separation first occurs at angles of attack well below 9°. However, recognizing the fact that the aft pressure station is approximately at the midchord position, it can be seen that apparently separation occurred at small angles of attack on the most aft portions of the wing and that this separation progressed forward such that it reached the midchord position at $9° \leq \alpha \leq 12°$. Again it should be noted that for the round-edge shape, potential flow peak negative pressures were realized at the transverse section extremities.

The aspect ratio 2.0 wing data for lift and moment have been correlated with the linear and the cross-flow theory and are shown in Figs. 8, 9, and 10. For the wing with beveled edges, it can be seen that use of the cross-flow theory results in a good prediction of both the lift and the moment for angles of attack up to about 18° where the lift and moment slopes begin to lessen as in a gentle stall. The fact that these correlations are good indicates that the cross flow separated at very small angles of attack, as was expected and as is borne out by the pressure distributions.

The lift and moment data for the round and elliptical-edge shapes are seen to correlate best with linear theory, though a small nonlinear effect on the round-edge wing is noted at low angles of attack. On the basis of these force data alone, it would appear that there is little or no cross-flow separation on these wings; however, the pressure distributions (see Figs. 11 and 12) show that separation is first present at angles of attack roughly equal to, or in some cases less than the angles of attack at which separation became apparent on the aspect ratio 1.5 wings having comparable edge shapes. It appears that the aspect ratio 2.0 wings are

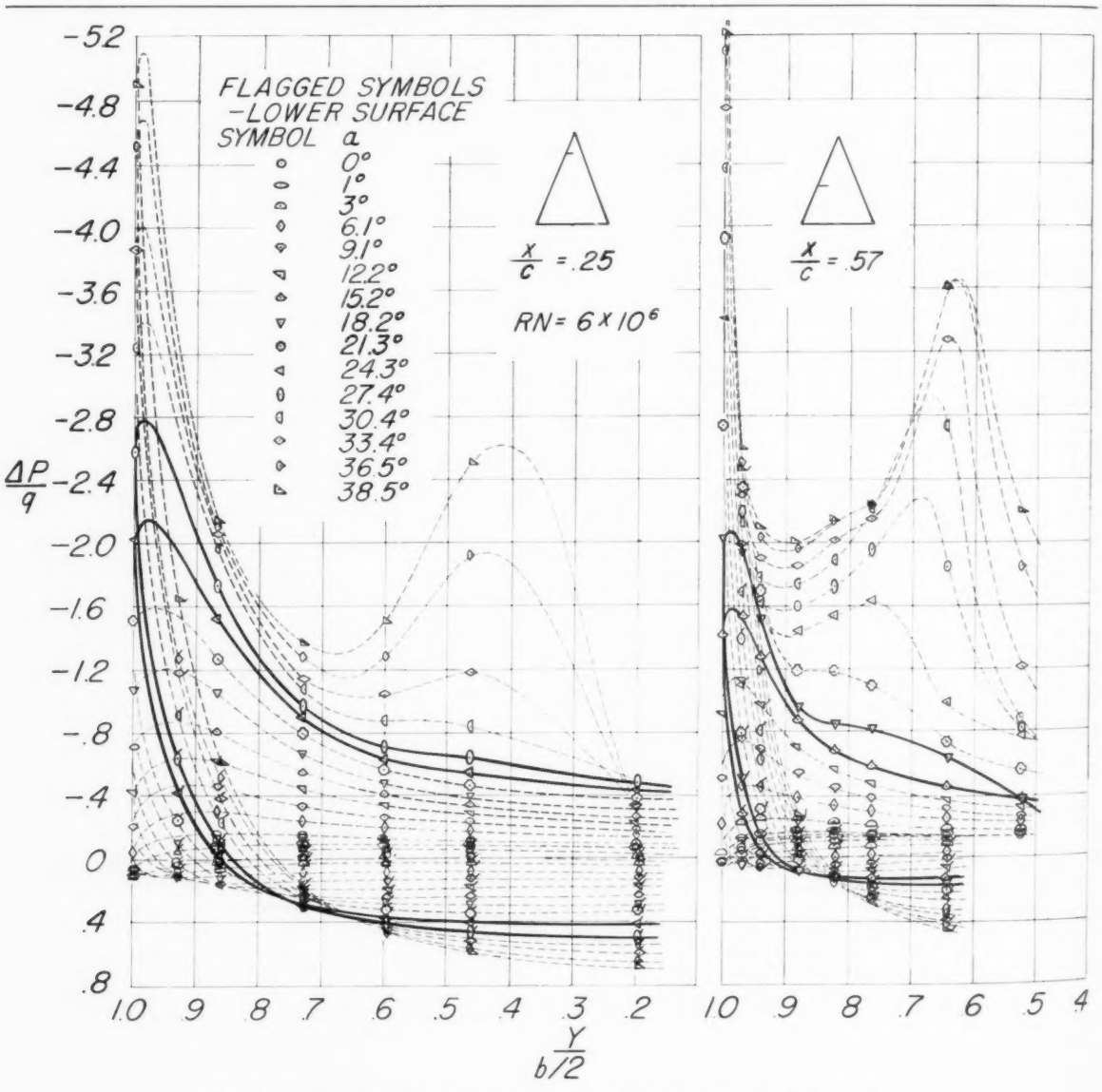

FIG. 6. Pressure distribution on an aspect ratio 1.5 delta wing with elliptical edges.

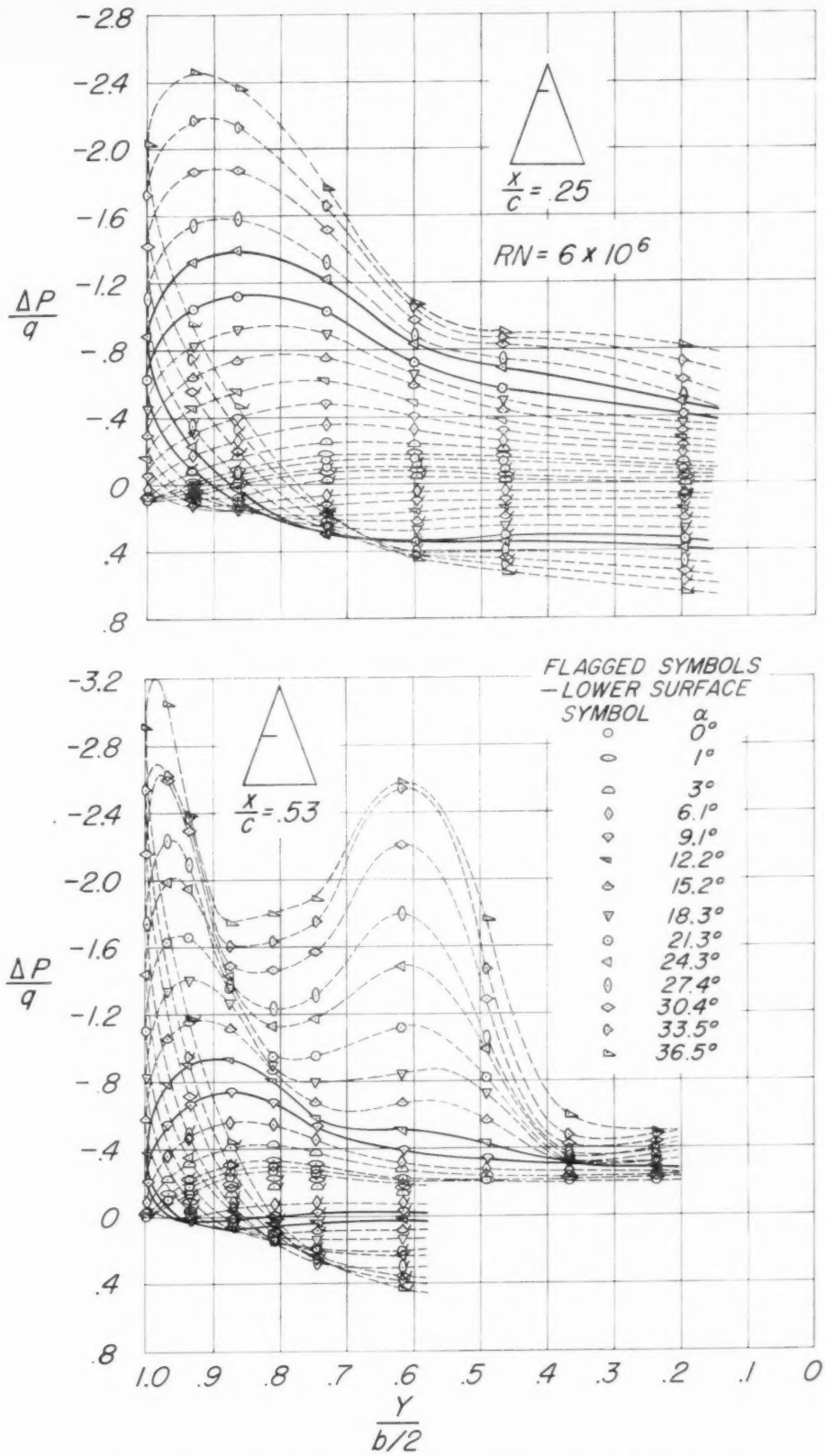

FIG. 7. Pressure distribution on an aspect ratio 1.5 delta wing with round edges.

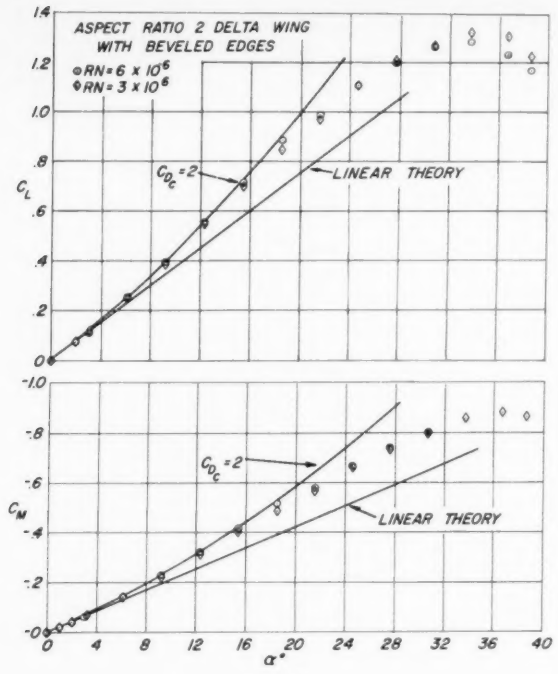

FIG. 8.

more strongly influenced by an additional separation phenomenon; that is, the separated flow permanently detaches from the upper surface earlier for the aspect ratio 2.0 wings than for the aspect ratio 1.5 wings. This conclusion is borne out by the beveled-edge wing data where it can be seen that the lift and moment data first deviate from the cross-flow theory at about $\alpha = 24°$ for the aspect ratio 1.5 wing, and at about $\alpha = 18°$ for the aspect ratio 2.0 wing. This effect has been previously noted[10] and it was proposed that the cross-flow theory ceased to apply for delta wings at an aspect ratio between 2 and 3. For higher aspect ratios the experimental data showed that the lift and moment fell below the linear predictions, and these "critical aspect ratios" were proposed as engineering criteria for the area where linear theory gives a better average prediction than the cross-flow theory. The present data qualitatively substantiate these criteria but also indicate that these criteria must also include edge shape as well as aspect ratio. These data indicate that for a round or elliptical-edge shape, linear theory more accurately predicts the lift and moment than does the cross-flow theory if the aspect ratio is greater than 2.0. For a beveled-edge wing, the data show that the critical aspect ratio is somewhat greater than 2.0, and that for aspect ratio 2.0 wings, the cross-flow theory satisfactorily predicts the aerodynamic characteristics to reasonably high lifts.

It is interesting to examine the effects of edge shape on the drag of these low aspect ratio delta wings. It can be shown that for a thin flat plate model, the resultant force acts normal to the surface and that the induced drag of the wing should be $C_L \tan \alpha$. For wings with elliptical span loadings at moderate angles of attack, classical wing theory indicates that the induced drag should be $C_L^2/\pi AR$. For low aspect ratio wings with elliptical loadings, it can be shown (see, for example, reference 28) that the resultant force lies halfway between the normal to the air stream and the normal to the surface, and the induced drag is $C_L \tan (\alpha/2)$. The drags of the aspect ratio 1.5 and 2.0 delta wings are compared with these drag formulations in

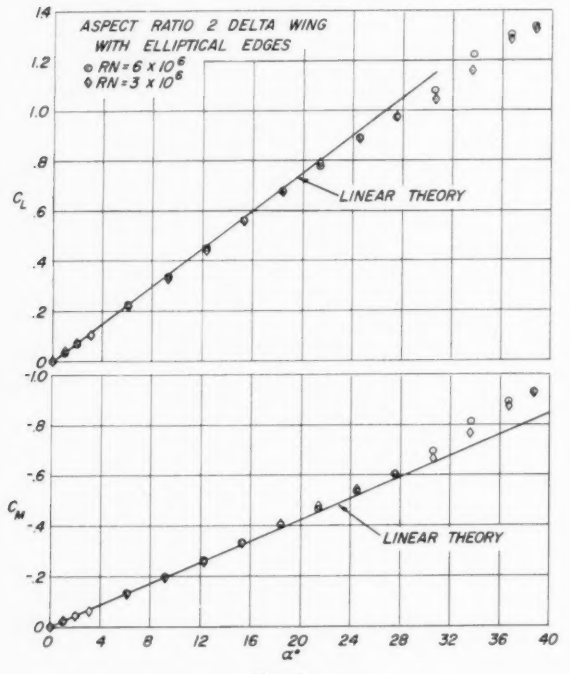

FIG. 9.

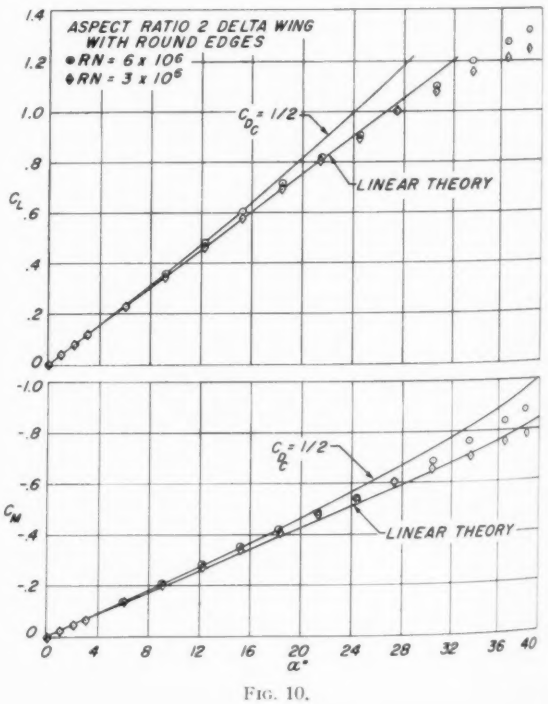

FIG. 10.

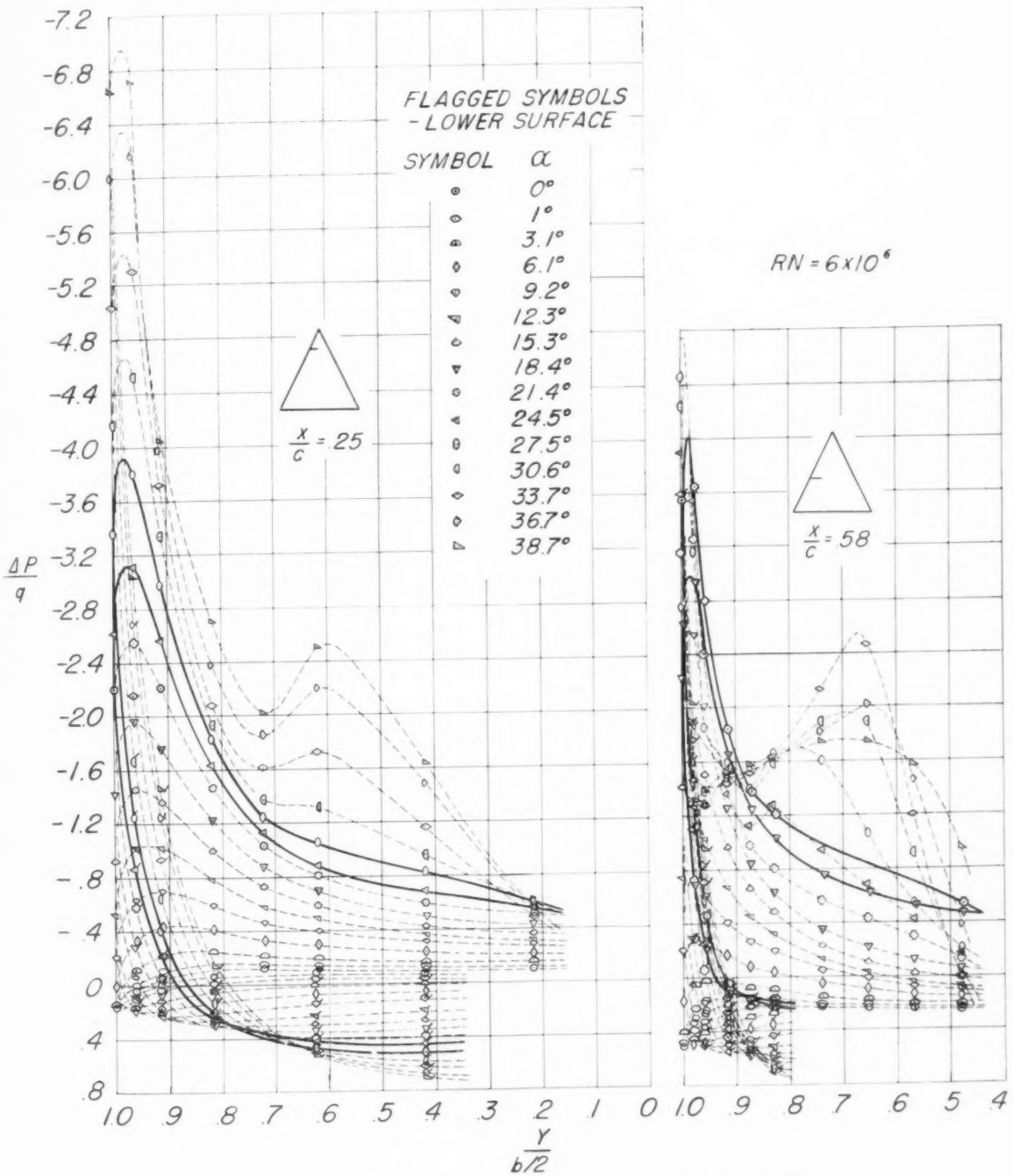

FIG. 11. Pressure distribution on an aspect ratio 2.0 delta wing with elliptical edges.

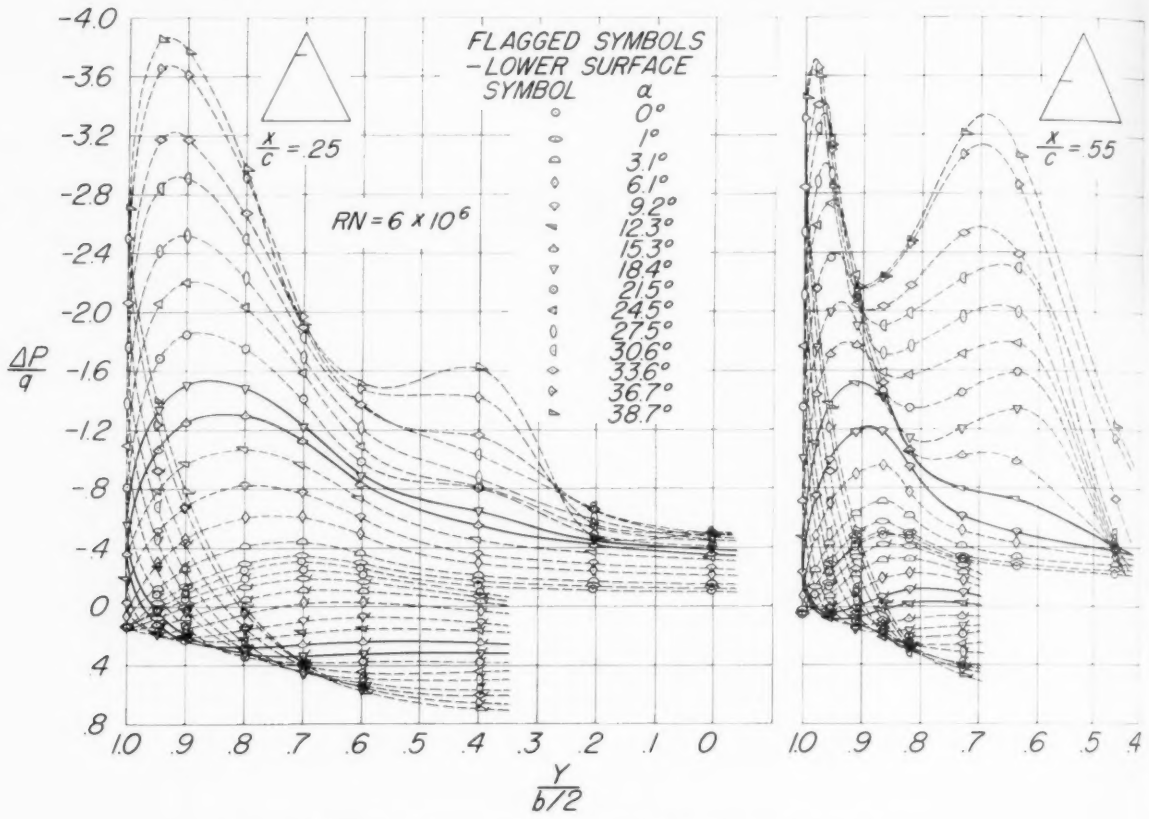

FIG. 12. Pressure distribution on an aspect ratio 2.0 delta wing with round edges.

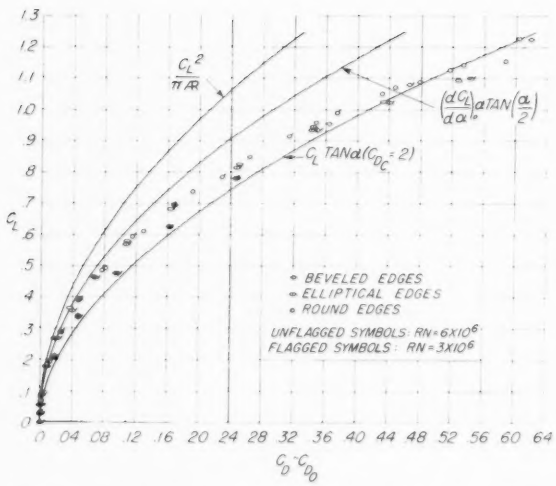

FIG. 13. Drag correlation for the aspect ratio 1.5 delta wings.

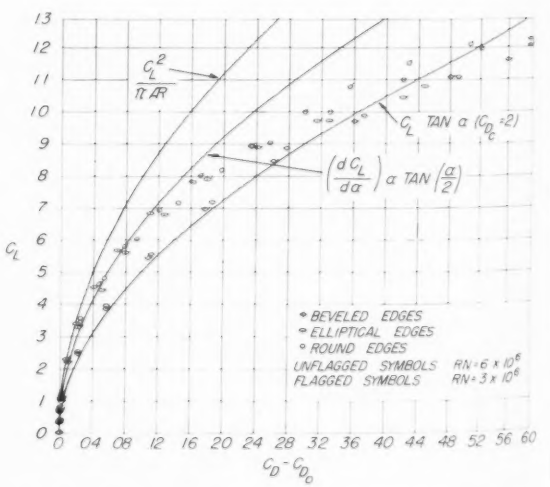

FIG. 14. Drag correlation for the aspect ratio 2.0 delta wings.

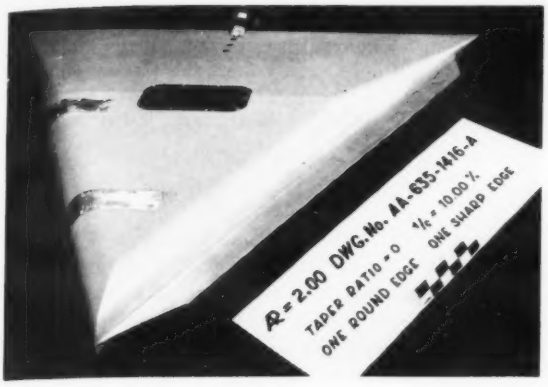

FIG. 15

Figs. 13 and 14. It can be seen that the drag of both beveled-edge wings is slightly less than the flat plate variation, and it has been concluded that this is a result of the airfoil geometry. As is shown in Fig. 1, the sharp edges on these wings were realized by beveling the extremities. Due to the separation phenomena, there exists a relatively high negative pressure region over these edges, and as a consequence, there is a small chordwise thrust force.

The drag of the wings with round and elliptical-edge shapes are seen to correlate well with $C_L \tan(\alpha/2)$, the low aspect ratio induced drag for wings with elliptical loadings. It can be seen that the aspect ratio 1.5 data correlate well with this variation up to the lift coefficient where the lift, moment, and pressure data indicate separation begins, and the drag data then falls roughly parallel to the $C_L \tan \alpha$ curve. The aspect ratio 2.0 data are seen to correlate well with the low aspect ratio variation up to lifts somewhat higher than would be expected from the force and pressure data. This would indicate that the low aspect ratio variation does not hold as well for the higher aspect ratio wing and that the correlation to high lifts is only fortuitous. This conclusion is based on the fact that separation is known to exist at the lower lifts and that this separation must be manifested in drags higher than those predicted by linear theory.

A rather interesting and quite possibly practical idea stemmed from this study of the influence of edge shapes. Lawrence has suggested the utilization of edge effects to achieve roll control of low aspect ratio wings at high angles of attack, since the edge shape influences the nonlinear part of the lift at those angles. The suggested means of achieving rolling moments is to use a side-edge "improver," so called because it increases the lift in the vicinity of the wing side edge where it is used. A simple "improver" could possibly operate by projecting a sharp plate through a slot on a round side edge, thus causing this normally rounded side edge to become aerodynamically a sharp edge. The added nonlinear lift resulting from the sharp edge would induce a rolling moment which could be sizable at high angles of attack for wings of low aspect ratio.

In order to check this idea, the aspect ratio 2.0 delta wing having round edges was fitted with a thin 1/8-in. steel plate that extended the entire length of the left side and projected out about 2 in. (see Fig. 15). The experimental rolling coefficients C_l, referred to body axis are compared with theory in Fig. 16. The theory, in this case, was based on the assumption that the center of viscous lift identified with a sharp edge acts at the centroid of area of one wing panel, and that identified with a round edge acts at the centroid of area of the other wing panel. Using this assumption, it can be readily shown that the rolling moment arising from the difference in viscous lift on the two panels is

$$C_l = (1/6)\alpha^2[(C_{D_{c_1}} - C_{D_{c_2}})/2] \tag{3}$$

where the subscripts 1 and 2 refer to the sharp and round edges respectively. In the light of the experimental results achieved on this wing without the sharp edge, it was assumed that $C_{D_{c_1}} = 2$ and $C_{D_{c_2}} = 1/2$, and the rolling moment for the wing with one sharp edge was

$$C_l = (1/8)\alpha^2 \tag{4}$$

The experimental verification of the predicted rolling moment coefficient is good, as can be seen from Fig. 16. The fact that the experimental rolling moment coefficient is higher than the predicted value at low angles can be attributed to the fact that, while the viscous lift develops on the sharp edge almost immediately upon departure from zero degrees attack angle, the viscous lift does not begin to develop on the round edge until some finite angle has been reached. The lower rolling moment, relative to the predicted curve, at high angles of attack can be due to stall effects and/or changing cross-flow drag, on the round edge particularly.

In order to illustrate more clearly the extent of the rolling influence realized on this test model there are shown, spotted on Fig. 16, the theoretical deflections required of each of the two ailerons on a similar delta wing to give an equivalent rolling moment. The ailerons are assumed to comprise the area along the outboard 25 per cent span of the trailing edge having a chord equal to 10 per cent of the root chord. The aileron deflections were determined by the method reported in reference 14 and are conservative in the sense that there is no effectiveness factor applied. Also ex-

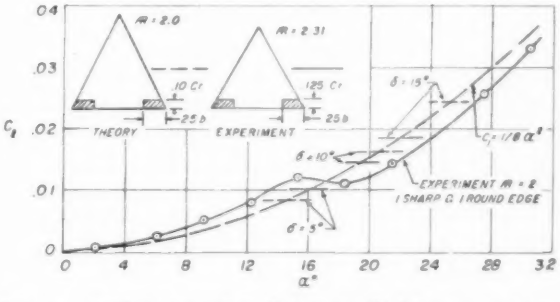

FIG. 16. Rolling moment coefficient for AR 2.0 wing—one improver extended.

hibited on this curve are required ailavator deflections, as determined from experimental results presented by Hawes and May,[20] for a delta wing of aspect ratio 2.31. The ailavators in this case comprise the outboard 25 per cent span of the trailing edge, having a chord equal to 12½ per cent of the root chord.

The "improver" might be used further as a substitute for a maneuvering flap on low aspect ratio wings at high angles of attack. By simultaneously projecting sharp plates from both wing side edges, added lift could be realized with very little pitching moment change.

Leading-Edge Influence

In examining the case of rectangular wings with round and sharp edges, it was found[10] that the cross-flow theory would satisfactorily predict the lift and pitching moment on these wings for any side-edge shape only if the leading edge were round. For the case of a sharp leading edge, it was found that the experimental lift and moment on the wing was substantially greater than expected, and the indications were that additional separation must be taking place. This conclusion was borne out by pressure distributions which showed that on a sharp leading edge, the flow separated at small angles of attack, but subsequently reattached to the upper surface at some distance downstream. This point of reattachment depended on angle of attack; as the angle of attack increased, the point of reattachment moved further aft on the surface. On low aspect ratio wings it was found that so long as the flow reattached to the airfoil, the lift continued to increase nonlinearly, and when this reattachment no longer took place, the airfoil appeared to be stalled.

In comparing the experimental pressure distributions over the sharp leading edge with the theoretical pressure distributions of linear theory, it was found that the overall effects of this leading-edge separation was to eliminate the peak negative pressures near the edge and to result in high negative pressures over a greater portion of the wing. As a consequence, the total lift on the wing was then increased due to the broadening of the negative-pressure region, and the center of the lift was moved aft on the wing. Since the cross-flow theory refers to linear theory for its basic term, it is desirable to visualize these changes due to leading-edge separation as additions to the potential-theory pressure distributions. Consequently, for the present purposes, this additional lift is treated as though it stems from an additional pressure distribution which can only add to and not subtract from the potential-flow pressure distribution. Using this concept, the center of the viscous lift appears to act well back on the wing and far distant from where the actual physical phenomenon takes place.

In correlating the effects of sharp leading edges with the cross-flow theory, it was found empirically in reference 10 that good lift correlation could be obtained if an additional α^2 term were incorporated in the expression for lift coefficient, and good moment correlation would be obtained if this additional lift were treated as though it acted a distance $6c(dC_M/dC_L)_0$ aft from the leading edge. The expressions for the lift and pitching moment become

$$C_L = (dC_L/d\alpha)_0\,\alpha + C_{D_c}\alpha^2 + 1\alpha^2 \tag{5}$$

$$C_M = (dC_M/d\alpha)_0\alpha - (\bar{x}/c)C_{D_c}\alpha^2 + 6(dC_M/dC_L)_0\,(1\alpha^2) \tag{6}$$

where C_{D_c} is the cross-flow drag coefficient of the side edges. It can be seen that this additional lift term is in keeping with the cross-flow concept by noting that the cross-flow drag coefficient for an infinite plate is 2, or the cross-flow drag coefficient per edge should be 1.

In examining sharp-edge delta wings and a certain class of sharp-edged tapered wings, it was found that the cross-flow theory based on side-edge effects ($C_{D_c} = 2$) agreed well with experiment, and that there was apparently no effect of the leading edge—that is, all edges acted as side edges. In considering all tapered wings falling between a rectangular wing and a delta wing, it might be anticipated that there was some leading-edge sweep angle or taper ratio at which the leading edge ceased to incur a separate and distinct separation, and began to act as a side edge. An attempt at determining this critical plan form was undertaken by correlating the available experimental data with the cross-flow theory. It was found that there was little experimental data available for the sweep-angle range of interest, and consequently a series of tapered wings for investigating this phenomenon was incorporated in this experimental program. These wings were derived from a basic $AR = 1.5$ sharp-edged rectangular wing by adding delta-shaped noses to the basic plan form. Four such wings were tested with leading-edge sweep angles of 0°, 10°, 20°, and 30°. Fig. 17 illustrates these wings and the pertinent physical characteristics of each are listed in Table 1. It will be noted that all four wings had the same bevel angle normal to the leading edge.

The force measurements obtained from the wind-tunnel tests were, at first glance, completely contrary to the previous results, in that the rectangular wing results correlated best with $C_{D_c} = 2$ (no leading-edge separation) while the 30° swept wing correlated best with $C_{D_c} = 3$ (full leading-edge separation). However, the pressure data for all wings indicated that leading-edge separation was present, but did not begin until the wing was pitched to an angle of attack of 3° to 6°. It appeared that this might be the source of the discrepancy between theory and experiment since the theory assumes separation to begin immediately at $\alpha > 0°$. Since the bevel angles on these wings were sizable (a half angle of 7.2° normal to the edge) it can be seen that leading-edge separation could not begin until the local flow at the leading edge was inclined at an angle greater than the bevel angle. It should be noted that the side-edge separation can begin immediately for $\alpha > 0°$ since the bevel is normal to stream direction. In order to take into account the effects of this delayed

leading-edge separation, the cross-flow theory was formulated as

$$C_L = (dC_L/d\alpha)_0\alpha + C_{D_{c_{S.E.}}}\alpha^2 + 1(\alpha - \alpha_S)^2 \quad (7)$$

$$C_M = (dC_M/d\alpha)_0\alpha - (\bar{x}/c)C_{D_{c_{S.E.}}}\alpha^2 + 6(dC_M/dC_L)_0(\alpha - \alpha_S)^2 \quad (8)$$

where α_S is the geometric angle of attack at which leading-edge separation first occurs, $C_{D_{c_{S.E.}}}$ is the cross-flow drag coefficient of the side edges, and $(\bar{x}/c)$ is the wing centroid of area. In order to estimate the separation angle of attack, it was assumed that separation occurred when the local angle of attack exceeded the bevel angle. Taking the induced angle of attack to be $(1/\pi\mathbf{R})\ (dC_L/d\alpha)_0\alpha$, the separation angle of attack is then

$$\alpha_S + (1/\pi\mathbf{R})\ (dC_L/d\alpha)_0\alpha_S = \epsilon$$

where ϵ is the half angle of the leading edge measured parallel to the air stream.

The above forms of the cross-flow theory have been used in correlating the lift and moment data obtained for the four wings, and these correlations are shown in Figs. 18, 19, 20, and 21. Examination of these figures shows that good correlation is obtained for all four wings and it appears that the leading edge continues to act as such for all leading-edge sweep angles up to 30° ($\lambda = 0.7$). It should be noted, however, that the above equations, when applied to tapered wings, assume the side-edge effect to exist over the entire wing and the superposition of an additional leading-edge effect. If there is some critical sweep angle at which there is no effect of a leading edge, it would be expected that the experimental data would rather suddenly cease to correlate with the above expressions and would then correlate with the original cross-flow formulations. The fact that this sudden lack of correlation was not encountered with these four wings could show that if a critical sweep angle or taper ratio does exist, it does not exist in the range covered by these wings. On the other hand, it is perhaps more logical to expect that such a critical parameter does not exist and that there is effectively a gradual degeneration of the leading edge into a side edge as the sweep angle is increased. At the limiting taper ratio of zero, this would then require that the nonlinear viscous effects on delta wings be a function of sweep angle or aspect ratio. The data previously discussed for delta wings (see Figs. 3 and 8) might be interpreted as showing some slight aspect ratio effect, but at best, it can only be said that such an effect is indeed small.

It is apparent that the data from these four wings are not sufficient for assessing the validity of these two concepts because of the small variations in viscous effects with plan form, and because of the limited range of plan forms considered. It would appear that the only possible way to determine this question would be to test a complete series of tapered wings ranging from a rectangular wing to a delta wing. If such a series of wings were to be tested, it would be important to ensure that the leading edges were similar in order to minimize such effects as encountered here—i.e., delayed leading-edge separation.

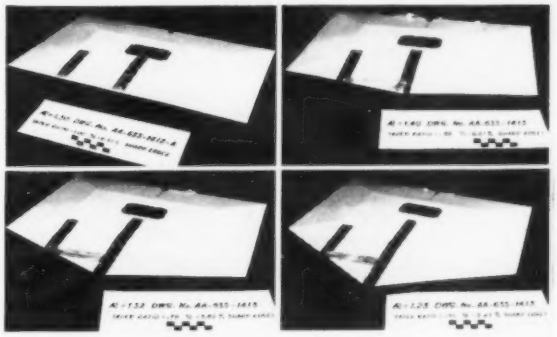

FIG. 17. Tapered sharp-edged wings

The lift due to leading-edge separation has often been considered only for the case of sharp leading edges. Since an aerodynamically round and sharp edge differ only in that the separation occurs at higher angles of attack and that the effects of the separation are of different magnitudes, it would be logical to expect that a wing with a rounded leading edge should exhibit characteristics similar to those of a sharp leading-edge wing. Again using the notion of an empirical C_{D_c} for the leading edge for thin rounded leading edges, the additional viscous term in the lift and moment should be proportional to $(1/2)\alpha^2$, while that for a thick rounded leading edge should be proportional to $(1/4)\alpha^2$. If such an effect for rounded leading edges does exist, it might be expected that this effect would not be in evidence until some angle of attack corresponding to a separation angle of attack for the leading edge. For a sufficiently thick leading edge on a relatively high aspect ratio wing, this effect might never be reflected in the forces due to the counter balancing effect of permanent-flow detachment on the tip portions of the wing. However, the effect might be expected on very low aspect ratio wings which appear to suffer least from permanent-flow detachment at small angles of attack.

An effect having all the characteristics of this leading-edge phenomena occurring on wings with rounded leading edges has been noted in another phase of this experimental program, as well as in other data.[21] However, both sets of data are for tapered wings rather than rectangular wings, thereby casting some doubt on the possibility of attributing the additional nonlinearities to leading-edge separation. The effect has also been noticed in Scholz's[4] data for rectangular wings, but since these wings had retreating side edges, this cannot be accepted as proof that the effect is entirely due to leading-edge separation. It would seem that in order to establish the existence of this phenomenon, it will be necessary to conduct a systematic investigation on a number of rectangular wings with various leading-edge shapes.

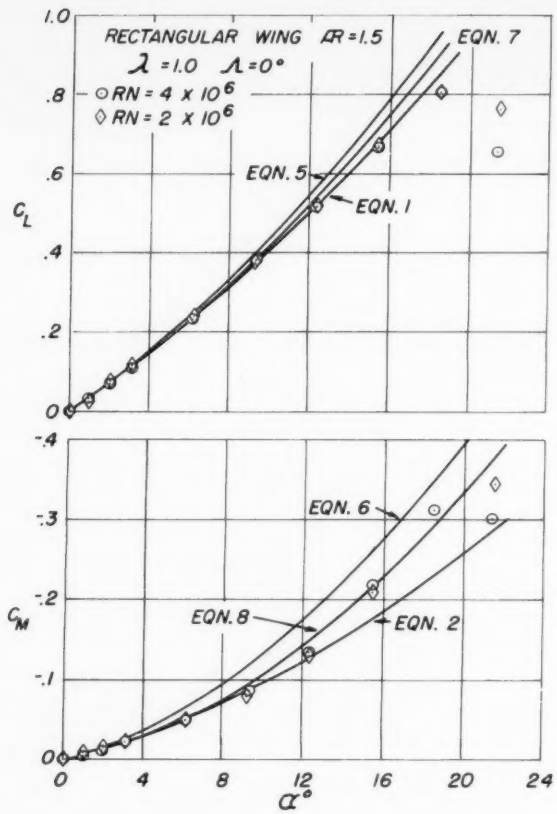

FIG. 18.

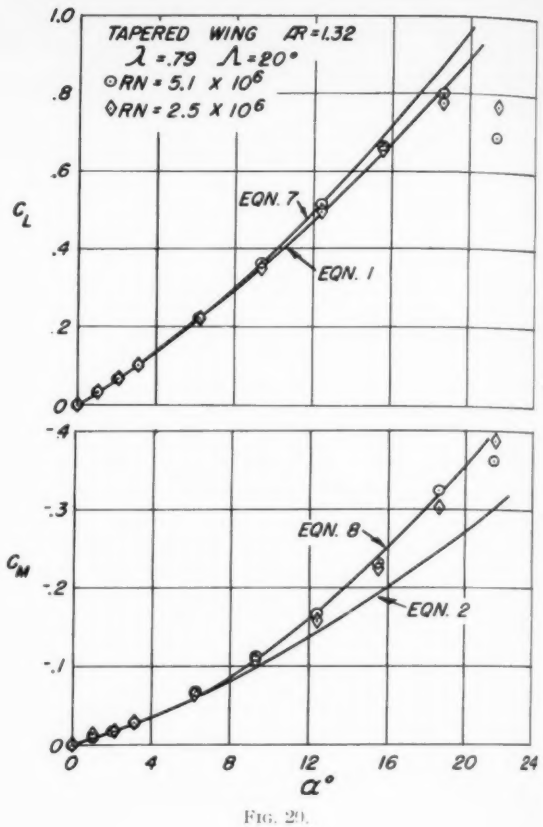

FIG. 20.

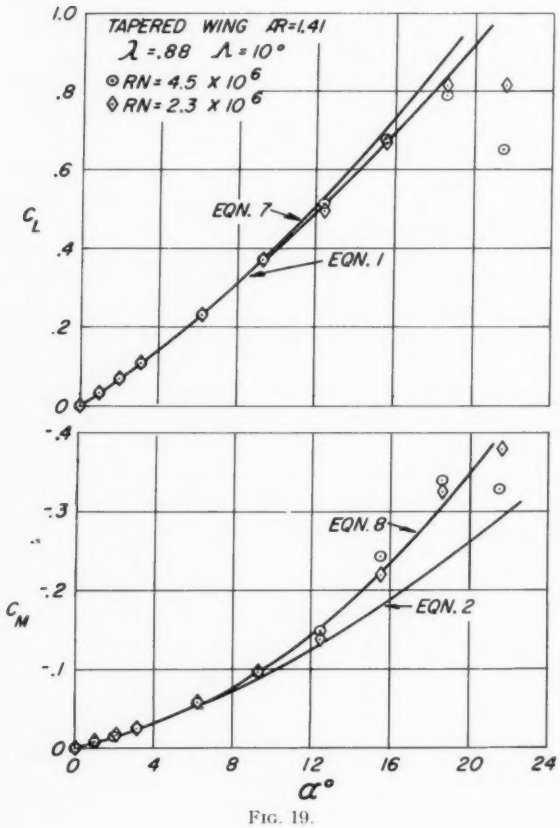

FIG. 19.

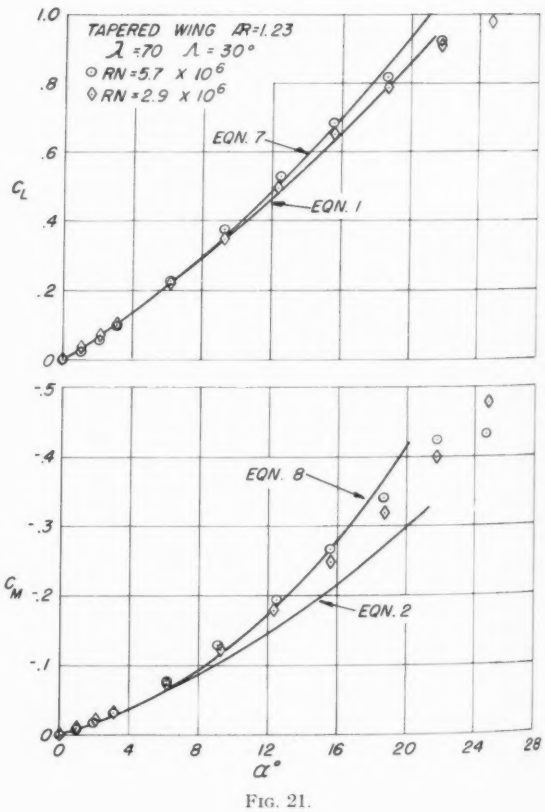

FIG. 21.

Retreating Side-Edge Effects

For the purposes of this investigation, a wing is said to have retreating side edges if there exists a chordwise station on the wing where the span is greater than the trailing-edge span. It can be seen that according to this definition many of the wings used today have retreating side edges.

Since these retreating side edges form a portion of the trailing edge, it must be decided whether or not the Kutta condition is satisfied along these edges before theoretical treatment is possible. Jones[29] treated the case of a wing with sharp retreating side edges, and in applying the Kutta condition along these edges, found the lift to be a function only of the maximum span and the lift on those portions aft of the maximum span to be zero. More exact theories show that if the Kutta condition is satisfied along the retreating side edges, the net lift on those same portions will be small and may be either positive or negative.

For rounded retreating side edges, it was concluded in reference 10 that the Kutta condition does not appear to be satisfied, and that Munk's[30] slender-body theory might lead to a better approximation for the aerodynamic characteristics. On this basis it was concluded that the wing lift would be a function only of trailing-edge span, and that the net lift on the area outboard of the trailing-edge span would be zero. For an estimation of the pitching moment contribution, slender-body theory was used to calculate the centers of pressure of the wing with tips, and of the wing defined by the trailing-edge span. This calculation showed that the effect of the retreating side edges was to cause a shift in center of pressure forward from that given by linear theory by an amount

$$\frac{x}{c} = \frac{1}{c}\int_0^c \left(\frac{b}{b_{t.e.}}\right)^2 dx - 1 \qquad (9)$$

where b is the local wing span and $b_{t.e.}$ is the trailing-edge span. This center-of-pressure location correlated with the available experimental data, but since these data were for a particular type of edge shape, it was decided to test a series of wings with extreme retreating side edges.

The retreating side-edge wings used in this program are illustrated in Fig. 22. Two basic wings of identical plan form were tested in this program—one with a thin round leading edge and sharp side edges, and one with thick round leading and side edges (see Table 1). In order to assess the importance of round and sharp retreating side edges, provision was made for the insertion of 2-in. wide plates along the retreating edge on the round-edge wing. This wing was then tested twice; once with the rounded retreating edges and once with the sharp plates installed.

The results of these tests when correlated with theory were at first somewhat conflicting in that the data from the thin sharp-edge wing agreed well with theory, but the data from the thick round-edge model, with and without the plates, showed relatively poor agreement. This was surprising in that it was anticipated that the only difference in the data from the sharp-edge model and the round-edge model with plates would be in the value of C_{D_c} in the cross-flow term. In addition it was found that the tip correction apparently overestimated the tip effects on pitching moment. These results lead to a re-examination of the retreating side-edge theory as well as an examination into the validity of the experimental data.

In examining the theory it was noted that the tip correction always overestimated the destabilizing tip effects when correlated with the existing experimental data. This tip correction was based on slender-body theory which for a rectangular wing predicts all positive lift to act at the leading edge. Realizing that in the actual case the center of pressure is well aft of the leading edge, the tip correction was altered to take this into account by assuming the negative lift predicted by slender-body theory to remain unchanged in magnitude and position, and the positive lift to be of the same magnitude but acting at the point predicted by lifting-

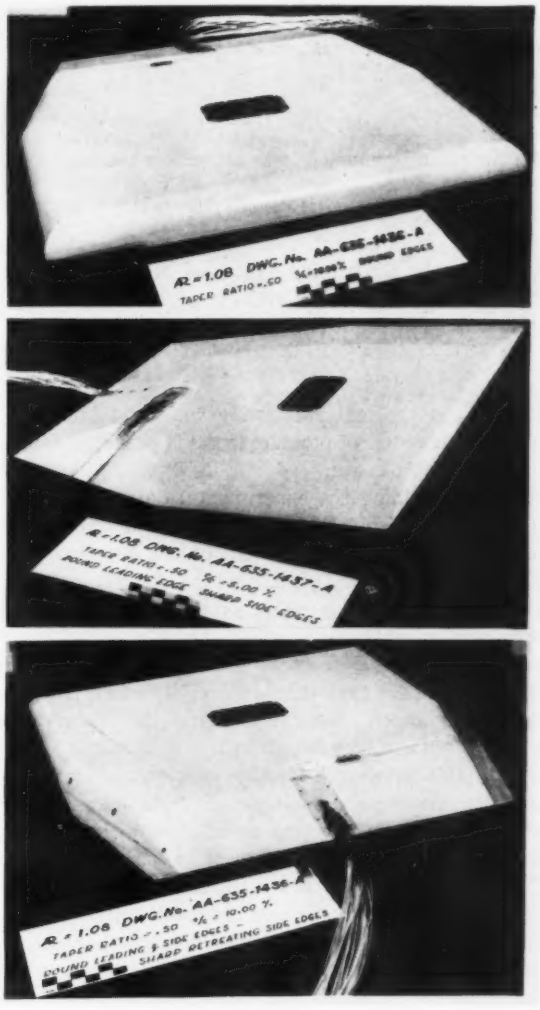
AR = 1.08 DWG. No. AA-635-1436-A
TAPER RATIO = .50
ROUND EDGES
AR = 1.08 DWG. No. AA-635-1437-A
TAPER RATIO = .50
ROUND LEADING EDGE
SHARP SIDE EDGES
AR = 1.08 DWG. No. AA-635-1436-A
TAPER RATIO = .50
ROUND LEADING & SIDE EDGES
SHARP RETREATING SIDE EDGES

FIG. 22. Retreating side-edge wings.

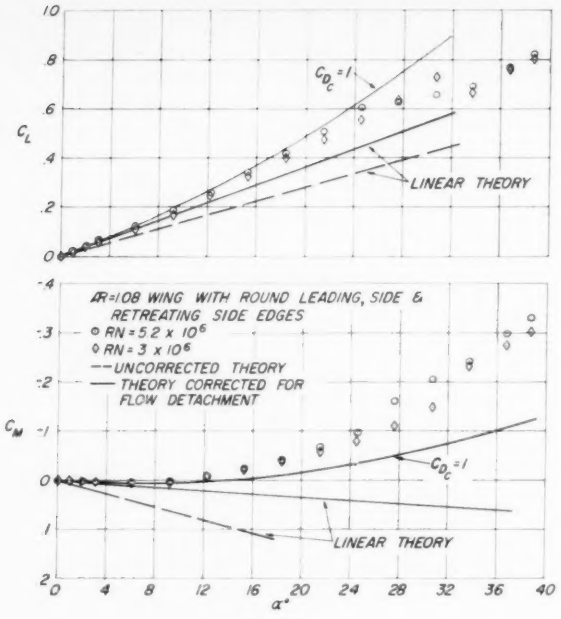

FIG. 23.

surface theory. The lift on the wing was then as originally proposed in reference 10

$$C_L = (S_e/S)\,(dC_L/d\alpha)_e\alpha + C_{D_c}\alpha^2 \qquad (10)$$

but the pitching moment was altered to become

$$C_M = (x/c)\,(S_e/S)\,(dC_L/d\alpha)_e\alpha - (\bar{x}/c)C_{D_c}\alpha^2 \quad (11)$$

where $(dC_L/d\alpha)_e$ is the lift curve slope and S_e is the area determined by the trailing-edge span, $\bar{x}/c$ is the centroid of the entire wing area S, and x/c is given by

$$\frac{x}{c} = \left(\frac{b_m}{b_{t.e.}}\right)^2 \frac{dC_M}{dC_L} + \frac{1}{c}\int_0^c \left(\frac{b}{b_{t.e.}}\right)^2 dx - 1 \quad (12)$$

where b_m is the maximum wing span and (dC_M/dC_L) is the linear center of pressure location predicted for the wing with sharp edges.

After examining the experimental data, it was concluded that a sizable portion of the conflicting results could be attributed to flow detachment from the blunt trailing edge of the thickest wing. It will be noted that the trailing-edge angle on the round side-edge wing was more than 28° while the same angle for all other wings in this program was only 14°. It is then logical to expect that the flow would detach from the thick wing much sooner than from the other wings. The effect of this flow detachment is particularly noticeable in this case since for the wing with rounded retreating side edges there is negative lift over the trailing-edge area while for the same wing with the sharp retreating side-edge plates, there is positive lift over the same regions. In order to estimate the effects of this flow detachment, it was assumed that 7/8 of the beveled trailing edge was under flow detachment, resulting in the complete loss in lift on that area. For the rounded retreating side edges, this loss in lift was calculated in accordance with slender-body theory by using a new trailing-edge span corresponding to that where detachment was assumed to occur. Such a calculation for the same wing with sharp plates attached is possible but very laborious since only the more exact theories predict the positive lift shown by the pressure distributions. Since the flow detachment assumptions did not warrant such calculations, the loss in positive lift was estimated by finding the experimental linear slope and comparing this with the theoretical lifting-surface result. In both cases, the change in pitching moment was estimated by applying the lift loss at the centroid of the assumed flow-detachment area.

The correlation between the experimental data and the theory with flow detachment correction applied are shown in Figs. 23 and 24 for the round side-edge wing with and without the sharp plates. Fig. 25 is the correlation of the sharp-edge wing data with the cross-flow theory, and the correlation is seen to be good up to high angles of attack. Consequently, it can be concluded that the cross-flow theory holds for the sharp-edge wing and that apparently the Kutta condition is satisfied on the sharp retreating side edges.

The correlations of Figs. 23 and 24 are also seen to be good, but owing to the correction for flow detachment, it cannot be said that these data establish the exactness of the rounded retreating side-edge correction. The fact that one round-edge wing configuration (with plates attached) differs from the sharp-edge wing only along a portion of the side edge which cannot alter the linear characteristics certainly lends support to the possibility of flow detachment. Even if this possibility is accepted, the calculations to account for this detachment can only be considered as crude approximations. If one wishes to discount the possibility of flow detachment occurring on the thicker wing, an indication of the effect of rounded retreating side edges and of the worth of a tip correction can be realized by comparing Figs.

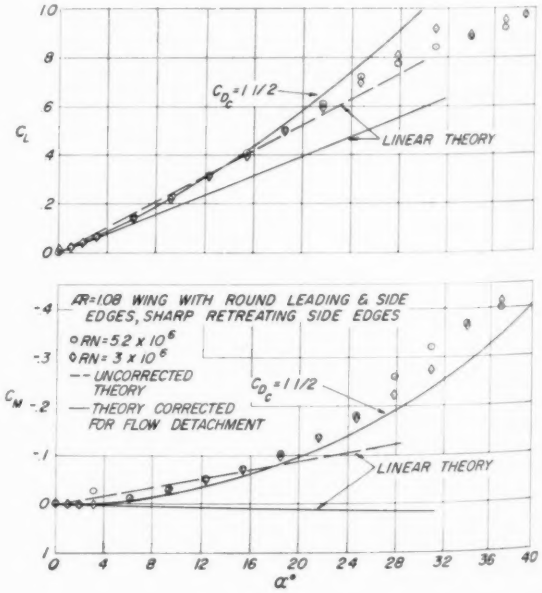

FIG. 24.

23 and 25. This comparison shows that by rounding the edges, a 30 per cent loss in linear lift was incurred, and the wing became, at best, neutrally stable.

In order to examine the validity of the new tip correction more accurately, the linear center-of-pressure data and the linear lift curve data of reference 4 have been compared with predictions based on the new tip correction and the original lift correction in Fig. 26. It can be seen that the new correction yields a good estimate of the edge effects, especially for aspect ratios above 1. The lack of more exact correlation at $b_{t.e.}/c = 1/2$ can be traced, in part, to the difficulty in measuring the linear moment slope at very small angles of attack. It should be noted that in spite of the inaccuracies of the tip correction, it does serve to predict the neutral stability near aspect ratios of 1, while linear theory predicts acceptable stability.

Concluding Remarks

It has become apparent that when dealing with the aerodynamic behavior of low aspect ratio wings, especially at high angles of attack, the shape of the wing edges is a significant parameter. As has been shown, the viscous contribution to the lift and pitching moment may be of a magnitude roughly equivalent to the potential contribution or there may be little or almost no viscous contribution, depending upon the edge shape.

Further research providing additional data on edge influences would be desirable and is to be hoped for.

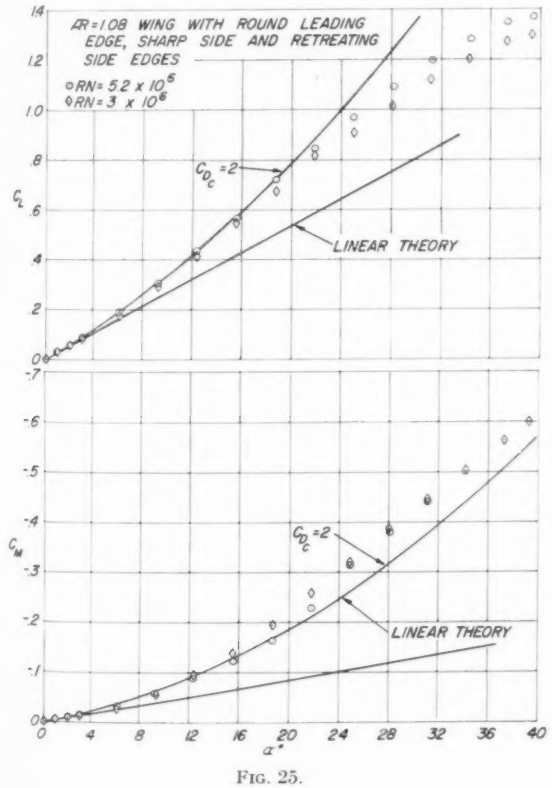

Fig. 25.

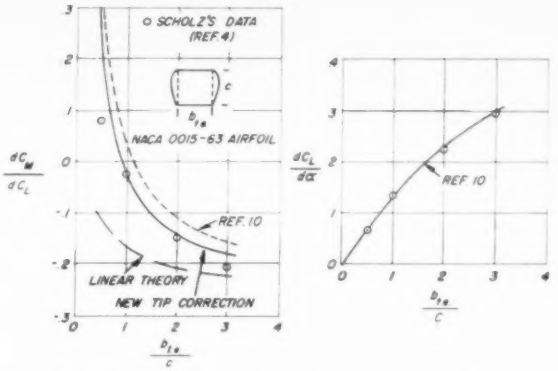

Fig. 26. The effects of round retreating side edges.

References

[1] Bollay, W., *A Nonlinear Wing Theory and its Application to Rectangular Wings of Small Aspect Ratio*, ZAMM Bd. 19, No. 1, pp. 21–35, February, 1939.

[2] Weinig, F., *Lift and Drag of Wings with Small Span*, NACA TM 1151, 1947.

[3] Kriesis, P., *Über rechteckige Tragflügen sehr grober Tiefe*, ZAMM Bd. 24, Heft. 1, pp. 1–5, 1944.

[4] Scholz, N., *Kraft-und Druckverteilungsmessungen an Tragflachen kleiner Streckung*, Forschung auf dem Gebiete des Ingenieurwesens, Part B, Vol. 16, No. 3, pp. 85–91, 1949–1950.

[5] Legendre, R., *Ecoulement au voisinage de la pointe avant d'une aile a forte flèche aux incidences moyennes*, La Recherche Aéronautique, Bulletin Bimestriel, de l'Office National d'Etudes et de Recherches Aéronautiques, Novembre–Decembre, 1952.

[6] Adams, M., *Leading-Edge Separation From Delta Wings at Supersonic Speeds*, Journal of the Aeronautical Sciences, Readers' Forum, Vol. 20, No. 6, p. 430, June, 1953.

[7] Brown, C., and Michael, W., Jr., *Effect of Leading-Edge Separation on the Lift of a Delta Wing*, Journal of the Aeronautical Sciences, Vol. 21, No. 10, pp. 690–694, October, 1954.

[8] Edwards, R., *Leading-Edge Separation From Delta Wings*, Journal of the Aeronautical Sciences, Readers' Forum, Vol. 21, No. 2, p. 134, February, 1954.

[9] Cheng, H., *Remarks on Nonlinear Lift and Vortex Separation*, Journal of the Aeronautical Sciences, Readers' Forum, Vol. 21, No. 3, pp. 212–214, March, 1954.

[10] Flax, A., and Lawrence, H., *The Aerodynamics of Low-Aspect-Ratio Wings and Wing-Body Combinations*, paper presented at the Third Anglo-American Aeronautical Conference, 1951.

[11] Lawrence, H., *The Lift Distribution on Low Aspect Ratio Wings at Subsonic Speeds*, Journal of the Aeronautical Sciences Vol. 18, No. 10, pp. 683–695, October, 1951.

[12] Lawrence, H., *The Pressure Distribution on Low Aspect Ratio Wings in Steady or Unsteady Incompressible Flow*, Journal of the Aeronautical Sciences, Readers' Forum, Vol. 20, No. 3, pp. 218–219, March, 1953.

[13] Goodman, T., *Calculation of Aerodynamic Characteristics of Low Aspect Ratio Wings at Subsonic Speeds*, Cornell Aeronautical Laboratory Report No. AF-743-A-1, August, 1951.

[14] Stone, H., *Aileron Characteristics and Certain Stability Derivatives for Low Aspect Ratio Wings at Subsonic Speeds*, Cornell Aeronautical Laboratory Report No. AF-743-A-3, July, 1952.

[15] Betz, A., "Applied Airfoil Theory," *Aerodynamic Theory*, W. F. Durand, Editor, Durand Reprinting Committee, Vol. IV, pp. 69–72, 1943.

[16] Allen, H., *Pressure Distribution and Some Effects of Viscosity on Slender Inclined Bodies of Revolution*, NACA TN 2044, 1950.

(*Continued on page 588*)

General Air-Frame Dynamics of a Guided Missile

BARNEY L. BYRUM* AND E. RUSSELL GRADY†

Chance Vought Aircraft, Inc.

ABSTRACT

A set of equations which represents the general air-frame dynamics of an intermediate range guided missile is derived and presented in a form suitable for the application of differential analyzer and digital computer techniques. The equations provide a somewhat realistic description of the motion of aerodynamically controlled winged vehicles and are applicable to terminal accuracy studies and dynamic stability studies where higher order effects are of interest.

The motion is referred by means of a set of modified Euler angles to a frame of reference fixed on the earth. The modified Euler angles are generalized coordinates that orient the coordinate system whose motion is described. It is shown that equations describing the motion of body axes are, in general, more useful in the three-dimensional case than those describing the motion of the relative wind system.

It is assumed that the missile is a rigid body of constant mass, that the earth has zero curvature and is not rotating, and that the gravity vector is constant in magnitude and direction. If the decrease in mass due to fuel consumption is not negligible during the time of interest or if jet vanes are used in combination with the aerodynamic control surfaces, the equations are amenable to the necessary modifications.

SYMBOLS

$X_p:(X_1, X_2, X_3)$ = principal axes of inertia or p-system, orthogonal (sense indicated in Fig. 1)

$X_s:(X_1, N, X_3')$ = skew axes or s-system (sense indicated in Fig. 2)

$X_i:(X_1', X_2', X_3')$ = inertial axes or i-system, orthogonal (sense indicated in Figs. 1 and 2)

$X_r:(X, Y, Z)$ = relative wind axes or r-system, orthogonal (sense indicated in Fig. 2)

$X_b(X', Y', Z')$ = body axes or b-system, orthogonal (sense indicated in Fig. 1)

$\vec{u}_k$ = unit vector along the k-axis

$\vec{\epsilon}_s$ = unit vector along the sth skew axis

T = kinetic energy

Q_s = generalized forces

ϕ, θ, ψ = modified Euler angles[1] or generalized coordinates (q_s)

Φ, Θ, Ψ = time rate of change of the generalized coordinates

ϕ = angle between $\vec{\epsilon}_2$ and $\vec{u}_2$ ($\vec{u}_\phi = \vec{\epsilon}_1$); $\vec{\epsilon}_1 = \vec{u}'$

θ = angle between $\vec{u}_1$ and $X_1'X_2'$-plane ($\vec{u}_\theta = \vec{\epsilon}_2$); $\vec{\epsilon}_2 = \vec{u}_N$

ψ = angle between $\vec{u}_{1'}$ and the projection of $\vec{u}_1$ on the $X_1'X_2'$-plane ($\vec{u}_\psi = \vec{\epsilon}_3$); $\vec{\epsilon}_3 = \vec{u}_{3'}$

$\vec{\omega}$ = angular velocity of the p-system

$\omega_p:(p, q, r)$ = components of $\vec{\omega}$ in the p-system

P, Q, R = time rates of change of the ω_p

$\vec{\Omega}$ = angular velocity of the r-system relative to the p-system

$\vec{\omega}^*$ = angular velocity of the r-system

$\{A\}$ = the matrix A

$\vec{M}$ = applied moment

$\vec{k}$ = linear momentum

$\vec{K}$ = time rate of change of linear momentum

$\vec{h}$ = angular momentum

$\vec{H}$ = time rate of change of angular momentum

a_{kl} = direction cosine between the axes k, l

α_{kl} = time rate of change of a_{kl}

N = intersection of the X_2X_3-plane and the $X_1'X_2'$-plane

$\vec{V}_g$ = velocity of the missile

$\vec{W}$ or $\vec{V}_w$ = velocity of the wind

$\vec{V}_r$ = velocity of the missile relative to the air

α = angle of attack,[2] measured from X' to the normal projection of $\vec{V}_r$ in the X_1X_3-plane

β = angle of sideslip,[2] measured from the normal projection of $\vec{V}_r$ in the X_1X_3-plane to $\vec{V}_r$

σ = angle between X_1 and X' (lies in X_1X_3-plane)

r_0 = perpendicular distance from missile c.g. to thrust axis

b = total wing span

S = total wing area, except in case of a hinge moment derivative when it is that portion of the hinged surface lying aft of the hinge line

$q = (1/2)\rho v_r^2$ = dynamic pressure

$\bar{c}$ = mean geometric chord

m = average mass of the missile, including equipment and fuel, during time of interest

$\vec{\Lambda}$ = aerodynamic reaction, which resolves into the conventional aerodynamic forces and moments

$\vec{L} = (-\vec{u}_z)L$ = lift force, acts through the c.g. perpendicular to $\vec{V}_r$ and parallel to the X_1X_3-plane

$\vec{D} = (-\vec{u}_x)D$ = drag force, acts through the c.g. parallel to $\vec{V}_r$ and oppositely directed

$\vec{Y} = \vec{u}_y Y$ = sideforce, acts through the c.g. and forms a right-handed orthogonal system with $\vec{L}$ and $\vec{D}$

$\vec{T}_e = \vec{u}_x' T_e$ = engine thrust, directed along the thrust axis that is parallel to but not coincident with X', Fig. 2

$\vec{mg} = \vec{u}_{3'} mg$ = force due to gravity

Received April 14, 1954.

* Senior Systems Engineer, Aerophysics. Now, Nuclear Design Specialist, The Glenn L. Martin Company.

† Senior Systems Engineer, Guidance.

$C_l qSb$ = total rolling moment about X', a body axis passing through the c.g. parallel to the thrust axis, Fig. 1

$C_m qSc$ = total pitching moment (excluding that due to thrust) about Y' (parallel to X_2), a body axis passing through the c.g. perpendicular to the X_1X_3-plane, Fig. 1

$C_n qSb$ = total yawing moment about Z', a body axis that forms a right-handed orthogonal system with X', Y', Fig. 1

ρ = density of air at flight altitude

Γ = time rate of change of moment of inertia (I)

J_s = generalized momentums

$\{A_k{}^I\}$ = components in the I-system of the time rate of change of $\{V_k{}^I\}$

(1.0) Introduction

A set of equations which represents the general air-frame dynamics of an intermediate range guided missile is derived and tabulated herein. The equations provide a somewhat realistic description of air-frame motion and are applicable to terminal accuracy studies and dynamic stability studies where higher order effects are of interest.

In order to guide a long-range, nonhoming type missile to a given point in space, its motion must be referred to the primary inertial system—i.e., the mean position of the fixed stars—or to a set of axes moving at a constant velocity with respect to the primary system. The motion of intermediate range missiles may be referred to a frame of reference fixed on the earth, however, as if the earth were a secondary inertial system. Although this is not a logically correct procedure, it can be shown that the detriment to terminal accuracy due to such an assumption is small (relative to that caused by equipment limitations and incomplete theory of certain physical phenomena).

The equation of motion may be referred to inertial axes through any set of body axes, Fig. 1, or through the relative wind axes, Fig. 2. Just which coordinate systems are most suitable for investigating the general motion of a guided missile is still an open question. Principal axes of inertia yield the simplest rotational equations, while relative wind axes yield the simplest translational equations. In the two-dimensional case, the present state of theoretical aerodynamics favors the relative wind axes, since the aerodynamic relationships are simpler in this system than in any system of body axes. Unfortunately, all moments of inertia and products of inertia become functions of the angle of attack (α) and the angle of side slip (β) when the motion of the relative wind system is described. If α and β are less than approximately 4°, the corrections are so small that it is sufficiently accurate to regard the relative wind axes as identical with the body axes. Since the corrections are not generally negligible during a terminal maneuver, however, equations describing the motion of body axes are usually more desirable in the three-dimensional case.

The mechanics of a rigid missile in three-dimensional space leads to six special, second-order, nonlinear differential equations: (a) a set of three equations representing the rotational motion of an axis system with origin at the center of gravity of the missile and (b) a set of three equations representing the translational motion of the origin of this axis system. The derivation contained in this paper is based on Lagrange's equations of motion

$$(d/dt)\,(\partial T/\partial \dot{q}_s) - (\partial T/\partial q_s) = Q_s$$

The salient assumptions in the derivation are:

(a) The missile is a rigid body of constant mass.

(b) The earth has zero curvature and is not rotating.

(c) The gravity vector is constant in magnitude and direction.

In order to note any mathematical simplifications and to facilitate procurement of data on the aerodynamic relationships, in general, two sets of equations are derived: (a) a set of equations describing the motion of the principal axes of inertia (and associated missile mass distribution) in the secondary inertial system and (b) a set of equations describing the motion of the relative wind axes (and associated missile mass dis-

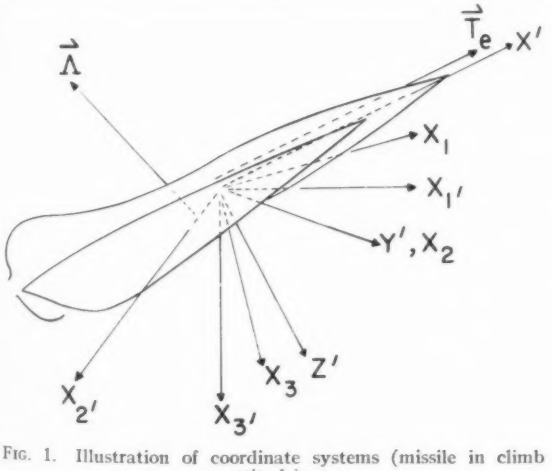

Fig. 1. Illustration of coordinate systems (missile in climb attitude).

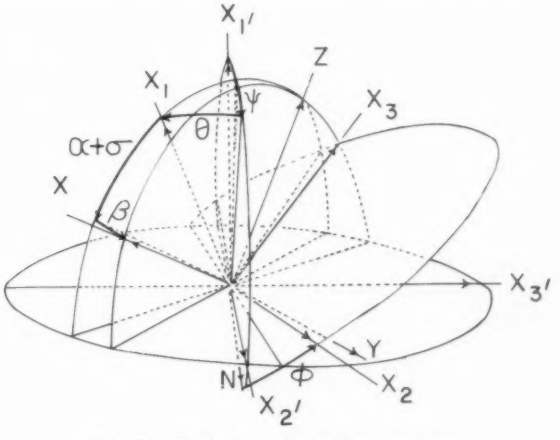

Fig. 2. Illustration of coordinate systems.

tribution) in the secondary inertial system. The motion of each coordinate system is referred by means of a set of modified Euler angles to a frame of reference fixed on the earth. This fixed frame of reference will hereinafter be called the inertial or i-system. The modified Euler angles (ϕ, θ, ψ), Fig. 2, are generalized coordinates that orient the axes whose motion is described in the inertial system. For infinitesimal rotations, these generalized angles become the conventional roll, pitch, and yaw angles.

Prior to launching, the $X_{1'}$, $X_{2'}$, $X_{3'}$ axes, Fig. 1, are established in the missile by means of gyros and are assumed to remain parallel to the corresponding axes of the inertial system throughout the time of interest.* The error-sensing device most often used in present-day aircraft having autopilot control—free or displacement gyros—generally gives pickoff indications at arbitrary plane attitudes for small deviations from these attitudes, which are functions of the direction cosines relating the body and inertial systems.[3, 4]

The ever increasing successful application of differential analyzers and digital computers as aids in the solution of equations describing the behavior of complicated physical systems,[5] the development of three-dimensional fluid flow theory, the evolution of the inertial guidance system, and the potential capacity of the guided missile both as a lethal weapon and a scientific tool justify the work presented in this paper.

(2.0) Dynamics of the p-System

Equations that describe the motion of the principal axis system are derived and presented in a form suitable for the application of simulation and digital computer facilities.

(2.1) Derivation Based on Lagrange's Equations

With reference to Table 2

$$\{\omega_p\} = \{a_{ps}\}\{\omega_s\} \tag{1}$$

$$\{\omega_s\} = \{a_{ps}\}^{-1}\{\omega_p\} \tag{2}$$

Hence†

$$\left.\begin{aligned} p &= \Phi - \Psi \sin\theta \\ q &= \Theta\cos\phi + \Psi\sin\phi\cos\theta \\ r &= -\Theta\sin\phi + \Psi\cos\phi\cos\theta \\ \Phi &= p + (q\sin\phi + r\cos\phi)\tan\theta \\ \Theta &= q\cos\phi - r\sin\phi \\ \Psi &= (q\sin\phi + r\cos\phi)\sec\theta \end{aligned}\right\} \tag{3}$$

In general, the rotational kinetic energy of a rigid body distributed in a given coordinate system may be expressed as

$$T = (1/2)\Sigma_k m_k \vec{v}_k^{\,2} = (1/2)\Sigma_k m_k(\vec{\omega}\times\vec{r}_k)^2 \tag{4}$$

where the origin of the coordinate system coincides with the center of mass of the body,‡ and m_k = kth incremental mass, $\vec{\omega}$ = angular velocity of the system, and $\vec{r}_k$ = vector from origin of the system to m_p.

When the rotational kinetic energy is that of the p-system,

$$\vec{r}_k = \sum_p X_k{}' \vec{u}_p$$

and it follows from Eq. (4) that

$$T = \frac{1}{2}\sum_p I_p\omega_p^2 \tag{5}$$

With reference to Eqs. (3) and (5), it may be shown that the equations describing the rotational motion of the p-system are

$$Q_\phi = H_1 \tag{6}$$

$$Q_\theta = H_2\cos\phi - H_3\sin\phi \tag{7}$$

$$Q_\psi = -H_1\sin\theta + H_2\sin\phi\cos\theta + H_3\cos\phi\cos\theta \tag{8}$$

where

$$\begin{aligned} H_1 &= PI_1 + qr(I_3 - I_2) \\ H_2 &= QI_2 + pr(I_1 - I_3) \\ H_3 &= RI_3 + pq(I_2 - I_1) \end{aligned}$$

The generalized forces, Section (5.0), are defined as follows:

$$\{Q_s\} = \{b_{ps}\}^{-1}\{M_p\} \tag{9}$$

Hence

$$\left.\begin{aligned} Q_\phi &= M_1 \\ Q_\theta &= M_2\cos\phi - M_3\sin\phi \\ Q_\psi &= -M_1\sin\theta + (M_2\sin\phi + M_3\cos\phi)\cos\theta \end{aligned}\right\} \tag{10}$$

where

$$\begin{aligned} M_1 &= (C_l\cos\sigma + C_n\sin\sigma)qSb \\ M_2 &= C_m qS\bar{c} - T_e r_0 \\ M_3 &= (C_n\cos\sigma - C_l\sin\sigma)qSb \end{aligned}$$

Eqs. (6), (7), and (8) show clearly that Lagrange's equations essentially express the fact that the applied torque equals the time rate of change of angular momentum.

The equations describing the translational motion of the p-system are given by

$$\{K_i\} = \{a_{pi}\}'\{K_p\} - \{a_{pi}\}'\{\alpha_{pi}\}\times\{a_{pi}\}'\{k_p\} = \{a_{pi}\}'\{F_p\} \tag{11}$$

where

$$\{F_p\} = \{a_{pr}\}\begin{Bmatrix} -D \\ Y \\ -L \end{Bmatrix} + \{a_{pb}\}\begin{Bmatrix} T_e \\ 0 \\ 0 \end{Bmatrix} + \{a_{pi}\}\begin{Bmatrix} 0 \\ 0 \\ mg \end{Bmatrix}$$

* Under a given set of conditions, analysis will indicate what refinements are warranted.

† The singular point ($\theta = \pi/2$) does not present any serious restrictions in practical applications. (See reference 5.)

‡ Since a homogeneous gravitational field is assumed in the present derivation, the center of mass coincides with the center of gravity.

TABLE 1
Tabulation of Certain Relationships

(a)† $\sum_i \alpha_{li}a_{mi} = -\sum_i \alpha_{mi}a_{li} = \omega_n$ $l, m, n = 1, 2, 3$ (cyclically) $l \neq m \neq n$

$\vec{\omega} = (\Phi - \Psi \sin\theta)\,\vec{u}_1 + (\Theta \cos\phi + \Psi \sin\phi \cos\theta)\vec{u}_2 + (\Psi \cos\theta \cos\phi - \Theta \sin\phi)\vec{u}$

(b) $\sum_p \alpha_{pl}a_{pm} = -\sum_p \alpha_{pm}a_{pl} = \Omega_n$ $l, m, n = X, Y, Z$ (cyclically) $l \neq m \neq n$

$\vec{\Omega} = (a_{2x}\vec{u}_x + a_{2y}\vec{u}_y)\,(d\alpha/dt) + (d\beta/dt)\vec{u}_z$

(c) $\sum_i \alpha_{il}a_{im} = -\sum_i \alpha_{im}a_{il} = \omega_n{}^*$ $l, m, n = X, Y, Z$ (cyclically) $l \neq m \neq n$

$\vec{\omega}^* = \vec{\Omega} + \sum_r (\vec{\omega}\cdot\vec{u}_r)\vec{u}_r$

(d) $\sum_j \alpha_{jm}a_{jn} = \frac{1}{2}\frac{d}{dt}\sum_j a_{jm}{}^2 = 0$

† The relationships (a), (b), (c), and (d) follow from conditions of orthogonality.

or, as an alternative,

$$\{K_i\} = \{a_{ir}\}\{K_r\} - \{a_{ir}\}\{\alpha_{ir}\}' \times \{a_{ir}\}\{k_r\} = \{a_{ir}\}\{F_r\} \quad (12)$$

where

$$\{a_{ir}\}\{F_r\} = \{a_{pi}\}'\{F_p\} \quad (13)$$

gives the relationship between the forces in the two systems.

(2.2) Procedure for Solving the Equations

The equations describing the rotational motion may be written in a form more suitable for solution by differential analyzers and digital computers. Since the generalized momenta

$$J_s = \partial T/\partial \dot{q}_s = A_s + \int (Q_s + \partial T/\partial q_s)dt \quad (14)$$

Eqs. (6), (7), and (8), may be written

$$J_\phi = A_\phi + \int [Q_\phi + 1/2\,(I_2 - I_3)\,(\Psi^2 \sin 2\phi \cos^2\theta - \Theta^2 \sin 2\phi + 2\Theta\Psi \cos\theta \cos 2\phi)]\,dt \quad (15)$$

$$J_\theta = A_\theta + \int [Q_\theta - I_1\Phi\Psi \cos\theta + (1/2)\Psi^2 \sin 2\theta \times (I_1 - I_2 \sin^2\phi - I_3 \cos^2\phi) - (1/2)\times (I_2 - I_3)\Theta\,\Psi \sin 2\phi \sin\theta]\,dt \quad (16)$$

$$J_\psi = A_\psi + \int Q_\psi\,dt \quad (17)$$

where the A_s are constants of integration, and

$$J_\phi = I_1(\Phi - \Psi \sin\theta)$$

$$J_\theta = (I_2 \cos^2\phi + I_3 \sin^2\phi)\Theta + (1/2)\,(I_2 - I_3)\Psi \sin 2\phi \cos\theta$$

$$J_\psi = (I_1 \sin^2\theta + I_2 \sin^2\phi \cos^2\theta + I_3 \cos^2\phi \cos^2\theta)\,\Psi - I_1\Phi \sin\theta + (1/2)\,(I_2 - I_3)\Theta \sin 2\phi \cos\theta$$

The generalized forces are given by Eq. (9).

Assuming $I_2 = I_3$ (which is a quite reasonable assumption in many cases), Eqs. (15), (16), and (17) simplify to a system that can be handled more efficiently:

$$\Phi = \frac{1}{I_1}(A_\phi + I_1\Psi \sin\theta + \int Q_\phi\,dt) \quad (18)$$

$$d\Theta/dt = (1/I_2)\,[Q_\theta + (\partial T/\partial\theta)] = (1/I_2)\,[Q_\theta - \Psi \cos\theta\,(J_\phi + I_2\Psi \sin\theta)] \quad (19)$$

$$\Psi = \frac{1}{I_2 \cos^2\theta}\,[A_\psi + \sin\theta(A_\phi + \int Q_\phi\,dt) + \int Q_\psi\,dt] \quad (20)$$

Beyond this point one may proceed in a variety of ways. The procedure suggested is somewhat as follows. Eqs. (15), (16), and (17) or (18), (19), and (20) may be solved simultaneously with Eqs. (25), (26), and (27) for α, β, $V_r{}^x$ and the instantaneous missile attitude (ϕ, θ, ψ) throughout the time of interest. The relationship $\vec{V}_g = \vec{V}_r + \vec{W}$ will then yield the $V_g{}^p$ or $V_g{}^r$, and application of (d) or (f) in Table 2 will give the $V_g{}^i$ from which the trajectory of the missile may be computed.

(2.3) Comments on Wind

The effects of a changing wind are considered, and a means of solving for α, β, and V_r is indicated.

In the presence of an arbitrary wind, the relative wind vector ($\vec{V}_r$) is defined to coincide at every instant with the x-axis of the r-system. There is a time delay, of course, between the application of a wind on the body system and the acquisition of this wind by that system.

With reference to Table 2,

$$\{V_g{}^r\} = \{a_{ir}\}'\{V_g{}^i\} \quad (21)$$

$$\{A_g{}^r\} = \{\alpha_{ir}\}'\{V_g{}^i\} + \{a_{ir}\}'\{A_g{}^i\}$$

or

$$\{a_{ir}\}'\{A_g{}^i\} = (1/m)\{F_r\} = \{A_g{}^r\} - \{\alpha_{ir}\}'\{V_g{}^i\} \quad (22)$$

Since

$$\{V_g{}^r\} = \{V_r{}^r\} + \{W^r\}$$

and

$$\{A_w{}^r\} = \{\alpha_{ir}\}'\{W^i\} + \{a_{ir}\}'\{A_w{}^i\}$$

Eq. (22) may be written

$$(1/m)\{F_r\} = \{A_r{}^r\} + \{a_{ir}\}'\{A_w{}^i\} - \{\alpha_{ir}\}'\{a_{ir}\}\{V_r{}^r\} \quad (23)$$

Eq. (23) gives the components of the acceleration of the missile along the axes of the r-system when the missile is in the process of acquiring the wind.

(2.3.1) *Resolution of α, β, and V_r*

Eq. (23) may be utilized, in conjunction with the equations describing rotational motion, to determine the angles of attack and sideslip, their respective rates, and the air speed for utilization in the aerodynamic forces and moments.

With reference to Table 1, Eq. (23) may be written

$$\frac{1}{m}\begin{Bmatrix}F_x\\F_y\\F_z\end{Bmatrix} = \begin{Bmatrix}A_r{}^x\\0\\0\end{Bmatrix} + \{a_{ir}\}'\{A_w{}^i\} + \{\Upsilon\}\begin{Bmatrix}V_r{}^x\\0\\0\end{Bmatrix} \quad (24)$$

where

$$\{\Upsilon\} = \begin{Bmatrix}0 & -w_z{}^* & w_y{}^*\\ \omega_z{}^* & 0 & -w_x{}^*\\ -\omega_y{}^* & \omega_x{}^* & 0\end{Bmatrix}$$

$$F_x = mga_{3'x} + T_e\cos\alpha\cos\beta - D$$
$$F_y = mga_{3'y} - T_e\sin\beta\cos\alpha + Y$$
$$F_z = mga_{3'z} + T_e\sin\alpha - L$$

$$\omega_y{}^* = a_{2y}\frac{d\alpha}{dt} + \sum_p \omega_p a_{py}$$

$$\omega_z{}^* = \frac{d\beta}{dt} + \sum_p \omega_p a_{pz}$$

Linearizing in and neglecting products of α and β, Eq. (24) yields

$$A_r{}^x = A_1 + A_2\beta - A_3(\alpha + \sigma) - (1/m)F_x \quad (25)$$

$$d\beta/dt = (1/V_r{}^x)\,[A_1\beta - A_2 - pV_r{}^x(\alpha + \sigma) - rV_r{}^x + (1/m)F_y] \quad (26)$$

$$d\alpha/dt = (1/V_r{}^x)\,[a_1(\alpha + \sigma) + A_3 + (p\beta - q)V_r{}^x - (1/m)F_z] \quad (27)$$

where

$$A_p = \sum_i a_{pi}A_w{}^i$$

(3.0) Dynamics of the r-System

Equations that describe the motion of the relative wind system are derived, and a number of simplifying assumptions that may be valid in a given case are mentioned. These equations are generally more difficult to manage than those resulting when the motion of a body axis system is considered. The variable moments of inertia, characteristic of the relative wind system, are discussed in Section (4.0).

(3.1) Derivation Based on Lagrange's Equations

Letting the generalized angles (ϕ, θ, ψ) orient the r-system in the inertial system, the equations describing the motion of the r-system are easily formulated.

Since the generalized angles now orient the r-system, it may be shown that the equations that describe the rotational motion are of the same form as Eqs. (6), (7), and (8), where the H_p are written as follows:

Table 2
Coordinate Transformations

Suppose that the missile has assumed an arbitrary orientation in the inertial system. The direction cosines relating the coordinate systems employed in this paper may then be derived from unit sphere transformations or methods of projective geometry. The basic transformation matrices are:

(a) $|X_p| = |a_{ps}|\,|X_s|$ (for the components of a contravariant vector)

where

$$|a_{ps}| = \begin{Bmatrix}1 & 0 & -\sin\theta\\ 0 & \cos\phi & \sin\phi\ \cos\theta\\ 0 & -\sin\phi & \cos\theta\ \cos\phi\end{Bmatrix}$$

(b) $|X_p| = |b_{ps}|\,|X_s|$ [for the components of a covariant vector; Section (5.0)]

where

$$|b_{ps}| = \begin{Bmatrix}1 & 0 & 0\\ \sin\phi\tan\theta & \cos\phi & \sin\phi\sec\theta\\ \cos\phi\tan\theta & -\sin\phi & \cos\phi\sec\theta\end{Bmatrix}$$

(c) $|X_p| = |a_{pr}|\,|X_r|$

where

$$|a_{pr}| = \begin{Bmatrix}\cos(\alpha+\sigma)\cos\beta & -\sin\beta\cos(\alpha+\sigma) & \sin(\alpha+\sigma)\\ \sin\beta & \cos\beta & 0\\ -\sin(\alpha+\sigma)\cos\beta & \sin(\alpha+\sigma)\sin\beta & \cos(\alpha+\sigma)\end{Bmatrix}$$

(d) $|X_p| = |a_{pi}|\,|X_i|$

where

$$|a_{pi}| = \begin{Bmatrix}\cos\theta\cos\psi & \sin\psi\cos\theta & -\sin\theta\\ \sin\theta\sin\phi\cos\psi - \sin\psi\cos\phi & \sin\theta\sin\phi\sin\psi + \cos\phi\cos\psi & \sin\phi\cos\theta\\ \sin\theta\cos\phi\cos\psi + \sin\phi\sin\psi & \sin\theta\sin\psi\cos\phi - \sin\phi\cos\psi & \cos\theta\cos\phi\end{Bmatrix}$$

(e) $|X_p| = |a_{pb}|\,|X_b|$

where

$$|a_{pb}| = \begin{Bmatrix}\cos\sigma & 0 & \sin\sigma\\ 0 & 1 & 0\\ -\sin\sigma & 0 & \cos\sigma\end{Bmatrix}$$

(f) $|X_i| = |a_{ir}|\,|X_r|$

where

$$|a_{ir}| = |a_{pi}|'\,|a_{pr}|$$

$$H_x = (PI_{xx} - QI_{xy} - RI_{xz}) + (p\Gamma_{xx} - q\Gamma_{xy} - r\Gamma_{xz}) + q(-pI_{xz} - qI_{yz} + rI_{zz}) + r(pI_{xy} - qI_{yy} + rI_{yz}) \quad (28)$$

$$H_y = (-PI_{xy} + QI_{yy} - RI_{yz}) + (-p\Gamma_{xy} + q\Gamma_{yy} - r\Gamma_{yz}) + p(pI_{xz} + qI_{yz} - rI_{zz}) + r(pI_{xx} - qI_{xy} - rI_{xz}) \quad (29)$$

$$H_z = (-PI_{xz} - QI_{yz} + RI_{zz}) + (-p\Gamma_{xz} - q\Gamma_{yz} + r\Gamma_{zz}) + p(-pI_{xy} + qI_{yy} - rI_{yz}) + q(-pI_{xx} + qI_{xy} + rI_{xz}) \quad (30)$$

The p, q, r, P, Q, R in Eqs. (28), (29), and (30) are to be interpreted as applying to the r-system; the I's and Γ's are to be determined from Eq. (37); and the generalized forces are given by

$$\{Q_s\} = \{b_{ps}\}^{-1} \{a_{pr}\}' \{M_p\} \quad (31)$$

The maximum values of the products of inertia are usually only a small percentage of those of the moments of inertia. The maximum value of β is usually considerably less than that of α. Since I_3 is usually greater than I_1, it is noted that for extremely small angles of sideslip, I_x is greater than I_1, I_y is approximately equal to I_2, and I_z is less than I_3. As in the body axis case, the assumption that $I_y = I_z$ is often valid and results in considerable simplification of the equations. Further simplification results when α, β remain less than approximately 4° throughout the time of interest. In such cases, the variations in the moments of inertia and products of inertia are so small that it is usually sufficiently accurate to regard the relative wind axes as identical with the body axes.

The equations describing the translational motion of the r-system are given by Eq. (11), where K_p, k_p, and F_p are to be replaced by K_r, k_r, and F_r. The relationship between the applied forces in the two systems is given by Eq. (13).

(4.0) Transformation of Moments of Inertia

Let (l) denote an orthogonal system that is rotating with respect to a rigid body. Suppose that the moments of inertia and products of inertia of the body are desired in the rotating system. In such a case these quantities become variables, since mass increments associated with "points" in the moving system are functions of time. This is the situation encountered in dynamic stability studies where the equations describe the motion of the relative wind system. Relationships are required which are functions of the instantaneous direction cosines orienting the rotating system with respect to an axis system fixed in the body.

The moment of inertia of the body about any axis (l) passing through the origin of an orthogonal system (B), fixed relative to the body, follows from the definition:

$$I_l = \sum_k m_k(\vec{r}_k x \vec{u}_l)^2 \quad (32)$$

where

$\vec{u}_l = \sum_B a_{Bl}\vec{u}_B$ (unit vector along l)

$\vec{r}_k = \sum_B X_B{}^k \vec{u}_B$ (vector from origin of the B-system to m_k)

$X_B: (\xi, \eta, \zeta)$ (axes of the B-system)

It may be shown that

$$I_l = \sum_{AB} I_{AB} a_{Al} a_{Bl} e^{AB}$$

where

$$A, B = \xi, \eta, \zeta$$

$$e^{AB} = \begin{cases} 1; A = B \\ -1; A \neq B \end{cases} \quad (33)$$

and $I_{AB} = I_{BA}$ = moments of inertia when $A = B$ and products of inertia when $A \neq B$. Thus, in general, the moment of inertia of a rigid body about an arbitrary axis is a quadratic function that contains both the moments of inertia and the products of inertia as expressed in a coordinate system wherein the body is fixed.

Expressions for the moments of inertia about the axes of the (l) system are found by repeated application of Eq. (33), but the determination of the products of inertia in this system requires an additional equation. Let λ, μ, ν denote the axes of (l) and let $I_{\epsilon\tau}$ denote the products of inertia in the (l) system; then by definition

$$I_{\epsilon\tau} = \sum_k m_k \epsilon_k \tau_k \qquad \epsilon, \tau = \lambda, \mu, \nu \quad (34)$$

In terms of the B-system,

$$\epsilon_k = \sum_B a_{\epsilon B} X_B{}^k$$

$$\tau_k = \sum_B a_{\tau B} X_B{}^k$$

and Eq. (34) becomes

$$I_{\epsilon\tau} = \sum_{AB} \sum_k m_k a_{\epsilon A} X_A{}^k a_{\tau B} X_B{}^k \qquad A, B = \xi, \eta, \zeta$$

$$= -\sum_B I_B a_{B\epsilon} a_{B\tau} + I_{\xi\eta}(a_{\xi\epsilon} a_{\eta\tau} + a_{\eta\epsilon} a_{\xi\tau} + I_{\eta\zeta}(a_{\eta\epsilon} a_{\zeta\tau} + a_{\zeta\epsilon} a_{\eta\tau}) + I_{\xi\zeta}(a_{\xi\epsilon} a_{\zeta\tau} + a_{\zeta\epsilon} a_{\xi\tau}) \quad (35)$$

If the axes of the B-system are principal axes of inertia, the products of inertia vanish in the body system, and Eqs. (33) and (35) simplify to

$$I_{\epsilon\tau} = \sum_p I_p a_{p\epsilon} a_{p\tau} e^{\epsilon\tau}$$

where

$$\epsilon, \tau = \lambda, \mu, \nu$$

$$e^{\epsilon\tau} = \begin{cases} 1; \epsilon = \tau \\ -1; \epsilon \neq \tau \end{cases} \quad (36)$$

By repeated application of Eq. (36), the following relationships result for the moments of inertia and products of inertia in the r-system:

$$\left.\begin{aligned} I_{xx} &= I_1 a_{1x}^2 + I_2 a_{2x}^2 + I_3 a_{3x}^2 \\ I_{yy} &= I_1 a_{1y}^2 + I_2 a_{2y}^2 + I_3 a_{3y}^2 \\ I_{zz} &= I_1 a_{1z}^2 + I_2 a_{2z}^2 + I_3 a_{3z}^2 \\ I_{xy} &= -(I_1 a_{1x} a_{1y} + I_2 a_{2x} a_{2y} + I_3 a_{3x} a_{3y}) \\ I_{yz} &= -(I_1 a_{1y} a_{1z} + I_2 a_{2y} a_{2z} + I_3 a_{3y} a_{3z}) \\ I_{zx} &= -(I_1 a_{1z} a_{1x} + I_2 a_{2z} a_{2x} + I_3 a_{3z} a_{3x}) \end{aligned}\right\} \quad (37)$$

(5.0) Transformation of Moments

The transformation matrix $\{b_{ps}\}$ is derived, and it is shown that the components of the applied moment transform in this manner. The conventional tensor notation is employed.

(5.1) Derivation of $\{b_{ps}\}$

Let X denote an arbitrary vector, then

$$X = X^\alpha \epsilon_\alpha = X_\beta \epsilon^\beta \qquad \alpha, \beta, \gamma = p\text{-system} \quad (38)$$

and

$$X = X^i \epsilon_i = X_j \epsilon^j \qquad i, j, k = s\text{-system} \quad (39)$$

where

$$X_\alpha = \alpha_{\alpha i} X^i \qquad \text{(contravariant transformation)} \quad (40)$$

From Eqs. (38) and (39),

$$X^\alpha (\epsilon_\alpha \cdot \epsilon^\gamma) = X_\beta (\epsilon^\beta \cdot \epsilon^\gamma)$$

$$X^\alpha \delta_\alpha{}^\gamma = X_\beta G^{\beta\gamma} \qquad \delta_\alpha{}^\gamma = \epsilon_\alpha \cdot \epsilon^\gamma = \begin{cases} 1; & \alpha = \gamma \\ 0; & \alpha \neq \gamma \end{cases}$$

$$X^\gamma = X_\beta G^{\beta\gamma}$$

or

$$X^\alpha = G^{\alpha\beta} X_\beta$$

and

$$X_\beta = G_{\alpha\beta} X^\alpha$$

Similarly,

$$X^i = G^{ij} X_j$$

and

$$X_i = G_{ij} X^j$$

Now, substituting in Eq. (40),

$$G^{\alpha\beta} X_\beta = a_{\alpha i} G^{ij} X_j$$

or, in matrix notation,

$$\{G^{\alpha\beta}\}\{X_\beta\} = \{a_{\alpha i}\}\{G^{ij}\}\{X_j\} \quad (41)$$

and, since,

$$\{G^{\alpha\beta}\}^{-1} = \{G^{\alpha\beta}\}'$$

$$\{X_\beta\} = \{a_{\alpha i}\}\{G^{\alpha\beta}\}\{G^{ij}\}\{X_j\} \quad (42)$$

where $\{a_{\alpha i}\} = \{a_{ps}\}$, $\{G^{\alpha\beta}\}$ is a unity matrix, and $\{G^{ij}\}$ is to be determined.

Since

$$\{G_{ij}\} = \begin{Bmatrix} 1 & 0 & -\sin\theta \\ 0 & 1 & 0 \\ -\sin\theta & 0 & 1 \end{Bmatrix}$$

$$G^{ij} = \frac{A_{ij}}{|G_{ij}|}; |G_{ij}| = \cos^2\theta$$

and thus

$$\{G^{ij}\} = \begin{Bmatrix} \sec^2\theta & 0 & \sin\theta \sec^2\theta \\ 0 & 1 & 0 \\ \sin\theta \sec^2\theta & 0 & \sec^2\theta \end{Bmatrix}$$

Hence

$$\{b_{\beta j}\} = \{a_{\alpha i}\}\{G^{\alpha\beta}\}\{G^{ij}\} = \{b_{ps}\} \quad (43)$$

and therefore

$$\{X_p\} = \{b_{ps}\}\{X_s\} \qquad \text{(covariant transformation)}$$

(5.2) Formulation of the Generalized Forces

The generalized forces—i.e., the Q_s—are defined as the components of the applied moment in the s-system. The manner in which the components of the applied moment transform is desired.

By definition

$$M = r \times F = II$$

With r and F defined in the p-system, M has a covariant description,

$$M = M_k \epsilon^k = M_\gamma \epsilon^\gamma = M^\gamma \epsilon_\gamma \qquad (M_\gamma = M^\gamma)$$

$$\frac{M_k (\epsilon_i \times \epsilon_j)}{\sqrt{|G_{ij}|}} = M^\gamma \epsilon_\gamma \quad (i, j, k; \text{cyclic}) \quad (45)$$

With the following substitutions,

$$\sqrt{|G_{ij}|} = \cos\theta, \{\epsilon_i\} = \{b_{ps}\}^{-1}\{\epsilon_\alpha\}$$

and collecting coefficients of the ϵ_γ, M is written

$$M = M_1 \epsilon_1 + \epsilon_2(\sin\phi \tan\theta\, M_1 + \cos\phi M_2 + \sin\phi \sec\theta M_3) + \epsilon_3(\cos\phi \tan\theta M_1 - \sin\phi M_2 + \cos\phi \sec\theta M_3) = M^\gamma \epsilon_\gamma \quad (46)$$

which yields the transformation

$$\{M_p\} = \{b_{ps}\}\{M_s\} \quad (47)$$

where $\{M_s\} = \{Q_s\}$.

References

[1] Duncan, W. J., *The Principles of the Control and Stability of Aircraft*, p. 77; Syndics of the Cambridge University Press, London, 1952.

[2] Bairstow, L., *Applied Aerodynamics*, 2nd Ed., p. 197; Longmans, Green and Co., London, 1939.

[3] Becker, Leonard, *Gyro Pickoff Indications at Arbitrary Plane Attitudes*, Journal of the Aeronautical Sciences, Vol. 18, No. 11, pp. 718–724, November, 1951.

[4] Poritsky, H., *Topics in Gyroscopic Motion*, Journal of Applied Mechanics, Vol. 20, No. 1, pp. 1–8, March, 1953.

[5] Gray, H. J., Jr., Rubinoff, M., and Sohon, H., *A Technique for Real Time Simulation of a Rigid Body Problem*, Mathematical Tables and Other Aids to Computation, VII, No. 42, pp. 73–77, April, 1953.

Propagation of Stall in a Compressor Blade Row*

FRANK E. MARBLE†
California Institute of Technology

ABSTRACT

Recent experimental observations on compressors, in particular those of Rannie and Iura, have clarified some features of the phenomenon of stall propagation. Using these observations as a guide, the process of stall in an airfoil cascade has been characterized by a static pressure loss across the cascade which increases discontinuously at the stall angle, the turning angle being affected in only a minor way. Deductions from this simple model yield the essential features of stall propagation such as dependence of the extent of stalled region upon operating conditions, the pressure loss associated with stall, and the angular velocity of stall propagation. Using two-dimensional approximation for a stationary or rotating blade row, free from interference of adjacent blade rows, extent of the stalled region, the total pressure loss and stall propagation speed are discussed in detail for a general cascade characteristic. Employing these results, the effect of stall propagation upon the performance of a single-stage axial compressor is illustrated and the mechanism of entering the regime of stall propagation is discussed. The essential points of the results seem to agree with experimental evidence.

INTRODUCTION

IF THE RATE AT WHICH FLUID passes through a compressor blade row is decreased while the rotative speed remains constant, the angles of attack of the compressor blades eventually exceed that for which unseparated flow is possible. Individual blades then behave in a manner somewhat resembling stalled isolated airfoils and the compressor is said to stall. The nature of compressor operation in the stall regime is of considerable importance not only because of the attending loss in efficiency and pressure rise, but also due to the fact that the onset of stall is accompanied by pulsation and oscillating blade loads which may lead to structural failure of the blades. The complexity and general irregularity of the flow during stalled operation have, in the past, discouraged a detailed study. Recently several experimental investigations have demonstrated some regularities in the process. It appears that the blades of a given blade row do not stall simultaneously, but initially only a few blades stall. Furthermore, it is observed that the stalled region of a blade row does not always consist of the same group of blades but that the region moves about the blade row at an appreciable fraction of the rotor velocity. The name stall propagation or rotating stall originates from this behavior. In addition to the reasons mentioned above, stall propagation is of importance through its possible connection with compressor surge and because the appearance of the more or less regular phenomenon may indicate that the compressor is operating near its surge line.

During the past few years experimental observations at several research institutions and manufacturing establishments have indicated stall propagation in a variety of compressors. Unfortunately, most of this information exists only in private communications. It is probable, however, that the regularity was first recognized by Emmons together with his co-workers at Harvard University, and some of their findings have recently been reported in reference 1. Of the available experimental results concerning stall propagation, the most detailed and complete are those of Rannie and Iura,[2] performed at the California Institute of Technology on a large three-stage axial compressor. Knowledge of these experiments has been the principal guide in the present formulation of the problem.

The results of Rannie and Iura indicate that two types of stall propagation occur which are, at least superficially, different; in one the stall covers the entire blade length, in the other only a portion of the blade length. As the compressor is throttled, a single stalled area is observed which covers only the root or tip regions of a few blades. With further throttling two, three, or more similar regions appear, uniformly spaced about the periphery. The propagation speed remains remarkably constant as throttling proceeds. Finally, with further decrease in flow, the pattern changes to a single region extending over the blade length; this change is accompanied by a small decrease in propagating speed. This type of pattern persists until the flow is nearly shut off, the peripheral extent of the stalled region increasing as the flow is reduced. Some information on experiences with other machines has been reported by Huppert and Benser.[3]

The basic features of the stall propagation phenomenon seem to be quite clear. When the blade row operates at nearly its stall angle, any small disturbance will cause one or more of the blades to stall. The stall reduces the blade force and decreases the local pressure rise across the blade row so that the flow will be retarded near the stalled region and diverted to either side. Depending upon the geometry of the blade row, the flow angles upstream of the blade row will be increased on one side and decreased on the other. Where the flow angles increase, neighboring blades stall and the stalled region propagates in that direction. Where flow angles are decreased, blades already

Received April 7, 1954.
* This work was performed, in part, under the financial support of the Office of Scientific Research, United States Air Force.
† Associate Professor, Daniel and Florence Guggenheim Jet Propulsion Center.

stalled may be relieved so that the stalled area retains a definite length. The rate of propagation depends upon some characteristic time associated with the stalling process. This characteristic time is related to the process of boundary-layer separation and establishment of a "stalled" flow pattern from an unstalled flow pattern. Some further results of Rannie and Iura clarify this point. They observed that the removal of every second blade from one or more of the blade rows had only a slight effect upon the speed of stall propagation. Consequently the influence of time required for boundary-layer separation must be rather small, since the propagating speed would be inversely proportional to the blade number if this were the governing phenomenon. Therefore the speed of propagation must be associated with the time required for the existing pressure difference across the blade row to transform the flow pattern. This time is not strongly dependent upon the blade geometry or the blade gap. On this basis an elementary model for the stalling process was constructed. Then it was not a difficult matter to deduce the resulting details of stall propagation.

It is a pleasure for the author to express his deep gratitude to Professor H. S. Tsien who supplied the impetus to start the investigation and the encouragement to finish it. The initial formulation of the problem and the requirements of the model for the stall process were suggested by Dr. Tsien. Professor W. D. Rannie likewise contributed greatly to the present picture of stall propagation through illuminating discussion of his experimental work. It was Dr. Rannie who first pointed out that considerable clarity could be gained by departing from the conventional formulation according to airfoil theory of cascades. Professor W. R. Sears, Cornell University, has been most helpful; first in communicating the results of his analysis prior to publication, and later through stimulating discussion.

The Physical Mechanism of Stall Propagation

An airfoil exhibits two modes of operation: the normal mode, many features of which are well described by the theory of ideal fluids, and the stalled mode which may be described roughly by the ideal flow about a boundary consisting of a portion of the airfoil and a constant pressure stream line that bounds the stagnant wake. The pressure associated with the stream line is, in this case, equal to the undisturbed static pressure of the free stream. When airfoils are arranged in a cascade or lattice, as they are in a compressor blade row, they possess similar normal and stalled modes of flow. In a compressor cascade, the blades act to reduce the flow velocity from upstream to downstream so that for the normal mode of operation a static pressure rise occurs across the blade row. Thus when one airfoil of a cascade is stalled for some reason, the situation is somewhat different from that of an isolated airfoil because now the pressure associated with the free stream line is that far downstream of the cascade which is considerably in excess of that upstream. Since the high pressure now penetrates to a point near the leading edge of the stalled airfoil, the pressure in the entire vicinity is increased. As a consequence the velocity approaching the channel formed by the stalled surface and the next blade is reduced, as shown in Fig. 1, and the quantity of fluid passing through the channel is proportionately decreased.

Now if, during normal operation of the entire cascade, one of the airfoils stalls, the flow pattern corresponding to stall develops through intermediate stages indicated in Fig. 2. As the separation point moves forward from the trailing edge, the wake begins to develop and spreads downstream with a velocity less than the local free-stream velocity. The growth of the stall region gradually reduces the flow through the passage by diverting the fluid ahead of the cascade. The time elapsed during transition from unstalled to stalled velocity fields consists of that needed to separate the boundary layer and that required for the existing pressure difference across the cascade to deform the flow pattern. The latter is a simple inertial effect, while the boundary-layer separation is more complicated; actually the processes are not strictly independent.

The mechanism of stall propagation may be seen by observing, from Fig. 2, that, during successive stages in development of stall for one airfoil, the angle of attack on the airfoil just above it is increased. When this airfoil reaches its critical angle of attack, it too stalls and the process continues as shown in Fig. 3. Just how soon the adjacent airfoil begins to stall depends upon the normal angle of attack and the cascade geometry as well as upon the rate with which the neighboring flow field is modified by the airfoil originally stalled. Furthermore, the angle of attack is decreased upon the airfoils below the stalled one. Therefore as the stall region grows upward, airfoils far below will eventually become unstalled and the process will settle down to a steady propagating stalled region of constant length. The actual length depends, in particular, upon the proximity of the normal angle of attack to the stall angle.

The time required for the stall of one blade to deform the flow sufficiently to stall the next airfoil is a most significant item, and the factors that affect it may be isolated by an approximate analysis of dynamic equilibrium of the flow while the airfoil is stalling. Suppose that during normal operation a static pressure rise Δp takes place across the blade row. If the pressure rise is small, it is related to the change Δw in velocity from inlet to outlet by $\Delta p = -\rho w \Delta w$. Now when the blade stalls, the fluid passes through the stalled blade channel with negligible rise in static pressure. Therefore, assuming the static pressure field downstream of the blade row to be only slightly affected by the stall, a pressure difference Δp is available for retarding the fluid which approaches from far upstream to flow through the stalled blade channel. Since the blade chord is neglected, the only characteristic length in the problem is the gap g (or length of stalled region), thus the pressure gradient that retards the flow is $\Delta p/\kappa g$,

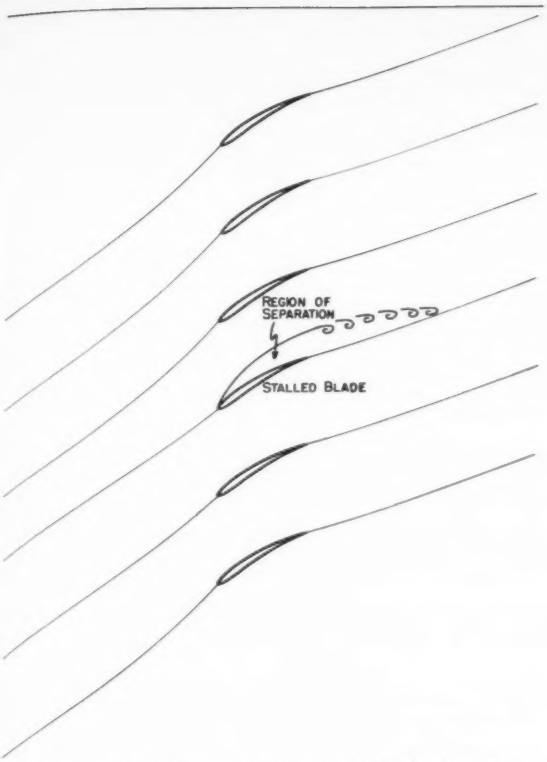

FIG. 1. Induced flow angles from stalled blade channel.

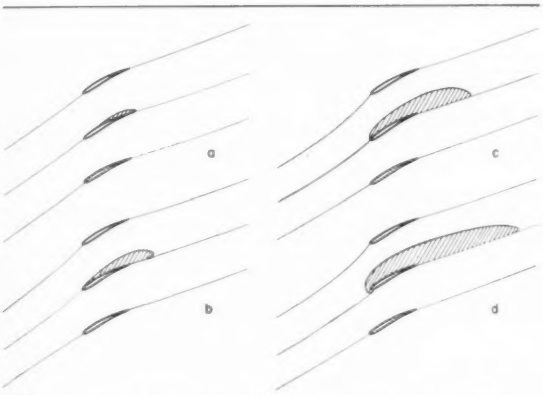

FIG. 2. Development of stalled region in a blade channel.

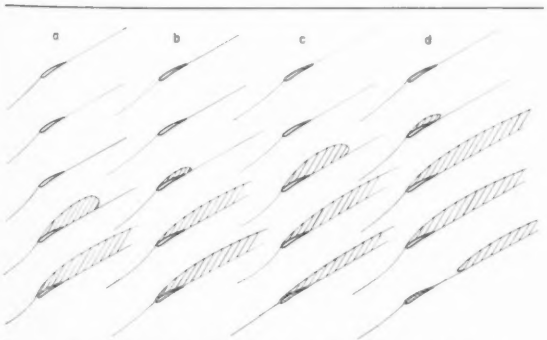

FIG. 3. Growth and distribution of stalled regions in blade row.

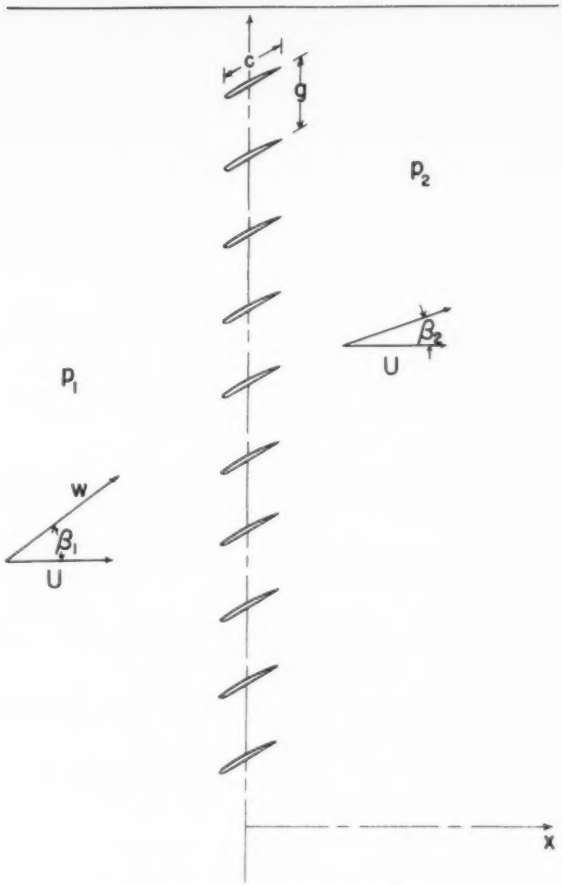

FIG. 4. Diagram of actuating line.

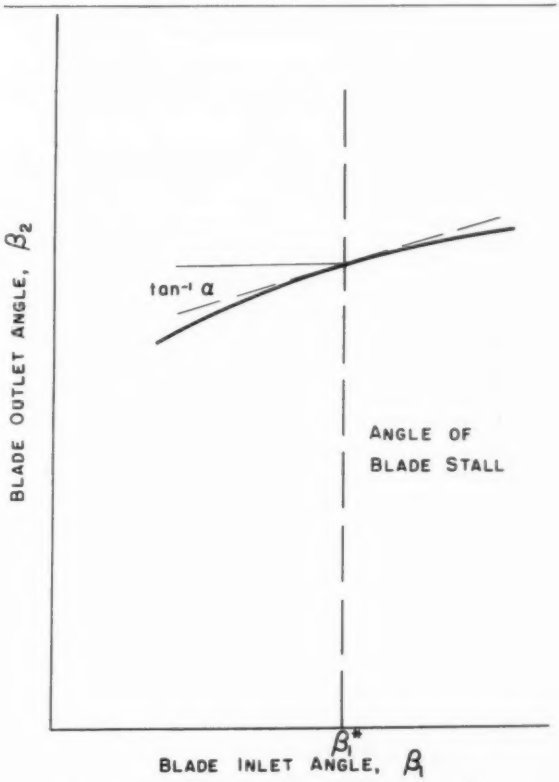

FIG. 5. Turning angle as function of inlet angle.

where κ is a constant of proportionality. At the initial instant of stall, where the approach velocity w does not vary with distance upstream of the airfoil, the rate of change of w is given by $\partial w/\partial t = -(1/\rho)(\Delta p/\kappa g)$. An estimate of the time τ required for the stalled pattern to develop may be obtained by assuming the transformation to continue at this rate. Now since there is no pressure rise through the blade row in stalled conditions, the flow approaching the blade row must undergo a change in velocity almost equal to Δw in order that it may discharge to the pressure downstream of the blade row. Therefore, approximating $\partial w/\partial t$ by $\Delta w/\tau$, it follows that $\Delta w/\tau = -(1/\rho)(\Delta p/\kappa g)$ so that employing the relations between Δp and Δw,

$$w\tau/g = \kappa$$

If the rotative speed of the compressor is ΩR and m is the number of blades, then

$$w\tau/g = [w/(\Omega R)]\,[(\Omega R m\tau)/(mg)]$$

where $w/(\Omega R)$ is usually about unity and for the present consideration is constant. But $mg = 2\pi R$ and the angular velocity of stall rotation is $\omega = 2\pi/m\tau$, since $m\tau$ is the time required to stall the total number of blades. Thus approximately $w\tau/g = \Omega/\omega$, the ratio of blade speed to that of stall propagation. Then since $w\tau/g = \kappa$ the ratio of stall propagation and rotor speeds is constant, $\omega/\Omega = 1/\kappa$, and in particular is independent of the blade gap as indicated in experiment.

It is usual that several blades are involved in observed stall propagation so that the blade spacing is not the significant dimension but rather the length of the stalled region. Consequently it is appropriate to simplify the model to an actuating line across which the velocities and pressure may change discontinuously. It is convenient to think of this simplification carried out by allowing the chord and gap to vanish simultaneously while their ratio remains fixed. Then it remains only to assign realistic conditions on the change of flow properties across the line.

To follow the convention found convenient in compressor practice, let the local inlet flow angle β_1 be the independent variable, Fig. 4, in describing the characteristics of the cascade. The performance of the cascade is completely defined by prescribing (1) the local turning angle or the outlet flow angle and (2) the local static pressure rise across the cascade. The discharge angle β_2 is a well-determined function of the inlet angle, and, in the absence of losses, the static pressure rise is then fixed also. For considering the flow with respect to the blade row in question and accounting for the fact that the velocity U normal to the cascade is equal ahead and behind the cascade, the Bernoulli relation gives simply $\Delta p = (1/2)\rho U^2(\tan^2\beta_1 - \tan^2\beta_2)$. By virtue of the dependence of β_2 upon β_1, the pressure rise across the cascade is determined. Now when a relation between Δp and β_1 different from this is assigned, it can be possible only because the total pressure changes. Consequently choosing $\Delta p(\beta_1)$ is equivalent to assigning a value of the total pressure loss at each value of the inlet angle.

During stall propagation the entire blade row is operating sufficiently close to the angle of stall that the cascade characteristic need be approximated near this value; let $\beta_1{}^*$ be the inlet flow angle for which the cascade stalls. Locally the turning angle is a linear function of the inlet angle as shown in Fig. 5, and there is experimental evidence to show that it is not profoundly influenced by the stall. Then it may be characterized by a discharge angle $\beta_2{}^*$ and a slope of magnitude a just prior to stall. The pressure rise may likewise be approximated by a linear function of the inlet angle below the stall angle, but it changes discontinuously at $\beta_1{}^*$. According to the discussion of the stalling mechanism, the static pressure rise across the cascade may be approximated reasonably well by assuming it to vanish above the stall angle, to have a value Δp^* at $\beta_1{}^*$, and to have a slope b just prior to stall. This approximation to the pressure rise characteristic is shown in Fig. 6.

Such characterization of the cascade performance and stalling process differs from that employed by Emmons or by Sears in either of his analyses.[4, 5] The differences are not of great importance so far as the unstalled cascade characteristic is concerned, for any pair of performance parameters which depend upon the upstream flow angle is adequate, although not equally convenient. For example, the performance of a cascade may be expressed by giving the lift coefficient C_L and the drag coefficient C_D as functions of the angle of attack. Properly these coefficients are based upon the geometric mean of the upstream and downstream velocity vectors and the angle of attack measured with respect to its direction β_m. Then if F_x and F_y are the blade force components in the x and y directions, respectively, referring to Fig. 7, the lift and drag coefficients are just

$$C_L = (-F_x \sin\beta_m + F_y \cos\beta_m) \div [(c/2)\rho U^2(1 + \tan^2\beta_m)]$$

$$C_D = (F_x \cos\beta_m + F_y \sin\beta_m) \div [(c/2)\rho U^2(1 + \tan^2\beta_m)]$$

and the angle of attack is simply

$$\beta_m - \alpha_0 \equiv \tan^{-1}[(\tan\beta_1 + \tan\beta_2)/2]$$

where α_0 is an arbitrary angle of zero lift. An elementary momentum calculation shows that $F_y = \rho U g(U\tan\beta_1 - U\tan\beta_2)$, while the axial force results from pressure difference and is $F_x = -\Delta p\ g$, where Δp is the static pressure rise across the blade row. Now if C_L and C_D are specified as functions of the angle of attack, then clearly the expressions for F_x and F_y given above determine β_2 and Δp as functions of β_1. Therefore this viewpoint is equivalent to that used in the present analysis. Using the blade channel approach, the outlet angle β_2 and the total pressure loss Δp_t are specified as functions of the inlet angle β_1.

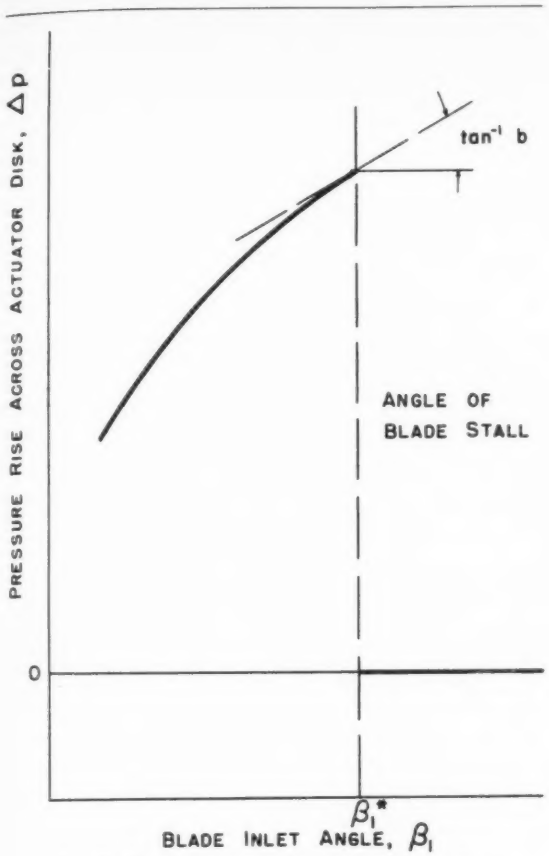

FIG. 6. Pressure rise as a function of inlet angle.

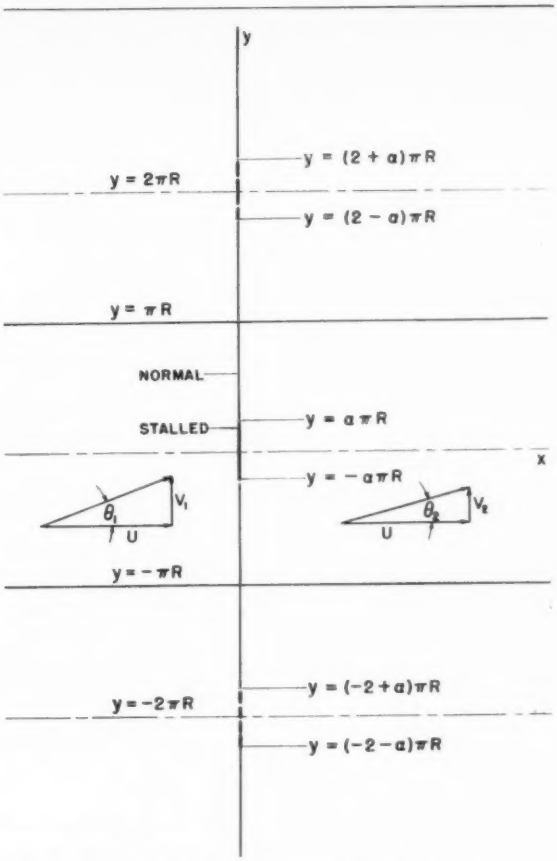

FIG. 8. Pattern of stalled and unstalled regions on actuating line.

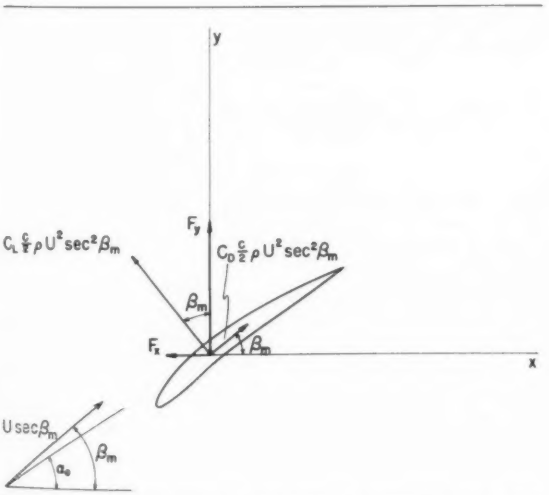

FIG. 7. Forces and velocities on cascade according to airfoil theory.

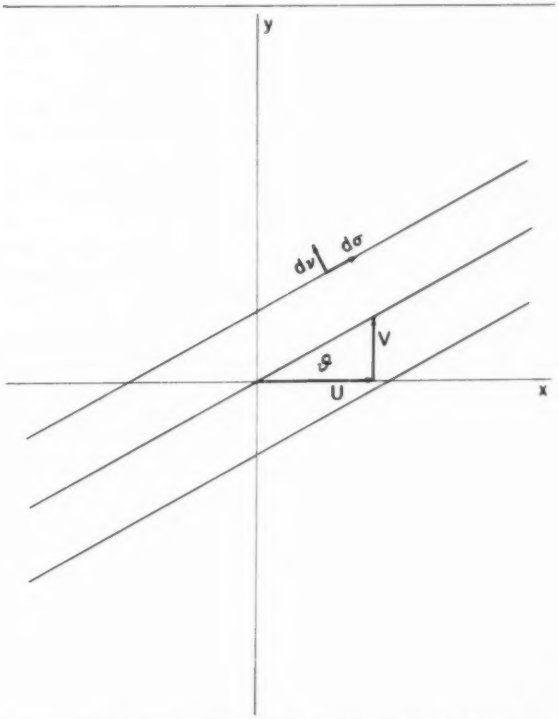

FIG. 9. Notation of coordinates and perturbations for flow along undisturbed streamlines.

This is closely related to the specification employed in the present analysis, for clearly

$$\Delta p = (1/2)\rho U^2(\tan^2 \beta_1 - \tan^2 \beta_2) - \Delta p_r$$

and hence $\Delta p(\beta_1)$ and $\beta_2(\beta_1)$ may be obtained directly.

It is interesting to compare the mechanisms of stall prescribed by Emmons[1] and that suggested in the present analysis. Emmons utilizes the fact that stall restricts the flow through a stalled blade channel and recognizes that the development of steady stalled flow from the initial separated flow requires a time that is the governing factor in the rate of stall propagation. However this time is not calculated from the details of the nonsteady motion, and consequently no stall propagation speed may be determined. Emmons and his co-workers seemingly overlook the fact that the characteristic time is proportional to the peripheral extent of the stalled region and therefore draw the erroneous conclusion that stall propagation speed is proportional to the wave length. It must be recognized, however, that Emmons' mechanism contains elements that, if pursued to their logical conclusion, would produce propagation speeds essentially in agreement with those of the present analysis. The fact that Emmons et al. do not account for the influence of flow downstream of the blade row is a significant but not a decisive shortcoming. The "amplitude" of stall and hence its peripheral extent and associated pressure loss are essentially nonlinear effects that, because his mechanism is not employed to full advantage, Emmons does not determine.

In his initial treatment, Sears[4] employs the approach of nonstationary airfoil theory, assuming an irregularity in lift near the stall angle but neglecting losses associated with stall. He assumes, moreover, that the actual stall lags a certain arbitrary phase behind the occurrence of critical inlet angle, this lag presumably being associated with the time required for boundary-layer separation, satisfying the Kutta condition or some other real fluid phenomena. It would seem that the most serious defect of this mechanism is its failure to account for the sharp increase in drag associated with stall. At the suggestion of Rannie, Sears improved his cascade characteristic in reference 5 to account for drag or pressure loss at the stall. He employed the conventional "channel theory" with the reasonable restriction that variation of discharge angle with inlet flow angle is neglected; the concept of stall phase lag, however, was retained. Since Sears solves the nonstationary flow problem for both cascade prescriptions, the velocity of stall propagation is determined except for influence of the arbitrary phase lag. Under special circumstances described later, the stall propagation speed computed under this channel theory agrees with the result developed herein. In both cases, however, Sears linearizes the cascade performance in the neighborhood of stall and consequently is unable to determine values for the extent of stall region or the pressure loss associated with stall.

General Theory of Stall Propagation in Single Blade Rows

Consider a cascade formed by an annular element of radius R from a rotating blade row. During normal operation the flow relative to the cascade is represented (Fig. 4) by a constant component U of axial velocity and constant flow angles β_1 upstream of the cascade and β_2 downstream. Corresponding uniform values of static pressure $p_1^{(0)}$ and $p_2^{(0)}$ exist ahead of and behind the blade row, and, if β_1 is close to the stall angle β_1^*, the pressures satisfy the relation

$$p_2^{(0)} - p_1^{(0)} \equiv \Delta p = \Delta p^* + b(\beta_1 - \beta_1^*)\,(1/2)\rho U^2$$

During stall propagation deviations from the uniform state occur which depend upon both location and time. The problem may be reduced to one of steady-state flow, however, by referring to a coordinate system x, y moving with the velocity ωR of the stalled region. Let V be the undisturbed tangential velocity component in this system; the quantities u, v are the velocity perturbations and p the pressure perturbation associated with stall propagation. A subscript 1 will denote conditions ahead of the blade row and a subscript 2, those behind.

The correspondence between inlet and outlet flow angles necessitates that perturbations $\Delta\beta_1$ and $\Delta\beta_2$ of the inlet and outlet flow angles satisfy the relation

$$\Delta\beta_2 = a\Delta\beta_1 \tag{1}$$

so long as the inlet angle is near the stalling angle. In prescribing the static pressure jump across the cascade, it is necessary to distinguish between stalled and unstalled regions. Denoting the compressor circumference by $2\pi R$ on the y axis, the stall will be assumed to cover a fraction α of the circumference extending over the interval $-\alpha\pi \leq y/R \leq \alpha\pi$. This pattern is repeated with a period 2π so that, as indicated in Fig. 8, the actuating line is stalled in the regions $(2n - \alpha)\pi \leq y/R \leq (2n + \alpha)\pi$ and unstalled elsewhere. Therefore the perturbation pressures $p_1(0, y)$ and $p_2(0, y)$ immediately ahead of and behind the cascade, satisfy the condition

$$\frac{p_2(0, y) - p_1(0, y)}{(1/2)\rho U^2} = \begin{cases} -\dfrac{\Delta p^*}{(1/2)\rho U^2} - b(\beta_1 - \beta_1^*); & (2n - \alpha)\pi \leq \dfrac{y}{R} \leq (2n + \alpha)\pi \\ b\Delta\beta_1 & \text{; elsewhere} \end{cases} \tag{2}$$

Due to the fact that the undisturbed flow fields ahead of and behind the cascade are initially uniform, the pressure perturbations satisfy the Laplace equation

$$(\partial^2 p_1/\partial x^2) + (\partial^2 p_1/\partial y^2) = (\partial^2 p_2/\partial x^2) + (\partial^2 p_2/\partial y^2) = 0 \tag{3}$$

Furthermore, the pressure perturbation due to the stall must vanish far upstream and assume, at most, a constant value far downstream. Then for a pre-

scribed state of steady operation the cascade performance given by Eqs. (1) and (2) determines completely the pressure field for the corresponding state of stall propagation. Now it is required further that the inlet flow angle exceed β_1^* in the stalled regions and be less than β_1^* in the unstalled regions. These conditions may be met only when the stall propagation speed ωR and the length $2\alpha\pi R$ of the stalled region are properly chosen. Thus if there is a condition of stall propagation which corresponds to a given set of inlet conditions, the peripheral extent of the stall and the rate of stall propagation are determined.

The flow angle deviations that are involved in the boundary values of the problem must be found from the pressure field. When the undisturbed flow angle is $\vartheta = \tan^{-1}(V/U)$, then the disturbed flow angle $\vartheta + \Delta\vartheta$ is related to the axial and tangential velocity perturbations as

$$\tan(\vartheta + \Delta\vartheta) = (V + v)/(U + u)$$

and since u and v are small

$$(1 + \tan^2\vartheta)\Delta\vartheta = (v/u) - (u/U)\tan\vartheta \qquad (4)$$

These velocity disturbances are related to the pressure distribution through the equations of motion which, for the present purpose, are most conveniently written along and normal to the streamlines of the undisturbed flow. Let the coordinate along the streamline be σ and that normal to the streamline, ν, as indicated in Fig. 9. The equation of equilibrium along the streamline is

$$\rho U(\partial/\partial\sigma)(u + v\tan\vartheta) = -\partial p/\partial\sigma \qquad (5)$$

and has an obvious integral which is the familiar linearized Bernoulli relation. The equilibrium equation normal to the streamline is

$$\rho U(\partial/\partial\sigma)(v - u\tan\vartheta) = -\partial p/\partial\nu \qquad (6)$$

and, by reference to Eq. (4), is clearly related to the angle deviation $\Delta\vartheta$. In fact, Eq. (6) is just

$$\rho U^2(1 + \tan^2\vartheta)(\partial/\partial\sigma)(\Delta\vartheta) = -\partial p/\partial\nu$$

Furthermore, the continuity relation for this coordinate system says simply that

$$(\partial/\partial\sigma)(u + v\tan\vartheta) = -(\partial/\partial\nu)(v - u\tan\vartheta)$$

and consequently Eq. (5) reads

$$\rho U^2(1 + \tan^2\vartheta)(\partial/\partial\nu)(\Delta\vartheta) = \partial p/\partial\sigma$$

Then two dependent variables may be defined

$$P = p/[(1/2)\rho U^2] \qquad (7)$$

$$\theta = 2(1 + \tan^2\vartheta)\Delta\vartheta$$

which reduce the equations of motion to

$$\partial P/\partial\sigma = \partial\theta/\partial\nu \qquad (8)$$

$$\partial P/\partial\nu = -\partial\theta/\partial\sigma \qquad (9)$$

These are the familiar Cauchy-Riemann relations which state not only that θ (and hence $\Delta\vartheta$) is an harmonic function but that it is indeed the harmonic conjugate of P and, further, that this useful relationship holds so long as the vorticity in the field is small.

Far upstream of the cascade both pressure and angle perturbations vanish and hence Eq. (5) may be integrated directly to

$$2[(u_1/U) + (v_1/U)\tan\vartheta_1] = -P_1$$

Noting that

$$\partial p_1/\partial v_1 = -(1/2)\rho U^2(\partial\theta_1/\partial\sigma)$$

Eq. (6) also integrates in a similar manner to

$$2[(v_1/U) - (u_1/U)\tan\vartheta_1] = \theta$$

The local flow velocities u_1 and v_1 are then simply

$$2(1 + \tan^2\vartheta_1)(u_1/U) = -P_1 - \theta_1\tan\vartheta_1 \qquad (10)$$

$$2(1 + \tan^2\vartheta_1)(v_1/U) = -P_1\tan\vartheta_1 + \theta_1 \qquad (11)$$

In order to reduce the problem to one of steady motion, the reference frame has been taken fixed in the rotating stall pattern, but when dealing with inlet and outlet angles of the blades it is necessary to consider angles that are measured with respect to the blades themselves. Since the variation in flow angle with respect to the blade is just

$$(1 + \tan^2\beta)\Delta\beta = (v/U) - (u/U)\tan\beta$$

it is convenient to write in general

$$(1 + \tan^2\beta)\Delta\beta = (1 + \tan^2\vartheta)\Delta\vartheta - (\omega R/U)(u/U) \qquad (12)$$

where account has been taken of the fact that

$$U\tan\beta - U\tan\vartheta = \omega R$$

where ω is the angular velocity of stall propagation. In particular, the variation of inlet angle to the blade row is, using Eq. (10),

$$2\sec\beta_1\sec\vartheta_1\Delta\beta_1 = P_1(0)\sin(\beta_1 - \vartheta_1) + \theta_1(0)\cos(\beta_1 - \vartheta_1) \qquad (13)$$

Now the condition for the pressure jump given by Eq. (2) may be written explicitly as

$$P_2(0) - P_1(0) = \begin{cases} -\left[\dfrac{\Delta p^*}{(1/2)\rho U^2} + b(\beta_1 - \beta_1^*)\right]; \\ \qquad (2n - \alpha)\pi \le y/R \le (2n + \alpha)\pi \\ \dfrac{b}{2}\cos^2\beta_1\left[\left(1 + \dfrac{\omega R}{U}\sin\vartheta_1\cos\vartheta_1\right)\theta_1(0) + \dfrac{\omega R}{U}\cos^2\vartheta_1 P_1(0)\right]; \text{ elsewhere} \end{cases} \qquad (14)$$

Downstream of the cascade the flow may be treated in a similar manner. In addition to satisfying the above condition on pressure jump, the discharge angle variation $\Delta\beta_2$ must bear the relation to the inlet angle prescribed by the cascade characteristic, Eq. (1).

Then utilizing Eq. (12) and the fact that the axial velocity is continuous across the cascade, Eq. (1) may be written

$$\cos^2 \beta_2 \{\theta_2(0) + (\omega R/U) \cos^2 \vartheta_1 [P_1(0) + \theta_1(0) \tan \vartheta_1]\} = a \cos^2 \beta_1 \{\theta_1(0) + (\omega R/U) \cos^2 \vartheta_1 [P_1(0) + \theta_1(0) \tan \vartheta_1]\} \quad (15)$$

Summarizing the problem, the pressure and angle perturbations vanish far upstream of the blade row while the pressure perturbation $p_2(\infty)$ and the angle perturbation $\Delta\vartheta_2(\infty)$ may at most have constant values far downstream. Taken together with Eqs. (14) and (15), which respectively express the physical conditions that the pressure jump and the cascade discharge angle are those prescribed by the cascade performance, the problem is completely specified.

Stall Propagation with Simple Cascade Characteristics

The details of stall propagation are particularly simple when the cascade discharge angle is unaffected by the inlet angle and when the pressure rise across the cascade is zero or Δp^* accordingly as the region in question is stalled or unstalled. In high solidity cascades this condition may be nearly realized; in the present formulation it corresponds to the case when $a = b = 0$. Then the pressure jump condition is simply

$$P_2(0) - P_1(0) = \begin{cases} -\dfrac{\Delta p^*}{(1/2)\rho U^2}; & (2n - \alpha)\pi \leq \dfrac{y}{R} \leq (2n + \alpha)\pi \\ 0 & \text{; elsewhere} \end{cases} \quad (16)$$

Since P_1 and P_2 are both harmonic functions, it is convenient to commence construction of the solution by obtaining the harmonic function that assumes the values $P_2(0) - P_1(0)$ along the y-axis, is regular elsewhere, and approaches at most finite constant values far ahead and far behind the blade row. This is easily done by recalling the ideal flow field associated with an infinite row of sources or sinks. The complex potential of a unit source at the origin is just $[1/(2\pi)] \log z$ where $z = x + iy$ is an arbitrary point in the plane. The imaginary part of this general potential, the stream function, represents the flux of fluid across a curve connecting the point z with any fixed point of the plane. If z moves upward along the y-axis at small negative values of x, the flux increases by half the source strength as z passes the origin, the change being discontinuous for sufficiently small values of x; and thus $Im(1/\pi) \log z$ possesses a unit jump at the origin. Then clearly the desired harmonic function may be constructed by a superposition of such jumps; more precisely it may be constructed by superposing a negative unit jump at each point $y = i(2n - \alpha)\pi$ and a positive unit jump at each point $y = i(2n + \alpha)\pi$. The positive jumps, considered separately, correspond to an infinite vertical row of sources with spacing $2\pi R$, and the resulting complex potential is known (see, for example, Lamb[6]) to be

$$(1/\pi) \log \{\sinh (1/2) [(z/R) + i\alpha\pi]\}$$

The potential representing the negative unit jumps is entirely similar so that the desired harmonic function is

$$F(x, y) = \frac{1}{\pi} Im \log \left\{ \frac{\sinh (1/2) [(z/R) - i\alpha\pi]}{\sinh (1/2) [(z/R) + i\alpha\pi]} \right\} = \frac{1}{\pi} \left(\tan^{-1} \left\{ \frac{\tan(1/2) [(y/R) - \alpha\pi]}{\tanh (1/2) (x/R)} \right\} - \tan^{-1} \left\{ \frac{\tan (1/2) [(y/R) + \alpha\pi]}{\tanh (1/2) (x/R)} \right\} \right) \quad (17)$$

The function $F(x, y)$ is odd in x; in fact

$$F(0^-, y) = \begin{cases} 1 \\ 0 \end{cases}$$

while

$$F(0^+, y) = \begin{cases} -1 \\ 0 \end{cases}$$

Furthermore, as $x \to \infty$,

$$F(\infty, y) = \frac{1}{\pi} \{(1/2) [(y/R) - \alpha\pi] - (1/2) [(y/R) + \alpha\pi]\} = -\alpha$$

and similarly

$$F(-\infty, y) = \alpha$$

Now the perturbation pressures P_1 and P_2 can differ from a multiple of F only by an harmonic function that is regular except at certain points of the cascade. Its form is determined by the remaining condition to be imposed, Eq. (15), on the cascade discharge angle. From the fact that P and θ are harmonic conjugates, it is clear that the supplementary harmonic function being sought can differ from the conjugate of F by, at most, a constant. Denote this function $G(x, y)$ such that

$$\partial G/\partial x = \partial F/\partial y, \partial G/\partial y = -\partial F/\partial x$$

Then the pressure field may be written

$$\left.\begin{aligned} P_1 &= A[F(x, y) - \alpha] + BG(x, y) \\ P_2 &= \left[\frac{\Delta p^*}{(1/2)\rho U^2} - A\right] [F(x, y) + \alpha] + BG(x, y) - \alpha \frac{\Delta p^*}{(1/2)\rho U^2} \end{aligned}\right\} \quad (18)$$

and the field of flow angle perturbations as

$$\left.\begin{aligned} \theta_1 &= -AG(x, y) + B[F(x, y) - \alpha] \\ \theta_2 &= -\left[\frac{\Delta p^*}{(1/2)\rho U^2} - A\right] G(x, y) + B[F(x, y) + \alpha] + \alpha C \end{aligned}\right\} \quad (19)$$

where A, B, and C are constants to be determined.

Now the angular velocity of stall propagation ω and the fraction α of the compressor circumference which

is stalled for a given inlet angle are determined by the perturbation of inlet angle which is induced by the stall itself. Referring to Eq. (13) and substituting the values for P_1 and θ_1, the inlet angle perturbation may be written

$$2 \sec \beta_1 \sec \vartheta_1 \Delta\beta_1 = [-A \cos(\beta_1 - \vartheta_1) + B \sin(\beta_1 - \vartheta_1)]G(0, y) + [A \sin(\beta_1 - \vartheta_1) + B \cos(\beta_1 - \vartheta_1)][F(0^-, y) - \alpha] \quad (20)$$

But since

$$G(x, y) = \frac{1}{\pi} Rl \log \left\{ \frac{\sin(1/2)[(z/R) - i\alpha\pi]}{\sin(1/2)[(z/R) + i\alpha\pi]} \right\}$$

it is clear that $G(0, y)$ and hence, in general, $\Delta\beta_1(0, y)$ have logarithmic singularities at the edges of the stalled region, $y/R = \pm\alpha\pi$. Therefore, the only possibility of satisfying the condition that $\beta_1 = \beta_1^*$ at these points is that the coefficient of $G(0, y)$ vanish in the expression for the inlet angle perturbation. Therefore

$$A \cos(\beta_1 - \vartheta_1) = B \sin(\beta_1 - \vartheta_1)$$

or

$$A(1 + \tan\beta_1 \tan\vartheta_1) = B(\tan\beta_1 - \tan\vartheta_1) \quad (21)$$

and employing this to simplify Eq. (20), the expression for the inlet angle perturbation becomes simply

$$\Delta\beta_1(0, y) = \frac{A[F(0^-, y) - \alpha]}{2(\tan\beta_1 - \tan\vartheta_1)} = \frac{A}{2(\omega R/U)}[F(0^-, y) - \alpha] \quad (22)$$

The determination of constants A and B requires imposing the condition on cascade discharge angle given by Eq. (15). In the present example where $a = 0$, $\Delta\beta_2 = 0$ and consequently

$$\theta_2(0) + (\omega R/U)\cos^2\vartheta_1[P_1(0) + \theta_1(0)\tan\vartheta_1] = 0 \quad (23)$$

Substitution of the proposed solutions [Eqs. (18) and (19)] gives, due to the linear independence of $F(0^-, y)$ and $G(0, y)$

$$[(\omega R/U)A] - [2(1 - \tan^2\vartheta_1) - (1 + \tan\beta_1\tan\vartheta_1)]B = 0 \quad (24)$$

$$[2(1 + \tan^2\vartheta_1) - (1 + \tan\beta_1\tan\vartheta_1)]A + [(\omega R/U)B] = \{\Delta p^*/[(1/2)\rho U^2]\}(1 + \tan^2\vartheta_1) \quad (25)$$

$$(1 + \tan^2\vartheta_1)C = [(\omega R/U)A] - [2(1 + \tan^2\vartheta_1) - (1 + \tan\beta_1\tan\vartheta_1)] \quad (26)$$

It appears immediately from Eq. (26) that the downstream flow angle $\Delta\vartheta_2(\infty)$ is unperturbed by the stall. Comparison of Eqs. (21) and (25) gives directly that

$$A = (1/2)\{\Delta p^*/[(1/2)\rho U^2]\} \quad (27)$$

There remain two homogeneous relations, Eqs. (21) and (24), to be satisfied and this may be accomplished only if their coefficients are related—that is, if there exists a relation between the inlet angle and the speed of stall propagation. Dividing these two relations gives simply

$$(\omega R/U)^2 = 1 + \tan^2\vartheta_1$$

or in terms of the inlet angle relative to the blades,

$$\omega R/U = (1/2)[(1 + \tan^2\beta_1)/\tan\beta_1] = \csc 2\beta_1 \quad (28)$$

As indicated while discussing the physical mechanism of stall, the propagation speed is independent of the peripheral extent of the stalled region in conformity with the experiments. Since the critical item in determining the propagation speed is the inlet angle to the cascade, it seems reasonable that the propagation speed is independent of the stream deflection in passing through the blade row. It is not surprising that this is identical with the result obtained by Sears,[5] when the phase lag associated with his assumed pressure loss vanishes.

The extent of the stalled region must be determined through consideration of the actual distribution of inlet flow angle which is now known explicitly to be

$$\Delta\beta_1 = \{1/[4(\omega R/U)]\}[F(0^-, y) - \alpha]\{\Delta p^*/[(1/2)\rho U^2]\} \quad (29)$$

The total angle of attack $\beta_1 + \Delta\beta_1$ must equal β_1^* at the edges of the stalled region, and, since $F(0^-, y)$ is discontinuous at these points, the proper limiting value is its mean, which is equal to $1/2$. Therefore the condition $\Delta\beta_1(0, \pm\alpha\pi R) = \beta_1^* - \beta_1$ determines the fraction of stalled blade region to be

$$\alpha = (1/2) - (\beta_1^* - \beta_1)(\csc 2\beta_1)4\{[(1/2)\rho U^2]/\Delta p^*\} \quad (30)$$

So far as the dependence of α upon β_1 is concerned, it is predominantly the factor $\beta_1^* - \beta_1$ which affects the result, the variation of $\csc 2\beta_1$ being small under usual circumstances. It is clear that the stall will first appear for angles below that which would cause the cascade to stall uniformly. On the other hand, the inlet angle β_1 must exceed β_1^* by a certain amount before the entire blade row is stalled. It must be kept in mind, however, that the solution becomes inaccurate long before this condition is reached since the linearization rests on the assumption that $\alpha \ll 1$.

The propagation speed $\omega R/U$ is shown in Fig. 10 as a function of the inlet angle. It is of interest to note that the propagation speed is particularly insensitive to variations of inlet flow angle in the neighborhood of $\beta_1 = \pi/4$, a value that is usual for normal axial compressors. This is certainly related to the observed fact that the propagation speed does not vary markedly as the compressor is throttled. The manner in which the stalled fraction α increases with inlet angle is shown in Fig. 11 for the particular values of $\beta_1^* = \pi/4$ and $\Delta p^*/[(1/2)\rho U^2] = 0.5$. It appears that a rather narrow range of inlet angle is involved in passing from the first appearance of stall propagation to a completely stalled blade row. While this is probably realistic near the onset of stall, it is certainly in error as the stalled region grows. The pressure rise Δp^* has

a strong influence upon the angle at which stall first appears as well as the range of angles over which stall propagation is possible. The angle β_1 for incipient stall propagation is decreased for a heavily loaded blade row. Physically this says simply that the "relief" on other blades due to a region of stalled blades is greater when the stall involves a larger loss of pressure. To illustrate this influence, the variation of α with β_1 is shown in Fig. 12 for values of $\Delta p^*/[(1/2)\rho U^2] = 0.5$, 1.0, and 2.0 with the inlet angle β_1^* at which stall occurs equal to 45°.

Stall Propagation with General Cascade Characteristics

The results of the previous section are somewhat modified when the pressure rise across the cascade and the discharge angle from the cascade depend upon the inlet angle near the stall. The pressure field ahead of the blade row is of the same form as before

$$P_1(x, y) = A[F(x, y) - \alpha] + BG(x, y) \qquad (31)$$

but the downstream pressure field must be modified in order to satisfy the general condition on pressure jump given by Eq. (2). In the stalled region the pressure drop is now $\{\Delta p^*/[(1/2)\rho U^2]\} + b(\beta_1 - \beta_1^*)$ so that the pressure field downstream of the cascade could be chosen as

$$P_2(x, y) = \left(\{\Delta p^*/[(1/2)\rho U^2]\} + b(\beta_1 - \beta_1^*) - A\right) \times [F(x, y) + \alpha] + BG(x, y) - \alpha\left(\{\Delta p^*/[(1/2)\rho U^2]\} + b(\beta_1 - \beta_1^*)\right)$$

were it not for the fact that the pressure rise across the cascade is proportional to the inlet angle perturbation in the installed region. Now since the formal expression for the upstream pressure field is identical with that employed in the solution for simple cascade characteristics, the expression for $\Delta\beta_1$ is general and hence

$$P_2(0, y) - P_1(0, y) = (b/2)\,[A/(\omega R/U)]\,(1 - \alpha)$$

in the unstalled region. The appropriate expression for $P_2(x, y)$ is therefore

$$P_2(x, y) = \left[\frac{\Delta p^*}{(1/2)\rho U^2} + b(\beta_1 - \beta_1^*) - A\right] \times [F(x, y) + \alpha] + BG(x, y) - \frac{b}{2}\frac{A}{(\omega R/U)}(1 - \alpha) \times [F(x, y) + 1] - \alpha\left[\frac{\Delta p^*}{(1/2)\rho U^2} + b(\beta_1 - \beta_1^*)\right] \qquad (32)$$

inasmuch as $F(0^+, y) + 1$ vanishes in the stalled region and is equal to unity elsewhere. The corresponding flow angle variations are then

$$\theta_1 = -AG(x, y) + B[F(x, y) - \alpha] \qquad (33)$$

$$\theta_2 = -\left[\frac{\Delta p^*}{(1/2)\rho U^2} + b(\beta_1 - \beta_1^*) - A\right] G(x, y) + B[F(x, y) + \alpha] + \frac{b}{2}\frac{A}{(\omega R/U)}(1 - \alpha)G(x, y) + \alpha C \qquad (34)$$

where, as before, C is a constant to be determined.

The condition on the outlet angle, given by Eq. (15), now gives, upon substitution of the explicit forms for the pressure and angle perturbation fields, three relations to determine the constants A, B, and C.

$$(\tan\beta_1 - \tan\vartheta_1)\,[1 - a(\cos^2\beta_1/\cos^2\beta_2)]A - \{2(1 + \tan^2\vartheta_1) - [1 - a(\cos^2\beta_1/\cos^2\beta_2)](1 + \tan\vartheta_1\tan\beta_1)\}B = 0 \qquad (35)$$

$$\left\{\left[2 + \frac{b}{2}\frac{(1 - \alpha)}{(\omega R/U)}\right](1 + \tan^2\vartheta_1) - \left(1 - a\frac{\cos^2\beta_1}{\cos^2\beta_2}\right) \times (1 + \tan\vartheta_1\tan\beta_1)\right\} A + (\tan\beta_1 - \tan\vartheta_1) \times \left(1 - a\frac{\cos^2\beta_1}{\cos^2\beta_2}\right) B = (1 + \tan^2\vartheta_1)\left[\frac{\Delta p^*}{(1/2)\rho U^2} + b(\beta_1 - \beta_1^*)\right] \qquad (36)$$

$$C = (\tan\beta_1 - \tan\vartheta_1)\,[1 - a(\cos^2\beta_1/\cos^2\beta_2)]A - \{2(1 - \tan^2\vartheta_1) - [1 - a(\cos^2\beta_1/\cos^2\beta_2)](1 + \tan\vartheta_1\tan\beta_1)\}B = 0 \qquad (37)$$

where as before the constant $C = 0$ so that the flow angle far downstream is unperturbed by the stall. Furthermore, it follows by comparison of Eq. (21) with Eq. (36) that the constant A is just

$$A = \frac{1}{2}\left\{\left[\frac{\Delta p^*}{(1/2)\rho U^2} + b(\beta_1 - \beta_1^*)\right] \div \left[1 + \frac{b}{4}\frac{(1 - \alpha)}{(\omega R/U)}\right]\right. \qquad (38)$$

which reduces to the previous result [Eq. (27)] when $b = 0$. Now by dividing Eqs. (35) and (21), as was done for the simple cascade characteristic, the corresponding result is obtained for the speed of stall propagation

$$(\omega R/U)^2 = 1 + \tan^2\vartheta_1 + [2a\cos^2\beta_1/(\cos^2\beta_2 - \cos^2\beta_1)] \times (1 + \tan\beta_1\tan\vartheta_1)$$

Upon elimination of ϑ_1, the relative inflow angle, the propagation speed becomes simply

$$\omega R/U = [1 + a(\cos^2\beta_1/\cos^2\beta_2)]\csc\beta_1 \qquad (39)$$

Since a is, in general, a positive quantity, it appears that the influence of discharge angle deviation is to increase the propagation speed over that which would be obtained with a fixed outlet angle, $a = 0$.

This value of the constant A, which has been obtained in Eq. (38), allows computation of the inlet angle perturbation according to Eq. (22). Thus

$$\Delta\beta_1 = \frac{1}{4}\left\{\frac{\Delta p^*}{(1/2)\rho U^2} + b(\beta_1 - \beta_1^*)\right\} \left\{(\omega R/U) + (b/4)(1 - \alpha)\right\} [F(0^-, y) - \alpha] \qquad (40)$$

and using the same reasoning as that employed in the problem of the simple characteristic, the fraction of the blade row periphery which is stalled is

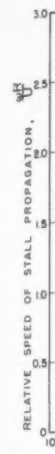

FIG. 1

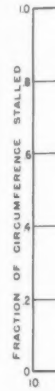

FIG. 11

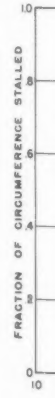

FIG. 1

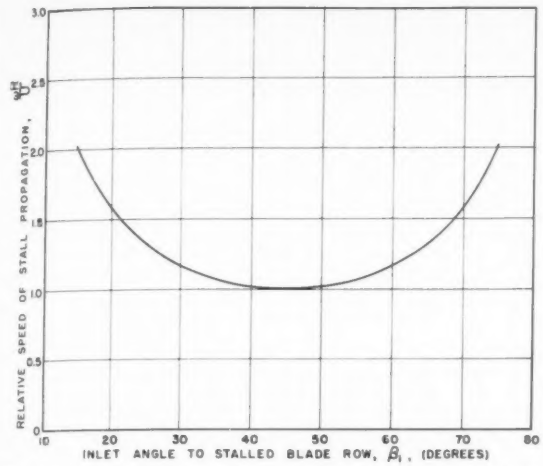

FIG. 10. Propagation speed for simple cascade characteristic.

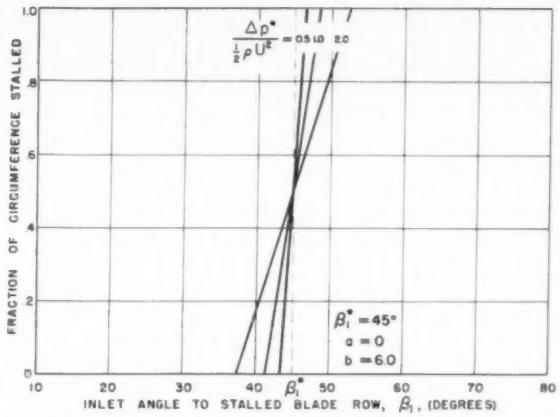
FRACTION OF CIRCUMFERENCE STALLED
$\frac{\Delta p^*}{\frac{1}{2}\rho U^2}$ = 0.5 1.0 2.0
β_1^* = 45°
a = 0
b = 6.0
INLET ANGLE TO STALLED BLADE ROW, β_1, (DEGREES)

FIG. 13. Effect of more general cascade characteristic upon length of stalled region, $a = 0$, $b = 6.0$.

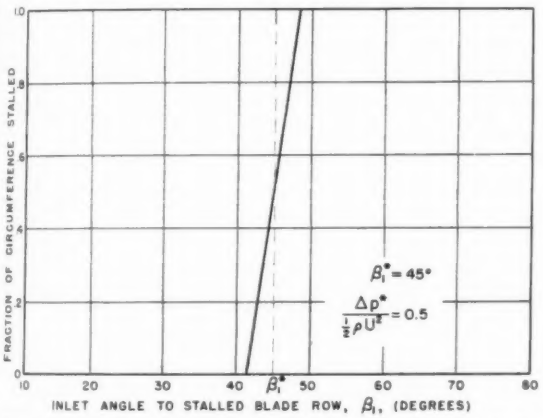

FIG. 11. Variation of length of stalled region with inlet angle for simple cascade characteristic.

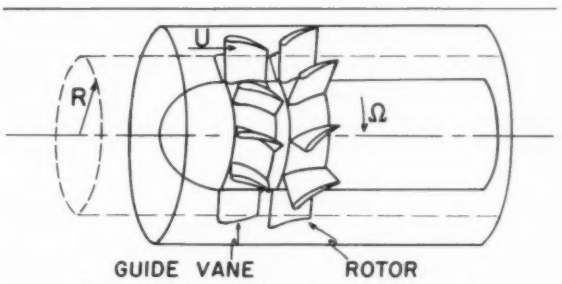

FIG. 14. Diagram of simple axial compressor.

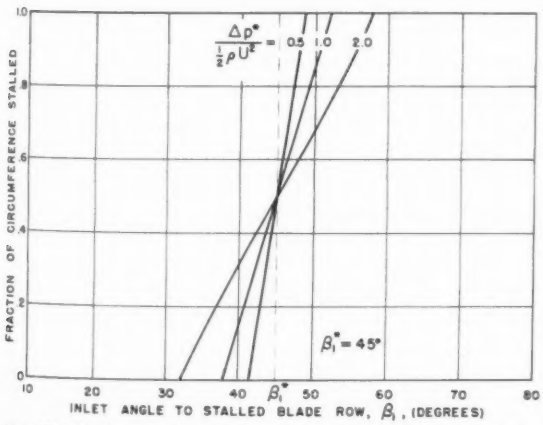
FRACTION OF CIRCUMFERENCE STALLED
$\frac{\Delta p^*}{\frac{1}{2}\rho U^2}$ = 0.5 1.0 2.0
β_1^* = 45°
INLET ANGLE TO STALLED BLADE ROW, β_1, (DEGREES)

FIG. 12. Variation of length of stalled region with inlet angle for various values of $\Delta p^*/[(1/2)\rho U^2] = 0.5, 1.0, 2.0$.

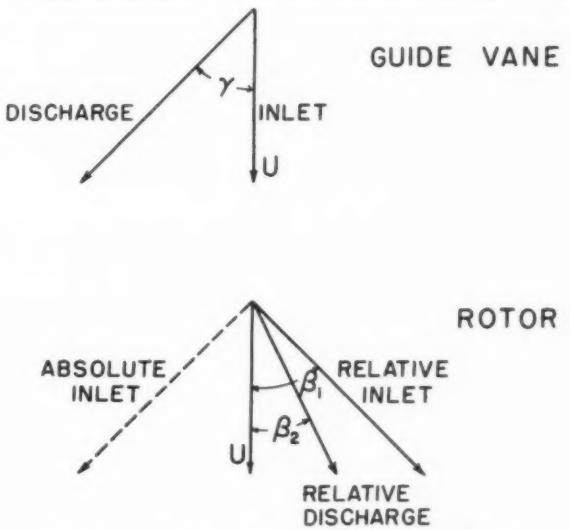

FIG. 15. Velocity diagram for simple compressor stage.

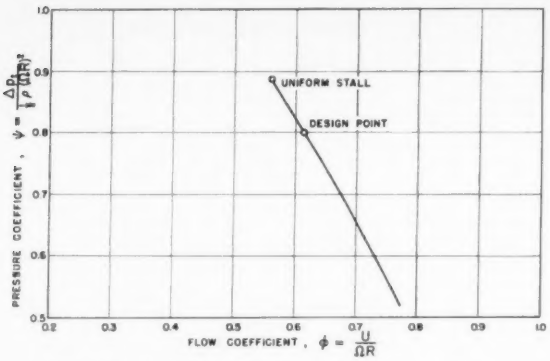

FIG. 16. Normal performance of compressor stage.

$$\alpha = \frac{1}{2} - 4(\beta_1^* - \beta_1)\frac{(1/2)\rho U^2}{\Delta p^*} \times \left[\left(1 + \alpha\frac{\cos^2\beta_1}{\cos^2\beta_2}\right)\csc 2\beta_1 + \frac{b}{8}\right] \quad (41)$$

where terms of higher order in $\beta_1^* - \beta_1$ have been deleted. Eqs. (39) and (41) give stall propagation speed $\omega R/U$ and the peripheral extent of stall α as functions of β_1 alone for fixed values of a, b, and $\Delta p^*/[(1/2)\rho U^2]$.

Since the value of a is usually small, the variation of outlet angle is not a strong influence on stall propagation speed. Since $\cos^2\beta_1/\cos^2\beta_2$ is usually less than unity, it is not probable that the propagation speed will be augmented by more than 25 per cent in this manner. The corresponding small influence upon the peripheral extent of the stall region is to decrease the range of inlet angles for which stall propagation may be expected. Similarly the inlet angle where stall propagation will first occur is increased by an increase in the cascade discharge deviation, a. The most influential factor in determining the extent of stall regions for a given inlet angle is the cascade pressure rise Δp^*, as was found to be true with the simple cascade characteristic. The influence of the slope of pressure characteristic at the stall is illustrated in Fig. 13 where the variation of α with β_1 is shown for the same values of $\Delta p^*(1/2)\rho U^2$ used in Fig. 12, with the exception that now the slope is taken equal to 6.0. A large slope of the pressure characteristic, such as that shown, may exert considerable influence in reducing the range of inlet angles for which stall propagation is observed.

Performance of a Stalled Compressor Stage

The results of the analysis of stalling performance of a cascade may be employed to estimate the performance of a simple compressor stage, Fig. 14, which consists of a rotor following an inlet guide vane, which will be considered infinitely far upstream. Then referring to Fig. 15, the absolute outlet angle from the guide vane is γ. It is convenient to discuss the compressor performance in terms of the two conventional parameters, ϕ, the flow coefficient, and ψ, the pressure coefficient. These are defined as

$$\phi = U/(\Omega R) \quad (42)$$

$$\psi = \Delta p_t/[(1/2)\rho(\Omega R)^2] \quad (43)$$

where Ω is the angular velocity of the rotor and Δp_t is the mean increase in total pressure across the stage. Then the compressor characteristic is given by plotting ψ versus ϕ as indicated in Fig. 16 where the performance is shown for normal operation up to the stall point that would be reached if all blades stalled simultaneously.

Now according to the velocity diagram the inlet angle β_1 to the rotor is

$$\tan\beta_1 = (1/\phi) - \tan\gamma \quad (44)$$

so that the value ϕ^* of the flow coefficient for which the normal stall occurs is $\phi^* = (\tan\beta_1 + \tan\gamma)^{-1}$. Furthermore, the total pressure rise Δp_t across the rotor is, for no losses in the blade row,

$$\Delta p_t = \rho\Omega R(U\tan\beta_1 - U\tan\beta_2)$$

or in terms of the pressure and flow coefficients

$$\psi = 2\phi(\tan\beta_1 - \tan\beta_2) \quad (45)$$

which holds up to the stall angle. Thus specification of the flow coefficient and pressure coefficient is equivalent to specifying the inlet and discharge angles from the rotor.

Referring to the compressor performance of Fig. 16, it is clear that, as the flow coefficient ϕ is reduced, a point is reached where stall propagation is first possible. This is just the condition that $\alpha = 0$ and, assuming for the moment the simplest cascade characteristic where $a = b = 0$, it follows from Eq. (30) that

$$\Delta p^*/[(1/2)\rho U^2] = 8(\beta_1^* - \beta_1)\csc 2\beta_1$$

Now according to Eq. (44) $\beta_1^* - \beta_1 \approx (\cos^2\beta_1/\phi^2)(\phi - \phi^*)$, and, consequently, the value ϕ_i of the flow coefficient for which stall propagation first appears is

$$\phi_i = \phi^*\left[1 + \frac{1}{4}(1 - \phi^*\tan\gamma)\frac{\Delta p^*}{(1/2)\rho U^2}\right] \quad (46)$$

Actually, of course, the stall can not start with a region of arbitrarily small peripheral extent but must involve at least one blade channel. Under usual circumstances this represents a negligible influence on ϕ_i.

The total pressure loss involved due to the propagating stalled region is simply equal to the static pressure perturbation far downstream of the blade row, the change in kinetic energy resulting from distortion of the flow field being of second order. Thus, according to Eq. (18), the pressure field perturbation far downstream is $P_2(\infty) = -\alpha\{\Delta p^*/[(1/2)\rho U^2]\}$ and hence the change $\Delta\psi$ in pressure coefficient due to stall is just

$$\Delta\psi \approx -\alpha\phi^2\{\Delta p/[(1/2)\rho U^2]\} \quad (47)$$

The pressure loss is thus simply proportional to the fraction α of the circumference which is stalled, so that utilizing Eq. (30) of the previous calculation

$$\Delta\psi = [-2\phi^*/(1 - \phi^* \tan \gamma)]\,(\phi_i - \phi) \quad (48$$

Therefore, as the compressor stage is throttled, stall propagation first becomes possible at a flow coefficient ϕ_i; as the flow coefficient is reduced farther, the pressure coefficient falls below that which would occur in the absence of stall by an amount proportional to the reduction of the flow coefficient below ϕ_i. To the present approximation this reduction continues until the periphery is entirely stalled—that is, $\alpha = 1$, at which point the loss in pressure coefficient is simply

$$\phi^2\{\Delta p^*/[(1/2)\rho U^2]\}$$

Actually the small perturbation analysis employed is invalid when α becomes of appreciable size, and losses computed under these circumstances are at best of the proper magnitude.

For the general cascade characteristic the flow coefficient for incipient propagating stall is

$$\phi_i = \phi^* \left(1 + \left\{\left[\frac{1}{4}(1 - \phi^* \tan \gamma)\frac{\Delta p^*}{(1/2)\rho U^2}\right] \div \left(1 + a\frac{\cos^2 \beta_1^*}{\cos^2 \beta_2^*} + \frac{9}{32} b \sin^2 \beta_1^*\right)\right\}\right) \quad (49)$$

while the change in pressure coefficient $\Delta\psi$ due to stall becomes, neglecting terms of small order,

$$\Delta\psi = -\left[\frac{2\phi^*}{1 - \phi^* \tan \gamma}\left(1 + a\frac{\cos^2 \beta_1^*}{\cos^2 \beta_2^*}\right) + \frac{b}{2(1 + \tan^2 \beta_1^*)}\right] \quad (50)$$

The principle effect of variations in pressure rise and cascade discharge angle due to changing inlet angle is, under normal circumstances, to increase the pressure loss somewhat.

To illustrate the influence of propagating stall upon the compressor performance, consider the arbitrary compressor characteristic given in Fig. 16. Under conditions of uniform flow the stage stalls at a rotor inlet angle of $\beta_1 \equiv \beta_1^* = 51° 30'$ and at a corresponding flow coefficient $\phi = \phi^* = 0.56$. Assume further that the guide vane discharge angle is $\gamma = 28°$, while $a = 0.25$ and $b = 6.5$. The parameters employed are approxi-

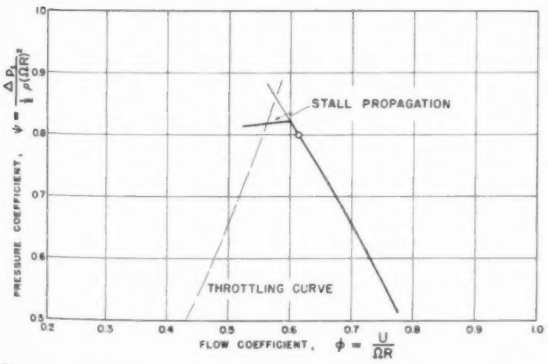

FIG. 17. Performance of compressor stage with stall propagation.

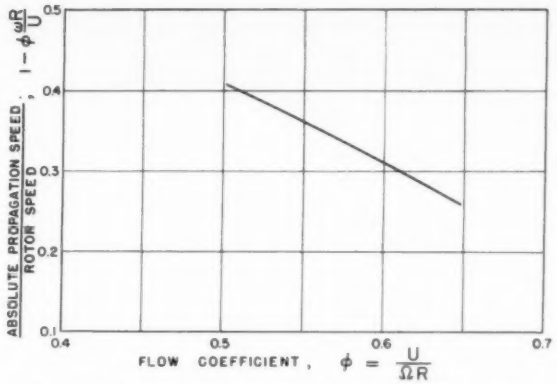

FIG. 18. Rate of stall propagation for compressor stage.

mately those values for the guide vane and first rotor near the root of the compressor employed in the experiments of Rannie and Iura using vortex blading. As the compressor is throttled, the first possibility of stall propagation occurs, according to Eq. (49), at $\phi_i = 0.6$. Then as the flow is further reduced, the pressure coefficient drops below the normal characteristic by an amount that is easily calculated from Eq. (50). The resulting performance with propagating stall is shown as a broken line in Fig. 17.

Now suppose, as is usually the case, the flow through the compressor is reduced by adjusting a throttle downstream of the compressor while the compressor speed is held constant. Then the pressure rise Δp_i imposed upon the compressor is proportional to U^2, or in terms of the compressor parameters $\psi = \kappa\phi^2$, where the coefficient κ depends upon the throttle setting. Therefore the states of normal operation and propagating stall which correspond to the same throttle setting lie along a parabolic "throttling" curve such as that indicated in Fig. 17. It is probable, there being some indication from the experiments of Rannie and Iura, that the stall propagation does not appear as soon as the flow coefficient ϕ_i is encountered, but, rather, the transition from normal operation to stall propagation takes place as the result of instability of the former at a flow coefficient somewhat less than ϕ_i. In this case the transition must be to that state of stall propagation connected by the appropriate throttling curve.

The values of stall propagation speed for the compressor stage follow directly from Eq. (39) using the relation between flow coefficient and rotor inlet angle given by Eq. (44). Since the speeds of propagation are usually observed relative to the fixed blade rows, the significant quantity is $(\Omega - \omega)R$, and the ratio of absolute angular velocity of stall propagation to the rotor angular velocity is just

$$1 - \phi(\omega R/U)$$

This speed of propagation for the compressor stage is shown in Fig. 18 at the performance conditions of Fig. 17. The stall propagation speed observed by Rannie and Iura is about 0.3, and it is of interest that the value of propagation speed computed near the onset of stall—

that is, at $\phi = 0.6$—is in remarkable agreement with their value. In view of the facts that a two-dimensional theory has been employed and that the interference of neither the guide vanes nor the stalled blade rows downstream of the first rotor is accounted for, the agreement must be considered, in a certain measure, fortuitous. Although the magnitude is essentially correct, the only discrepancy seems to be the variation of calculated propagation speed with flow coefficient, while the experimental value appears constant over a wide range. This feature, however, is simply a result of the linearization. For whereas in the linearized analysis the flow approaches the stalling blades at nearly the undisturbed upstream flow angle, the real flow approaching the blades is strongly disturbed by stall and seems to adjust itself to almost a constant flow angle, regardless of how severely the compressor is throttled. Consequently, as was clear at the outset, accuracy of the calculation can be expected only near the condition of incipient stall.

Concluding Remarks

From the experimental data that are available at the present time, it appears that the model upon which the foregoing analysis is based is a realistic one and contains the essence of the phenomena that have been observed. Based upon this model, the features of stall propagation—that is, the extent of stall region—the pressure loss associated with stalled operation together with its attending effect upon performance, as well as the speed of stall propagation arise naturally and simply. Discrepancies in comparison with experimental results on propagation speed cannot be interpreted as inadequacy of the model until either a more detailed experimental investigation of the mechanism is undertaken or the results are extended to situations more nearly approximating those on which observations have been made. Extensions appear logical in two directions: the effect of mutual interference between adjacent blade rows in relative motion and stall propagation in a three-dimensional actuator desk.

References

[1] Emmons, H. W., Pearson, C. E., and Grant, H. P., *Compressor Surge and Stall Propagation*, Presented at Annual Meeting, American Society of Mechanical Engineers, New York, December, 1953.

[2] Iura, T., and Rannie, W. D., *Experimental Investigation of Propagating Stall in Axial Flow Compressors*, Paper No. 53-SA-69, American Society of Mechanical Engineers, presented in Los Angeles, July 29, 1952.

[3] Huppert, M. C., and Benser, W. A., *Some Stall and Surge Phenomena in Axial Flow Compressors*, Presented at Twenty-First Annual Meeting, Institute of the Aeronautical Sciences, New York, January, 1953.

[4] Sears, W. R., *On Asymmetric Flow in an Axial-Flow Compressor Stage*, Journal of Applied Mechanics, pp. 57–62, March, 1953.

[5] Sears, W. R., *A Theory of "Rotating Stall" in Axial-Flow Compressors*, Report in Partial Fulfillment of Contract AF 33(038)-21406, Office of Scientific Research, U.S. Air Force.

[6] Lamb, Sir Horace, *Hydrodynamics*, Sixth Edition, p. 71, Cambridge University Press, 1932.

IAS Twenty-Fourth Annual Meeting

Hotel Sheraton-Astor, New York City, January 23–27, 1956

The Meetings Committee is planning sessions on Aerodynamics, Aeroelasticity, Structures, Rotating Wing, Aircraft Design, Meteorology, etc.

Authors wishing to have papers considered for presentation at this meeting should submit outlines or short abstracts to the Meetings Committee, 2 East 64th St., New York 21, N.Y., no later than September 1, 1955.

An Application of Variation Methods to the Computation of the Deformation of a Cantilever Plate Subjected to Nonuniform and Aeroelastically Induced Loads

EUGENE E. COVERT*

Massachusetts Institute of Technology

SUMMARY

The equations that govern the shape of the deflection surface of a cantilever plate subjected to an arbitrary transverse load are solved in terms of an influence surface which is approximated by the Rayleigh-Ritz procedure. If the loading is also dependent upon the deflection, this procedure results in an integral equation. The deformation surfaces of rectangular plates with one edge clamped and the remaining edges free, for both uniform thickness distribution and double wedge thickness distribution have been calculated and are compared with measurements. The increment in the slope of the lift coefficient caused by the deformation was calculated for a wing of aspect ratio unity flying at a Mach Number of $\sqrt{2}$.

SYMBOLS

A_{mn}	=	coefficients in series expansion
b	=	semi-span
c	=	semi-chord
D	=	plate modulus $= Et^3/[12(1-\nu^2)]$
E	=	Young's modulus
h	=	semi-thickness distribution
C_1, C_2	=	Busemann's pressure-distribution coefficients
$C_{L\alpha}$	=	slope of the lift curve
f_m, g_n	=	mode function
K	=	kernel function $= p(x_0, y_0)\ (\partial w_1/\partial y)$
k	=	constant of proportionality resulting from solution of Eq. (18)
M	=	Mach Number
n	=	direction normal to plate edge
S	=	direction along plate edge
t	=	plate thickness at maximum thickness point
q	=	dynamic pressure $= (1/2)\rho V^2$
Δp	=	pressure difference across surface
P, p	=	loading distributions
u	=	constant part of loading
v	=	deformation dependent part of loading
V	=	flight velocity
w_1	=	plate deformation due to a unit point load
w_2	=	plate deformation due to loading $p(x, y)$
w	=	plate deformation in z direction
w_0	=	approximate solution
x_0	=	x coordinate of unit load
y_0	=	y coordinate of unit load
α	=	aerodynamic angle of attack
π	=	plate energy
δ	=	variation operator
∇^2	=	$(\partial^2/\partial x^2) + (\partial^2/\partial y^2)$, Laplacian operator
ρ	=	air density
ν	=	Poisson's ratio

Received August 2, 1954.

* Aeronautical Engineer, Naval Supersonic Laboratory.

INTRODUCTION

IN THE DESIGN of high-speed aircraft and missiles, the wing and tail surfaces are frequently of a high solidity ratio and can be analyzed in terms of thin plate theory. This analysis is used by the designer to compute the stresses in the surfaces and by the aerodynamicist to compute the increment in the aerodynamic characteristics due to the elastic deformation. In this application, the plate is subjected to mixed boundary conditions (clamped at one edge and free at the remaining edges) which are such that exact solutions of the governing equations are rarely found. The most common engineering approach is the application of the minimum energy theorems and the calculus of variations, and here several alternate methods of getting the approximate solution are practical. Fung[1, 2] and Luce[3, 4] have used the Ritz procedure to find approximate solutions for cases with uniform lateral loading, pure torsion, and uniform shear located along the edge opposite the clamped edge. Reissner and Stein[5] have applied a semidirect method that consists of substituting a set of approximating functions which are known in one direction and undetermined in the other direction into the energy integral. The first variation of the energy integral leads to a family of linear differential equations whose solution defines the latter set of approximating functions. This approach has been used successfully for torsional and uniform lateral load distributions.[5, 6]

The solutions to the plate bending that have been cited are all for fairly simple loading systems. While the methods are applicable to problems where the loading is nonuniform, the procedure is cumbersome, and due to its nature, the solution cannot be expressed algebraically for a completely arbitrary load distribution.

This difficulty is eliminated herein by computing the plate deformation due to a unit load using the same variational methods that the previous investigations employed. Once this solution is known, the problem of computing the deformation for an arbitrary nonuniform loading reduces to one of integration of the product of the load distribution and the unit load solution over the plate. This approach is then generalized to include the case where the load is not only nonuniform, but may also depend linearly on the deflection or its derivatives.

This latter problem arises in estimating the aeroelastic influences upon aerodynamic characteristics of flexible structures.

Analysis

Assumptions

The analysis that follows contains within it the usual assumptions of thin plate theory—namely:

(1) the thickness of the plate is small compared to the other dimensions of the plate, and

(2) the deformation of the plate is small compared to the thickness of the plate.

The first assumption implies that both the stress in the Z direction (see Fig. 1 for the coordinate system) and the shear stresses about the X and Y axes are so much smaller than both the stresses in the X and Y direction and the shear about the Z axis, that the former stresses may be neglected. The second assumption implies that the only stresses are those due to the bending. Since the deflection surface is anticlastic, it would be expected to set up tension in the midplane and thereby increase its rigidity, but the small deformation assumption limits the deflections so that these tensile forces are negligible; therefore it also follows that the midplane is unstretched. The assumptions allow for the effects of two-dimensional stress—i.e., the deflections are reduced by the lateral extension. The latter statement is, in some cases, equivalent to replacing the Young's modulus (E) by $E/(1 - \nu^2)$.

Formulation of the Problem

Since the governing differential equation is linear, a solution may be constructed by superposition of suitable primary solutions.[7] In other words, if a known solution for a unit point loading at the point x_0, y_0 is $w_1(x, y, x_0, y_0)$, then the solution for an arbitrary loading $[P(x, y)]$ is

$$w(x, y) = \iint_S w_1(x, y, x_0, y_0) P(x_0, y_0) dx_0 dy_0 \qquad (1)$$

If the loading is dependent upon the deformation in some manner, which may be written

$$P = u(x, y) + v(x, y) f(w)$$

where $f(w)$ is either w or any one of its derivatives, then the solution is

$$w(x, y) = \iint_S w_1(x, y, x_0, y_0) u(x_0, y_0) dx_0 dy_0 + \iint_S w_1(x, y, x_0, y_0)\, v(x_0, y_0) f(w) dx_0 dy_0 \qquad (2)$$

Further, if the first integral on the right-hand side is bounded, and if $w_1(x, y, x_0, y_0)$, $v(x_0, y_0)$ and $f(w)$ are bounded over the region of integration, it can be shown that the integral equation may be solved by repeated substitution and the series so obtained is convergent and converges to the solution.[8] It will be noted that if $f(w)$ depends upon w and its derivatives, Eq. (2) becomes a fairly complicated integro-differential equation.

The problem now becomes that of defining the function $w_1(x, y, x_0, y_0)$. This will be done by application of the minimum energy principle[1, 2, 7, 9]

$$\delta\pi = \delta \left[\frac{D}{2} \iint_S h^3(y) \left\{ (\nabla^2 w)^2 + 2(1 - \nu) \times \left[\left(\frac{\partial^2 w}{\partial x \partial y} \right)^2 - \frac{\partial^2 w}{\partial x^2} \frac{\partial^2 w}{\partial y^2} \right] \right\} dx dy - \iint_S w P(x, y)\, dx dy + \int M_n \frac{\partial w}{\partial n} dS - \int w \left(Q_n - \frac{\partial H_{nt}}{\partial S} \right) dS \right] = 0 \qquad (3)$$

where $h(y)$ is the normalized semithickness distribution $[h(y) = h(-y)]$, M_n, Q_n, and H_{nt} are respectively the bending moment, the shear, and the torsional moment at the edges, and the last two integrals on the right-hand side of the equation are line integrals about the edge of the plate.[1] If the first variation vanishes and if the following inequalities are satisfied,

$$0 \leq \nu \leq 0.7 \qquad (4)$$

$$D > \nu \qquad (5)$$

and if the deflection is such that each spanwise line of the deflection surface intersects the X-Y plane only at the root, then the necessary and sufficient conditions for a "weak minimum"[9] are satisfied. A weak minimum is adequate, for the deformation and its slope are small, and the loadings are such that the first derivative of the deformation surface is continuous.

Approximate Method of Solution

There are at least four methods of approximately satisfying the minimum energy requirements [Eq. (3)]; however, the Ritz method will be used herein and the sequence of approximating functions (see Appendix) will be chosen in the manner prescribed by Fung[1, 2]—i.e., let the solution be of the form

$$w(x, y) = w_0(x, y) + \sum_m \sum_n A_{mn} w_{mn} \qquad (6)$$

where

$$w_{mn} = f_m(x) g_n(y)$$

and $f_m(x)$ and $g_n(y)$ are the complete set of mode shapes of a vibrating beam having the *proper* thickness distribution and the *proper* boundary conditions. Eq. (6) is substituted into Eq. (3) and the resulting equa-

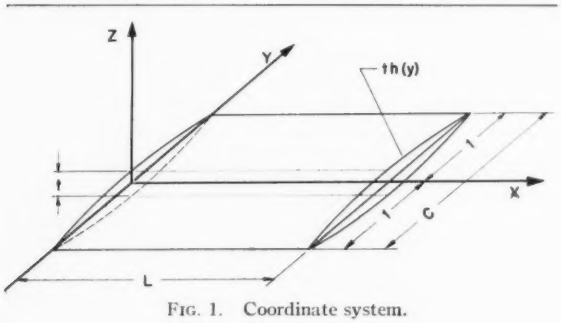

Fig. 1. Coordinate system.

tions for the A_{mn} are found [using $\delta w = (\partial w / \partial A_{mn}) \times \delta A_{mn}$], such that the integral, Eq. (3), is zero. The trial solution (w_0) is chosen to be the beam bending and torsion solution for a load distribution typical of the class of loadings being studied with E replaced by $E/(1 - \nu^2)$. This will reduce the correction terms as much as possible, so that the number of terms to be carried is small. This procedure leads to a set of $m \times n$ linear algebraic equations in the $m \times n$ unknowns (A_{mn}) which generally has the additional property (if the trial solution is not too poor an approximation) that the terms in the main diagonal (A_{mn}) are predominant. Thus the procedure given by Timoshenko[7] can be used to compute the A_{mn}. This procedure will be illustrated below with $m = 1, n = 3$. Let the system be

$$\left.\begin{aligned} a_{11}A_{11} + a_{12}A_{12} + a_{13}A_{1t} &= b_1 \\ a_{21}A_{11} + a_{22}A_{12} + a_{23}A_{1t} &= b_2 \\ a_{t1}A_{11} + a_{t2}A_{12} + a_{33}A_{1t} &= b_3 \end{aligned}\right\} \tag{7}$$

where the a_{ij} are known constants found by the integration. Now under the assumption of the importance of the main diagonal terms let

$$A_{11}^0 = b_1/a_{11} \tag{8}$$

and

$$A_{12}^0 = (b_1 - a_{21}A_{11}^0)/a_{22} \tag{9}$$

$$A_{13}^0 = (b_3 - a_{31}A_{11}^0 - a_{32}A_{12}^0)/a_{33} \tag{10}$$

and by resubstitution into Eq. (7) a second approximation is

$$\left.\begin{aligned} A_{11}^1 &= (b_1 - a_{12}A_{12}^0 - a_{13}A_{13}^0)/a_{11} \\ A_{12}^1 &= (b_2 - a_{21}A_{11}^1 - a_{23}A_{13}^0)/a_{22} \end{aligned}\right\} \tag{11}$$

and so forth. The rate of convergence is dependent upon the relative unimportance of the coupling terms and in the cases tried, the third iteration was adequate.

Examples

Calculation for Particular Static Loadings

It is desirable that the method outlined above be checked by experimental data, and such data had been obtained by the M.I.T. Aeroelastic and Structures Laboratory.[10] Fig. 2 shows the experimental and calculated influence surfaces for two load positions on a flat plate, and Fig. 3 shows the same results for a double wedge cross section. The approximate solution shows the correct curvature variation, but overestimates the centerline deformation in the flat plate case and underestimates the centerline deformation of double wedge by about 8 per cent. It will be noted in Fig. 3 that the agreement is poor at the edges. Some qualitative estimates indicate that the convergence is slower at the edges, due to the taper. It is expected that increasing the number of terms would improve the agreement in the calculation of the influence surfaces. Fig. 4 shows a comparison of the deflection surface of a uniformly loaded double wedge and as is expected, the integration improves the overall accuracy.

On the basis of these results, it appears that the method is reasonable.

*Calculation of Lift Due to Elastic Deformation**

Now the method will be applied to the problem of computing the aerodynamic induction effects upon the loading, deformation, and the aerodynamic coefficients themselves.

Symbolically, the process may be written as follows: Let the local angle of attack distribution be α_1, where

$$\alpha_1 = \alpha + (\partial w/\partial y) \tag{13}$$

and assume that the load at each point is proportional to the local incidence

$$\Delta p/q = p(x, y)\,[\alpha + (\partial w/\partial y)] \tag{14}$$

It will be observed that the derivative of w appears in Eq. (14), rather than w. Since the basic solution, Eq. (2), can be written in terms of $(\partial w)/(\partial y)$, as well as w, and since it represents a simplification to write the solution in this way, then $w_1(x, y, x_0, y_0)$ will be replaced by $(\partial w_1)/(\partial y)$ (x, y, x_0, y_0), so that Eq. (2) becomes

$$\frac{\partial w}{\partial y} = \alpha \iint_S p(x_0, y_0) \frac{\partial w_1}{\partial y}\, dx_0 dy_0 + \iint_S p(x_0, y_0) \frac{\partial w_1}{\partial y} \frac{\partial w}{\partial y_0}\, dx_0 dy_0 \tag{15}$$

or, letting

$$\frac{\partial w_2}{\partial y} = \iint_S p(x_0, y_0) \frac{\partial w_1}{\partial y}\, dx_0 dy_0$$

and

$$K(x, y, x_0, y_0) = p(x_0, y_0)\,(\partial w_1/\partial y)$$

$$\frac{\partial w}{\partial y} = \alpha \frac{\partial w_2}{\partial y} + \iint_S K(x, x_0, y_0) \frac{\partial w}{\partial y_0}\, dx_0 dy_0 \tag{16}$$

and upon applying the resubstitution technique†

* After the work described below was completed, an English Electric Company, Naval Projects Division Report L.A.t.038, entitled "The Theory of the Aeroelastic Load Distribution and Deformation of a Lifting Wing at Supersonic Speeds" of Oct. 6, 1952, by B. W. Bolton-Shaw came to the attention of the author. Dr. Bolton-Shaw's method of approach is essentially the same as that given below; however his solution for the particular problem of a supersonic wing is finally written in the form of a difference equation involving an experimentally determined influence surface.

† If the cross sections come to a sharp edge and the loading is finite at the edge, the slope of the deflection surface is infinite and the resubstitution will not converge. In fact such a curling has been observed at the NSL during wind-tunnel tests on an adiabatic flat plate with a carefully honed leading edge. Generally, this effect will not be encountered, and there are several obvious methods of avoiding this singularity—i.e., compute the kernel for a finite thickness at the edges.

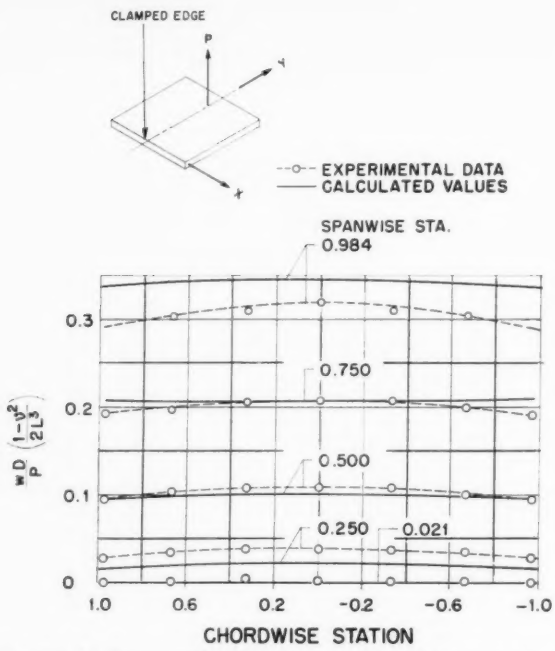

FIG. 2a. Influence surface for a 4.2 per cent thick square plate loaded at 98 per cent span and at mid-channel.

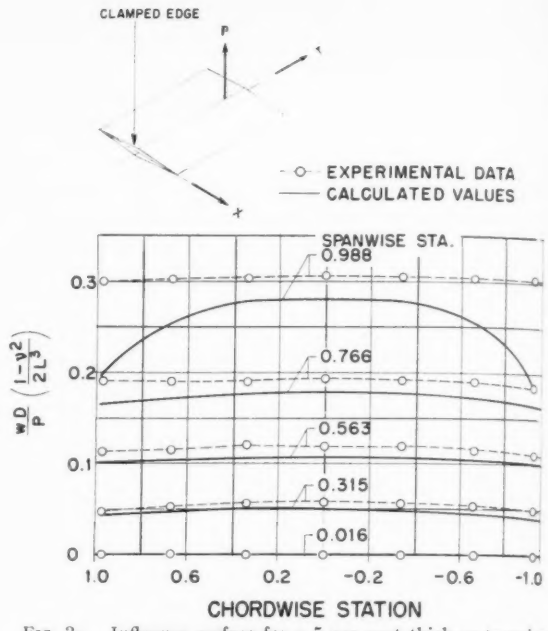

FIG. 3a. Influence surface for a 5 per cent thick rectangular plate ($AR = 1.33$) of double wedge cross section loaded at 98 per cent span and at mid-channel.

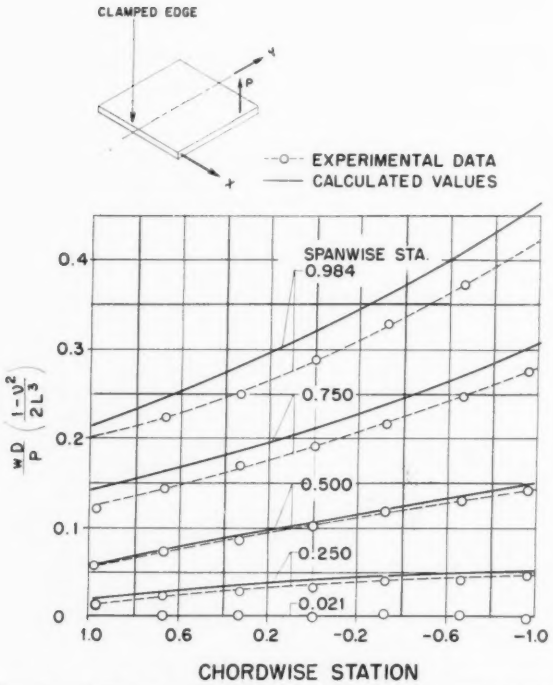

FIG. 2b. Influence surface for a 4.2 per cent thick square plate loaded at 93 per cent span and at chord station −0.96.

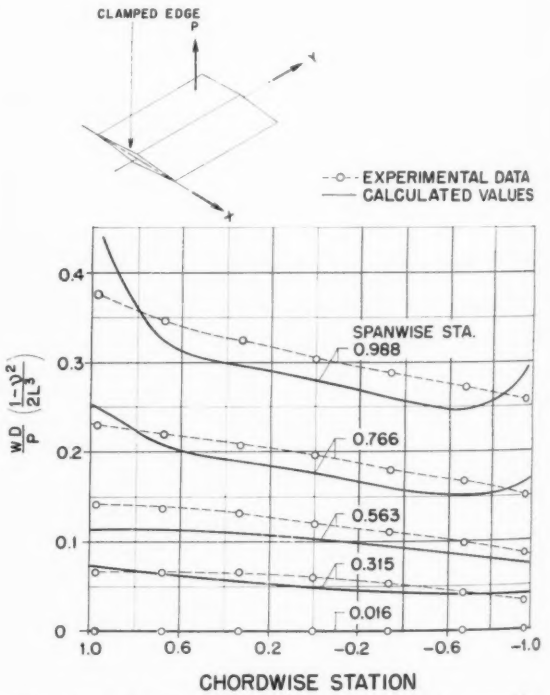

FIG. 3b. Influence surface for a 5 per cent thick rectangular plate ($AR = 1.33$) of double wedge cross section loaded at 90 per cent span and at chord station 0.67.

$$\frac{\partial w}{\partial y} = \alpha \frac{\partial w_2}{\partial y} + \iint_S K \frac{\partial w_2}{\partial y_0} dx_0 dy_0 + \sum_{i=2}^{\infty} \iint_S \times$$
$$K(x, y, x_0, y_0) \iint_S K(x_1, y_1, x_2, y_2) \ldots \times$$
$$\iint_S K(x_{i-1}, y_{i-1}, x_i, y_i) \frac{\partial w}{\partial y_i} dx_i dy_i \ldots dx_0 dy_0 \quad (17)$$

so that after substituting in Eq. (14), the increment in the pressure coefficient due to the flexibility is

$$\frac{\Delta p}{q_{\text{flex.}}} - \frac{\Delta p}{q_{\text{rigid}}} = p(x, y) \frac{\partial w}{\partial y} = \alpha p(x, y) \frac{\partial w_2}{\partial y} +$$
$$\iint_S K \frac{\partial w_2}{\partial y_0} dx_0 dy_0 + \ldots \quad (18)$$

The change in the aerodynamic characteristics can easily be found by integrating the local loading increment. Inspection of Eq. (18) indicates that the effects of the static elastic deformation on the aerodynamic characteristics is linear in the angle of attack and dynamic pressure and involves a function of $1/D$ that here appears as a power series in $(1/D)^n$, since K involves $1/D$.

In linearized supersonic flow, $p(x, y)$ may be approximated by $4/\sqrt{M^2 - 1}$ in the two-dimensional region, and $4(b - x)/(c - y)$ in the tip region. The ratio $C_{L_\alpha}/C_{L_{\alpha\text{rigid}}}$ was computed for an aspect ratio unity flat wing at $M = \sqrt{2}$ to the order of $(1/D)^2$ to be

$$\frac{C_{L_\alpha}}{C_{L_{\alpha\text{rigid}}}} = 1 + \frac{kq}{(t/c)^3 10^3} \text{ where } k = \begin{matrix} 0.319 \text{ for steel wings} \\ 1.055 \text{ for aluminum wings} \end{matrix} \quad (19)$$

The largest source of error in the above calculation of C_{L_α} is due to the fact that the linearized pressure distribution does not place the center of pressure at the proper point. The accuracy of the calculation could undoubtedly have been improved by using Busemann's second order term

$$\Delta p/q = C_1 \alpha + (\partial w/\partial y) + C_2 \alpha + (\partial w^2/\partial y)$$

and retaining only terms of order $(\partial w)/(\partial y)$, so that

$$\Delta p/q = C_1\alpha + C_2\alpha^2 + (C_1 + 2C_2\alpha)(\partial w/\partial y)$$

If this were done then the structure of Eq. (18) would be

$$\frac{\Delta p}{q_{\text{flex.}}} - \frac{\Delta p}{q_{\text{rigid}}} = \alpha(C_1 + C_2\alpha) \frac{\partial w_2}{\partial y} +$$
$$(C_1 + 2C_2\alpha)(C_1 + C_2\alpha) \int_S K \frac{\partial w_2}{\partial y} dS + \ldots$$

which is nonlinear in α.

Concluding Remarks

The examples have all dealt with rectangular plates that are either flat or have a double wedge cross section. The generalization to arbitrary plan forms can be effected, usually, by the introduction of a coordinate system which is geometrically similar to the wing plan form, and by writing the energy equation in this coordinate system. It is not difficult to make the variable change; however, the form of the equation is fairly complicated in the general case. The details for specific plan forms are given by Fung[2] for a sweptback wing and Stein *et al.*[6] for delta wings.

Appendix

The complete set of functions that were used to make the calculations shown in the figures are listed below for the applicable cases.[1] It will be noted that the semispan of the surfaces is b and the semichord is unity. The terms w_{mn} in Eq. (6) are written $w_{mn}(x, y) = f_m(x)g_n(y)$[1, 2] as shown below.

Case 1. Uniform Thickness

$$f_m(x) = \frac{1}{b} \cosh \frac{p_m x}{b} \cosh \frac{p_m x}{b} -$$
$$\sigma_m \left(\sinh \frac{p_m x}{b} - \sin \frac{p_m x}{b} \right)$$

where

$$\sigma_m = \frac{\cosh p_m + \cos p_m}{\sin p_m + \sinh p_m}$$

and the p_m are the roots of

$$\cosh p \cos p + 1 = 0$$

$f_m(x)$ represents the clamped-free vibrating-beam mode shape.

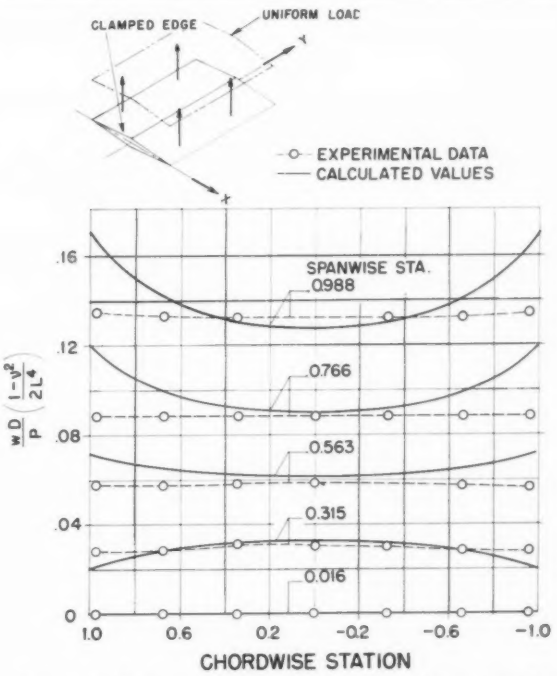

FIG. 4. Deflection surface for a 5 per cent thick rectangular plate ($\mathcal{R} = 1.33$) of double wedge cross section for a uniformly distributed load.

$$g_n(y) = \frac{\cosh q_n \cos q_n y + \cos q_n \cosh q_n y}{\sqrt{\cosh^2 q_n + \cos^2 q_n}}$$

if n is even, and the q_n are the roots of

$$\tan q + \tan hq = 0$$
$$q_0 = 0$$

When n is odd

$$g_n(y) = \frac{\sinh q_n \sin q_n y + \sin q_n \sinh q_n y}{\sqrt{\sinh^2 q_n - \sin^2 q_n}}$$

and q_n is defined as before. Note that

$$g_0(y) = 1/\sqrt{2}$$
$$g_1(y) = (3/\sqrt{2})y$$

Case 2. Rectangular Double Wedge Surface

$f_m(x)$ are the same as in Case 1. Using Nicholson's results[11]

$$g_n(y) = \frac{G_n J_1[2q_n\sqrt{(1 - |y|)}]}{\sqrt{(1 - |y_1|)}}$$

if n is even and G_n is a normalizing factor where $2q_n$ are the roots of $J_2(2q_n) = 0$ and

$$G_n = \frac{\sqrt{2}\cdot 2q_n}{\sqrt{(2q_n)^2 - 1}} \cdot \frac{1}{J_1(2q_n)}$$

For the odd n

$$q_n(y) = G_n \frac{J_1[2q_n\sqrt{(1 - |y_1|)}]}{\sqrt{(1 - |y_1|)}} - \frac{J_1(2q_n)}{I_1(2q_n)} \frac{I_1[2q_n\sqrt{(1 - y_1)}]}{\sqrt{(1 - y_1)}}$$

and

$$g_n(-y) = -g_n(y)$$

The q_n are the roots of $J_2(2q_n)I_2'(2q_n) - J_2'(2q_n)I_2(2q_n) = 0$ and

$$G_n = \left[\frac{I_0 I_2 J_1^2 - J_0 J_2 I_1^2}{I_1^2} + \frac{2}{2q_n}\frac{J_1^2 I_2 - J_1 I_2 J_2}{I_1}\right]^{-1} \times (-1)^{(n-1)/2}$$

and the argument of the Bessel function is $2q_n$, J_n is the Bessel function of the first kind, nth order with real argument, I_n is the Bessel function of the first kind, nth order with imaginary argument.

Note that here $g_0(y) = 1$ and $g_1(y) = 3y$. The $f_m(x)$ and $g_n(y)$ have been made normal and orthogonal—i.e.,

$$\int_0^L f_m(x) f_n(x) dx = \delta_n^m$$

$$\int_{-1}^{1} k(y) g_m(y) g_n(y) dy = \delta_n^m \begin{cases} 1 & m = n \\ 0 & m \neq n \end{cases}$$

where $k(y)$ is the appropriate weighing function. For Case 1, $k(y) = 1$. For Case 2, $k(y) = (1 - |y|)$.

References

[1] Fung, Yuan-Cheng, *Elastostatic and Aeroelastic Problems Relating to Wings of High Speed Airplanes*, California Institute of Technology, Ph.D. Thesis, 1948.

[2] Fung, Yuan-Cheng, *Theoretical and Experimental Effect of Sweep Upon the Stress and Deflection Distribution in Aircraft Wings of High Solidity, Part II, Stress and Deflecting Analysis of Swept Plates*, California Institute of Technology, final report on Contract No. W-33-038-001-16961 (17583), June 30, 1949.

[3] Luce, Richard W., *Variational Methods of Elasticity and Their Application to Cantilever Plates*, Massachusetts Institute of Technology Naval Supersonic Laboratory Memo A and R 100-37, June 20, 1949.

[4] Luce, Richard W., *Deflections of Cantilever Wings with Varying Geometrical Properties*, Massachusetts Institute of Technology Naval Supersonic Laboratory Memo A and R 100-40, August 11, 1949.

[5] Reissner, Eric, and Stein, Manuel, *Torsion and Transverse Bending of Cantilever Plate*, NACA TN 2369, June, 1951.

[6] Stein, M., Anderson, J. E., and Hedgeparth, J. H., *Deflection and Stress Analysis of Thin Solid Wings of Arbitrary Planform with Particular Reference to Delta Wings*, NACA TN 2621, February, 1952.

[7] Timoshenko, S., *Theory of Plates and Shells*, pp. 121–123, McGraw-Hill Company, Inc., New York, 1940.

[8] Whittaker, E. T., and Watson, G. N., *A Course in Modern Analysis*, 4th Edition, reprinted by the Cambridge University Press, Cambridge, England, 1940.

[9] Forsyth, A. R., *Calculus of Variation*, Cambridge University Press, Cambridge, 1927.

[10] Lang, A. L., and Hallowell, F. C., Jr., *On Experimental Studies of Thin Wing Structures of High Solidity for the Supersonic Laboratory of M.I.T.*, Structures Memo No. 7, Aeroelastic and Structures Research Group of Massachusetts Institute of Technology, April 16, 1951.

[11] Nicholson, J. W., *Lateral Vibrations of Bars of Variable Section*, Proc. Roy. Soc., Vol. 93, Series A, pp. 506–519, 1916–1917.

Analysis of Peak-Holding Optimalizing Control

H. S. TSIEN* AND S. SERDENGECTI†
California Institute of Technology

SUMMARY

The peak-holding optimalizing control is analyzed under the assumption of first-order input linear group and output linear group. Design charts are constructed for determining the required input drive speed and the consequent hunting loss with specified time constants of the input and output linear groups, the hunting period, and the critical indicated difference for input drive reversal.

INTRODUCTION

OPTIMALIZING CONTROL WAS INVENTED BY C. S. Draper, Y. T. Li, and H. Laning, Jr.[1, 2] Their basic idea can be summarized as follows: In almost all engineering systems, within the restrictions of operation, there is an optimum state of the system for performance. For instance, in an internal combustion engine, within the restriction of producing the load torque at the specified speed, there are optimum settings for the manifold pressure and the ignition timing for minimum fuel consumption. Another example is an airplane under cruising condition; then under the restriction of engine cruising r.p.m. and assigned altitude, there is an optimum combination of trim setting and engine throttle for maximum fuel economy or maximum miles per gallon of fuel. But more important than the existence of an optimum operating state is the fact that the optimum operating state cannot be exactly predicted in advance because of the natural changes in the environment of the engineering system: In the case of the internal combustion engine, it is the changes in the temperature and the humidity of the air; in the case of the airplane, it is unavoidable changes in the aerodynamic properties of the airplane and the engine performance with age. Therefore if the purpose is to operate always near the optimum state in spite of the "drift" of the system, then the control device for the engineering system must be so designed as to search out automatically the optimum state of operation and to confine the operation close to this state. This is the basic idea of optimalizing control.

The application of Draper's optimalizing control to the general cruise control of airplanes was discussed by Shull.[3] Shull emphasized the possible elimination of extensive flight testing of new airplanes for performance determination, because the optimalizing control will automatically measure the performance whenever the airplane is flown. This in itself would constitute a great saving. But moreover, in critical circumstances such as flight through icing atmosphere, the ability of the optimalizing control to extract the best performance of a radically changed system (through ice deposition on the airplane) could be of utmost importance.

There are two fundamental problems in the theory of optimalizing control. One of the problems is the dynamic effects of the controlled system on the performance of the control. The other problem is the elimination of the noise interference. The two problems are somewhat interrelated, because if large deviations from the optimum state or the optimum operating point and hence large loss can be tolerated, then the noise interference will not be critical. The basic design aim of optimalizing control is to have the smallest loss or to operate as close to the optimum state as possible without the danger of having the control misled by the noise interference. Both of these problems were considered by the original inventors of optimalizing control. The noise problem is essentially the problem of detection of a sinusoidal variation under heavy random interference, a subject of much current research. The purpose of the present paper is to solve completely the first problem of dynamic effects under the assumption that the dynamic properties of the controlled system can be approximated by a first-order linear system. We shall begin with the brief review of the operating principles of an optimalizing control of the peak-holding type—a type least affected by the noise interference.[1, 2]

PRINCIPLE OF OPERATION

The heart of an optimalizing control system is the nonlinear component that characterizes the optimum operating condition of the controlled system. For simplicity of discussion, it is assumed that this basic component has a single input and a single output. For the time being the dynamic effects will be neglected and the output is assumed to be determined by the instantaneous value of the input. Since there is an optimum point, output as a function of input has a maximum at the output y_0 at the input x_0, as shown in Fig. 1. It is convenient to refer the output and the input to the optimum point and put the physical input as $x + x_0$ and the physical output as $y^* + y_0$. The optimum point is then the point $x = y^* = 0$. The purpose of an optimalizing control is then to search out this optimum point and to keep the system in the immediate neighborhood of this point. In this neighbor-

Received April 30, 1954.

* Robert H. Goddard Professor of Jet Propulsion, Daniel and Florence Guggenheim Jet Propulsion Center.

† Daniel and Florence Guggenheim Jet Propulsion Fellow.

hood, the relation between x and y^* can be represented as

$$y^* = -kx^2 \tag{1}$$

where k is a characteristic constant of the controlled system.

The operation of a peak-holding optimalizing control, neglecting the dynamic effects, then would be as follows: Say the input x is below the optimum value and is thus negative. The input drive is then set to increase the input at a constant rate. At the time instant 1 (Fig. 2) the input changes from negative to positive and passes through the optimum point. The output y^* is thus maximum at the time instant 1 and is decreasing after the instant 1. Now if an output sensing instrument is so designed as to follow the output exactly when the output is increasing, but hold to the maximum value after the maximum is passed and the output starts to decrease; then there will be a difference between the reading of this output sensing instrument and the output itself after the time instant 1. This difference is shown in the lower graph of Fig. 2. When this difference is built up to a critical value c at the time instant 2, the input drive is tripped and the direction of the input drive is reversed, but still at the same constant rate as before. After the instant 2 then, the input decreases and the output increases till a maximum in output is again reached at the time instant 3. At time instant 3, the input, of course, again passes from positive to negative, and the indicated difference between the output sensing instrument and the output itself again builds up. At the time instant 4, the difference reaches the critical value c again, and the input drive direction is again reversed. At the time instant 5, the input x becomes zero again and another maximum of the output is reached. The period of input variation is thus the time interval from the instant 1 to the instant 5, and the input, when plotted as a function of time, consists of a series of straight line segments forming a saw-tooth variation. The period of output variation is the time interval from the instant 1 to the instant 3, and the output, when plotted as a function of time, consists of a series of parabolic arcs. The periodic variations of input and output are called the hunting of the system, and the period of output variation is called the hunting period T. The period of input variation is thus $2T$.

The extreme variation of output Δ (Fig. 2) is called the hunting zone. If a is the amplitude of the saw-tooth variation of the input (Fig. 2), then due to Eq. (1),

$$\Delta = ka^2 \tag{2}$$

The difference between the maximum output and the average output of the hunting system is called the hunting loss D (Fig. 2). Because of the fact that the output is a series of parabolic arcs,

$$D = (1/3)\Delta = (1/3)ka^2 \tag{3}$$

For this idealized case, the critical indicated difference c between the output sensing instrument and the output itself is equal to Δ, the hunting zone. It is then clear from this discussion that in order to reduce the hunting loss for better efficiency of the system, one must try to reduce the hunting zone or the amplitude of input variation. Unfortunately the critical indicated difference is also reduced by such modification, and a limit is set by the noise interference on the proper tripping operation of the input drive.

The dynamic effects are so far neglected. But in any physical system, this is not possible because of the ever present inertial and damping forces. The output y^* given by Eq. (1) has to be considered then as the fictitious "potential output" but not the actual output y measured by the output indicating and sensing instrument. y^* is equal to y only when the period T of hunting becomes extremely long. The relation between y^* and y is determined by the dynamical effects. For the conventional engineering systems, these dynamical effects are determined by a linear relation. For instance, in the case of an internal combustion engine, the potential output is essentially the corrected effective pressure generated in the engine cylinders, while the actual output is the brake mean effective pressure of the engine. The dynamical effects are here mainly due to the inertia of the piston, the crankshaft, and other moving parts of the engine. For small changes in the operating conditions of the engine, such dynamical effects can be represented as a linear differential equation with constant coefficients.

Since the reference level of input and output is taken to be the optimum input x_0 and the optimum output y_0, the physical potential output is $y^* + y_0$ and the physical actual output is $y + y_0$. Thus the relation between the physical potential output and the physical actual output can be written as an operator equation

$$y + y_0 = F_0(d/dt)\,(y^* + y_0) \tag{4}$$

where F_0 is generally the quotient of two polynomials in the time differential operator d/dt. In the language of the Laplace transform then $F_0(s)$ is the transfer function. Let the linear system which transforms the potential output to actual output be called the output linear group. Then $F_0(s)$ is, specifically, the transfer function of the output linear group. By implication however, when the dynamical effects are negligible or when $s = 0$, the potential output is equal to the actual output. Therefore

$$F_0(0) = 1 \tag{5}$$

Since the optimum output y_0 only varies extremely slowly by the drift of the controlled system, during a time interval of many hunting periods y_0 can be taken as a constant. Then the condition of Eq. (5) simplifies Eq. (4) to

$$y = F_0(d/dt)y^* \tag{6}$$

In a similar manner, let x^* be the "potential input" that is actually the forcing function generated by the optimalizing control system but not the actual input

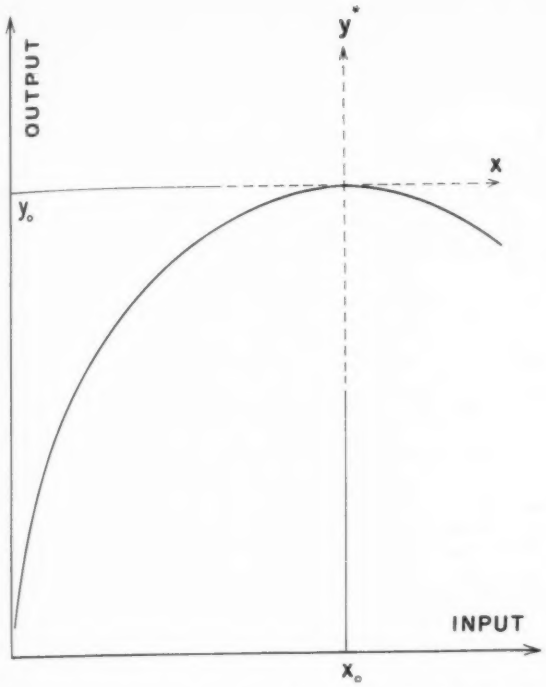

FIG. 1. Input-output characteristic of controlled system.

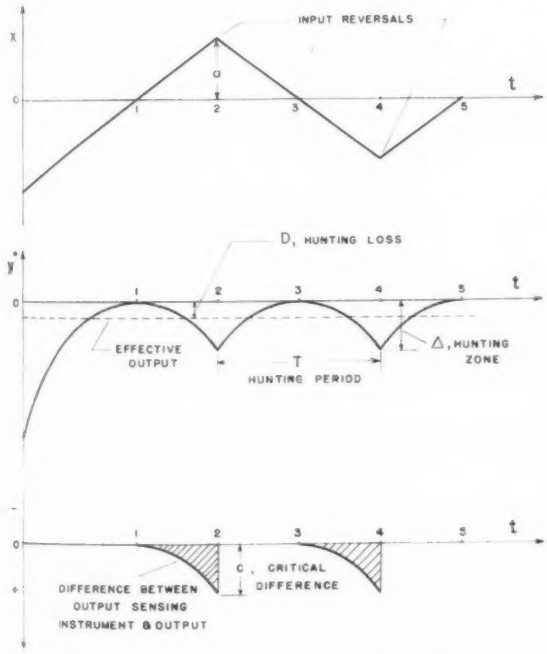

FIG. 2. Typical performance diagram for an ideal peak-holding optimalizing control system.

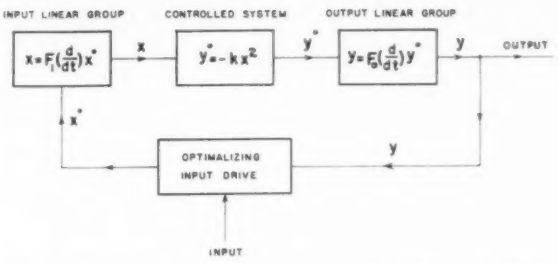

FIG. 3. Block diagram of a complete peak-holding optimalizing control system.

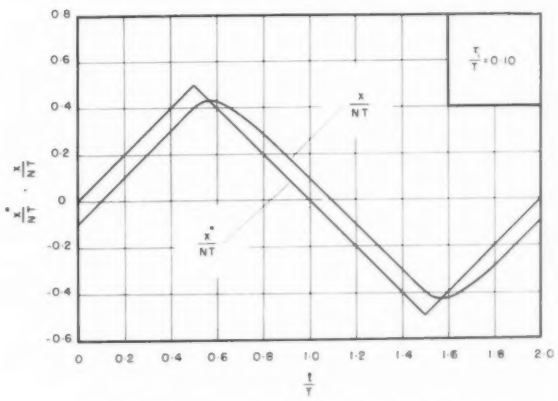

FIG. 4. "Potential" input and actual input for value of $\tau_i/T = 0.1$.

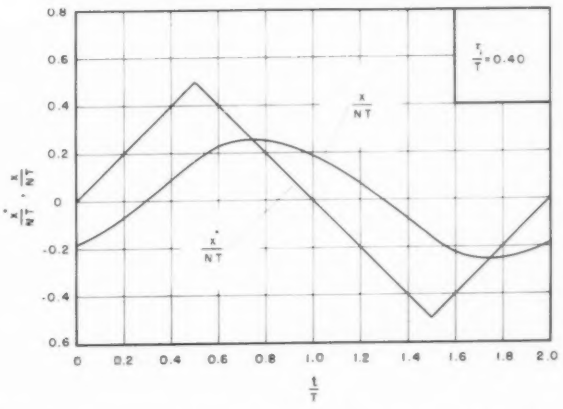

FIG. 5. "Potential" input and actual input for value of $\tau_i/T = 0.4$.

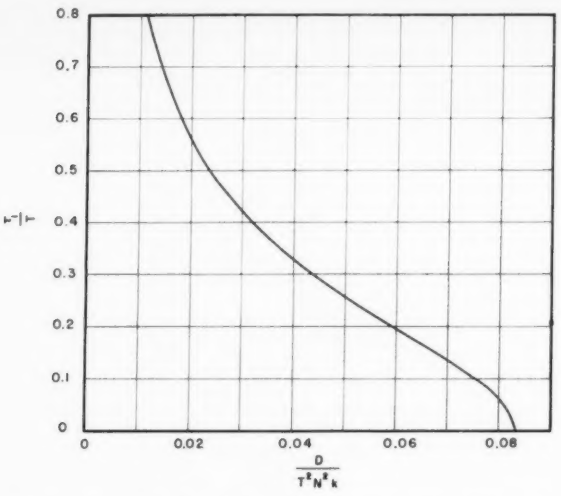

FIG. 6. Variation of dimensionless hunting loss, $D/(T^2N^2k)$ with τ_i/T.

x. It is x^* that has the saw-tooth form shown in Fig. 2, but not x. The relation between x^* and x is determined by the inertial and dynamical effects of the input drive system. This input drive system can be called the "input linear group" of the optimalizing control. The operator equation between the potential input x^* and the actual input x is

$$x = F_i(d/dt)x^* \tag{7}$$

$F_i(s)$ is thus the transfer function of the input linear group. Similar to Eq. (5), the meaning of potential and actual inputs implies

$$F_i(0) = 1 \tag{8}$$

Thus a simple representative block diagram of the complete optimalizing control system can be drawn as shown in Fig. 3. The nonlinear components of the system are thus the optimalizing input drive and the controlled system itself.

Formulation of the Mathematical Problem

The general relation between the input x and the output y is determined by the system of Eqs. (1), (6), and (7), with the potential input x^* specified as a saw-tooth curve with period $2T$ and amplitude a. Let ω_0 be the hunting frequency defined by

$$\omega_0 = 2\pi/T \tag{9}$$

then x^* can be expanded into a Fourier series,

$$x^* = \frac{8a}{\pi^2}\sum_{n=0}^{\infty}\frac{(-1)^n}{(2n+1)^2}\sin(2n+1)\frac{\omega_0 t}{2}$$
$$= \frac{8a}{\pi^2}\sum_{n=0}^{\infty}\frac{(-1)^n}{(2n+1)^2}\frac{1}{2i}\left(e^{[(2n+1)/2]i\omega_0 t} - e^{-[(2n+1)/2]i\omega_0 t}\right) \tag{10}$$

Therefore by using Eq. (7), the actual input x is given by

$$x = \frac{8a}{\pi^2}\sum_{n=0}^{\infty}\frac{(-1)^n}{(2n+1)^2(2i)}\times\left[F_i\left(\frac{2n+1}{2}i\omega_0\right)e^{[(2n+1)/2]i\omega_0 t} - F_i\left(-\frac{2n+1}{2}i\omega_0\right)e^{-[(2n+1)/2]i\omega_0 t}\right] \tag{11}$$

By using Eqs. (11) and (16), the actual output y is given by

$$y = \frac{16a^2k}{\pi^4}\sum_{n=0}^{\infty}\sum_{m=0}^{\infty}\frac{(-1)^{n+m}}{(2n+1)^2(2m+1)^2}\times\Big\{F_0[(n+m+1)i\omega_0]F_i\left(\frac{2n+1}{2}i\omega_0\right)\times F_i\left(\frac{2m+1}{2}i\omega_0\right)e^{(n+m+1)i\omega_0 t} - F_0[(n-m)i\omega_0]\times F_i\left(\frac{2n+1}{2}i\omega_0\right)F_i\left(-\frac{2m+1}{2}i\omega_0\right)e^{(n-m)i\omega_0 t} - F_0[-(n-m)i\omega_0]F_i\left(-\frac{2n+1}{2}i\omega_0\right)\times F_i\left(\frac{2m+1}{2}i\omega_0\right)e^{-(n-m)i\omega_0 t} + F_0[-(n+m+1)i\omega_0]\times F_i\left(-\frac{2n+1}{2}i\omega_0\right)F_i\left(-\frac{2m+1}{2}i\omega_0\right)\times e^{-(n+m+1)i\omega_0 t}\Big\} \tag{12}$$

By comparing Eqs. (11) and (12), it is seen that the input has half the frequency of the output. This is, of course, to be expected from the basic parabolic relation of input and output as specified by Eq. (1).

The average of the actual output y with respect to time t, being here referred to the optimum output y_0, gives directly the hunting loss D. Equation (12) shows that this average value is the sum of terms with $n = m$ from the second and the third terms of that equation. Therefore, using Eq. (5),

$$D = \frac{32a^2k}{\pi^4}\sum_{n=0}^{\infty}\frac{1}{(2n+1)^4}F_i\left(\frac{2n+1}{2}i\omega_0\right)\times F_i\left(-\frac{2n+1}{2}i\omega_0\right) \tag{13}$$

This equation can be easily checked by observing that when the dynamic effects are absent, $F_i \equiv 1$, then the series can be easily summed and $D = (1/3)a^2k$ as required by Eq. (3). Equation (13) also shows that the average output and hence the hunting loss are independent of the output linear group. This agrees with the one's physical understanding: Only detailed time variation of the output is modified by the dynamics of the output linear group. In the case of an internal combustion engine, the average output specifies the power of the engine. The dynamics of the output linear group is determined by the inertia of the moving parts. The power of the engine is certainly independent of the inertia of the moving parts.

Equations (11) to (13) fully determine the performance of the optimalizing control system once the values of a, k, and ω_0 are specified and the transfer

functions $F_i(s)$ and $F_0(s)$ of the input linear group and the output linear group are given. The following sections give the detailed calculations and results for the case of first-order input and output groups.

First-Order Input and Output Groups

The frequency ω_0 of the optimalizing control is usually low, and the important dynamic effects come from the inertia in the input and the output linear groups. Then these linear groups can be closely approximated by first-order systems. In other words, their transfer functions are

$$F_i(i\omega) = 1/(1 + i\omega\tau_i) \tag{14}$$

$$F_0(i\omega) = 1/(1 + i\omega\tau_0) \tag{15}$$

where τ_i and τ_0 are the characteristic time constants of the input linear group and the output linear group, respectively. It is evident that these transfer functions satisfy the conditions of Eqs. (5) and (8).

By substituting Eq. (14) into Eq. (11), the actual output x is given by

$$x = \frac{8a}{\pi^2}\sum_{n=0}^{\infty}\frac{(-1)^n}{2i(2n+1)^2}\left[\frac{e^{[(2n+1)/2]i\omega_0 t}}{1+(2n+1)i(\omega_0\tau_i/2)} - \frac{e^{-[(2n+1)/2]i\omega_0 t}}{1-(2n+1)i(\omega_0\tau_i/2)}\right] \tag{16}$$

When the summation is carried out, Eq. (16) yields the following equations for the input x:

$$x = NT\left[\frac{t}{T} - \frac{\tau_i}{T} + \frac{\tau_i}{T}\frac{e^{-[(t/T)/(\tau_i/T)]}}{\cosh\,(T/2\tau_i)}\right] \quad \text{for } -\frac{1}{2} \leqslant \frac{t}{T} \leqslant \frac{1}{2} \tag{17a}$$

and

$$x = -NT\left[\frac{t}{T} - \left(1 + \frac{\tau_i}{T}\right) + \frac{\tau_i}{T}\frac{e^{(1-t/T)/(\tau_i/T)}}{\cosh\,(T/2\tau_i)}\right] \quad \text{for } \frac{1}{2} \leqslant \frac{t}{T} \leqslant \frac{3}{2} \tag{17b}$$

where N is the constant input drive speed—i.e.,

$$N = 2a/T \tag{18}$$

By using these equations, the variation of actual input x with respect to time can be calculated for any specified data. Examples of such calculations are shown in Figs. 4 and 5 for $\tau_i/T = 0.1$ and $\tau_i/T = 0.4$, respectively. Both show the expected effect of rounding-off of the sharp corners of the saw-tooth curve and a time delay. It is of interest to note that while the delay is almost equal to τ_i itself for small τ_i/T, the delay is less than τ_i for larger τ_i/T.

With the first-order transfer function of Eq. (14), the hunting loss given by Eq. (13) becomes

$$D = \frac{32a^2k}{\pi^4}\sum_{n=0}^{\infty}\frac{1}{(2n+1)^4\{1+[(2n+1)/2]^2\omega_0^2\tau_i^2\}} \tag{19}$$

By carrying out the summation, Eq. (19) gives the hunting loss as

$$D = (N^2T^2k/12)\,[1 - 12(\tau_i/T)^2 + 24(\tau_i/T)^3\tanh\,(T/2\tau_i)] \tag{20}$$

Fig. 6 shows a dimensionless plot of this equation.

To calculate the actual output y, both Eqs. (14) and (15) have to be substituted into Eq. (12)—i.e.,

$$y = \frac{4T^2N^2k}{\pi^4}\sum_{n=0}^{\infty}\sum_{m=0}^{\infty}\frac{(-1)^{n+m}}{(2n+1)^2(2m+1)^2}\times\left\{\frac{e^{i(n+m+1)\omega_0 t}}{[1+(n+m+1)i\omega_0\tau_0]\,[1+(2n+1)i(\omega_0\tau_i/2)]\,[1+(2m+1)i(\omega_0\tau_i/2)]} - \frac{e^{i(n-m)\omega_0 t}}{[1+(n-m)i\omega_0\tau_0]\,[1+(2n+1)i(\omega_0\tau_i/2)]\,[1-(2m+1)i(\omega_0\tau_i/2)]} - \frac{e^{-i(n-m)\omega_0 t}}{[1-(n-m)i\omega_0\tau_0]\,[1-(2n+1)i(\omega_0\tau_i/2)]\,[1+(2m+1)i(\omega_0\tau_i/2)]} + \frac{e^{-i(n+m+1)\omega_0 t}}{[1-(n+m+1)i\omega_0\tau_0]\,[1-(2n+1)i(\omega_0\tau_i/2)]\,[1-(2m+1)i(\omega_0\tau_i/2)]}\right\} \tag{21}$$

By changing the summation indices, Eq. (21) can also be written as

$$y = \frac{4T^2N^2k}{\pi^4}\left(\sum_{s=-\infty}^{\infty}\frac{(-1)^{s-1}e^{is\omega_0 t}}{(1+is\omega_0\tau_0)}\times\sum_{n=0}^{\infty}\frac{1}{(2n+1)^2[(2n+1)-2s]^2\,[1+(2n+1)i(\omega_0\tau_i/2)]\,\{1-[(2n+1)-2s]i(\omega_0\tau_i/2)\}} + \sum_{s=-\infty}^{\infty}\frac{(-1)^{s-1}e^{-is\omega_0 t}}{(1-is\omega_0\tau_0)}\sum_{n=0}^{\infty}\frac{1}{(2n+1)^2[(2n+1)-2s]^2\,[1-(2n+1)i(\omega_0\tau_i/2)]\,\{1+[(2n+1)-2s]i(\omega_0\tau_i/2)\}}\right)$$

or

$$y = \frac{8T^2N^2k}{\pi^4}\left\{-\sum_{n=0}^{\infty}\frac{1}{(2n+1)^4[1+(2n+1)^2(\omega_0\tau_i/2)^2]}+\sum_{s=1}^{\infty}\frac{(-1)^{s-1}e^{is\omega_0 t}}{(1+is\omega_0\tau_0)}\times\right.$$
$$\sum_{n=0}^{\infty}\frac{[(2n+1)^2+4s^2]\,[(1+i\omega_0\tau_i s)+(\omega_0\tau_i/2)^2(2n+1)^2]+8(\omega_0\tau_i/2)^2s^2(2n+1)^2}{(2n+1)^2[(2n+1)^2-4s^2]^2\,[1+(\omega_0\tau_i/2)^2(2n+1)^2]\,[(1+i\omega_0\tau_i s)^2+(\omega_0\tau_i/2)^2(2n+1)^2]}+$$
$$\sum_{s=1}^{\infty}\frac{(-1)^{s-1}e^{-is\omega_0 t}}{(1-is\omega_0\tau_0)}\sum_{n=0}^{\infty}\times$$
$$\left.\frac{[(2n+1)^2+4s^2]\,[(1-i\omega_0\tau_i s)+(\omega_0\tau_i/2)^2(2n+1)^2]+8(\omega_0\tau_i/2)^2s^2(2n+1)^2}{(2n+1)^2[(2n+1)^2-4s^2]^2\,[1+(\omega_0\tau_i/2)^2(2n+1)^2]\,[(1-i\omega_0\tau_i s)^2+(\omega_0\tau_i/2)^2(2n+1)^2]}\right\} \quad (22)$$

The last two summations in Eq. (22) are complex conjugate of each other, thus

$$y = \frac{8T^2N^2k}{\pi^4}\left\{-\sum_{n=0}^{\infty}\frac{1}{(2n+1)^4\,[1+(2n+1)^2(\omega_0\tau_i/2)^2]}+2\mathrm{R1}\sum_{s=1}^{\infty}\frac{(-1)^{s-1}e^{is\omega_0 t}}{(1+is\omega_0\tau_0)}\sum_{n=0}^{\infty}\times\right.$$
$$\left.\frac{[(2n+1)^2+4s^2]\,[(1+i\omega_0\tau_i s)+(\omega_0\tau_i/2)^2(2n+1)^2]+8(\omega_0\tau_i/2)^2s^2(2n+1)^2}{(2n+1)^2[(2n+1)^2-4s^2]^2[1+(\omega_0\tau_i/2)^2(2n+1)^2]\,[(1+i\omega_0\tau_i s)^2+(\omega_0\tau_i/2)^2(2n+1)^2]}\right\} \quad (23)$$

where R1 means the real part of the expression following it. In order to carry out the summation with respect to the index n, Eq. (23) is resolved into the following partial fraction form:

$$y = \frac{8T^2N^2k}{\pi^4}\left(-\sum_{n=0}^{\infty}\frac{1}{(2n+1)^4[1+(2n+1)^2(\omega_0\tau_i/2)^2]}+2\mathrm{R1}\sum_{s=1}^{\infty}\frac{(-1)^{s-1}e^{is\omega_0 t}}{(1+is\omega_0\tau_0)}\times\right.$$
$$\left\{\frac{1}{4s^2(1+is\omega_0\tau_i)}\sum_{n=0}^{\infty}\frac{1}{(2n+1)^2}+\frac{(\omega_0\tau_i/2)^4}{2(1+is\omega_0\tau_i)^2\,[1+is(\omega_0\tau_i/2)]}\sum_{n=0}^{\infty}\frac{1}{[1+(\omega_0\tau_i/2)^2(2n+1)^2]}+\right.$$
$$\frac{(\omega_0\tau_i/2)^4}{2(1+is\omega_0\tau_i)\,[1+is(\omega_0\tau_i/2)]}\sum_{n=0}^{\infty}\frac{1}{[(1+i\omega_0\tau_i s)^2+(\omega_0\tau_i/2)^2(2n+1)^2]}-$$
$$\left.\left.\frac{[1+is\omega_0\tau_i+4(\omega_0\tau_i/2)^2s^2]}{4s^2(1+is\omega_0\tau_i)^2}\sum_{n=0}^{\infty}\frac{1}{[(2n+1)^2+(i2s)^2]}+\frac{2}{(1+is\omega_0\tau_i)}\sum_{n=0}^{\infty}\frac{1}{[(2n+1)^2+(i2s)^2]^2}\right\}\right) \quad (24)$$

By using the summation formulas given in the Appendix, the sums with respect to n can be evaluated and the result is, noting that $\tan \pi s = 0$ for integer values of s,

$$y = \frac{8T^2N^2k}{\pi^4}\left(-\left[\frac{\pi^4}{96}-\frac{\pi^2}{8}\left(\frac{\omega_0\tau_i}{2}\right)^2+\frac{\pi}{4}\left(\frac{\omega_0\tau_i}{2}\right)^3\tanh\frac{\pi}{\omega_0\tau_i}\right]+\right.$$
$$\left.2\mathrm{R1}\sum_{s=1}^{\infty}\frac{(-1)^{s-1}e^{is\omega_0 t}}{(1+is\omega_0\tau_0)}\left\{\frac{\pi^2}{4}\frac{1}{(4s^2)\,(1+is\omega_0\tau_i)}+\frac{\pi}{4}\frac{(\omega_0\tau_i/2)^3\tanh[\pi/(\omega_0\tau_i)]}{(1+is\omega_0\tau_i)^2\,[1+is\,(\omega_0\tau_i/2)]}\right\}\right) \quad (25)$$

Eq. (25) is again resolved into partial fractions in order to carry out the summation with respect to s, viz.,

$$y = \frac{8T^2N^2k}{\pi^4}\left[-\left[\frac{\pi^4}{96}-\frac{\pi^2}{8}\left(\frac{\omega_0\tau_i}{2}\right)^2+\frac{\pi}{4}\left(\frac{\omega_0\tau_i}{2}\right)^3\tanh\frac{\pi}{\omega_0\tau_i}\right]+\right.$$
$$\frac{\pi}{2}\left(\frac{(\omega_0\tau_0/2)^3}{[(\omega_0\tau_0/2)-(\omega_0\tau_i/2)]}\left\{\frac{2(\omega_0\tau_i/2)^3\tanh[\pi/(\omega_0\tau_i)]}{[(\omega_0\tau_0/2)-(\omega_0\tau_i/2)][\omega_0\tau_0-(\omega_0\tau_i/2)]}-\pi\right\}\mathrm{R1}\sum_{s=1}^{\infty}\frac{(-1)^{s-1}e^{is\omega_0 t}}{(1+is\omega_0\tau_0)}+\right.$$
$$\frac{(\omega_0\tau_i/2)^3}{[(\omega_0\tau_0/2)-(\omega_0\tau_i/2)]}\left\{\pi-\frac{2(\omega_0\tau_i/2)^2\tanh[\pi/(\omega_0\tau_i)]}{[(\omega_0\tau_0/2)-(\omega_0\tau_i/2)]}\right\}\mathrm{R1}\sum_{s=1}^{\infty}\frac{(-1)^{s-1}e^{is\omega_0 t}}{(1+is\omega_0\tau_i)}-\frac{\pi}{2}\left(\frac{\omega_0\tau_0}{2}+\frac{\omega_0\tau_i}{2}\right)\times$$
$$\mathrm{R1}\sum_{s=1}^{\infty}\frac{(-1)^{s-1}ie^{is\omega_0 t}}{s}+\frac{\pi}{4}\mathrm{R1}\sum_{s=1}^{\infty}\frac{(-1)^{s-1}e^{is\omega_0 t}}{s^2}-\frac{(\omega_0\tau_i/2)^4\tanh[\pi/(\omega_0\tau_i)]}{[2(\omega_0\tau_0/2)-(\omega_0\tau_i/2)]}\mathrm{R1}\sum_{s=1}^{\infty}\frac{(-1)^{s-1}e^{is\omega_0 t}}{[1+is(\omega_0\tau_i/2)]}-$$
$$\left.\left.\frac{2(\omega_0\tau_i/2)^4\tanh[\pi/(\omega_0\tau_i)]}{[(\omega_0\tau_0/2)-(\omega_0\tau_i/2)]}\mathrm{R1}\sum_{s=1}^{\infty}\frac{(-1)^{s-1}e^{is\omega_0 t}}{(1+is\omega_0\tau_i)^2}\right)\right] \quad (26)$$

The result of carrying out the summations in Eq. (26) and simplifying the expressions is,

$$y = 2T^2N^2k\left[-\left\{\frac{1}{2}\left(\frac{t}{T}\right)^2-\left(\frac{\tau_i}{T}+\frac{\tau_0}{T}\right)\left(\frac{t}{T}\right)+\left[\frac{1}{2}\left(\frac{\tau_i}{T}\right)^2+\frac{\tau_i\tau_0}{T^2}+\left(\frac{\tau_0}{T}\right)^2\right]\right\}+\right.$$
$$\frac{1}{2}\left(-\frac{(\tau_0/T)^2}{(\tau_0/T-\tau_i/T)}\left\{\frac{2(\tau_i/T)^3\tanh(T/2\tau_i)}{[(\tau_0/T)-(\tau_i/T)]\,[2(\tau_0/T)-(\tau_i/T)]}-1\right\}\frac{e^{-(t/T)/(\tau_0/T)}}{\sinh(T/2\tau_0)}+\right.$$
$$\left.\left\{\frac{t}{T}+\frac{(\tau_i/T)^2}{[(\tau_0/T)-(\tau_i/T)]}\right\}\frac{2(\tau_i/T)^2\,e^{-(t/T)/(\tau_i/T)}}{[(\tau_0/T)-(\tau_i/T)]\cosh(T/2\tau_i)}+\frac{(\tau_i/T)^3}{[2(\tau_0/T)-(\tau_i/T)]}\frac{e^{-(2t/T)/(\tau_i/T)}}{\cosh^2(T/2\tau_i)}\right)\Bigg] \quad (27a)$$

for $-(1/2) \leqslant t/T \leqslant 1/2$ and

$$y = 2T^2N^2k\left[-\left\{\frac{1}{2}\left(\frac{t}{T}\right)^2 - \left(\frac{\tau_0}{T}+\frac{\tau_i}{T}+1\right)\left(\frac{t}{T}\right) + \left[\frac{1}{2}\left(\frac{\tau_i}{T}\right)^2 + \frac{\tau_i\tau_0}{T^2} + \left(\frac{\tau_0}{T}\right)^2 + \frac{\tau_0}{T} + \frac{\tau_i}{T} + \frac{1}{2}\right]\right\} + \frac{1}{2}\left(-\frac{(\tau_0/T)^2}{[(\tau_0/T)-(\tau_i/T)]}\left\{\frac{2(\tau_i/T)^3\tanh(T/2\tau_i)}{[(\tau_0/T)-(\tau_i/T)]\,[2(\tau_0/T)-(\tau_i/T)]} - 1\right\}\frac{e^{(1-t/T)/(\tau_0/T)}}{\sinh(T/2\tau_0)} + \left[\frac{t}{T} + \frac{(\tau_i/T)^2}{(\tau_0/T)-(\tau_i/T)} - 1\right]\frac{2(\tau_i/T)^2 e^{(1-t/T)/(\tau_i/T)}}{[(\tau_0/T)-(\tau_i/T)]\cosh(T/2\tau_i)} + \frac{(\tau_i/T)^3 e^{2(1-t/T)/(\tau_i/T)}}{[2(\tau_0/T)-(\tau_i/T)]\cosh^2(T/2\tau_i)}\right)\right] \quad (27b)$$

for $1/2 \leqslant t/T \leqslant 3/2$.

In Eqs. (27a) and (27b), there are apparent singularities whenever $\tau_0/T = \tau_i/T$ and $2\tau_0/T = \tau_i/T$; that is, the value of output y seemingly cannot be determined for these values of time constants. However this is deceptive. By using a simple limit procedure or by direct evaluation of Eq. (25) for these two cases, it can be shown that this is not the case. For example, for $\tau_i/T = \tau_0/T$

$$y = 2T^2N^2k\left\{-\frac{1}{2}\left(\frac{t}{T}\right)^2 + 2\left(\frac{\tau_i}{T}\right)\left(\frac{t}{T}\right) - \frac{5}{2}\left(\frac{\tau_i}{T}\right)^2 + \left[-\left(\frac{\tau_i}{T}\right)^2 - \frac{1}{2}\left(\frac{t}{T}\right)^2 + \left(\frac{\tau_i}{T}\right)\left(\frac{t}{T}\right) + \frac{1}{8}\right]e^{-[(t/T)/(\tau_i/T)]}\operatorname{sech}\frac{T}{2\tau_i} + \frac{3}{2}\left(\frac{\tau_i}{T}\right)e^{-(t/T)/(\tau_i/T)}\operatorname{csch}\frac{T}{2\tau_i} + \frac{1}{2}\left(\frac{\tau_i}{T}\right)^2 e^{-(2t/T)/(\tau_i/T)}\operatorname{sech}^2\frac{T}{2\tau_i}\right\} \quad (28)$$

for $-(1/2) \leqslant t/T \leqslant 1/2$, and, for $2\tau_0/T = \tau_i/T$,

$$y = -2T^2N^2k\left\{\frac{1}{2}\left(\frac{t}{T}\right)^2 - \frac{3}{2}\left(\frac{\tau_i}{T}\right)\left(\frac{t}{T}\right) + \frac{5}{4}\left(\frac{\tau_i}{T}\right)^2 + \left[\left(\frac{\tau_i}{T}\right)\left(\frac{t}{T}\right) + 2\left(\frac{\tau_i}{T}\right)^2 + \frac{1}{2}\left(\frac{\tau_i}{T}\right)\operatorname{ctnh}\frac{T}{\tau_i} + \frac{1}{8}\left(\frac{\tau_i}{T}\right)\operatorname{ctnh}\frac{T}{2\tau_i}\right]\frac{e^{-[(2t/T)/(\tau_i/T)]}}{\cosh^2 T/2\tau_i} + \left(\frac{\tau_i}{T}\right)\left(2\frac{t}{T} - 4\frac{\tau_i}{T}\right)\frac{e^{-[(t/T)/(\tau_i/T)]}}{\cosh T/2\tau_i}\right\} \quad (29)$$

for $-(1/2) \leqslant t/T \leqslant 1/2$.

An analysis for the continuity of Eqs. (27a) and (27b) at $t/T = 1/2$ shows that the values of y and its derivative with respect to t are the same at $t/T = 1/2$ whether they are computed from Eq. (27a) or from Eq. (27b).

Now the computation of the potential output y^* can be accomplished by letting $\tau_0/T = 0$ in Eqs. (27a) and (27b). Thus,

$$y^* = 2T^2N^2k\left[-\frac{1}{2}\left(\frac{t}{T}\right)^2 + \left(\frac{\tau_i}{T}\right)\left(\frac{t}{T}\right) - \frac{1}{2}\left(\frac{\tau_i}{T}\right)^2 - \left(\frac{t}{T} - \frac{\tau_i}{T}\right)\left(\frac{\tau_i}{T}\right)\frac{e^{-[(t/T)/(\tau_i/T)]}}{\cosh(T/2\tau_i)} - \frac{1}{2}\left(\frac{\tau_i}{T}\right)^2\frac{e^{-[(2t/T)/(\tau_i/T)]}}{\cosh^2(T/2\tau_i)}\right] \quad (30a)$$

for $-(1/2) \leqslant t/T \leqslant 1/2$ and

$$y^* = 2T^2N^2k\left\{-\frac{1}{2}\left(\frac{t}{T}\right)^2 + \left(1+\frac{\tau_i}{T}\right)\left(\frac{t}{T}\right) - \frac{1}{2}\left(1+\frac{\tau_i}{T}\right)^2 - \left(\frac{\tau_i}{T}\right)\left[\frac{t}{T} - \left(\frac{\tau_i}{T}+1\right)\right]\frac{e^{(1-t/T)/(\tau_i/T)}}{\cosh(T/2\tau_i)} - \frac{1}{2}\left(\frac{\tau_i}{T}\right)^2\frac{e^{[2(1-t/T)]/(\tau_i/T)}}{\cosh^2(T/2\tau_i)}\right\} \quad (30b)$$

for $1/2 \leqslant t/T \leqslant 3/2$.

These expressions check with the result of direct calculation of y^* by Eqs. (1) and (17).

Figures 7 and 8 show the dimensionless plots of actual output y and potential output y^* for the particular values of τ_0/T and τ_i/T. In these figures it is clearly seen that the dynamic effects not only decrease the output of the system but also introduce a time lag and lower the maximum output of the system. Figure 8 with $\tau_i/T = 0.4$, $\tau_0/T = 0.6$, has the maximum value of y almost at the very instants of input drive reversal points, $t/T = n + (1/2)$. This is indeed an extreme case.

Design Charts

From the principle of operation of the peak-holding optimalizing control, it is seen that the most important quantity to be specified for its design is the critical indicated difference c between the reading of the special output sensing instrument and the output itself. By definition, c is the difference of the maximum of the actual output y and the value of y at the tripping instant of the input drive. The instant of reversing the input drive is typified by $t/T = 1/2$. If the corresponding instant of maximum y is t^*, then the critical indicated difference c is calculated as

$$c = y(t^*/T) - y(1/2) \quad (31)$$

by using any one of Eqs. (27), (28), or (29). Since the instant of input drive reversal must come after the instant of maximum output, $t^*/T < 1/2$.

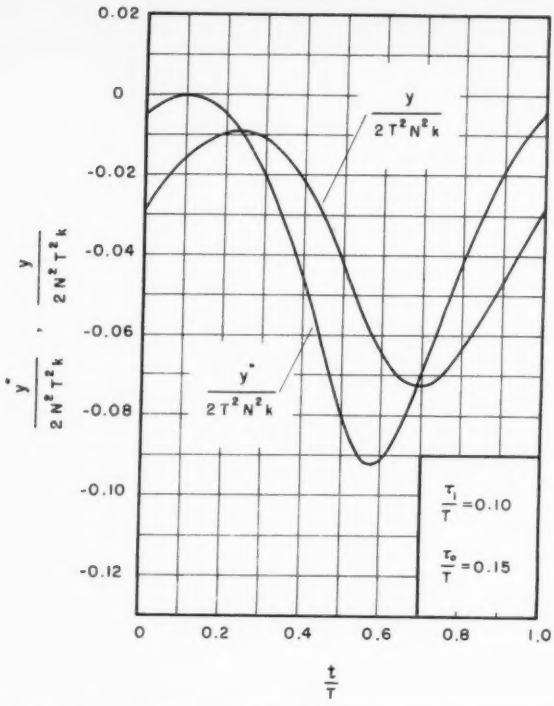

FIG. 7. "Potential" output and indicated output for values of $\tau_i/T = 0.1$ and $\tau_o/T = 0.15$.

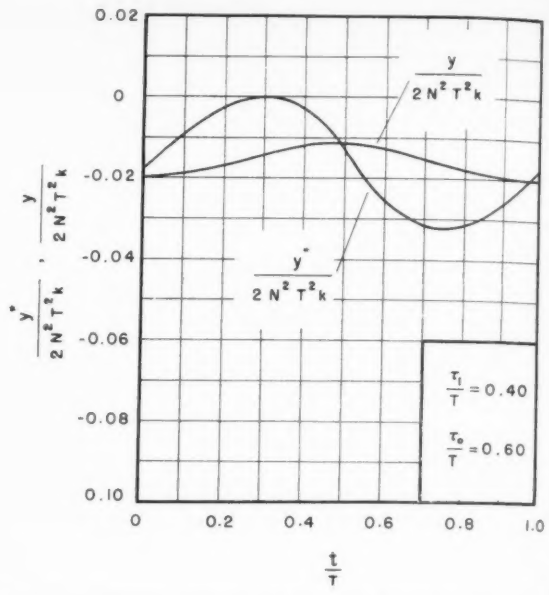

FIG. 8. "Potential" output and indicated output for values of $\tau_i/T = 0.4$ and $\tau_o/T = 0.6$.

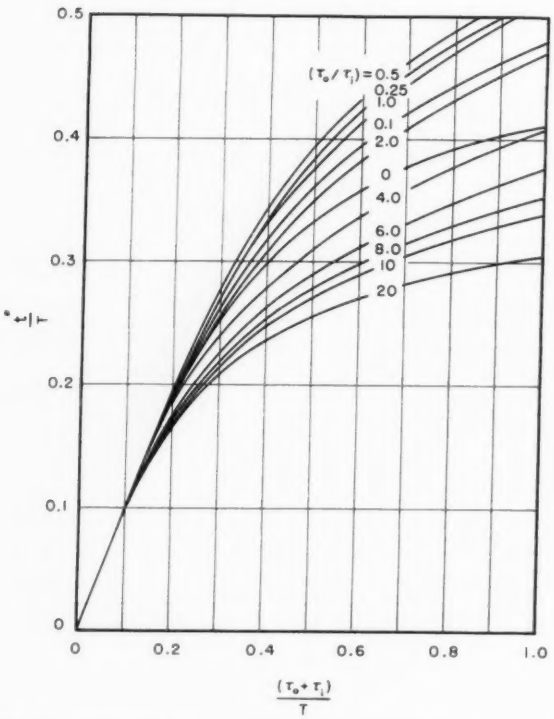

FIG. 9. Maximum output occurrence instant, t^*/T in interval $(0 \leq t/T \leq 1/2)$ versus $(\tau_0 + \tau_i)/T$ with τ_0/τ_i as parameter.

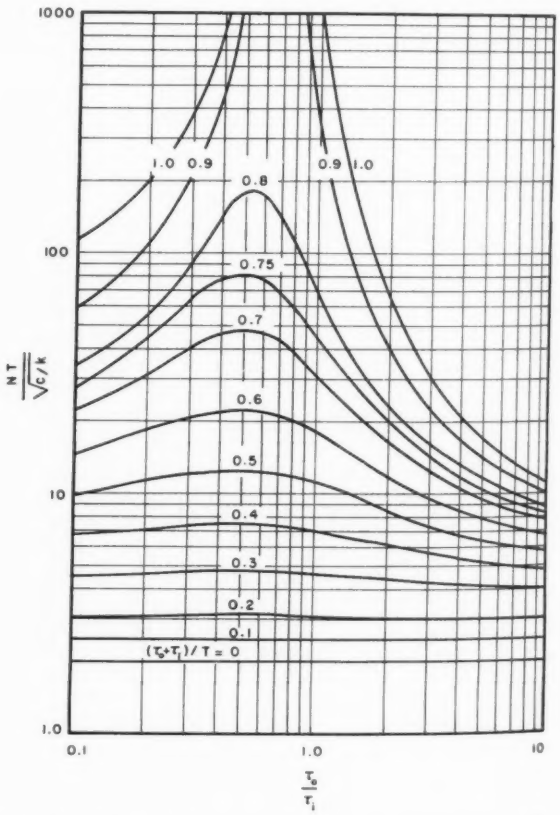

FIG. 10. Critical indicated difference parameter, $TN/\sqrt{c/k}$ versus τ_0/τ_i with $(\tau_0 + \tau_i)/T$ as parameter.

To determine t^*, one may use the condition of zero slope—i.e., $dy/dt = 0$. Then Eq. (27a) gives

$$-\left[\frac{t^*}{T}-\left(\frac{\tau_0}{T}+\frac{\tau_i}{T}\right)\right]+\frac{(\tau_0/T)}{2[(\tau_0/T)-(\tau_i/T)]}\left\{\frac{2(\tau_i/T)^3\tanh(T/2\tau_i)}{[(\tau_0/T)-(\tau_i/T)]\,[2(\tau_0/T)-(\tau_i/T)]}-1\right\}\frac{e^{-[(t^*/T)/(\tau_0/T)]}}{\sinh(T/2\tau_0)}+$$
$$\left\{1-\left(\frac{t^*}{T}\right)\left(\frac{T}{\tau_i}\right)-\frac{(\tau_i/T)}{[(\tau_0/T)-(\tau_i/T)]}\right\}\frac{(\tau_i/T)^2\,e^{-[(t^*/T)/(\tau_i/T)]}}{[(\tau_0/T)-(\tau_i/T)]\cosh(T/2\tau_i)}-$$
$$\frac{(\tau_i/T)^2\,e^{-[(2t^*/T)/(\tau_i/T)]}}{[2(\tau_0/T)-(\tau_i/T)]\cosh^2(T/2\tau_i)}=0 \qquad (32)$$

This transcendental equation for t^*/T may be solved by iteration. For instance, for small τ_0/T and τ_i/T, only terms within the first brackets are of importance, then $t^*/T \simeq (\tau_0+\tau_i)/T$. This is already recognized by Draper and co-workers.[1,2] The complete results of calculation are shown in Fig. 9, which shows that t^*/T is almost only a function of $(\tau_0+\tau_i)/T$ with minor modifications from the parameter τ_0/τ_i, the ratio of characteristic times of the output linear group and the input linear group. Values of t^*/T beyond $1/2$ are not shown, as clearly then the maxima of the output will occur after the corresponding input drive reversal points and proper operation of the control will be difficult if not impossible.

With t^*/T determined, Eq. (31) gives c by substituting Eq. (27a). However the specified quantities of an optimalizing control are k, the characteristics of the controlled system, and τ_i, τ_0, the characteristics of the linear group. From considerations on the noise interference, the designer can make an appropriate choice of the period T and the critical indicated difference c for input drive reversal. Therefore the quantities that the designer wishes to know, after he has the values of k, τ_i, τ_0, T, and c, are N, the input drive speed, and D, the hunting loss. Thus the result of calculation with Eq. (31) should be written as follows:

$$\frac{TN}{\sqrt{c/k}}=\left(\left[\frac{1}{4}-\left(\frac{t^*}{T}\right)^2\right]+2\left(\frac{\tau_i}{T}\right)\left(\frac{\tau_0}{\tau_i}+1\right)\left(\frac{t^*}{T}-\frac{1}{2}\right)-\frac{(\tau_0/\tau_i)^2\,(\tau_i/T)}{[(\tau_0/\tau_i)-1]\sinh(\tau_i/\tau_0)(T/2\tau_i)}\times\right.$$
$$\left\{\frac{2(\tau_i/T)\tanh(T/2\tau_i)}{[(\tau_0/\tau_i)-1]\,[2(\tau_0/\tau_i)-1]}-1\right\}\left(e^{-[(t^*/T)/(\tau_0/\tau_i)\;(\tau_i/T)]}-e^{-[1/[2(\tau_0/\tau_i)\;(\tau_i/T)]]}\right)+$$
$$\frac{2(\tau_i/T)}{[(\tau_0/\tau_i)-1]\cosh(T/2\tau_i)}\left\{\left[\frac{t^*}{T}+\frac{(\tau_i/T)}{(\tau_0/\tau_i)-1}\right]e^{-[(t^*/T)/(\tau_i/T)]}-\left[\frac{1}{2}+\frac{(\tau_i/T)}{(\tau_0/\tau_i)-1}\right]e^{-(T/2\tau_i)}\right\}+$$
$$\left.\frac{(\tau_i/T)^2(e^{-[(2t^*/T)/(\tau_i/T)]}-e^{-(T/\tau_i)})}{[2(\tau_0/\tau_i)-1]\cosh^2(T/2\tau_i)}\right)^{-(1/2)} \qquad (33)$$

When N is determined, Eq. (20) then gives the hunting loss D.

Figures 10 and 11 are the design charts for peak-holding optimalizing control computed from the equations of the preceding analysis. Figure 10 gives $TN/\sqrt{c/k}$ as a function of τ_0/τ_i with $(\tau_0+\tau_i)/T$ as parameter. Figure 11 gives relative hunting loss D/c again as a function of τ_0/τ_i with $(\tau_0+\tau_i)/T$ as parameter. The peaks of curves near $\tau_0/\tau_i = 1$ indicate a sort of resonant effect between the input linear group and output linear group. The hunting loss for fixed $(\tau_i+\tau_0)/T$ and c is smaller for τ_0/τ_i away from unity. For fixed τ_i, τ_0, and c, clearly the way to reduce the hunting loss is by increasing the period T.

Concluding Remarks

The present analysis gives the necessary input drive speed N and the hunting loss D for any specified hunting period T, time constants τ_i and τ_0 for the input linear group and the output linear group, and the chosen critical indicated difference c. T and c are fixed by considerations on the noise interference. The analysis shows that whenever the hunting period is relatively short with respect to the time constants τ_i, τ_0, or whenever $(\tau_i+\tau_0)/T$ is relatively large, the hunting loss will be large, especially when τ_i and τ_0 are nearly equal. To avoid such unfavorable condition, the designer should improve his input drive system so as to reduce the constant τ_i. τ_0 is, however, a constant of the intrinsic characteristic of the controlled system, due to, say, the inertia of the moving parts of the system. τ_0 is thus not at the disposal of the designer of the control system. However, suppose there is a compensating circuit between the output y and optimalizing input drive unit (Fig. 3), such that the effects of the output linear group is completely compensated. Then the effective signal for input drive reversal is not the actual output y, but the potential output y^*. In other words, the value of τ_0 is made to be effectively zero. Even if complete compensation is not achieved, the effective value of τ_0 can still be greatly reduced. For difficult cases then, such a compensating unit should certainly be added to reduce the hunting loss. This will be just a minor complication when compared with the additional equipment required for satisfactory noise filtering.

Appendix

Typical Summation Formulas

Rl and Im mean, respectively, the "real part of" and the "imaginary part of" the expression following it.

$$(1)\quad \sum_{n=0}^{\infty} \frac{1}{(2n+1)^2} = \frac{\pi^2}{8}$$

$$(2)\quad \sum_{n=0}^{\infty} \frac{1}{(2n+1)^4} = \frac{\pi^4}{96}$$

$$(3)\quad \sum_{n=0}^{\infty} \frac{1}{[1+(2n+1)^2 z^2]} = \frac{\pi}{4z} \tanh \frac{\pi^2}{2z}$$

$$(4)\quad \mathrm{Rl} \sum_{s=1}^{\infty} \frac{(-1)^{s-1} e^{is\omega_0 t}}{1+i2sb} = \frac{1}{2} - \frac{\pi}{4b} \frac{e^{-[(\omega_0 t)/(2b)]}}{\sinh \pi/2b}$$

when $-\pi < \omega_0 t < \pi$

$$= \frac{1}{2} - \frac{\pi}{4b} \frac{e^{\pi/b}}{\sinh \pi/2b} \times e^{-[(\omega_0 t)/(2b)]}$$

when $\pi < \omega_0 t < 3\pi$, etc.

$$(5)\quad \mathrm{Im} \sum_{s=1}^{\infty} \frac{(-1)^{s-1} e^{is\omega_0 t}}{s} = \frac{\omega_0 t}{2}$$

when $-\pi < \omega_0 t < \pi$

$$= \frac{\omega_0 t}{2} - \pi$$

when $\pi < \omega_0 t < 3\pi$, etc.

$$(6)\quad \mathrm{Rl} \sum_{s=1}^{\infty} \frac{(-1)^{s-1} e^{is\omega_0 t}}{s^2} = \frac{\pi^2}{12} - \left(\frac{\omega_0 t}{2}\right)^2$$

when $-\pi < \omega_0 t < \pi$

$$= 2\pi \left(\frac{\omega_0 t}{2}\right) - \left(\frac{\omega_0 t}{2}\right)^2 - \frac{11}{12}\pi^2$$

when $\pi < \omega_0 t < 3\pi$, etc.

$$(7)\quad \mathrm{Rl} \sum_{s=1}^{\infty} \frac{(-1)^{s-1} e^{is\omega_0 t}}{(1+i2sa)^2} = \frac{1}{2} - \frac{\pi}{4a^2} \frac{e^{-[(\omega_0 t)/(2a)]}}{\sinh^2 (\pi/2a)} \times \left(\frac{\omega_0 t}{2} \sinh \frac{\pi}{2a} + \frac{\pi}{2} \cosh \frac{\pi}{2a}\right)$$

when $-\pi < \omega_0 t < \pi$

$$= \frac{1}{2} - \frac{\pi}{4a^2} \frac{e^{\pi/a} e^{-[(\omega_0 t)/(2a)]}}{\sinh^2 (\pi/2a)} \times \left[\left(\frac{\omega_0 t}{2} - \pi\right) \sinh \frac{\pi}{2a} + \frac{\pi}{2} \cosh \frac{\pi}{2a}\right]$$

when $\pi < \omega_0 t < 3\pi$, etc.

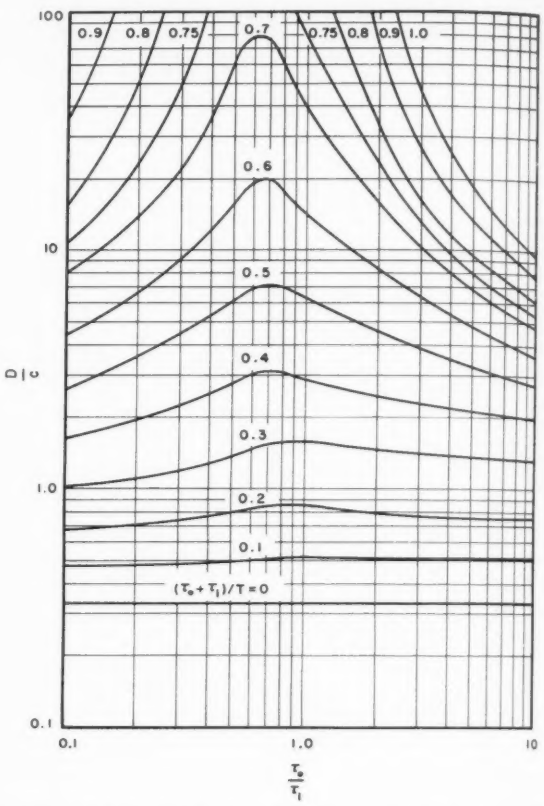

FIG. 11. Relative hunting loss, D/c versus τ_0/τ_i with $(\tau_0 + \tau_i)/T$ as parameter.

REFERENCES

[1] Draper, C. S., and Li, Y. T., *Principles of Optimalizing Control Systems and an Application to the Internal Combustion Engine*, American Society of Mechanical Engineers Publication, September, 1951.

[2] Li, Y. T., *Optimalizing System for Process Control. Instruments*, Vol. 25, pp. 72–77, January, 1952; pp. 190–193, 228, February, 1952; pp. 324–327, 350–352, March, 1952.

[3] Shull, R., Jr., *An Automatic Cruise Control Computer for Long Range Aircraft*, Trans. I.R.E., Professional Group on Electronic Computers, pp. 47–51, December, 1952.

Readers' Forum

BRIEF REPORTS of investigations in the aeronautical sciences and discussions of papers published in the JOURNAL are presented in this special department. Publication is completed as soon as possible after receipt of the material. The Editorial Committee does not hold itself responsible for the opinions expressed by the correspondents.

Solution of Combined Bending and Torsion Problems by Means of the Electrical Conducting Sheet Analogy

N. E. Friedmann and D. Rosenthal
Department of Engineering, University of California at Los Angeles
February 18, 1955

Symbols

A	= enclosed area, (in.^{2})
E	= modulus of elasticity, (lb./in.^{2})
G	= modulus of rigidity, (lb./in.^{2})
P	= applied load, (lb.)
x, y, z	= coordinate directions
s	= tangential direction
n	= normal direction
u, v, w	= displacements in x, y, z directions respectively
σ, τ	= normal and tangential stresses (lb./in.^{2})
ν	= Poisson's ratio
θ	= angle of rotation per unit length (rad./in.)
ϕ, ψ	= stress function
M_t	= twisting couple (in.lbs.)
$I_{xx}, I_{yyx} \ldots$	= moments and products of inertia

$I_{xx} = \iint_R y^2\,dA$, $I_{xxx} = \iint_R y^3\,dA$, $I_{yyx} = \iint_R x^2 y\,dA$ $I_{yy} = \iint_R x^2\,dA$

In previous papers[1, 2] it has been shown that a modification of the electrical conducting sheet analogy proposed by Waner and Soroka[3] and the Gilberts[4] affords a rapid and convenient method for the solution of problems related to plane state of stress and torsion. The advantage of the modified procedure lies in the ease with which electrical potential gradients can be imposed along a boundary of any complex shape by means of a resistance paint as compared to the procedures requiring the establishment of a prescribed current density distribution throughout the field. In view of this advantage, other problems associated with previously proposed analogies—e.g., the Griffith and Taylor analogy[5]—can now be solved more readily. This is particularly true for the combined bending and torsion of beams having a multiply-connected cross section (holes) for which the location of the shear center by means of the shear flow approximation is no longer valid.

To demonstrate this point, consider a cantilever beam of arbitrary shape. The origin of the x, y, z, Cartesian coordinate system is taken at the centroid of the fixed end with x and y directed along the principal axes of the cross section. The free end, at $z = l$, is subjected to a twisting couple M_t and a load P acting at the point $x = a$, $y = 0$ in the direction of the y axis.* With the symbols defined above, it is shown in reference 6† that the differential equations of equilibrium of forces are satisfied by neglecting body forces and putting

$$\sigma_x = \sigma_y = \tau_{xy} = 0 \tag{1}$$

$$\sigma_z = -P[(l - z)x/I_{xx}] \tag{2}$$

and

$$\tau_{xz} = \frac{\partial \phi}{\partial y} + \frac{P}{2I_{xx}}\left(\frac{\nu}{1+\nu}y^2 - x^2\right) - G\theta y,$$

$$\tau_{yz} = -\frac{\partial \phi}{\partial x} + G\theta x \tag{3}$$

where $\phi(x, y)$ is a harmonic function.

The boundary condition for $\phi(x, y)$ on any bounding curve Γ_i is

$$\frac{d\phi}{ds} = \left[\frac{P}{2I_{xx}}\left(x^2 - \frac{\nu}{1+\nu}y^2\right) + G\theta y\right]\frac{dy}{ds} + G\theta x\frac{dx}{ds} \tag{4}$$

or alternatively in the Dirichlet form

$$\phi = \frac{P}{2I_{xx}}\int_{\Gamma_i} x^2\,dy - \frac{\nu}{6(1+\nu)}\frac{P}{I_{xx}}y^3 + \frac{1}{2}G\theta(x^2 + y^2) + C_i$$

$$i = 1, 2, \ldots, N \tag{5}$$

where C_i is a constant of integration and the curves Γ_i are described as positive if the enclosed area is to the left of an observer moving in the direction of description. If the region of integration is simply connected then we may let the constant C_i be zero. If the solid is multiply-connected we can still set C_i equal to zero on the external boundary Γ_1, but we cannot assume that C_i vanishes on internal boundaries Γ_i. The constants C_i for these curves are determined from the condition‡

$$\oint_{\Gamma_i}\frac{d\phi}{dn}\,ds = 0 \qquad i = 2, 3, \ldots, N \tag{6}$$

Finally the applied moment, M_t, can be calculated from the relation

$$M_t = \iint_R (x\tau_{yz} - y\tau_{xz})\,dA + Pa \tag{7}$$

which by virtue of expressions (3) can be put into the form

$$M_t = 2\iint_R \phi\,dA - \sum_{i=1}^{N}\oint_{\Gamma_i}\phi(x\,dy - y\,dx) + G\theta(I_{xx} + I_{yy}) - \frac{P}{2I_{xx}}\left(\frac{\nu}{1+\nu}I_{xxx} - I_{yyx}\right) + Pa \tag{8}$$

The value of M_t is readily computed once the distribution of ϕ has been determined.

In the analog problem, potential gradients required by condition (4) can be easily imposed on the boundary of a facsimile conducting sheet model. The function $\phi(x, y)$ is then obtained by a simple mapping of the field in the interior of the model.

For multiply-connected regions the constants C_i appearing in expression (5) can be evaluated as follows. Substitute the series representation

$$\phi(x, y) = \sum_{s=1}^{N} m_s\,\phi_s(x, y) \tag{9}$$

with $\sum_{s=1}^{N} m_s = 1$ into the requirement (6). This leads to the matrix set

* A restricted class of problems can be treated for other load distributions, such as those discussed in reference 6.

† To put the results appearing here into the notation used in reference 6, we introduce the following transformations; $M = \phi$, $\mu = G = E/2(1 + \nu)$, $\sigma = \nu$, $\alpha = \theta$, $W_x/I_y = P/I_{xx}$.

‡ The method for demonstrating expression (6) is outlined in the appendix.

$$\begin{bmatrix} 1 & 1 & \dots & 1 \\ a_{21} & a_{22} & \dots & a_{2N} \\ \dots & \dots & \dots & \dots \\ a_{N1} & a_{N2} & \dots & a_{NN} \end{bmatrix} \begin{Bmatrix} m_1 \\ m_2 \\ \vdots \\ m_N \end{Bmatrix} = \begin{Bmatrix} 1 \\ 0 \\ \vdots \\ 0 \end{Bmatrix} \tag{10}$$

where the coefficients a_{is} are expressed as

$$a_{is} = \oint_{\Gamma_i} \left(\frac{d\phi_s}{dn}\right) ds \qquad \begin{matrix} i = 2, 3, \dots, N \\ s = 1, 2, \dots, N \end{matrix} \tag{11}$$

The harmonic functions ϕ_s are the solutions of a series of boundary value problems in which C_1 is zero and the coefficients $C_i = b_{is}$, $(i = 2, 3, \dots N)$ are arbitrarily assigned. Thus for each b_{is} there corresponds an a_{is} given by expression (11). The weighting terms m_s can be found from Eq. (10) by a simple inversion provided the square matrix a is nonsingular. Using the values so obtained, it can be shown that the coefficients C_i are determined from the relation

$$C_i = \sum_{s=1}^{N} m_s b_{is} \qquad (i = 2, 3, \dots, N) \tag{12}$$

As an example, we write for $N = 2$

$$a_{21} m_1 + a_{22} m_2 = 0$$
$$m_1 + m_2 = 1$$

which yields

$$m_1 = \frac{a_{22}}{a_{22} - a_{21}} \qquad m_2 = \frac{a_{21}}{a_{21} - a_{22}}$$

and

$$c_1 = 0 \qquad c_2 = m_1 b_{21} + m_2 b_{22}$$

The solution of the problem of (a) shear center, (b) torsion, and (c) bending can be obtained from Eq. (7) by putting θ and M_t, P, and M_t equal to zero, respectively. From case to case only a slight modification of the boundary conditions is involved.

Appendix

To derive relation (6) in the main body of the note we consider the expressions for displacement as follows:

$$u = \frac{P}{2EI_{xx}} \left[\left(l - \frac{z}{3} \right) z^2 + \nu (l - z)(x^2 - y^2) \right] - \theta yz \tag{I}$$

$$v = (\nu P / 2EI_{xx}) [(l - z)xy] + \theta xz \tag{II}$$

$$w = \theta \psi(x, y) - \frac{Px}{EI_{xx}} \left[\left(l - \frac{z}{2} \right) z - \frac{\nu}{2} y^2 + \frac{(2 + \nu)}{6} x^2 \right] \tag{III}$$

where $\psi(x, y)$ is a harmonic function. Introducing the conjugate harmonic function $\phi(x, y)$ as

$$G\theta(\partial\psi/\partial x) = \partial\phi/\partial y \qquad G\theta(\partial\psi/\partial y) = -(\partial\phi/\partial x) \tag{IV}$$

and making use of Hooke's laws, it can be shown that these expressions are compatible with expressions (1)–(5) of the main text.

By virtue of Eq. (IV) we can write

$$d\phi/dn = -G\theta(d\psi/ds) \tag{V}$$

Solving for $d\psi/ds$ from Eq. (III) and using Green's theorem for the plane, we are led to the result (6) since w is single valued.

References

[1] Rosenthal, D., Mackey, R. C., and Dahl, P. R., *Discussion of Paper: "Stress Concentrations for Structural Angles in Torsion by the Conducting Sheet Analogy,"* Experimental Stress Analysis, II, No. 1, pp. 27–30, 1953.

[2] Friedmann, N. E., Yamamoto, Y., and Rosenthal, D., *Solution of Torsional Problems With the Aid of the Electrical Conducting Sheet Analogy*, presented at the First International Instrument Congress and Exposition, Philadelphia, Pa., September 23, 1954.

[3] Waner, N. W., and Soroka, W. W., *Stress Concentrations for Structural Angles in Torsion by the Conducting Sheet Analogy*, Experimental Stress Analysis, II, No. 1, pp. 19–26, 1953.

[4] Gilbert, E. O., and Gilbert, E. G., *A Capacitively Coupled Fluid Mapper or 2-Dimensional Distributed Source Field Problems*, A.I.E.E., Commun. and Elect., pp. 345–351, 1953.

[5] Griffith, A. A., and Taylor, G. I., *Solution of Torsion Problems by the Soap Film Analogy*, Technical Report of the Advisory Committee for Aeronautics (British), 1917–1918.

[6] Sokolnikoff, I. S., *Mathematical Theory of Elasticity*, McGraw-Hill, New York, 1946.

Turbulent Boundary Layers on Nozzle Liners

R. E. Meyer

Department of Aeronautics, University of Sydney, Australia

February 28, 1955

ESTIMATES OF THE GROWTH of displacement thickness are usually based on two groups of simplifying assumptions. Firstly, a Prandtl Number of unity and absence of heat transfer at the wall are assumed. Secondly, the velocity profile is approximated by a definite power law and the skin friction by some empirical relation. Ruptash,[1] for instance, suggests four different relations for the skin friction, two of which are

$$c_f = 0.0262 \, [\mu_1/(\rho_1 u_1 x)]^{1/7} \tag{1}$$

and

$$c_f = 0.045 \, [\mu_w/(\rho_w u_1 \delta')]^{1/4} \tag{2}$$

where suffixes 1 and w indicate values taken in the mainstream and at the wall, respectively, and δ' denotes the total boundary-layer thickness. Both Eq. (1) and Eq. (2) have been used to calculate by his method* the growth of displacement thickness on a certain nozzle liner for Mach Number 2.41. The thicknesses found at the end of the liner differ by 55 per cent. Moreover, Eqs. (1) and (2) lead to different laws of variation of displacement thickness with stagnation pressure!

The purpose of this note is to draw attention to a simple method of boundary-layer estimation that avoids the assumptions of the second group. If the approximation $\mu/T = \text{const.}$ is added to the first group of assumptions, the Illingworth-Stewartson transformation[2, 3] would apply if the boundary layer was laminar. It is plausible, and experimental evidence tends to confirm,[4] that this transformation is also relevant to the turbulent boundary layer. Assume, then, that it applies.

The stagnation conditions of the correlated incompressible layer may be chosen equal to those of the nozzle and the two main streams are then related by[2]

$$U(s_i) = a_0 M(s) \tag{3}$$

and

$$ds/ds_i = (T_0/T_1)^{(3\gamma-1)/(2\gamma-2)} = [1 + (1/2)(\gamma - 1)M^2]^{(3\gamma-1)/(2\gamma-2)} \tag{4}$$

where U denotes the incompressible mainstream velocity and s the length measured along the wall; suffixes i and 0 refer to the incompressible layer and stagnation, respectively. The growth of the incompressible layer so defined may be estimated with confidence. Following Tetervin,[5] its momentum thickness is given by

$$[\theta_i U^{H+2}]^{n+1} = [\theta_{iv} U_v^{H+2}]^{n+1} + (n + 1) k \nu_0^n \int_{s_{iv}}^{s_i} U^{(H+1)(n+1)+1} \, ds_i \tag{5}$$

where a suffix v denotes values at any one fixed station and k and n are constants chosen such that $2k(U\theta_i/\nu_0)^{-n}$ closely approximates the incompressible skin friction coefficient for the range of $(U\theta_i/\nu_0)$ occurring. Since nozzle boundary layers are usually thin at the throat, the values of k and n are usually close to 1/80 and 1/4, respectively. The shape-factor, H, lies between 1.4 and 1.6 and is assumed constant.

The Illingworth-Stewartson transformation also implies the relation

$$\rho u \, dy = \rho_0 u_i \, dy_i \tag{6}$$

* With velocity profile $u/u_1 = (y/\delta')^{1/7}$ and with $\delta' = 0$ at the throat.

between the distances, y, from the wall, and the relation

$$u/u_1 = u_i/U \tag{7}$$

between the velocity profiles, at corresponding stations. For a Prandtl Number of unity and no heat transfer, moreover,

$$T/T_1 = 1 + (1/2)(\gamma - 1)M^2[1 - (u/u_1)^2]$$

and hence, the compressible displacement thickness is

$$\left.\begin{aligned}\delta &= \frac{\rho_0 U}{\rho_1 u_1}\int_0^\infty \left(\frac{T}{T_1} - \frac{u_i}{U}\right) dy_i \\ &= [1 + (1/2)(\gamma - 1)M^2]^{(\gamma+1)/(2\gamma-2)} \times \\ &\qquad \{\delta_i + (1/2)(\gamma - 1)M^2(\theta_i + \delta_i)\}\end{aligned}\right\} \tag{8}$$

by Eqs. (3), (6), (7). Since $H = \delta_i/\theta_i$, and by Eqs. (4), (5), (8),

$$\left.\begin{aligned}(E\delta)^{n+1} &= (E_e\delta_e)^{n+1} + (n+1)k(\nu_0/a_0)^n \int_{s_v}^{s} B ds \\ &\text{with} \\ E &= M^{H+2}[1 + (1/2)(\gamma - 1)M^2]^{-(\gamma+1)/(2\gamma-2)} \times \\ &\qquad \{H + (1/2)(\gamma - 1)M^2(1 + H)\}^{-1} \\ B &= M^{(H+1)(n+1)+1}[1 + (1/2)(\gamma - 1)M^2]^{(1-3\gamma)/(2\gamma-2)}\end{aligned}\right\} \tag{9}$$

Fig. 1 shows E and B for $\gamma = 7/5$, $H = 3/2$, and $n = 1/4$. Note that δ is proportional to the $[-n/(n+1)]$th power of the stagnation pressure; when $n = 1/4$, this agrees with the prediction obtained from Eq. (2) by Ruptash's method.[1]

For comparison, Eq. (9) was also evaluated for the liner mentioned above, again with $\delta = 0$ at the throat. The results* obtained from Eqs. (1) and (9) are shown in Fig. 2. That obtained from Eq. (2) agreed closely with that from Eq. (9), which may be regarded as further evidence in favor of agreement between the predictions of the Illingworth-Stewartson transformation and experimental skin-friction distributions, within the present limits of measurement. For fuller comparison Fig. 2 shows also the results obtained from Eq. (9) for $10^3\delta = 5.2$ and 3.2 in. at the throat. It would appear from these curves that the correct value of δ at the throat cannot differ greatly from 5.10^{-3} in. in this case.

The nearly linear variation of δ with x, from near the throat to the test-rhombus, is due to the variation of B and E with M (see Fig. 1); for any conventional nozzle they balance so that δ/x is not far from constant, at any rate up to $M \approx 2.5$, if x is measured from the throat. This constant, $\delta(l)/l$, can be estimated quickly from Eq. (9), with $\delta_e = 0$, $s_e = 0$, and $s = l$, the length of liner from the throat. The local rate of growth, $d\delta/dx$, varies more markedly but it can be shown by the method of reference 6 that the difference $d\delta/dx - \delta(l)/l$ on the supersonic part of the liner corresponds to Mach Number variations of only about

* All are based on a stagnation pressure of 110 p.s.i.g. and ambient stagnation temperature.

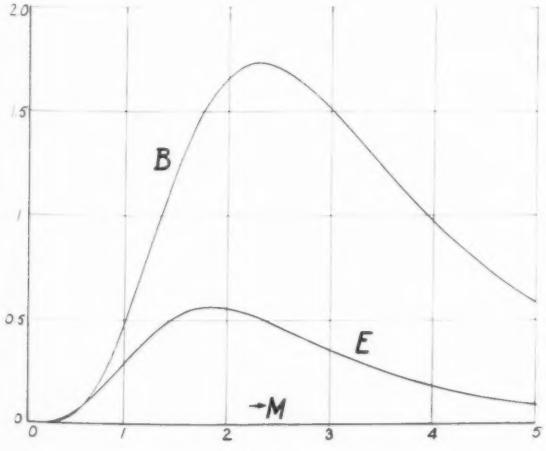

FIG. 1.

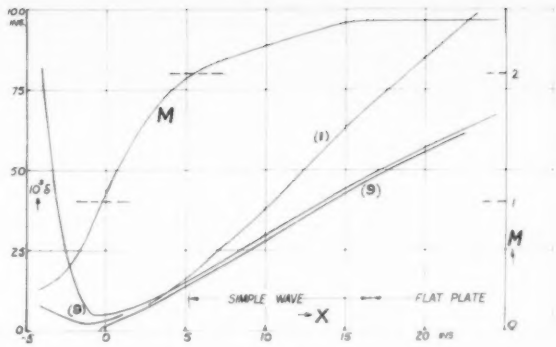

FIG. 2.

0.003 in the test-rhombus, most of which are due to the values of this difference not far from the throat.

REFERENCES

[1] Ruptash, J., *Supersonic Wind Tunnels—Theory, Design and Performance*, U.T.I.A. Review No. 5, 1952.

[2] Illingworth, I. R., Steady Flow in the Laminar Boundary Layer of a Gas, Proc. Roy. Soc., A, Vol. 199, p. 533, 1949.

[3] Stewartson, K., *Correlated Incompressible and Compressible Boundary Layers*, Proc. Roy. Soc., A, Vol. 200, p. 84, 1949.

[4] Crocco, L. and Lees, L., *A Mixing Theory for the Interaction Between Dissipative Flows and Nearly Isentropic Streams*, Journal of the Aeronautical Sciences, Vol. 16, No. 10, pp. 649-676, October, 1952.

[5] Tetervin, N., *A Method for the Rapid Estimation of Turbulent Boundary Layer Thickness for Calculating Profile Drag*, NACA, A.C.R., No. L4G14, 1944.

[6] Meyer, R. E., *Perturbations of Supersonic Nozzle Flows*, In press.

On a Class of Two-Dimensional Channel Flows with a Straight Sonic Line

A. J. A. Morgan
Aercon, Inc., Altadena, Calif.

February 28, 1955

WE CONSIDER a compressible two-dimensional inviscid flow governed by the transonic equation[1]

$$[(\gamma + 1)/a^*]\varphi_x\varphi_{xx} + \varphi_{yy} = 0 \tag{1}$$

where φ is the perturbation velocity potential, γ the ratio of the specific heats of the gas, a^* the critical speed of sound, the subscript notation for partial differentiation is used, and the velocity components (U,V) in the positive (x,y) directions are given by:

$$U = a^* - \varphi_x, \qquad V = -\varphi_y \tag{2}$$

Eq. (1) holds under the assumptions

$$\text{(I)}\ \frac{\varphi_x}{a^*} \ll 1 \qquad \text{(II)}\ \frac{\varphi_y}{a^*} \ll 1 \qquad \text{(III)}\ \frac{\partial U}{\partial y} \ll \frac{\partial U}{\partial x}$$

The transonic Eq. (1) can be put into the normalized form

$$\varphi_\xi\varphi_{\xi\xi} + \varphi_{yy} = 0 \tag{3}$$

upon application of the transformations

$$x = \lambda^{-(2/3)}\xi \qquad y = y \qquad \lambda^2 = a^*/(\gamma + 1) \tag{4}$$

The title flows arise from an investigation of the possible *invariant* (similarity) *solutions*† of Eq. (3). To determine the functional form of such solutions, we consider the invariance of Eq. (3) under the following continuous one-parameter group of transformations:

† Those solutions of partial differential equations whose functional form is such that the number of independent variables in these equations is reduced by one. See reference 2 for precise definitions.

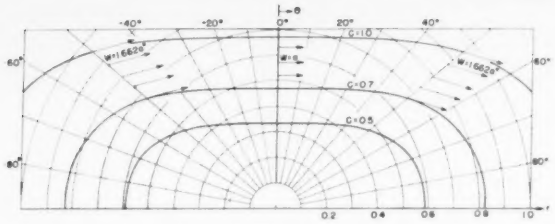

FIG 1 - THE STREAMLINE PATTERN

$$\bar{\varphi} = a^p \varphi, \qquad \bar{\xi} = a^m \xi, \qquad \bar{y} = a^n y \tag{5}$$

where a ($\neq 0$) is the numerical parameter and m, n, p ($\neq 0$) are, as yet, undetermined numerical constants. A complete set of absolute invariants of Eqs. (5) is given by

$$\eta = \xi^{-(n/m)} y \qquad \xi^{-(p/m)} \varphi \tag{6}$$

Now, the normalized transonic Eq. (3) will be constant conformally invariant† under the group of transformations (5) if m, n, and p satisfy the relation

$$n/m = (3/2) - (1/2)(p/m) \tag{7}$$

Thus, with $q = p/m$, Eq. (3) will, by Theorem 3 of reference 2, be reduced to an ordinary differential equation by the substitutions

$$\varphi = \xi^q f(\eta) \qquad \eta = \xi^{(1/2)(q-3)} y \tag{8}$$

The resulting ordinary differential equation is

$$[qf + (1/2)(q-3)\eta(df/d\eta)]\,[q(q-1)f + (5/4)(q-1) \times (q-3)\eta(df/d\eta) + (1/4)(q-3)^2\eta^2(d^2f/d\eta^2)] + (d^2f/d\eta^2) = 0 \tag{9}$$

All of the invariant (similarity) solutions of the transonic equation under the group (5) are then characterized by Eq. (9).

† See footnote on page 573.

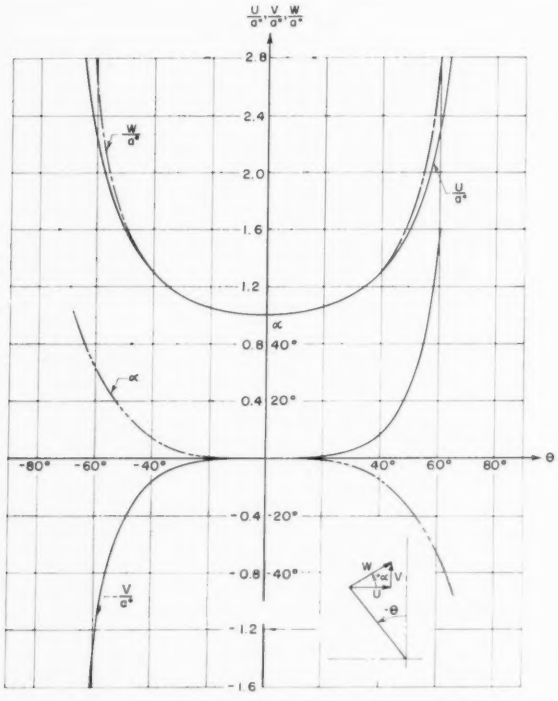

FIG 2 - THE VELOCITY AND ANGLE DISTRIBUTIONS

In order to determine q, we must impose additional (side) conditions on the flow. For instance, if we require that the velocity component U be unchanged (absolutely invariant) under Eqs. (5), then $q = 1$. If, on the other hand, it is required that φ be absolutely invariant under Eqs. (5), then $q = 0$. Additionally, the side condition that the transonic equation itself be absolutely invariant under the group of transformations (5) imposes the restriction $q = 3/2$.

Our present investigation, however, will be restricted to that class of flows, characterized by Eq. (9), for which $q = 0$—i.e., $\varphi = \bar{\varphi}$. Under this restriction Eq. (9) becomes

$$27\eta^3 f_\eta f_{\eta\eta} + 45\eta^2 f_\eta^2 - 8 f_{\eta\eta} = 0 \tag{10}$$

where the η subscripts on the f's denote ordinary differentiation with respect to η. On letting $\zeta = f_\eta$, and interchanging the roles of the independent and dependent variables, we obtain from Eq. (10) the following ordinary differential equation for η in terms of ξ:

$$45\eta^2\zeta^2(d\eta/d\zeta) + 27\eta^3\zeta = 8 \tag{11}$$

whose solution is found to be given by

$$\eta = [C_1\zeta^{-9/5} + (2/3)\zeta^{-1}]^{1/3} \tag{12}$$

where C_1 is a constant of integration.

Further considerations will now be restricted to those flows for which $C_1 = 0$ in Eq. (12). Since $\zeta = f_\eta$ we then find that

$$\varphi = f(\eta) = -\frac{1}{3}\eta^{-2} + C_2 = -\frac{1}{3}\frac{a^*}{\gamma+1}\frac{x^2}{y^2} + C_2 \tag{13}$$

where C_2 is a constant of integration and the expressions for the velocity components U and V are

$$U = a^*\left(1 + \frac{1}{\gamma+1}\frac{x^2}{y^2}\right) \qquad V = -\frac{2}{3}\frac{a^*}{\gamma+1}\frac{x^3}{y^3} \tag{14}$$

In a polar coordinate system, with θ measured with respect to the y-axis, such that

$$x = r\sin\theta \qquad y = r\cos\theta \tag{15}$$

the expressions (14) for the velocity components U and V become

$$U = a^*\left(1 + \frac{1}{\gamma+1}\tan^2\theta\right) \qquad V = -\frac{2}{3}\frac{a^*}{\gamma+1}\tan^3\theta \tag{16}$$

We immediately note that for this flow the sonic line ($W = a^*$) is straight and located on the y-axis. Also, the velocities U and V are singular on the x-axis. Furthermore, the velocities U and V are constant along any one ray issuing from the origin.

The stream lines for the flow defined by Eqs. (16) are determined by the differential equation

$$dy/dx = V/U \tag{17}$$

Upon substituting Eqs. (16) in Eq. (17), this differential equation may be integrated by standard methods to give the following expression, in the polar coordinates (15), for the stream lines:

$$r = C\frac{\exp\left\{\dfrac{3}{4\sqrt{6[\gamma+(5/8)]}}\tan^{-1}\dfrac{4\tan^2\theta+3}{2\sqrt{6[\gamma+(5/8)]}}\right\}}{\cos\theta[2\tan^3\theta + 3\tan^2\theta + 3(\gamma+1)]^{(1/4)}} \tag{18}$$

where C is a constant of integration. Note that r/C is a dimensionless quantity. When $\theta = 90°$, Eq. (18) becomes $r = 1.180C$. The stream lines given by Eq. (18), which are symmetrical about the line $\theta = 0°$, are shown, for $C = 0.5$, 0.7, and 1.0, in Fig. 1.

The velocities U, V, and $W = [U^2 + V^2]^{1/2}$ and the angle $\alpha = \tan^{-1} V/U$ for the class of flows given by Eq. (16) are depicted in Fig. 2. It is seen that the assumptions (I), (II), and (III) are violated for, say, $\theta > 40°$. However, for $\theta < 40°$ these assumptions are not violated and, with appropriate boundary-layer corrections, the analysis indicates that slightly supersonic flows may be turned through small angles. For instance, such a channel with entrance and exit sections located at $\theta = \pm 40°$ respectively could be used to turn a flow with $w = 1.31a^*$ through a total angle of approximately 14°.

One of the solutions of Eq. (9) for $q = 1$ also yields a flow pattern with U and $V + C$ given by the right hand sides of Eqs. (14), that is, a constant V-velocity component is superimposed on the flow field described by Eqs. (14).

References

[1] Cole, J. D., *Problems in Transonic Flow*, Ph.D. Thesis, California Institute of Technology, 1949.

[2] Morgan, A. J. A., *The Reduction by One of the Number of Independent Variables in Some Systems of Partial Differential Equations*, The Quarterly Journal of Mathematics, Oxford Second Series, Vol. 3, No. 12, pp. 250–259, 1952.

Simultaneous Measurements of Velocity and Temperature Profiles for Adiabatic Supersonic Flow of Air in a Tube

Joseph Kaye,* George A. Brown,† Julius C. Westmoreland,‡ and Edward F. Kurtz, Jr.**

Massachusetts Institute of Technology, Cambridge, Mass.

March 1, 1955

VELOCITY AND TEMPERATURE PROFILES for adiabatic supersonic flow of air in a round tube have been obtained simultaneously by means of a small combination probe which measures both impact pressure and temperature of the air stream from the tube wall to the centerline. The need for simultaneous measurements of velocity and temperature profiles recently became evident in a research program whose goal is to obtain reliable heat-transfer coefficients for supersonic flow. This program, sponsored by the Office of Naval Research, has produced accurate and reliable measurements for the rate of heat transfer to a supersonic stream of air[1, 2] and has also obtained theoretical predictions by solution of the equations of momentum, energy, and continuity for flow in the entrance region of a tube.[3] The interpretation of the experimental results and the assumptions used in the theory have been based, however, on a simple intuitive model used to understand the phenomena occurring in supersonic flow in a round tube. This model assumes a laminar boundary layer originates at the tube inlet and grows in thickness in the direction of flow; coexistent with this laminar boundary layer is a central core of fluid which undergoes an isentropic process and which decreases in size in the direction of flow.

Previous measurements of velocity profiles[4] by means of small impact pressure probes have demonstrated the existence of this laminar boundary layer for a wide range of inlet stagnation conditions, and for both adiabatic and diabatic flow. It was also shown[4] that the measured Mach Number profiles of a laminar boundary layer for tube flow agree well with similar profiles, measured and predicted, for a laminar boundary layer on a flat plate with supersonic velocities in the free stream. The present measurements of velocity profiles, taken with a new and different type of combination probe, confirm quantitatively previous velocity measurements. In addition, new experimental evidence based on the measured temperature profiles has been obtained to confirm independently the existence of the laminar boundary layer in the tube flow.

The details of the apparatus used in this work are given in previous reports.[1, 2, 4] The details of a combination probe are shown in Fig. 1. The dimensions of this probe are of the same order of magnitude as those used for the simple impact probes.[4] The thermocouple tip is almost at the inlet plane of the probe. A new and more accurate traversing rig was constructed for positioning of the combination probe, but the method of use is essentially the same as described previously.[4] The combination

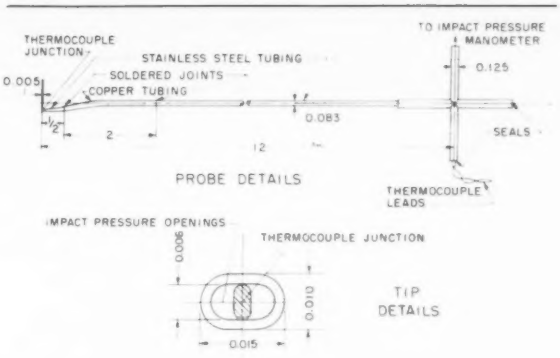

FIG. 1 – DIMENSIONS OF PROBE W-2

probe was used to measure impact pressure of the air stream from tube wall to tube centerline in the usual fashion.

For measurements of temperature, the combination probe was calibrated mainly in a subsonic stream of known temperature, utilizing a probe recovery factor, defined by

$$r_p \equiv (T_p - T)/(T_0 - T) \qquad (1)$$

where T_p is the measured probe temperature, T and T_0 are the static and stagnation temperatures of the stream, respectively. The stagnation conditions were measured upstream of a subsonic nozzle, and the static temperature was computed from the measured wall pressure at the probe and the condition of isentropic flow for the core of the subsonic stream. The probe was also calibrated in supersonic flow in a similar fashion for a Mach Number of about 2.3. The results of the calibrations for subsonic and supersonic flow are shown in Fig. 2. A constant value of probe recovery factor between 0.83 and 0.85 fits the experimental data, as shown by the solid lines in Fig. 2.

In order to reduce the size of this note, only two representative samples of the measured and computed quantities are shown in detail in Fig. 3. These two samples were selected to show the measured and computed profiles for a low value and for a high value of the inlet diameter Reynolds Number, for the case of adiabatic supersonic flow in the 0.5 in. tube with a laminar boundary layer present. The ratio of the local probe temperature to the local value at the centerline is shown plotted versus the radial position, y/a, at the top of Fig. 3. The effect of increasing the inlet diameter Reynolds Number from 35,600 to 106,000 is to reduce slightly the thickness of the thermal boundary layer, without a major change in the shape of the probe-temperature profile in the laminar boundary layer.

The measured static pressure at tube wall and the local impact probe pressure were used to compute the local Mach Number, employing the Rayleigh pitot-tube equation for supersonic flow and the assumption of isentropic deceleration for subsonic flow.

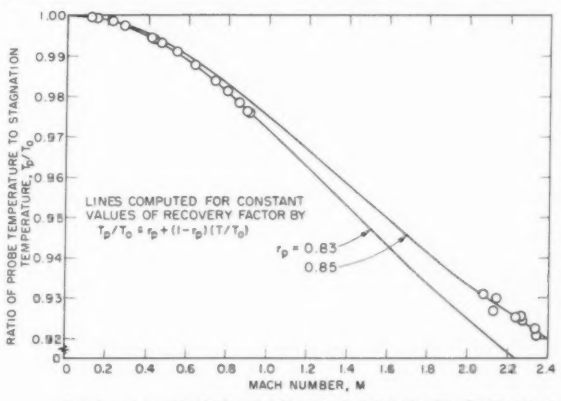

FIG. 2 – CALIBRATION DATA FOR COMBINATION PROBE W-2

* Associate Professor of Mechanical Engineering, M.I.T.
† Instructor, Mechanical Engineering, M.I.T.
‡ Research Engineer, Mechanical Engineering, M.I.T.
** Research Engineer, Allied Research Associates, Boston, Mass.

The local stagnation temperature was computed from the probe temperature by

$$T_p/T_0 = r_p + (1 - r_p)T/T_0 \qquad (2)$$

using a constant value of the probe recovery factor of 0.84.

The local stream velocity was computed from

$$u = M\sqrt{gkRT} \qquad (3)$$

The profiles for velocity ratio and Mach Number ratio are in good agreement with those measured previously with a simple impact probe.[4] These results will not be discussed further.

The profiles of static-temperature ratio are also shown in Fig. 3. The effect of increasing the inlet diameter Reynolds Number is to decrease but slightly the thickness of the thermal boundary layer. These profiles indicate the degree of reproducibility obtained by this combination probe as a temperature measuring device.

The most interesting profiles shown in Fig. 3 are those for the ratio of local stagnation temperature to the centerline value. In the first attempts to obtain such profiles, the experimental values were taken at widely separated intervals of the radial position. Although some preliminary measurements indicated that there could be a region with an excess of local stagnation temperature compared with the centerline stagnation temperature, it was decided to eliminate the possibilities of errors in such measurements by repeating them carefully with small intervals of the radial position of the probe. The results are shown in Fig. 3; many more similar results were obtained for other conditions. The region of this excess of stagnation temperature or enthalpy in the laminar boundary layer was studied in detail in order to compare these profiles with theoretical predictions.

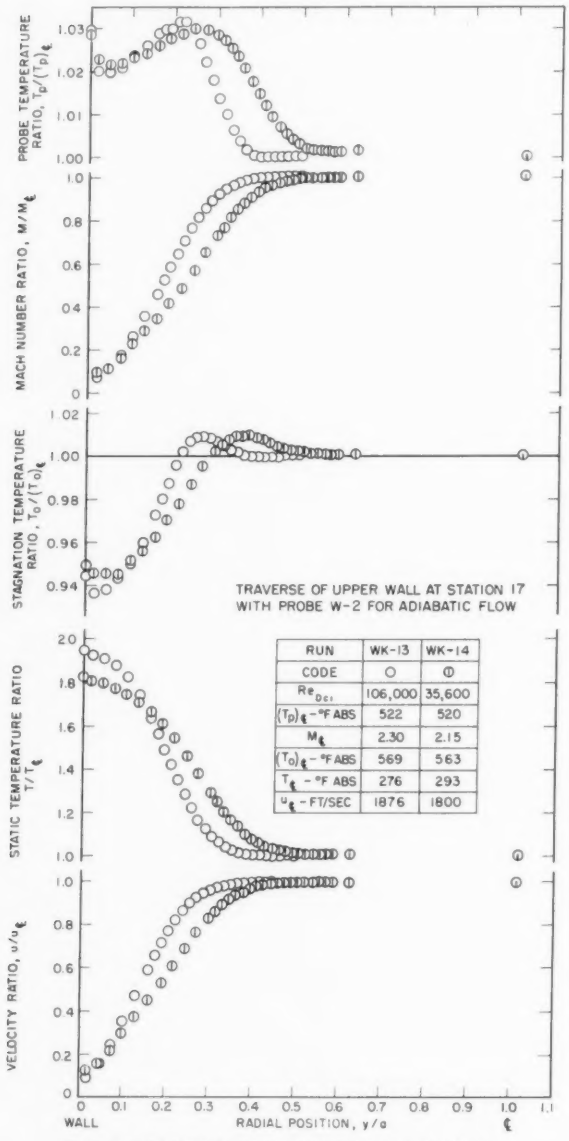
PROBE TEMPERATURE RATIO, $T_p/(T_p)_{\ell}$
MACH NUMBER RATIO, M/M_{ℓ}
STAGNATION TEMPERATURE RATIO, $T_0/(T_0)_{\ell}$
TRAVERSE OF UPPER WALL AT STATION 17 WITH PROBE W-2 FOR ADIABATIC FLOW
STATIC TEMPERATURE RATIO T/T_{ℓ}
VELOCITY RATIO, u/u_{ℓ}
WALL
RADIAL POSITION, y/a
ℓ

RUN	WK-13	WK-14
CODE	○	⊕
$Re_{D_{c1}}$	106,000	35,600
$(T_p)_{\ell}$ - °F ABS	522	520
M_{ℓ}	2.30	2.15
$(T_0)_{\ell}$ - °F ABS	569	563
T_{ℓ} - °F ABS	276	293
u_{ℓ} - FT/SEC	1876	1800

FIG 3 - EFFECT OF INLET DIAMETER REYNOLDS NUMBER ON PROFILES

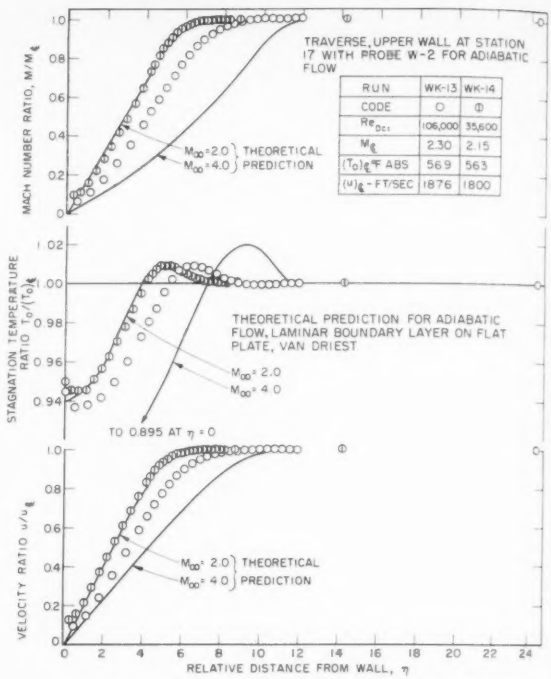
MACH NUMBER RATIO, M/M_{ℓ}
TRAVERSE, UPPER WALL AT STATION 17 WITH PROBE W-2 FOR ADIABATIC FLOW
M_{∞}=2.0 } THEORETICAL
M_{∞}=4.0 } PREDICTION
STAGNATION TEMPERATURE RATIO $T_0/(T_0)_{\ell}$
THEORETICAL PREDICTION FOR ADIABATIC FLOW, LAMINAR BOUNDARY LAYER ON FLAT PLATE, VAN DRIEST
M_{∞}= 2.0
M_{∞}= 4.0
TO 0.895 AT η = 0
VELOCITY RATIO u/u_{ℓ}
M_{∞}= 2.0 } THEORETICAL
M_{∞}= 4.0 } PREDICTION
RELATIVE DISTANCE FROM WALL, η

RUN	WK-13	WK-14
CODE	○	⊕
$Re_{D_{c1}}$	106,000	35,600
M_{ℓ}	2.30	2.15
$(T_0)_{\ell}$ °F ABS	569	563
$(u)_{\ell}$ - FT/SEC	1876	1800

FIG. 4 - COMPARISON OF MEASURED PROFILES FOR ADIABATIC TUBE FLOW WITH PREDICTED PROFILES FOR ADIABATIC PLATE FLOW

Fig. 4 compares the experimental profiles for adiabatic tube flow with the theoretical predictions of Van Driest[5] for supersonic flow on a flat plate with a laminar boundary layer. The abscissa is the customary one used in the analyses of flat-plate flows—namely,

$$\eta \equiv (y/L)\sqrt{Re_L} \qquad (4)$$

where L is the distance from the leading edge, and the length Reynolds Number, Re_L, is given by

$$Re_L \equiv u_{\infty}L/\nu_{\infty} \qquad (5)$$

where u_{∞} and ν_{∞} denote the free-stream velocity and kinematic viscosity, respectively. For the case of tube flow, however, where the centerline velocity and fluid properties vary with the distance downstream from tube entrance, a convenient though arbitrary definition of η is used here—namely,

$$\eta \equiv (y/L)\sqrt{Re_{L17}} \qquad (6)$$

where L is the distance from entrance plane of the tube and the Reynolds Number is arbitrarily chosen for convenience to be

$$Re_{L17} \equiv u_{c1}L_{17}/\nu_{c1} \qquad (7)$$

in which the fluid properties are to be evaluated at tube entrance (to correspond to flat-plate flow), or at station 1, and by assuming that an isentropic core exists for the flow at tube entrance.

The experimental profiles for velocity and Mach Number for tube flow are in excellent agreement with the predictions for plate flow, corroborating similar measurements published previously.[4]

The measured stagnation temperature profiles for tube flow agree well with those predicted for plate flow by Van Driest.[5] In fact, Fig. 4 shows that the measured excess of stagnation temperature in the laminar boundary layer agrees within a few tenths of one per cent with the excess predicted by Van Driest, based on taking into account the actual variation of properties of air with temperature.

The measurements made with the combination velocity and temperature probe were used to secure independent checks on the supersonic flow phenomena in a tube, since velocity, temperature, and static pressure are sufficient to define the local behavior of the flow. These checks included the integration of the local flow conditions to obtain the mass rate of flow of air, and the integration of the local energy flux to obtain the total enthalpy flux. The integrated flow and enthalpy agreed, within experimental error, with the flow and flux based on the calibrations of the supersonic nozzle and on the measured stagnation conditions. Comparison of the defect and excess of stagnation enthalpy flux in the laminar boundary layer at a given section in the flow is also being investigated as an independent check on the reliability of the combination probe.

References

[1] Kaye, J., Keenan, J. H., Shoulberg, R. H., and Brown, G. A., *Heat-Transfer Measurements in an Inexpensive Supersonic Wind Tunnel, Part I—Apparatus, Data, and Results for a Laminar Boundary Layer Based on a Simple One-Dimensional Flow Model*, Annual Meeting ASME, November, 30, 1954.

[2] Kaye, J., and Brown, G. A., *Heat-Transfer Measurements in an Inexpensive Supersonic Wind Tunnel, Part II—Results for a Laminar Boundary Layer Based on a Two-Dimensional Flow Model for the Entrance Region of a Tube*, Annual Meeting, ASME, November 30, 1954.

[3] Toong, T. Y., and Kaye, J., *Theoretical Velocity and Temperature Profiles for the Laminar Boundary Layer of the Flow of a Compressible Fluid in the Entrance Region of a Tube*, Second U.S. National Congress of Applied Mechanics, June, 1954.

[4] Kaye, J., Brown, G. A., Dieckmann, J. J., and Sziklas, E. A., *Experimental Velocity Profiles for Supersonic Flow of Air in a Tube With and Without Heat Transfer*, Second U.S. National Congress of Applied Mechanics, June, 1954.

[5] Van Driest, E. R., *Investigation of Laminar Boundary Layer in Compressible Fluids Using the Crocco Method*, NACA TN 2597, January, 1952.

Brachistocronic Maneuvers of a Variable Mass Aircraft in a Vertical Plane

Placido Cicala and Angelo Miele*

Professor, Politecnico di Torino, Italy, and Research Assistant Professor of Aeronautical Engineering, Polytechnic Institute of Brooklyn, Brooklyn, N.Y., respectively

March 2, 1955

Introduction

In a previous Readers' Forum note[4] the brachistocronic problem has been treated for a constant mass aircraft and for a propulsion mechanism operated in such a way that the thrust (T) depends on the velocity (V) and altitude (h) only.

With the present note the writers generalize their previous conclusions to the case of an aircraft whose mass $m = m(t)$ is arbitrarily time-dependent and whose thrust $T = T(h, V, t)$ is a generic function of velocity, altitude and time (t). A more general field of problems is now investigated, insofar as the horizontal distance traveled by the aircraft is considered, as it is the case with analyses involving the range or with interception problems. In addition, the variability $g = g(h)$ of the acceleration of gravity with the altitude is also accounted for, having in mind possible applications of the present theory to flight patterns penetrating into the upper regions of the atmosphere.

The following hypotheses are used: (1) the small angle between the vectors thrust and velocity is neglected; (2) only flight paths contained in a vertical plane are considered; (3) the aerodynamic lag is disregarded—i.e., lift (L) and drag (D) forces are calculated as in steady flight. This last hypothesis is equivalent to assuming a drag function of the form $D = D(h, V, L)$, the effects of the Mach and Reynolds Numbers on the polar being accounted for.

The expressions for the velocity components ($\dot{x}$, $\dot{h}$) and the equations of the motion on the tangent and on the normal to the flight path are written as follows:

$$J_1 \equiv \dot{x} - V\cos\theta = 0 \tag{1}$$

$$J_2 \equiv \dot{h} - V\sin\theta = 0 \tag{2}$$

$$J_3 \equiv \dot{V} + g\sin\theta + (D - T)/m = 0 \tag{3}$$

$$L - m(g\cos\theta + V\dot{\theta}) = 0 \tag{4}$$

where x denotes horizontal distance, θ is the inclination of the flight path with respect to a horizontal plane, and the dot sign refers to (total) derivative with respect to the time.

Necessary Conditions for the Existence of an Extremum

The determination of the path of minimum time between a set of initial conditions 1 and a set of final conditions 2 to be reached by the aircraft consists in general in a variational problem of Mayer[6] type, insofar as the time to be minimized appears in Eqs. (1), (2), (3), and (4). By assuming t as an independent variable the brachistocronic problem is formulated as follows: "to determine the four unknown functions $V(t)$, $\theta(t)$, $h(t)$, $x(t)$ which make $\int_1^2 dt$ stationary under the subsidiary conditions† (1), (2), and (3)."

By introducing the three Lagrangian multipliers $\lambda_1(t)$, $\lambda_2(t)$, $\lambda_3(t)$, the following necessary conditions‡ are obtained for the optimum path:

$$\dot{\lambda}_3 + \lambda_3(T_V - D_V)/m - \lambda_3 D_L\dot{\theta} + \lambda_2\sin\theta + \lambda_1\cos\theta = 0 \tag{5}$$

$$d(\lambda_3 V D_L)/dt + \lambda_3 g(D_L\sin\theta - \cos\theta) + V(\lambda_2\cos\theta - \lambda_1\sin\theta) = 0 \tag{6}$$

$$\dot{\lambda}_2 + \lambda_3(T_h - D_h)/m - \lambda_3 g'(\sin\theta + D_L\cos\theta) = 0 \tag{7}$$

$$\dot{\lambda}_1 = 0 \tag{8}$$

where

$$D_h = (\partial D/\partial h)_{V,\,L} \qquad D_V = (\partial D/\partial V)_{h,\,L} \qquad D_L = (\partial D/\partial L)_{h,\,V}$$
$$T_h = (\partial T/\partial h)_{V,\,t} \qquad T_V = (\partial T/\partial V)_{h,\,t} \qquad g' = dg/dh$$

Eqs. (1), (2), (3), (5), (6), (7), and (8) form a differential system whose general solution depends on 8 integration constants, to be defined by the boundary conditions of the problem. It is to be noted that Eqs. (5), (6), (7), and (8) are homogeneous in λ_1, λ_2, λ_3. As a consequence, an arbitrary (provided $\neq 0$) value may be imposed to one of the three multipliers—e.g., $\lambda_2 = 1$—at a generic point of the flight pattern in view of the fact that this circumstance does not affect at all the remaining unknown functions $h(t)$, $V(t)$, $x(t)$, $\theta(t)$. In addition to the above *idle condition*, seven conditions may be imposed to the flight path, for instance, the initial set of values for h, t, V, θ, x, and the final set for h, V, θ, x.

The following general remarks are of importance:

(1) The above differential system holds also for the extremals of several analogous problems, such as maximum range, maximum increase in altitude, and maximum increase in velocity. In each case the initial and final set of values for the remaining variables must be given.

(2) With the help of convenient boundary conditions (transversality conditions) the above equations may also be used to

* Now, Associate Professor, School of Aeronautics, Purdue University, Lafayette, Indiana.

† If the lift L is eliminated from Eq. (3) by using Eq. (4), one obtains an expression of the type $J_3(t, h, \theta, \theta, V, \dot{V}) = 0$.

‡ Eqs. (5) to (8) may be formally deduced as Euler's equations for $\int_1^2 (\sum_1^3 \lambda_i J_i)\, dt$.

solve the interception problem—i.e., to determine the brachistocronic path for an aircraft A which has to reach another aircraft B, performing an arbitrary maneuver $x_B(t)$, $h_B(t)$ in the same vertical plane. In addition, also problems of conditioned optima may be treated with the above equations, for instance the important case ($h \geqslant h_1$) where the aircraft is forbidden to go to altitudes below the initial one, because of the presence of obstacles, such as the ground level.

(3) Eq. (1) could be replaced with an equivalent isoperimetric condition by prescribing the value for $I = \int_1^2 V \cos\theta \, dt$. In such a case the solution of the differential system would depend on seven integration constants. For instance, (h, t, V, θ) may be prescribed at 1 and (h, V, θ) at 2, in addition to the idle condition and to the value for I. Eq. (1), however, has been preferably used by the writers, with the main object of treating the actual variational problem within the general frame of Mayer problems.

Special Cases

The integration of the above differential system is to be performed by approximated methods in the most general case. Under particular circumstances, however, the problem may be simplified.

(A) *Free Horizontal Distance*

If no condition is imposed to the values of x_1 and x_2, Eqs. (1) and (8) disappear. The new set of Euler's equations is obtained as a particular case of Eqs. (5), (6), (7), and (8) for $\lambda_1 = 0$. The number of integration constants reduces to 6, with an idle condition at an arbitrary point of the flight path. The values for h, V, θ, t at point 1 and for h, V, θ at point 2 may be prescribed. Should the Lagrangian multipliers be eliminated, the order of the resulting system would be reduced to 5, the idle condition disappearing.

(B) *Constant Mass, Thrust Independent of the Time*

The hypotheses $\dot{m} = 0$, $\partial T/\partial t = 0$ lead to a first integral for the differential system constituted by Eqs. (5), (6), (7), and (8):

$$\lambda_3(\dot{V} + D_L V\dot{\theta}) + V(\lambda_2 \sin\theta + \lambda_1 \cos\theta) = C \qquad (9)$$

By replacing one of the above equations with Eq. (9), a new system, homogeneous in λ_1, λ_2, λ_3 and C, is obtained. It follows that an alternative form of the idle condition could be $C = 1$.

If the time is eliminated by using Eq. (2), the number of integration constants for the differential system reduces to seven. After accounting for the idle condition, six other conditions may be imposed—e.g., by prescribing the values for h, V, θ, x at points 1 and 2.

For the particular case $T = D = 0$ the order of differential system obtained by eliminating the time variable and the Lagrange multipliers reduces to three and the solution degenerates into the well-known brachistocronic of the gravitational field—i.e., the cycloidal path.

(C) *Free Horizontal Distance, Constant Mass, Thrust Independent of the Time*

For $\lambda_1 = 0$, $\dot{m} = 0$, $\partial T/\partial t = 0$, the elimination of the time variable and of the Lagrange multipliers leads to a fourth order problem, which has been already treated in a previous Readers' Forum Note[4] by the same authors.

(D) *Free Horizontal Distance, Negligible Centrifugal Forces*

For $L = mg\cos\theta$ Euler's equations (5) and (6) modify insofar as the terms $\lambda_3 D_L\dot{\theta}$ and $d(\lambda_3 D_L V)/dt$ disappear. For $\lambda_1 = 0$, moreover, the elimination of the Lagrange multipliers λ_2 and λ_3 from Eqs. (5), (6), and (7) leads to the following result:

$$W\dot{u} + (D_V - T_V)\,gu + W\,g\,u^2 \sin\theta + D_h - T_h + m\,D_L\,g'/\cos\theta = 0 \qquad (10)$$

where

$$u = (D_L \tan\theta - 1)/V \qquad (11)$$

Eqs. (2), (3) and (10) form a differential system of order three, for which the initial set (h, V, t) and the final set (h, V) may be prescribed. It is to be noted that for a parabolic polar with coefficients depending on both the Mach and Reynolds Numbers the solution $\cos\theta = 0$ is found in addition to the solution (10).

(E) *Free Horizontal Distance, Required Lift Independent of Centripetal Acceleration and Path Inclination*

For $\lambda_1 = 0$, $L = mg$, Eqs. (5), (6), and (7) lead to a solution which is composed of arcs of equation:

$$\cos\theta = 0 \qquad (12)$$

and arcs of equation:

$$T - D + (D_h - T_h)V^2/g + (T_V - D_V)V + V^2 D_L\, g'm/g = 0 \qquad (13)$$

Eq. (13) may also be written as:

$$(\partial/\partial V)(TV - DV) - (V^2/g)(\partial/\partial h)(T - D) = 0 \qquad (14)$$

The above expression is a relationship of the type $f(h, V, t) = 0$. For the particular case $\dot{m} = 0$, $\partial T/\partial t = 0$, Eq. (14) degenerates into an expression in finite terms between h and V (see references 1, 2, 4).

(F) *Free Horizontal Distance, Negligible Induced Drag*

For $\lambda_1 = 0$, $D_L = 0$, Eqs. (12), (13), and (14) hold with obvious simplifications ($D = D_0$, where D_0 = zero-lift drag). For the particular case $\partial T/\partial t = 0$ Eq. (14) reduces to an equation in finite terms, as shown by the junior author in reference 5.

References

[1] Miele, A., *Problemi di Minimo Tempo nel Volo Non-Stazionario degli Aeroplani*, Atti della Accademia delle Scienze di Torino, Classe di Scienze Matematiche, Fisiche e Naturali, Vol. 85, pp. 41–52, 1950–1951.

[2] Miele, A., *Soluzioni Generali di Problemi di Ottimo in Volo Non-Stazionario*, L'Aerotecnica, Vol. 32, No. 3, pp. 135–142, 1952.

[3] Cicala, P., and Miele, A., *Evoluzioni Brachistocrone di un Aereo*, Atti della Accademia delle Scienze di Torino, Classe di Scienze Mathematiche, Fisiche e Naturali, (in publication).

[4] Cicala, P., and Miele, A., *Brachistocronic Manoeuvres of a Constant Mass Aircraft in a Vertical Plane*, Readers' Forum, Journal of the Aeronautical Sciences, Vol. 22, No. 4, April, 1955.

[5] Miele, A., *Optimum Climbing Technique for a Rocket-Powered Aircraft*, Jet Propulsion (in publication).

[6] Pascal, E., *Repertorium der Höheren Analysis*, Vol. I, p. 655, B. G. Teubner, Leipzig, 1927.

Note on a Formula of H. W. Emmons

J. A. Steketee

Department of Mathematics, University of Toronto, Ontario, Canada

March 9, 1955

In the paper "The Laminar-Turbulent Transition in a Boundary Layer"[1] Prof. H. W. Emmons develops a theory of boundary-layer transition starting from the observation of "turbulence spots" which grow while they are washed away by the flow.

Fundamental for the applications of the theory is the formula (4) which gives an expression for the probability that a point on the watertable at a certain moment will be covered with turbulent flow. If the mean flow is steady one is justified in interpreting (4) as the expression for the fraction of the time that a point on the watertable will be covered with turbulent flow. The derivation of the formula (4) was felt to be rather complicated through the introduction of the $\Psi(PP_0)\,dV_0$ functions which were introduced to eliminate "overlaps." It is the purpose of this note to give a derivation of formula (4) which is believed to be more straightforward as there is no need for the $\Psi(PP_0)\,dV_0$ functions.

We first consider the following case of probability theory: there are given n simple, independent events. The probability that the kth event occurs is p_k, while the probability that the kth event does not occur is $1 - p_k$. The p_k's are constant and unequal. (If all the p_k's are equal we have the case of n Bernoulli trials.) The simple events are not mutually exclusive and we

ask for the probability that at least one of the first k events occurs. (There is no loss of generality in asking for at least one of the first k events as it will always be possible to renumber the events in such a way that the events we wish to consider will be the first k in the new numbering system.) Let this probability be denoted as $p_{1,\,k}$. We have then immediately that

$$p_{1,\,2} = p_1 + p_2 - p_1p_2 = 1 - (1 - p_1)(1 - p_2)$$

$$p_{1,\,3} = p_3 + p_{1,\,2} - p_3p_{1,\,2} = 1 - (1 - p_1)(1 - p_2)(1 - p_3)$$

and generally

$$p_{1,\,k} = 1 - \prod_{i=1}^{k} (1 - p_i) \tag{1}$$

In particular for $k = n$

$$p_{1,\,n} = 1 - \prod_{i=1}^{n} (1 - p_i) \tag{2}$$

This answers our question but to relate it to formula (4) of Emmons' paper we proceed as follows: we suppose that a volume V is given and let this volume be divided in n cells. The volume of the ith cell will be denoted by ΔV_i, and P_i will be a point in this cell and representing this cell. Each event of our problem can then be associated with a cell in the volume V. The probability that the ith event occurs becomes in this new situation the probability that the event in the ith cell occurs and we write $g(P_i)\Delta V_i$ instead of p_i. If we put

$$B_k = \prod_{i=1}^{k} (1 - p_i)$$

this expression becomes in the new notation

$$B_k = \prod_{i=1}^{k} \left\{1 - g(P_i)\Delta V_i\right\} = \exp\left\{\sum_{i=1}^{k} \ln\left[1 - g(P_i)\Delta V_i\right]\right\}$$

Remembering that

$$\ln\left\{1 - g(P_i)\Delta V_i\right\} = -\sum_{m=1}^{\infty} \frac{[g(P_i)\Delta V_i]^m}{m}$$

we have

$$B_k = \exp\sum_{i=1}^{k}\left\{-\sum_{m=1}^{\infty}\frac{[g(P_i)\Delta V_i]^m}{m}\right\}$$

and in particular

$$p_{1,\,n} = 1 - \exp\sum_{i=1}^{n}\left\{-\sum_{m=1}^{\infty}\frac{[g(P_i)\Delta V_i]^m}{m}\right\} \tag{3}$$

We suppose now that the number of cells in V increases indefinitely in such a way that each of the ΔV_i's becomes smaller and smaller. The second and higher terms in the series for the logarithm can then be neglected compared to the first term as they are of second or higher order of smallness in the infinitesimal ΔV_i, while the $\sum_{i=1}^{n}$ becomes an integral over V.

When we further associate a point P with V and write $f(P)$ instead of $p_{1,\,n}$ for the probability that at least one event occurs in V, we finally obtain the relation

$$f(P) = 1 - \exp\left\{-\int_V g(P_0)\,dV_0\right\} \tag{4}$$

which is formula (4) in the paper of Emmons. The volume V associated with P is the volume of the backward cone of P as described in the paper.

It is now easy to construct the analogues of the other formulas obtained by Emmons. When we introduce ν_m defined by

$$\nu_m = p_{1,\,m+1} - p_{1,\,m}$$

it follows immediately from Eq. (1) that

$$\nu_m = p_{m+1}\prod_{i=1}^{m}(1 - p_i) \tag{5}$$

Further we rewrite Eq. (1) in the form

$$\prod_{i=1}^{m}(1 - p_i) = 1 - p_{1,\,m} = 1 - p_1 + p_1 - p_{1,\,2} + p_{1,\,2} \cdots - p_{1,\,m-1} + p_{1,\,m-1} - p_{1,\,m}$$

$$= 1 - p_1 - \sum_{i=1}^{m-1}\nu_i$$

Substitution of this expression in Eq. (5) gives

$$\nu_m = p_{m+1}\left(1 - p_1 - \sum_{i=1}^{m-1}\nu_i\right) \tag{6}$$

The ν_m corresponds to the $\Psi(PP_0)\,dV_0$ while our Eq. (5) is easily reduced to a form similar to (A13) if we use the expression developed for B_k. Finally our Eq. (6) corresponds to the integral equation (2) in the Emmons paper.

Reference

[1] Emmons, H. W., *The Laminar-Turbulent Transition in a Boundary Layer—Part I*, Journal of the Aeronautical Sciences, Vol. 18, No. 7, pp. 490–498, July, 1951.

A Simplified Expression for the Dihedral Effect of a Flexible Wing

W. P. Rodden
Assistant Engineer, Missiles Division, The RAND Corporation, Santa Monica, Calif.

March 14, 1955

Symbols

α	=	local angle of attack, rad.
β	=	angle of sideslip, rad.
Γ	=	local dihedral angle, rad.
y	=	wing spanwise coordinate, ft
z	=	wing deflection, ft.
b	=	wing span, ft.
L_w	=	wing lift, lbs.
W	=	airplane gross weight, lbs.
n_z	=	airplane normal load factor
k	=	wing tip spring constant, ft./lb.
p	=	rolling angular velocity, rad. per sec.
V	=	airplane velocity, ft. per sec.
C_l	=	rolling moment coefficient
C_{lp}	=	$\partial C_l/\partial(pb/2V)$
$C_{l\beta}$	=	$\partial C_l/\partial\beta$

Subscripts

$(\ )_a$	=	rigid
$(\ )_f$	=	flexible
$(\ )_t$	=	wing tip

Discussion

By making two reasonable approximations a variation of sideslip rolling moment coefficient with load factor can be obtained for an airplane. The first approximation is to replace the wing normal load factor by the airplane normal load factor; the second is to assume the wing deflection mode to be parabolic.

The local angle of attack of a sideslipping wing with variable dihedral is

$$\alpha = \beta\Gamma \tag{1}$$

where $\Gamma = \Gamma_o + \Gamma_f$. Assuming a parabolic deflection mode

$$z = z_t\,(2y/b)^2 \tag{2}$$

and the tip deflection, which is proportional to the wing lift, can be written

$$z_t = kL_w \cong kWn_z$$

if k is defined as a spring constant depending on the wing rigidity and spanwise lift distribution.

The variation in dihedral becomes

$$\Gamma_f = dz/dy = 8z_t(y/b^2) = 8(kW/b^2)n_zy \tag{3}$$

The deviation of the local angle of attack from the rigid condition then is

$$\Delta\alpha = \beta\,\Gamma_f = 8(kW/b^2)n_z\beta y \tag{4}$$

This is of the same form as the spanwise angle of attack variation in roll where

$$\alpha = py/V \tag{5}$$

For this reason

$$C_{lp} = \frac{\partial C_l}{\partial(pb/2V)} = \frac{\partial C_l}{\partial[(4kW/b)n_z\beta]} = \frac{b}{4kWn_z}\,\Delta C_{l_\beta} \tag{6}$$

Therefore

$$\Delta C_{l_\beta} = (4kW/b)n_z C_{lp} \tag{7}$$

and

$$C_{l_\beta} = (C_{l_\beta})_0 + \Delta C_{l_\beta} \tag{8}$$

This expression shows the dependence of the dihedral effect on the gross weight and the normal load factor. It allows a simple correction to wind-tunnel data from rigid models and also offers a convenient estimate of dihedral effect in the preliminary design stage since spring constants can be readily calculated from estimated rigidities and the Schrenk approximation to the lift distribution and variations of C_{lp} with plan form and Mach Number are given in the literature. The author has obtained good correlation of this theory with some Douglas El Segundo low-speed wind-tunnel tests of a flexible model.

Some Static Aeroelastic Design Considerations Relating to Flap-Type Control Surfaces

Martin Zlotnick
Aerodynamicist, Aerophysics Section, Republic Aviation Corporation
March 10, 1955

ALTHOUGH METHODS FOR CALCULATING the aeroelastic loading of flap-type control surfaces have appeared in the literature, the author is not aware of any published paper that considers the flapped surface and the main surface to be independently flexible. The assumption usually made in aeroelastic analysis is that the angle between the flap surface and the main surface (the angle of deflection, δ) remains constant spanwise. Such an assumption is completely valid where the control surface actuators are not sensitive to load and are distributed along the span. However, where the control surface is actuated at one end of a torsion bar, the assumption of constant δ is invalid and could, of course, yield completely misleading results. In the following, some qualitative results from a series of recent aeroelastic calculations are discussed, and the condensed derivation of the aeroelastic equation for the independently flexible control surface is given. The latter is quite straightforward and is included on account of its previous omission in the literature.

The aeroelastic equation is derived from the relations between (1) the applied aerodynamic load and the resulting streamwise change in angular displacement due to flexibility, (2) the streamwise angular displacement and the resulting aerodynamic load, and (3) the angular displacement at equilibrium and the initial displacement.

If α_s and δ_s are the streamwise angular displacements on the main surface and flap, respectively, due to the equilibrium aerodynamic load while l_m/q and l_f/q are the equilibrium loadings on these surfaces, then relations (1) are

$$\left.\begin{aligned}\alpha_s &= qS_{mm}{}^{\mathrm{I}}\frac{l_m{}^{\mathrm{I}}}{q} + qS_{mm}{}^{\mathrm{II}}\frac{l_m{}^{\mathrm{II}}}{q} + qS_{mf}{}^{\mathrm{I}}\frac{l_f{}^{\mathrm{I}}}{q} + qS_{mf}{}^{\mathrm{II}}\frac{l_f{}^{\mathrm{II}}}{q}\\ \delta_s &= qS_{fm}{}^{\mathrm{I}}\frac{l_m{}^{\mathrm{I}}}{q} + qS_{fm}{}^{\mathrm{II}}\frac{l_m{}^{\mathrm{II}}}{q} + qS_{ff}{}^{\mathrm{I}}\frac{l_f{}^{\mathrm{I}}}{q} + qS_{ff}{}^{\mathrm{II}}\frac{l_f{}^{\mathrm{II}}}{q}\end{aligned}\right\} \tag{1}$$

where the superscript I denotes a loading due to α and II a loading due to δ, where S denotes the appropriate matrix of structural influence coefficients, and where the first subscript indicates the affected surface and the second the affecting surface. The subscript m refers to the main surface and f refers to the flap.

Relations (2) are

$$\left.\begin{aligned}\frac{l_m{}^{\mathrm{I}}}{q} &= A_{mm}\alpha \qquad \frac{l_m{}^{\mathrm{II}}}{q} = A_{mf}\,\delta\\ \frac{l_f{}^{\mathrm{I}}}{q} &= A_{fm}\alpha \qquad \frac{l_f{}^{\mathrm{II}}}{q} = A_{ff}\,\delta\end{aligned}\right\} \tag{2}$$

where A denotes the appropriate matrix of aerodynamic influence coefficients and where α and δ represent the equilibrium angular displacements of the main surface and flap, respectively. Relations (3) are simply

$$\alpha = \alpha_0 + \alpha_s \qquad \delta = \delta_0 + \delta_s - \alpha_s \tag{3}$$

where α_0 and δ_0 are the initial angular displacements.

These relations can be combined and expressed as a pair of simultaneous matrix equations or as a single partitioned matrix equation for α and δ in terms of α_0 and δ_0 as follows:

$$\left[\left[I\right] - q\left[\begin{array}{c|c} S_{mm}{}^{\mathrm{I}}A_{mm} + S_{mf}{}^{\mathrm{I}}A_{fm} & S_{mm}{}^{\mathrm{II}}A_{mf} + S_{mf}{}^{\mathrm{II}}A_{ff} \\ \hline S_{fm}{}^{\mathrm{I}}A_{mm} + S_{ff}{}^{\mathrm{I}}A_{fm} - I & S_{fm}{}^{\mathrm{II}}A_{mf} + S_{ff}{}^{\mathrm{II}}A_{ff} \end{array}\right]\right]\left\{\begin{array}{c}\alpha\\ \delta\end{array}\right\} = \left\{\begin{array}{c}\alpha_0\\ \delta_0 + \alpha_0\end{array}\right\} \tag{4}$$

where I denotes the unit matrix.

The structural influence coefficients giving the flap deflection due to a load applied to the main surface (the S_{fm} matrices) will not always be available from the usual stress analysis. A valid assumption for most practical configurations where the main surface is rigid compared to the flap and the loads are applied near the elastic axis of the main surface is that δ_s is due only to aerodynamic torsion loads on the flap. This restriction implies that the flap will act as a rigid extension to the main surface when the main surface is under load. Under these conditions

$$S_{fm}{}^{\mathrm{I}}\frac{l_m{}^{\mathrm{I}}}{q} + S_{fm}{}^{\mathrm{II}}\frac{l_m{}^{\mathrm{II}}}{q} = \alpha_s$$

That is, the flap deflection due to loads on the main surface is equal to the main surface deflection. Eq. 4 may then be rewritten

$$\left[\left[I\right] - q\left[\begin{array}{c:c} S_{mm}{}^{\mathrm{I}}A_{mm} + S_{mf}{}^{\mathrm{I}}A_{fm} & S_{mm}{}^{\mathrm{II}}A_{mf} + S_{mf}{}^{\mathrm{II}}A_{ff} \\ \hdashline S_{ff}{}'^{\mathrm{I}}A_{fm} & S_{ff}{}'^{\mathrm{II}}A_{ff} \end{array}\right]\right]\left\{\begin{array}{c}\alpha\\ \delta\end{array}\right\} = \left\{\begin{array}{c}\alpha_0\\ \delta_0\end{array}\right\} \tag{5}$$

where the primes on the S_{ff} matrices indicate that they represent flap deflections due only to the aerodynamic torsion loads.

It might be expected that if the independent flexibility of the flap were neglected, the total load on both surfaces would be unaffected because of compensating effects—that is, neglecting the flap torsion would impose more load on the main surface and result in a greater loss in lift on the main surface but none on the flap, whereas including the flap torsion would give a greater loss in lift on the flap but a smaller loss on the main surface. Certainly this could be the case for some configurations, although the correct estimate of the distribution of load would depend on the correct assumptions in all cases.

However, the calculations made for practical configurations do not always show this trend. It was found that the effectiveness factor due to δ, $\eta_{N\delta} = (C_{N\delta})_{\text{flexible}}/(C_{N\delta})_{\text{rigid}}$ as computed on the assumption of independent flexibility was on the order of half that computed on the basis of constant δ for some configurations. The results based on the constant δ computation may lead to the conclusion that the control is satisfactory when in fact it is not. It may be noted here, however, that the parameter $\eta_{N\alpha}$ was practically unaffected by the flexibility of the flap.

It would be worth while to make a series of calculations to determine if there is a ratio of (GJ) of the flap to (GJ) of the main surface when the independently flexible flap would give about the same effectiveness as the constant δ flap for a given range of dynamic pressure. This would indicate the circumstances under which distributed actuators could be dispensed with in favor of the simpler design involving a single actuator and a torsion bar. A single actuator with a torsion bar might also be favorable if the main object is to delay aeroelastic reversal at high dynamic pressures where only relatively small effectiveness is required. It is possible, however, that the most favorable design where high aeroelastic effectiveness is a critical factor will be with actuators distributed spanwise.

In considering the effectiveness of an independently flexible flap-type control surface, the parameter, $\eta_{N\delta}$, is of primary importance as a "figure of merit" only when the flap is actuated by position-sensitive servos. If the airplane is manually controlled or "hinge-moment sensitive" servos are used, the appropriate "figure of merit" would be $\eta_{I\delta} = \eta_{N\delta}/\eta_{H\delta}$ where $\eta_{H\delta}$ is the hinge moment ratio corresponding to $\eta_{N\delta}$. In either case, the factor $\eta_{I\delta}$ is the parameter which corresponds to the normal force available for a given hinge moment and is an aeroelastic parameter of primary importance for the control system design.

On Approximate Solutions for the Compressible Flow Around Oscillating Thin Wings

Marten Landahl, Holt Ashley, and Erik Mollo-Christensen
Massachusetts Institute of Technology, Cambridge, Mass.
March 14, 1955

CONSIDER A THIN WING with root semichord $b = 1$ oscillating in a free stream of velocity $U = 1$ with reduced frequency of $k = \omega b/U$, ω being the circular velocity. The velocity of sound is then $1/M$ and, assuming linearization, the perturbation velocity potential of the flow, $\Phi(x, y, z, t) = \varphi(x, y, z)e^{i\omega t}$, follows the equation

$$(1 - M^2)\varphi_{xx} + \varphi_{yy} + \varphi_{zz} - 2kiM^2\varphi_x + M^2k^2\varphi = 0 \tag{1}$$

The boundary condition to be fulfilled on the wing is

$$\varphi_z(x, y, 0) = \bar{h}_x(x, y) + ik\bar{h}(x, y) = i\bar{w}(x, y) \tag{2}$$

where the position of the wing mean surface at any instant is defined by

$$z = h(x, y)e^{i\omega t} \tag{3}$$

The pressure difference across the wing is given by

$$\frac{\Delta p}{q} = -4(\varphi_x + ik\varphi)e^{i\omega t} \tag{4}$$

Exact solutions of Eq. (1) can only be obtained in special cases such as the two-dimensional supersonic case. However, by neglecting one or several terms in Eq. (1), simple solutions can be obtained. Three particular approximations will be discussed here, applicable for different ranges of k and M as indicated below:

$$-M^2\varphi_{xx} + \varphi_{yy} + \varphi_{zz} - 2kiM^2\varphi_x + k^2M^2\varphi = 0 \tag{5}$$

for

$$M^2 \gg 1 \text{ and/or } k \gg 1$$

$$\varphi_{yy} + \varphi_{zz} - 2kiM^2\varphi_x + k^2M^2\varphi = 0 \tag{6}$$

for

$$k \gg (M - 1)$$

$$\varphi_{yy} + \varphi_{zz} + k^2M^2\varphi = 0 \qquad \text{for } k \gg 1 \tag{7}$$

It is also necessary in all these cases to impose the condition $(1 - M^2) = 0(M^2)$

The validity of Eq. (5) for $M^2 \gg 1$ is immediately evident by comparison with Eq. (1); the alternative condition for large values of k and supersonic flow was established by Hjelte[1] using the Laplace transformation. Simple solutions of Eq. (5) are possible to obtain by introducing

$$\varphi = \psi e^{-ikx} \tag{8}$$

giving

$$-M^2\psi_{xx} + \psi_{yy} + \psi_{zz} = 0 \tag{9}$$

Lomax, Heaslet, and Fuller[2] also used a corresponding approximation for treating indicial problems.

Eq. (6) has been applied for a small aspect ratio delta wing in reference 3. Eq. (7) was treated in reference 4.

An easy way to estimate the errors involved in the different approximations is to calculate the two-dimensional case where the φ_{yy} term drops out; it is then readily shown that Eqs. (2), (3), (8) and (9) lead to the remarkably simple solution

$$\Delta p/q = -[4\ \bar{w}(x)/M]e^{i\omega t} \tag{10}$$

The result agrees with that of Lighthill[5] for a wing of zero thickness and constitutes, in fact, the linearized counterpart of the "piston theory," numerical results of which were given by two of the authors.[6] Although Table 1 of reference 6 is correct, the derivation of "piston theory" given there is superseded by the one in the present paper, which is more satisfactory in every respect and involves less restrictions on the sizes of the parameters.

The solution of Eq. (6) can directly be obtained from the $M = 1$ solution by means of a simple transformation.

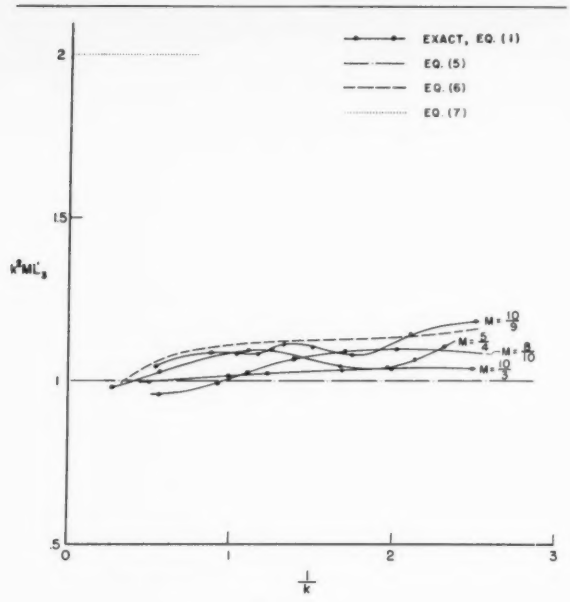

FIG. 1.

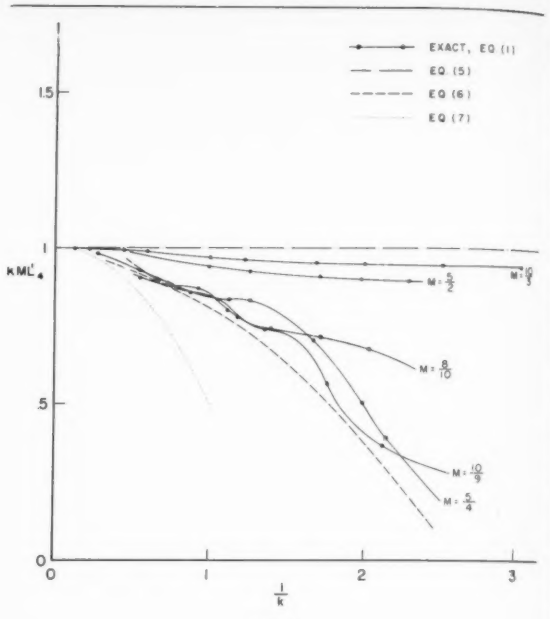

FIG. 2.

Eq. (7) gives the one-dimensional acoustic theory. Retaining for comparison all terms in the boundary condition, Eq. (2), and the pressure coefficient, Eq. (4), the result reads

$$\frac{\Delta p}{q} = -4\left(\frac{\bar{w}_x + ik\bar{w}}{ikM}\right)e^{i\omega t} \tag{11}$$

For high reduced frequencies the result thus approaches that of Eq. (10).

To illustrate the ranges of validity of the various theories, the coefficients L_3' and L_4' (defined by Garrick and Rubinow[7] as the real and imaginary parts of the dimensionless lift on an airfoil oscillating about its leading edge) have been calculated according to the above results and are plotted in Figs. 1 and 2.

It is seen from the graphs that for flutter, where usually $1/k = 0(1)$, the transonic approximation could probably be used in the range, $M = 0.9 - 1.25$. The piston theory seems adequate for $M > 2.5$. For high frequency flutter, any of the theories can be used. The one-dimensional acoustic theory, however, requires the frequency to be very high. Eq. (7) leads to much more accurate solutions in the three-dimensional case when the aspect ratio is sufficiently small (cf. reference 4).

As an amplification of the numerical results presented in reference 6, it is worth noting that "piston theory" formulas like Eq. (10) are proving most useful in dealing with complicated high-speed aeroelastic problems. For example, the supersonic bending-torsion flutter calculation performed by Garrick and Rubinow[7] with considerable numerical labor reduces, in the most general case, to evaluation of a single radical. In the special circumstances when the bending-torsion frequency ratio is small and the wing center of gravity does not lie too close to the mid-chord line, the expression for reduced flutter speed reads

$$\frac{v_F}{b\omega_\alpha} \cong \sqrt{\mu M r_\alpha^2}\sqrt{\frac{(x_\alpha + a)^2 + (1/3)}{(x_\alpha + a)\left[(x_\alpha + a)^2 + r^2_\alpha - x^2_\alpha + (1/3)\right]}} \tag{12}$$

(The notation here is that of ref. 7 and is familiar to aeroelasticians.) Calculations by Eq. (12) reproduce curves like those in Figs. 17 and 18 of reference 7 to an accuracy of better than 10 per cent above $M = 2.5$. The asymptotic behavior for large values of the Mach Number is, of course, exact.

REFERENCES

[1] Hjelte, F., *Methods for Calculating Pressure Distributions on Oscillating Wings of Delta Type at Supersonic and Transonic Flow*, Swedish K.T.H. AERO T.N. 39 (to be published).

[2] Lomax, H., Heaslet, M. A., Fuller, F. B., and Sluder, L., *Two- and Three-Dimensional Unsteady Lift Problems in High-Speed Flight*, NACA Rept. 1077, 1952.

[3] Landahl, M. T., *The Flow Around Oscillating Low Aspect Ratio Wings at Transonic Speeds*, Swedish K.T.H. AERO T.N. 40, 1954.

[4] Merbt, H., and Landahl, M. T., *Aerodynamic Forces on Oscillating Low Aspect Ratio Wings in Compressible Flow*, Swedish K.T.H. AERO T.N. 30, 1953.

[5] Lighthill, M. J., *Oscillating Airfoils at High Mach Number*, Journal of the Aeronautical Sciences, Vol. 20, No. 6, pp. 402–407, June, 1953.

[6] Mollo-Christensen, E., and Ashley, H., *Applicability of Piston Theory to the Flow Around Wings in Unsteady Motion*, Journal of the Aeronautical Sciences, Vol. 27, No. 11, pp. 779–780, November, 1954.

[7] Garrick, I. E., and Rubinow, S. J., *Flutter and Oscillating Air-Force Calculations for an Airfoil in Two-Dimensional Supersonic Flow*, NACA Rept. 846, 1946.

[8] Nelson, H. C., and Berman, J. H., *Calculations on the Forces and Moments for an Oscillating Wing-Aileron Combination in Two-Dimensional Potential Flow at Sonic Speed*, NACA TN 2590, 1952.

[9] Anonymous, *Tables of Aerodynamic Coefficients for an Oscillating Wing-Flap System in a Subsonic Compressible Flow*, N.L.L., Amsterdam, Rept. F. 151, 1954.

A Remark on "A Simple Laminar Boundary Layer with Secondary Flow"

M. Z. v. Krzywoblocki
Professor, Department of Aeronautical Engineering, University of Illinois, Urbana, Ill.

March 15, 1955

IN REFERENCE 1 Loos talks about an exact solution of the boundary-layer equations. This probably refers to the Blasius solution as well, which is cited in the text. Let me mention that with the usually assumed boundary conditions we cannot talk in the present state of available mathematical tools about exact solutions of the boundary-layer equations. It is possible that there exists no solution at all and that the so-called solutions of the boundary-layer equations represent something which cannot be judged by mathematics in its present state, or that there exist more than one solution, perhaps even the whole family of solutions. Moreover, H. Weyl, Oudart and Ostrowsky have shown that the Blasius solution breaks down at a certain

point. All these things are too complicated to be discussed in an engineering journal, but I may refer the reader to my papers on that subject published in recent years in various mathematical and scientific journals.

Reference

[1] Loos, H. G., *A Simple Laminar Boundary Layer with Secondary Flow*, Journal of the Aeronautical Sciences, Vol. 22, No. 1, pp. 35–40, January, 1955.

A Short Cut in Computing Product of Inertia

Kenneth G. Merriam
Professor of Aeromechanics, Worcester Polytechnic Institute, Worcester, Mass.
March 17, 1955

In published properties of structural sections, it is customary to include values of I_x, I_y, and I_{min}, from which one can compute I_{max} using the well-known relationship

$$I_{max} + I_{min} = I_x + I_y$$

From the geometric properties of the inertia circle, it is not difficult to show that

$$(I_{xy})^2 = I_x I_y - I_{max} I_{min}$$

Using the two relationships, the calculation of I_{xy}, from known values of I_x, I_y, and I_{min}, becomes a simple operation.

Interaction Equation for the Buckling of Unstiffened Cylinders Under Combined Bending, Torsion, and Internal Pressure

Bertram Klein
Research Engineer, Los Angeles, Calif.
March 16, 1955

Frequently it is necessary to determine margins of safety for unstiffened cylinders under combined loadings in the presence of internal pressure. The cases of compression and internal pressure[1] and torsion and internal pressure[2] have been considered. Also previously treated is the case of bending and torsion without pressure.[3] It is the purpose of this note to show how to treat the case of simultaneous action of bending, torsion, and internal pressure.

The proposed interaction equation for buckling is:

$$R_b^2 + R_s^2 = R_p(1 - R_b^2) + 1$$

where

$$R_b = \sigma/(\sigma_{cr})_p \qquad R_s = \tau/(\tau_{cr})_0 \qquad R_p = p/p_{cr}$$

and

- σ = applied extreme fiber compressive stress including effect of internal pressure
- $(\sigma_{cr})_p$ = allowable extreme fiber compressive stress for bending in the presence of internal pressure
- τ = applied shear stress
- $(\tau_{cr})_0$ = allowable shear stress without pressure
- p = internal pressure
- p_{cr} = allowable external hydrostatic pressure

This interaction equation reduces to the above mentioned results when the proper quantities are set equal to zero. Furthermore, the shapes of the interaction curves plotted in Fig. 1 are what one expects for this type of problem.

In conclusion, it must be remembered to check for possible fracture under combined stress at the extreme tensile fibers of the cylinder whenever internal pressure is present.

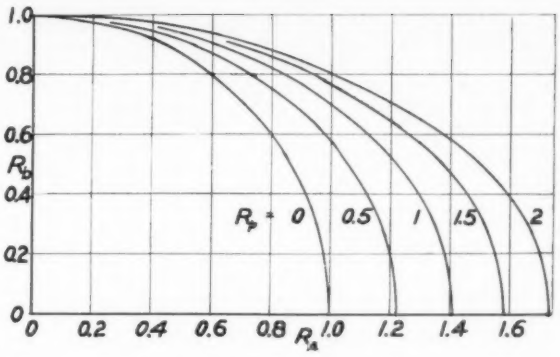

Fig. 1. Interaction curves for the buckling of unstiffened cylinders under combined bending, torsion, and internal pressure.

References

[1] Lo, H., Crate, H., and Schwartz, B. E., *Buckling of Thin-walled Cylinders Under Axial Compression and Internal Pressure*, NACA TN 1027, 1951.

[2] Crate, M., Batdorf, S. B., and Baab, G. W., *The Effect of Internal Pressure on the Buckling of Thin-walled Circular Cylinders under Torsion*, NACA ARR NO. L4 E 27, May, 1944.

[3] Bruhn, E. F., *Tests on Thin-walled Celluloid Cylinders to Determine Interaction Curves under Combined Bending, Torsion, and Compression or Tension Loads*, NACA TN 951, 1945.

The Effect of Axial Flow in a Burner on Combustion Oscillation Frequencies

R. T. Newton and J. C. Truman*
Small Aircraft Engine Department, General Electric Company, Lynn, Mass., and Aeronautical Engineering Department, USAF Institute of Technology, Wright-Patterson Air Force Base, Ohio, Respectively
March 21, 1955

Certain types of combustion oscillations are found to have frequencies equal to resonant frequencies of the gas in the combustion chamber. It was shown in a previous note[1] that the effect of an axial flow through the chamber is to decrease the longitudinal resonant frequency by a factor $(1 - M^2)$; that is,

$$f_L = f_{L_0}(1 - M^2) \qquad (1)$$

where

- f_L = longitudinal resonant frequency of the gas in the chamber, cycles per sec.
- f_{L_0} = longitudinal resonant frequency of the gas in the chamber for $M = 0$, cycles per sec.
- M = average Mach Number of the axial flow

To examine the effect of axial flow on transverse resonant frequencies, a result obtained by Woolston and Runyan[2] may be employed. In considering a wing oscillating in a subsonic compressible flow of Mach Number M in a tunnel of circular test section, they have shown that the transverse resonant frequencies are given by

$$f_T = (c\alpha_{mn}/\pi D)\sqrt{1 - M^2} \qquad (2)$$

where

- f_T = transverse resonant frequency of the gas in the tunnel (or chamber), cycles per sec.
- c = velocity of sound
- D = tunnel (or chamber) diameter
- α_{mn} = characteristic numbers for Bessel functions

* Now, Small Aircraft Engine Department, General Electric Company, Lynn, Mass.

Eq. (2) may be written in a form analogous to that of Eq. (1), as

$$f_T = f_{T_0}\sqrt{1 - M^2} \tag{3}$$

where, again, the subscript zero denotes the condition $M = 0$. Eq. (3) also follows if one considers the axial and transverse velocity components of a pressure wave transmitted by a signal source located on the axis. This approach is noted by Runyan and Watkins.[3]

These results are based on the assumption that the Mach Number of the axial flow is constant. In most combustion systems, Mach Number varies significantly throughout the burner, both along the axis and in a transverse plane. The accuracy of these results, applied to a given burner, may therefore be questionable, although, qualitatively, one would expect the predicted reductions in frequencies to occur.

References

[1] Truman, J. C., and Lipstein, N. J., *A Note on Organ-Pipe Resonance in Ducted Burners*, Journal of the Aeronautical Sciences, Vol. 20, No. 12, pp. 846–847, December, 1953.

[2] Woolston, Donald S., and Runyan, Harry L., *Some Considerations on the Air Forces on a Wing Oscillating Between Two Walls for Subsonic Compressible Flow*, Journal of the Aeronautical Sciences, Vol. 22, No. 1, pp. 41–50, January, 1955.

[3] Runyan, Harry L., and Watkins, Charles E., *Considerations on the Effect of Wind-Tunnel Walls on Oscillating Air Forces for Two-Dimensional Subsonic Compressible Flow*, NACA TN 2552, December, 1951.

Note on the Compressible Laminar Boundary Layer with Heat Transfer and Pressure Gradient

Eli Reshotko and Clarence B. Cohen
Lewis Flight Propulsion Laboratory, NACA, Cleveland, Ohio

March 16, 1955

Symbols

f'	=	ratio of velocity within the boundary layer to local external velocity
$g'(0)$	=	wall temperature gradient parameter
M	=	Mach Number
Nu	=	Nusselt Number, $Nu = x(\partial T/\partial y)_w/T_{aw} - T_w$
Re_w	=	Reynolds Number based on wall fluid properties
T_{aw}	=	adiabatic wall temperature
T_s	=	stagnation temperature
T_{s_1}	=	free-stream stagnation temperature
T_w	=	wall temperature
β	=	pressure gradient parameter
η	=	boundary layer similarity variable
σ	=	Prandtl Number

Discussion

LEVY[1] POINTS OUT ON THE BASIS of approximate calculations that for a Prandtl Number (σ) different than one, there is a Mach Number effect on the heat-transfer parameter $[-g'(0)] \div [(T_w/T_{s_1}) - 1]$. However, Levy's approximate calculations seem to be even qualitatively inaccurate. Reproduced here (Fig. 1) is Fig. 13 of Levy's paper on which are also indicated a number of exact solutions to Eqs. (14) and (18) of reference 1 obtained by the writers using an IBM Card-Programmed Calculating machine. The fact that the quantity $g'(0)/[(T_w/T_{s_1}) - 1]$ indicated by Levy for $M \to \infty$, $\sigma = 0.7$ is finite through the value $T_w/T_{s_1} = 1$ requires a recovery factor of one. The exact solutions obtained by the present writers for $T_w/T_{s_1} = 1$ show that $g'(0) \neq 0$ for this case, thus $g'(0)/[(T_w/T_{s_1}) - 1]$ is infinite. However, for $M \to \infty$, $g'(0)$ is zero when $T_w/T_{s_1} = 0.80$ and for $M = \sqrt{5}$, $g'(0)$ is zero when $T_w/T_{s_1} = 0.90$, corresponding in both cases to recovery factors of 0.80. For cases where $T_{aw} \neq T_{s_1}(\sigma \neq 1, M \neq 0)$ the heat transfer quantity related to $Nu \div \sqrt{Re_w}$ would be $[-g'(0)]/[(T_w/T_{s_1}) - (T_{aw}/T_{s_1})]$. The present solutions for $M = \infty$ and $M = \sqrt{5}$ as well as solutions for

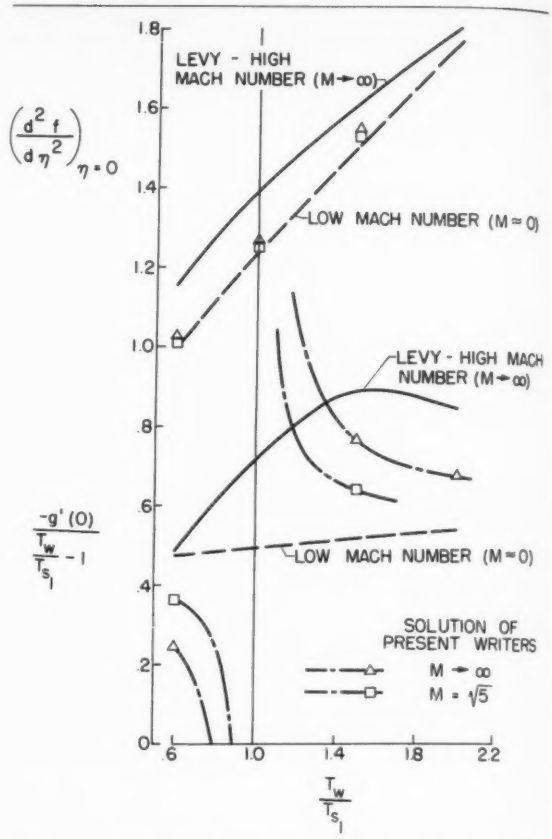

FIG. 1. Effect of Mach Number on shear and heat-transfer functions for $\beta = 1$, Prandtl Number = 0.7.

$M = 0$ are plotted in Fig. 2 in terms of this suggested parameter. It is seen from Fig. 2 that the additional term in Eq. (18) of reference 1 contributes only slightly to the heat-transfer parameter when referred to the adiabatic wall temperature. Furthermore, the values for $M = 0$, $\sigma = 0.7$ are easily obtained from Prandtl Number one solutions (arbitrary Mach Number) as discussed in reference 2. Thus the correction for Prandtl Number which is used for low-speed flows appears to be adequate for high-speed flows.

In reference 1, Levy has briefly commented on the uniqueness of the solutions. Some further details may be of general interest. Eqs. (14) and (17) of reference 1 have been solved by digital calculation for $\sigma = 1$ by the writers and the results have been tabulated.[3] For adverse pressure gradients a lack of uniqueness has been observed. Previously, Hartree[4] also observed for constant fluid properties that the boundary conditions: $f(0) = f'(0) = 0$, $f'(\infty) = 1$ are not sufficient to determine a unique solution in the region $\beta < 0$. That is, there are an infinite number of values of the shear function at the wall, f_w'', for a given pressure gradient parameter, β. Some of the properties of these solutions can be related to the coefficients in the following expression for velocity ratio valid for large η with $Pr = 1$:

$$f' = 1 + [\alpha_1(\eta - \kappa)^{-(2\beta+1)} + (\alpha_1/2)(\eta - \kappa)^{-1}] \times \exp\{-[(\eta - \kappa)^2/2]\} + \alpha_2(\eta - \kappa)^{2\beta} \tag{1}$$

Here f' is the ratio of velocity within the boundary layer to the local external velocity, α_1, α_2 and κ are arbitrary integration constants and α_3 is an integration constant related to the distribution of stagnation enthalpy in the asymptotic region through the relation

$$T_s/T_{s_1} = 1 + \alpha_3(\eta - \kappa)^{-1} \exp\{-[(\eta - \kappa)^2/2]\} \tag{2}$$

For $\beta > 0$ (favorable pressure gradient) α_2 is necessarily zero in

order to satisfy the boundary condition $f'(\infty) = 1$. A unique solution results under these circumstances. For $\beta < 0$, α_2 is chosen as zero to avoid infinite values of displacement thickness (related to the integral $\int_0^\infty (1 - f')d\eta$). However, in solving the equations for adverse pressure gradients with $\alpha_2 = 0$, *two* solutions with finite displacement thickness still remain. These correspond to the maximum and minimum values of wall shear obtainable without incurring velocities within the boundary layer in excess of the free-stream velocity. For Hartree's problem ($T_w/T_{s_1} = 1$), T_s/T_{s_1} is identically unity so that α_3 is identically zero. Hartree[4] presented the maximum wall shear solutions. The minimum wall shear solutions for this problem have a negative shear at the wall (further details are given in reference 3).

The phenomenon of velocity ratios in excess of unity in the outer portion of the boundary layer has been termed "velocity overshoot" in reference 3. Two distinct types of velocity overshoot are possible. The first of these occurs when $\alpha_2 \neq 0$ (and $\beta < 0$) and therefore must be excluded. The second occurs in favorable pressure gradient flow over heated surfaces. The existence of this type of velocity overshoot can be demonstrated analytically. For favorable pressure gradients, ($\beta > 0$) with α_2 set equal to zero as previously mentioned, the α_3 term in Eq. 1 is dominant for large η. Thus $(f' - 1)$ and α_3 are of the same sign. Hence for a heated wall (α_3 positive, Eq. 2), the velocity ratio must approach unity from above. This excess velocity is associated with the acceleration of a layer of fluid in the outer portion of the boundary layer with density less than the external density. Since this layer is subject to the external pressure field and is restrained only slightly by the viscous forces acting on it, it is accelerated more than the external flow. This velocity overshoot may in certain circumstances be large enough to produce negative momentum thicknesses. This is completely unrelated to the phenomenon of negative displacement thickness discussed in reference 2. The displacement thickness can become negative for large rates of cooling with favorable pressure gradient because of the high density within the lower portions of the cooled boundary layer.

With regard to the integral technique for the calculation of laminar boundary layers proposed in reference 1, it is surprising that it does not agree with Rott and Crabtree.[5] The integral technique devised by the present writers for compressible laminar boundary layer with heat transfer and pressure gradient[2] does reduce to that of Rott and Crabtree for the insulated surface.

References

[1] Levy, Solomon, *Effect of Large Temperature Changes (Including Viscous Heating) upon Laminar Boundary Layers with Variable Free-Stream Velocity*, Journal of the Aeronautical Sciences, Vol. 21, No. 7, pp. 459–474, July, 1954.

[2] Cohen, Clarence B., and Reshotko, Eli, *The Compressible Laminar Boundary Layer with Heat Transfer and Arbitrary Pressure Gradient*, NACA TN 3326, 1955.

[3] Cohen, Clarence B., and Reshotko, Eli, *Similar Solutions for the Compressible Laminar Boundary Layer with Heat Transfer and Pressure Gradient*, NACA TN 3325, 1955.

[4] Hartree, D. R., *On an Equation Occurring in Falkner and Skan's Approximate Treatment of the Equations of the Boundary Layer*, Proc. Cambridge Phil. Soc., Vol. 33, Pt. 2, pp 223–239, April, 1937.

[5] Rott, Nicholas, and Crabtree, L. F., *Simplified Laminar Boundary Layer Calculations for Bodies of Revolution and for Yawed Wings*, Journal of the Aeronautical Sciences, Vol. 19, No. 8, pp. 553–566, August, 1952.

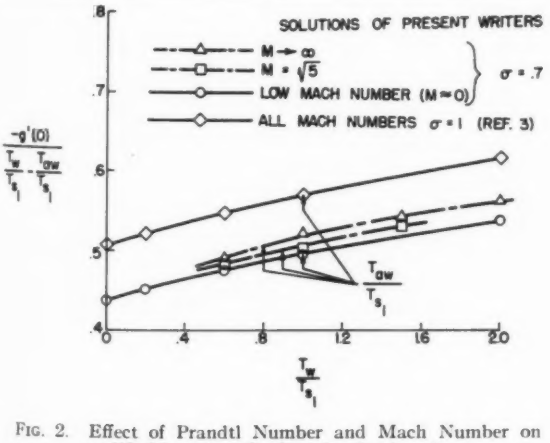

FIG. 2. Effect of Prandtl Number and Mach Number on modified heat-transfer function for $\beta = 1$.

Engineering Relations for Friction and Heat Transfer to Surfaces in High Velocity Flow

E. R. G. Eckert*
Professor of Mechanical Engineering, University of Minnesota

March 23, 1955

Symbols

c_f	=	friction factor
c_p	=	specific heat at constant pressure
h	=	heat-transfer coefficient
i	=	enthalpy
k	=	thermal conductivity
q	=	heat flow per unit area and time
r	=	temperature recovery factor
r_i	=	enthalpy recovery factor
x	=	distance from leading edge
T	=	absolute temperature
V	=	velocity
γ	=	ratio of specific heats at constant pressure and volume
μ	=	viscosity
ρ	=	density
τ	=	shearing stress
Re	=	Reynolds Number
Ma	=	Mach Number
St	=	Stanton Number
Pr	=	Prandtl Number

Subscripts

i	=	based on enthalpy
m	=	maximum
r	=	recovery
s	=	in stream outside boundary layer
w	=	at wall surface
$*$	=	reference condition

Discussion

IN THE DESIGN OF MISSILES for large supersonic Mach Numbers, special consideration must be given to the temperature which the skin of the missile assumes. This requires calculations determining the heat transfer and skin temperature for a considerable number of flight conditions. Such calculations are very time-consuming unless simple relations are available which describe with sufficient accuracy the friction and heat transfer to surfaces in high velocity flow. It has been pointed out previously that values for those parameters calculated with relationships which hold for constant property fluids describe actual conditions in a supersonic boundary layer in many cases satisfactorily when the properties of the fluid are introduced at a proper reference temperature (see references 1, 2). This is in itself surprising because the properties vary for large supersonic velocities extensively throughout the boundary layer. The validity of this procedure, however, has been verified again recently in a survey (see reference 3*) on heat transfer at high velocities in which a relationship for the reference temperature was developed. The introduction of the properties at this reference temperature describes friction factors and heat-transfer coefficients on a flat plate with constant wall temperature in such a way that it agrees

* Permission of the Wright Air Development Center, Air Research and Development Command, USAF, for publication is gratefully acknowledged.

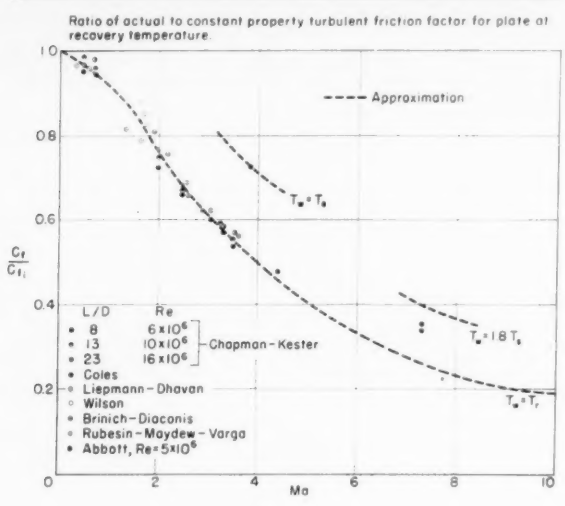

FIG. 1.

within a few per cent with the results of exact boundary-layer solutions for two-dimensional flow in a range of Mach Numbers up to 20, at stream temperatures between 400 and 800°R and wall temperatures between 400 and 2000°R. It also gives very satisfactory agreement with measurements on turbulent boundary layers. As a result of these investigations the following calculation procedure is proposed.

Laminar Boundary Layer

The local heat-transfer coefficient at a distance x from the leading edge for laminar two-dimensional flow with constant velocity over a surface with constant temperature is defined by the following equation:

$$q_w = h(T_r - T_w) \tag{1}$$

when the temperature variation throughout the boundary layer is such that the specific heat c_p in this temperature range can be considered constant. For very large temperature variations throughout the boundary layer which cause the specific heat to vary considerably the heat-transfer coefficient is better based on an enthalpy difference instead of a temperature difference and is defined by an equation proposed by E. Van Driest[6]

$$q_w = h_i(i_r - i_w) \tag{2}$$

The recovery temperature and the recovery enthalpy respectively are determined by the following relations:

$$T_r = T_s + r(V_s^2/2c_p) \tag{3}$$

$$i_r = i_s + r_i(V_s^2/2) \tag{4}$$

The recovery factor appearing in both of the above equations is calculated from the equation

$$r = \sqrt{Pr^*} \tag{5}$$

into which the Prandtl Number has to be introduced at a reference temperature described by the equation

$$T^* = T_s + 0.5(T_w - T_s) + 0.22(T_r - T_s) \tag{6}$$

for constant specific heat or by a reference enthalpy

$$i^* = i_s + 0.5(i_w - i_s) + 0.22(i_r - i_s) \tag{7}$$

for variable specific heat. Both of these equations have been determined by comparisons with exact boundary-layer solutions for air. There are, however, indications that they can be used for other gases as well. The second term in both of these equations can also be expressed by the Mach Number of the flow outside the boundary layer.

$$T^* = T_s + 0.5(T_w - T_s) + 0.22r[(\gamma_s - 1)/2]\,(Ma)^2 T_s \tag{8}$$

$$i^* = i_s + 0.5(i_w - i_s) + 0.22r_i[(\gamma_s - 1)/2]\,(Ma)^2 i_s \tag{9}$$

Recovery factors calculated in this way agree within ± 2½ per cent with the results of exact boundary-layer solutions.[1-6] Eqs. 3 to 9 require an iteration for the calculation of the recovery temperature. This is accomplished easily since the dependence of the Prandtl Number on temperature is only slight.

The local wall shearing stress can be calculated from the following equation:

$$\tau_w = c_f(\rho^* V_s^2/2) \tag{10}$$

with the friction factor given by the relationship

$$c_f = 0.664/\sqrt{Re^*} = 0.664/\sqrt{\rho^* V_s x/\mu^*} \tag{11}$$

The property values ρ and μ are introduced into both of the above equations at a reference temperature which can be calculated from Eq. 6 to 9. A comparison of the results obtained with this procedure with exact boundary-layer solutions (see references 2 to 5) shows agreement within ±4 per cent.

The heat-transfer coefficient appearing in Eqs. 1 and 2 are best calculated from the Stanton Numbers

$$St = h/\rho c_p V_s \tag{12}$$

for constant specific heat or

$$St = h_i/\rho V_s \tag{13}$$

for variable specific heat. The Stanton Numbers are obtained from the relationship

$$St = (c_f/2)\,(Pr^*)^{-(2/3)} \tag{14}$$

into which the Prandtl Number has again to be introduced at the reference temperature given by one of Eqs. 6 to 9. Heat-transfer coefficients calculated in this way agree within ±3 per cent with the result of exact boundary-layer solutions for stream temperatures above 300°R when the same dependence of the properties on temperature is used for the above calculation as for the exact boundary-layer solutions. The procedure used by Van Driest for the solution of the boundary-layer equations leads to an expression for the heat flow at the wall surface which contains a difference between the wall temperature and another value which Van Driest calls generalized recovery enthalpy. The latter value is a function of i_w/i_s and transforms only for $i_w/i_r = 1$ into the enthalpy which an unheated wall assumes. The procedure recommended here takes care of this situation automatically, since the recovery enthalpy calculated for a heat-transfer situation with Eqs. 4, 5 and 7 or 9 agrees with the generalized recovery enthalpy. The main uncertainty in the calculation of recovery factors and heat-transfer coefficients is caused by the insufficient present-day knowledge of Prandtl Numbers for air

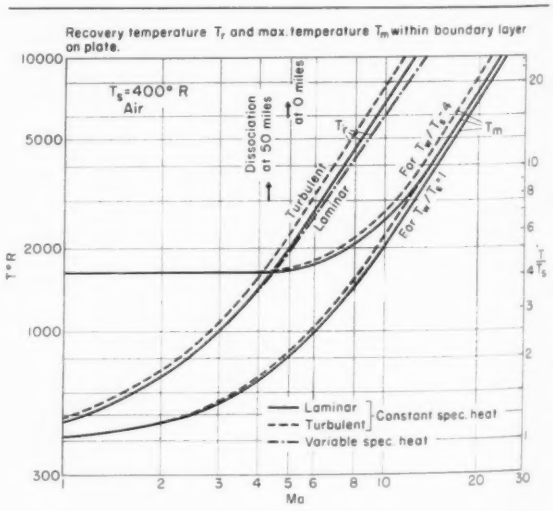

FIG. 2.

at high temperature. Prandtl Numbers as given in the Gas Tables and as recommended by the National Bureau of Standards differ, for instance, at a temperature of 2000°R by 12 per cent and accordingly the recovery factors calculated with those Prandtl Numbers differ by 6 per cent and heat-transfer coefficients by 8 per cent.

Turbulent Boundary Layer

Good agreement with available experimental information is also obtained when the calculation procedure outlined above is used and when appropriate relationships describing friction factor, recovery factor, and heat-transfer coefficient in incompressible turbulent flows are introduced. A relation which is in common use to describe the turbulent friction factor of a flat plate is the equation by Kármán-Schoenherr.[3] Very good agreement with experimental results in the whole Reynolds Number range is also obtained by a relation for the local friction factor which has been published by Schultz Grunow.

$$c_f = 0.370/(\log_{10} Re^*)^{2.584} \tag{15}$$

The temperature or enthalpy recovery factor can be described with good accuracy by the equation

$$r = \sqrt[3]{Pr^*} \tag{16}$$

and the Stanton Number by

$$St = (c_f/2)\,(Pr^*)^{-(2/3)} \tag{17}$$

The last relation has been proposed by A. P. Colburn and seems to be the one which also satisfactorily describes newer experiments for air and generally in a Prandtl Number range not too far away from the value one. A comparison between friction factors determined by the proposed method and values obtained from experiments is shown in Fig. 1. In this figure the ratio of the actual friction factor c_f in a supersonic boundary layer of air to the friction factor c_{fi} for an incompressble fluid is plotted over the Mach Number. The friction factors in the group c_f/c_{fi} are not based on properties at the reference temperature but on the properties at the static temperature in the stream outside the boundary layer, a procedure which is frequently used in the presentation of such data. The points indicate the results of experimental investigations (for references see reference 3) and the dashed lines give the relations obtained from the above described calculation procedure. It can be recognized that very good agreement is obtained not only for the case where the wall is unheated (the wall temperature equal to the recovery temperature) but also for a wall temperature equal to the stream temperature. The two experimental points at a Mach Number 7.2 and for the condition $T_w = 1.8\,T_s$ are somewhat lower than the calculated curve. However, it has been pointed out in the corresponding publication that the accuracy of these tests is not as high as the one for the measurements at Mach Number 3.8 and $T_w = T_s$. Information on heat transfer is more scarce than on friction. There are, however, indications that the recommended procedure describes also the conditions for heat transfer satisfactorily. No experimental information is available at large Mach Numbers, at large temperature differences, and at high temperatures, and the above recommendations have to be considered as tentative for these ranges.

It should be pointed out once more that the relations presented here are restricted to constant pressure along the surface, to two-dimensional flow, and to constant wall temperature. They can be used to obtain information on rotationally symmetric flow when an appropriate transformation is made and also as a basis to calculate friction and heat transfer for a wall temperature which varies along the surface. The relations are also restricted to the condition in which the boundary-layer equations describe friction and heat transfer satisfactorily, especially for conditions where no slip or boundary-layer shock interaction occurs and where the air within the boundary layer is not dissociated as a consequence of high temperatures. The slip condition restricts the relation to flight below approximately 30 miles. The maximum temperature to be expected within the boundary layer can be determined from Fig. 2. From this figure it can also be estimated whether dissociation in the boundary layer will occur. In this figure the maximum temperature T_m within the boundary layer is plotted over the Mach Number for flow along a flat plate. When the surface is not cooled or heated then the recovery temperature is the largest temperature within the boundary layer. Usually the surface temperature of missiles will be kept at lower values either by heat storage in the skin or by radiation. For two temperature conditions the maximum temperature within the boundary layer is also indicated in Fig. 2. It may be observed that for a ratio of the absolute wall temperature T_w to the static temperature in the stream T_s equal to 4 dissociation must not be expected at an altitude of around 50 miles below a Mach Number around 14 and for zero miles altitude for Mach Numbers up to 18. Recent calculations[7, 8] have also indicated that a certain amount of dissociation will not effect heat transfer and friction when the dissociation does not occur in the layers immediately adjacent to the surface. This would indicate that the recommended relations can be used even up to higher Mach Numbers.

References

[1] Rubesin, M. W., and Johnson, H. A., *A Critical Review of Skin-Friction and Heat-Transfer Solutions of the Laminar Boundary Layer of a Flat Plate*, Trans. ASME, Vol. 71, pp. 385–388, 1949.

[2] Young, A. B. W., and Janssen, E., *The Compressible Boundary Layer*, Journal of the Aeronautical Sciences, Vol. 19, pp. 229–236, 288, 1952.

[3] Eckert, E. R. G., *Survey On Heat Transfer at High Speeds*, WADC Tech. Report 54–70, 1954, Wright-Patterson Air Force Base, Ohio.

[4] Klunker, E. B., and McLean, F. E., Laminar Friction and Heat Transfer at Mach Numbers From 1 to 10, NACA TN 2499, 1951.

[5] Klunker, E. B., and McLean, F. E., *Effect of Thermal Properties on Laminar Boundary Layer Characteristics*, NACA TN 2916, 1953.

[6] Van Driest, E. R., The Laminar Boundary Layer With Variable Fluid Properties, Preprints of papers, 1954 Heat Transfer and Fluid Mechanics Institute, p. 127, University of California, Berkeley.

[7] Moore, L. L., *A Solution of the Laminar Boundary-Layer Equations for a Compressible Fluid with Variable Properties, Including Dissociation*, Journal of the Aeronautical Sciences, Vol. 19, pp. 505–518, 1952.

[8] Crown, J. C., *The Laminar Boundary Layer at Hypersonic Speeds*, NAVORD Report 2299, 1952.

Remark on Supersonic Nozzle Design

R. E. Meyer

Department of Aeronautics, University of Sydney, Australia

March 21, 1955

RENEWED INTEREST has been shown recently in these columns in the problem of calculating the flow in the transonic part of two-dimensional supersonic wind-tunnel nozzles.[1, 2] It appears, however, that an earlier paper by Cherry[3] giving the solution of the *exact* hodograph equation for the nozzle problem in a practical form has escaped the knowledge of aerodynamicists. It may therefore be desirable to point out briefly the usefulness of Cherry's method of nozzle design.

Cherry's solution is in the form of a series of eigenfunctions of the hodograph equation, the first of which possesses the particular sonic singularity of nozzle flows with nonzero pressure gradient at the throat. The solution for any prescribed analytic distribution of pressure along the axis of symmetry can be obtained by a suitable choice of the coefficients of the series.

The pressure distribution on the axis of symmetry need not, however, be prescribed in detail. Each eigenfunction is an exact solution of the hodograph equation, and a finite number of them suffice to meet all physical requirements of nozzle design. A nozzle for $M = 2.41$ has been designed for the Sydney University Supersonic Tunnel from computations kindly supplied by Professor Cherry, and it was found that only two eigenfunctions were required! The Mach Number distributions on axis and liner are shown in Fig. 1.

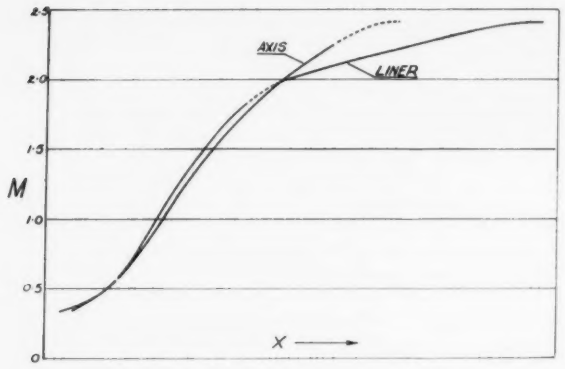

FIG. 1.

The low-speed contraction was completed, for $M < 0.34$, by methods of incompressible, three-dimensional duct design. At the other end of the nozzle, the hodograph solution was joined to the simple wave region by a narrow transition strip computed by the conventional method of characteristics, in order to avoid any discontinuity of pressure gradient and liner curvature; this transition is indicated by the dashed segments of the curves.

REFERENCES

[1] Ehlers, F. E., *On some Solutions of the Hodograph Equation which yield Transonic Flows through a Laval Nozzle*, Journal of the Aeronautical Sciences, Vol. 22, No. 2, pp. 107–123, February, 1955.

[2] Chaix, B., and Henrici, P., *On the design of Two-dimensional Supersonic Nozzles by the Method of Characteristics*, Journal of the Aeronautical Sciences, Vol. 22, No. 2, pp. 140–142, February, 1955.

[3] Cherry, T. M., *A Transformation of the Hodograph Equation and the Determination of Certain Fluid Motions*, Phil. Trans. Roy. Soc. A, Vol. 245, No. 904, pp. 583–626, 1953.

Experimental Investigation of Influence of Edge Shape on . . .

(*Continued from page 533*)

[17] Van Dyke, M., *First- and Second-Order Theory of Supersonic Flow Past Bodies of Revolution*, Journal of the Aeronautical Sciences, Vol. 18, No. 3, pp. 161–178, March, 1951.

[18] Lange and Wacke, *Test Report on Three- and Six-Component Measurements on a Series of Tapered Wings of Small Aspect Ratio (Partial Report: Triangular Wing)*, NACA TM 1176, May, 1948.

[19] Low, L., and Stone, H., *The Subsonic Characteristics of Wings in Combination With Slender Bodies of Revolution*, Cornell Aeronautical Laboratory Report No. CAL/CM-679, July, 1951.

[20] Hawes, J., and May, R., Jr., *Investigation at Low Speed of the Effectiveness and Hinge Moments of a Constant-Chord Ailavator on a Large-Scale Triangular Wing With Section Modification*, NACA RM L51A26, April, 1951.

[21] Berndt, S., *Three-Component Measurement and Flow Investigation of Plane Delta Wings at Low Speeds and Zero Yaw*, KTH-Aero TN4, June, 1948.

[22] Anderson, A., *Chordwise and Spanwise Loadings Measured at Low Speed on Large Triangular Wings*, NACA RM A9B17, April, 1949.

[23] Tosti, L., *Low-Speed Static Stability and Damping-in-Roll Characteristics of Some Swept and Unswept Low Aspect Ratio Wings*, NACA TN 1468, October, 1947.

[24] Flachsbart, O., *Messungen an ebenen und gewölbten Platten*, Ergebnisse der Aerodynamischen Versuchsanstalt zu Göttingen, IV, Lief, p. 96, 1932.

[25] Anderson, A., *An Investigation at Low Speed of a Large-Scale Triangular Wing of Aspect Ratio Two. I—Characteristics of a Wing Having a Double-Wedge Airfoil Section With Maximum Thickness at 20-Percent Chord*, NACA RM A7F06, November, 1947.

[26] Jaquet, B., Queijo, M., and Lichtenstein, J., *Low-Speed Static Longitudinal Stability and Control Characteristics of a 60° Triangular-Wing Model Having Half-Delta Tip Controls*, NACA RM L51D20a, June, 1951.

[27] Winter, H., *Flow Phenomena on Plates and Airfoils of Short Span*, NACA TM 798, July, 1936.

[28] Kolbe, C., and Tinling, B., *Tests of a Triangular Wing of Aspect Ratio 2 in the Ames 12-Foot Pressure Wind Tunnel. III—The Effectiveness and Hinge Moments of a Skewed Wing-Tip Flap*, NACA RM A8E21, September, 1948.

[29] Jones, R., *Properties of Low Aspect Ratio Pointed Wings at Speeds Below and Above the Speed of Sound*, NACA TR 835, 1946.
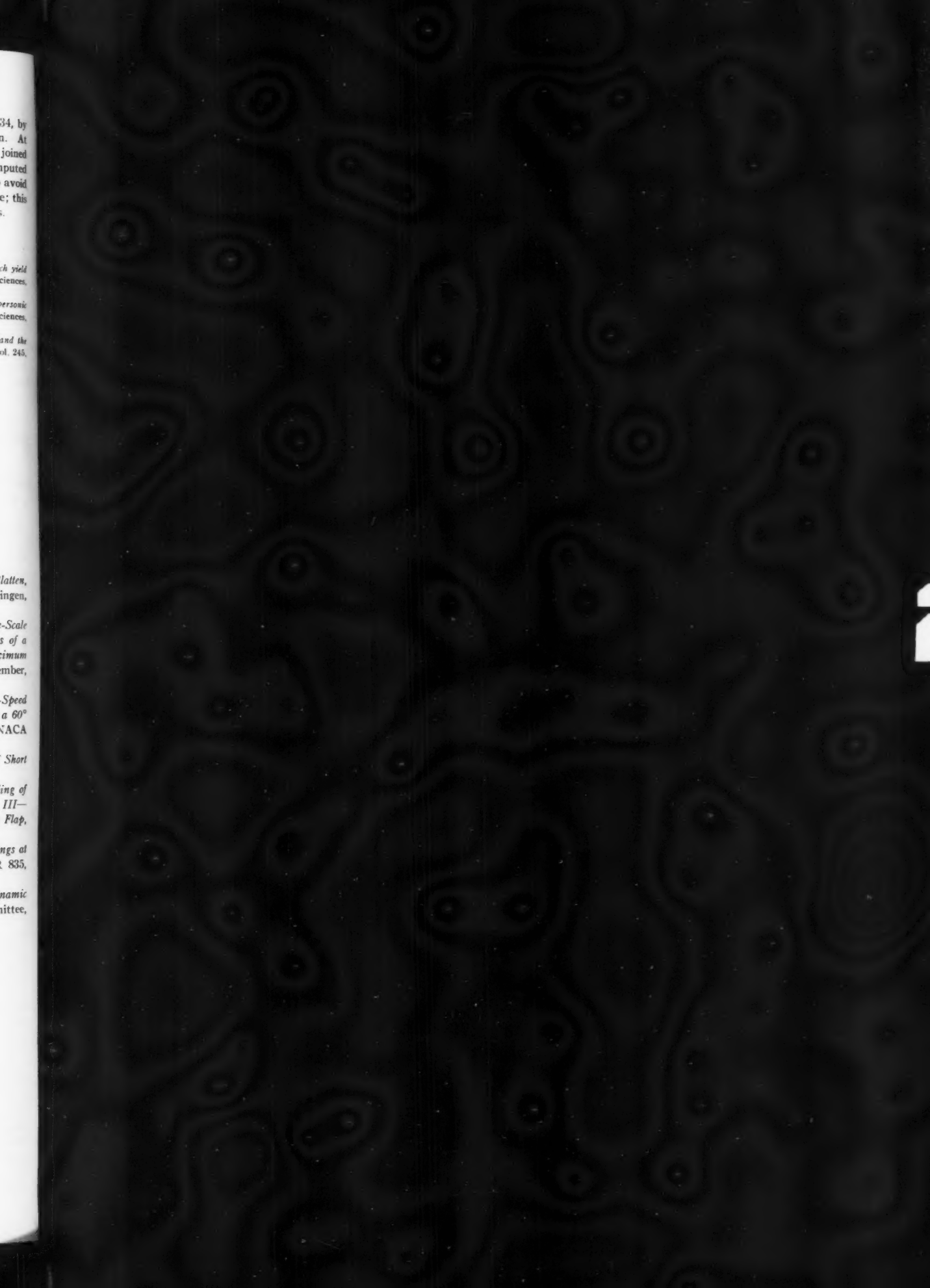
[30] Munk, M., "Fluid Mechanics Part II." *Aerodynamic Theory*, W. F. Durand, Editor, Durand Reprinting Committee, Vol. I, pp. 273–275, 1943.